

In vivo **quantification of absorption changes
in the human brain by time-domain
diffuse near-infrared spectroscopy**

vorgelegt von
Dipl.-Phys.
Alexander Jelzow
aus St. Petersburg

von der Fakultät II - Mathematik und Naturwissenschaften
der Technischen Universität Berlin
zur Erlangung des akademischen Grades

Doktor der Naturwissenschaften
- Dr. rer. nat. -

genehmigte Dissertation

Promotionsausschuss:

Vorsitzender: Prof. Dr. A. Knorr
Berichter: Prof. Dr. R. Macdonald
Berichter: Prof. Dr. U. Woggon
Berichter: Dr. J. Steinbrink

Tag der wissenschaftlichen Aussprache: 24. Oktober 2013

Berlin 2013
D 83

Моим родителям.

И Лиде.

Contents

Abstract	ix
Kurzzusammenfassung	x
Acknowledgements	xii
1 Introduction	1
References	5
2 Theory and Models	7
2.1 Functional Near-Infrared Spectroscopy	7
2.1.1 Anatomy of the Head	8
2.1.2 Tissue Compounds	11
2.1.3 Haemodynamics	13
2.1.4 Neuroscientific Measurement Modalities	15
2.2 Light Propagation in Tissue	19
2.2.1 Light Attenuation	19
2.2.2 Light Scattering	21
2.2.3 Modified Beer-Lambert Law	23
2.2.4 Time-Domain Reflectance of a Homogeneous Semi-Infinite Turbid Medium	25
2.3 Modalities of fNIRS	26
3 Instrumentation	31
3.1 PTB Brain Imager	31
3.2 Concurrent Measurement of fNIRS and Systemic Physiological Signals	35
3.3 Concurrent fNIRS and EEG	37
3.4 Concurrent fNIRS and fMRI	38

Contents

3.5	High Density and Large Area Measurement on a Human Head	40
4	Analysis of Time-Domain NIRS Signals by Moments	43
4.1	Moments of DTOFs	44
4.1.1	Convolution Properties	45
4.1.2	Influence of the Finite Integration Range	46
4.1.3	Correction Algorithm for Calculation of Moments	49
4.1.4	Uncertainty of Moments	54
4.2	Optical Properties Determined from Moments of DTOFs	64
4.2.1	Moments and Optical Properties of the Homogeneous Semi-Infinite Medium	65
4.2.2	Optical Properties of the Head <i>in vivo</i>	66
4.3	Sensitivity Factors for Retrieval of Absorption Changes	71
4.3.1	Sensitivity Factors for Moments and Homogeneous Absorption Changes	72
4.3.2	Sensitivity Factors <i>in vivo</i>	73
4.3.3	Correlations of <i>in vivo</i> Sensitivity Factors with Anatomical Parameters	77
4.4	Sensitivity Factors and Retrieval of Absorption Changes in a Layered Medium	81
4.4.1	Dependence on Background Optical Properties	82
4.4.2	Reconstruction Procedure for Two Layers	87
4.4.3	Comparison of the Reconstruction in Layered and Homogeneous Media	89
4.5	Summary	93
5	Validation of Data Analysis by Moments Using a Two-Layered Phantom	95
5.1	Two-layered Phantom Setup	96
5.1.1	Phantom Design and Preparation	96
5.1.2	Light Emission and Detection	98
5.1.3	Reproducibility of Fibre Reattachment	100
5.2	Basic Experimental Results	102
5.2.1	Absolute Moments and Relative Contrasts	102
5.2.2	Depth Sensitivity and Selectivity of Moments	106
5.3	Reconstruction of Absorption Changes	107
5.4	Optical Properties Derived by a Homogeneous Model	110
5.5	Future Layered Phantom Design	113
5.6	Summary	114

6	Applications of Time-Domain fNIRS <i>in vivo</i>	117
6.1	Concurrent Measurement of fNIRS and Systemic Physiological Signals	117
6.1.1	Subjects and Tasks	118
6.1.2	Brain Activation	119
6.1.3	Systemic Physiological Signals	124
6.1.4	Correlation Between fNIRS and Systemic Physiological Signals	126
6.2	Concurrent fNIRS and EEG	127
6.2.1	Subjects and Task	128
6.2.2	Data Analysis and Results	128
6.3	Concurrent td-fNIRS and fMRI	131
6.3.1	Subjects and Task	132
6.3.2	Data Analysis and Results	132
6.4	Summary	137
7	Summary	139
A	Supplementary Materials	143
A.1	Moments of Homogeneous SIM	143
A.2	Uncertainty of Moments Due to Photon Noise	145
A.3	Correction Algorithm for Moments Calculation: SPAD and HPM Detectors	149
B	Publications and Output	151
B.1	Publications	151
B.2	Awards	153
B.3	Conferences	154
C	List of Acronyms	155
	References	161

Abstract

Measurement of the brain activity is essential for the understanding of brain function and potentially for the diagnosis of brain pathologies. Human brain activity is accompanied by cerebral haemodynamics, i.e. local concentration changes of oxy- and deoxyhaemoglobin. These changes can be measured non-invasively and *in vivo* by functional near-infrared spectroscopy (fNIRS) which thereby provides an indirect measure of the brain activity. However, accurate quantification of haemoglobin concentrations is hampered by the strong light scattering of tissue, the heterogeneous structure of the head and the depth of the brain cortex. Moreover, non-cerebral haemodynamics overlay the desired cerebral signals and can mask the actual brain activity.

In this thesis a time-domain NIRS technique together with data analysis based on moments of distributions of time of flight of photons was employed to improve the quantification. For retrieval of haemoglobin concentration changes an improved method was developed. It is based on an approximation of the head by a layered structure and uses experimental data to adapt reconstruction related parameters to the individual measurement. This method was validated on a two-layered phantom and applied to data obtained on healthy subjects *in vivo*. The results were also compared to data from a reconstruction based on a homogeneous semi-infinite medium. This method benefits from the intrinsic depth selectivity of the higher order moments only. In addition, time-domain fNIRS *in vivo* measurements were performed in combination with other neuroimaging modalities and the recording of systemic physiological signals. The obtained data was used for validation based on the complimentary information provided by the different modalities.

With a two-layered heterogeneous phantom absorption changes were retrieved using the approach based on the layered medium with an accuracy of $\pm 10\%$. In the *in vivo* case it was possible to separate superficial and cerebral haemodynamics. Furthermore, the intrinsic underestimation of the cerebral absorption changes obtained using the model of the homogeneous medium was strongly reduced if the new approach based the layered structure was used. In the *in vivo* case this results in up to tenfold higher haemoglobin concentration changes.

The approach presented here allows for improved quantification of cerebral haemodynamics in fNIRS studies. The separation of the superficial signal contribution leads to more reliable detection of the brain activation.

Kurzzusammenfassung

Das Vermessen der Gehirnaktivität ist essentiell für das Verständnis von Hirnfunktion und potentiell auch für die Diagnose von Hirnerkrankungen. Die Hirnaktivität wird begleitet von zerebralen hämodynamischen Prozessen, die durch lokale Konzentrationsänderungen von Oxy- und Desoxyhämoglobin in Erscheinung treten. Mittels der funktionellen Nahinfrarotspektroskopie (fNIRS) können diese Änderungen, und damit indirekt die Hirnaktivität, *in vivo* und nicht-invasiv gemessen werden. Jedoch wird eine genaue Quantifizierung der Konzentrationsänderungen durch die starke Lichtstreuung im Gewebe, die heterogene Kopfstruktur und das tiefliegende Gehirn erschwert. Darüber hinaus überlagern nicht-zerebrale hämodynamische Prozesse das zerebrale Signal und können die eigentliche Hirnaktivierung verschleiern.

In dieser Arbeit wurde die Quantifizierung der Konzentrationsänderungen mit Hilfe der zeitaufgelösten Nahinfrarotspektroskopie in Verbindung mit der Momentenmethode zur Analyse von Photonen-Laufzeit-Verteilungen verbessert. Zur Berechnung von Hämoglobinkonzentrationsänderungen wurde basierend auf einem Schichtmodell des Kopfes eine Rekonstruktionsmethode entwickelt, bei der die Rekonstruktionsparameter individuell anhand der experimentellen Daten anpasst werden. Diese Methode wurde mit Hilfe eines Zwei-Schicht-Phantoms validiert und auf Messdaten angewendet, die *in vivo* an gesunden Probanden gewonnen wurden. Die Ergebnisse der Rekonstruktion wurden auch mit denen aus einer Rechnung verglichen, die auf einem Modell des homogenen semi-infiniten Mediums basiert und ausschließlich von der intrinsischen Tiefenselektivität der Momente höherer Ordnung profitiert. Außerdem wurde die zeitaufgelöste fNIRS-Technik mit anderen Neuroimaging-Techniken und Aufzeichnungen von systematisch-physiologischen Signalen bei *in vivo*-Messungen kombiniert. Die unterschiedlichen Modalitäten lieferten komplementäre Informationen, die zur Validierung von fNIRS benutzt wurden.

Am heterogenen Zwei-Schicht-Phantom konnten mit Hilfe der auf dem Schichtmodell basierenden Methode Absorptionsänderungen mit einer Genauigkeit von $\pm 10\%$ rekonstruiert werden. In Falle von *in vivo*-Daten war es damit möglich, die oberflächlichen und zerebralen hämodynamischen Verläufe zu trennen. Während der homogene Ansatz Absorptionsänderungen immanent unterschätzt, ist die schichtbasierte Methode in der Lage dies zu kompensieren. Das resultiert in bis zu zehnfach größeren Werten von Hämoglobinkonzentrationsänderungen.

Die hier vorgeschlagene schichtbasierte Methode ermöglicht, die Quantifizierung zerebraler hämodynamischer Verläufe zu verbessern. Die Abtrennung der oberflächlichen Signalanteile führt zur zuverlässigeren Detektion der Hirnaktivität.

Acknowledgements

First of all, I would like to thank my supervisor Prof. Dr. R. Macdonald for his critical feedback and the support in the recent years. I am also very thankful to Prof. Dr. U. Woggon and Dr. J. Steinbrink for being the referees of this thesis.

Dr. H. Wabnitz was a supportive and critical colleague and supervisor during the whole period of my thesis. This work would not be possible without her. Dr. E. Kirilina was the most enthusiastic scientist I had the pleasure to work with. I thank Dr. P. Koch with whom I planned and accomplished the most exhausting *in vivo* experiments. I thank my colleagues Dr. O. Steinkellner, Dr. M. Mazurenka, Dr. B. Ebert, Dr. A. Hagen, Dr. R. Brühl and Dr. T. Dziekan for the many informative discussions but also for the non-scientific conversations.

Peter Pawlak hat als Feinmechaniker indirekt an allen von mir durchgeführten Experimenten mitgewirkt. Ohne seine Erfahrung und sein Geschick hätte so mancher experimenteller Aufbau nicht realisiert werden können. Herr Walter und Herr Jagemann haben mir unzählige Male im Bereich Elektronik geholfen. Kein Experiment hätte ohne die kleinen „Kästchen“ aus ihrem Labor so durchgeführt werden können. Ein besonderer Dank geht an Frank Wojcik für seinen scheinbar unermesslichen Vorrat an Computerzubehör und sein stets offenes Ohr.

I had the unique opportunity to work within the nEUROpt project. It was a pleasure to collaborate with all the great scientist in the field of time-domain fNIRS from Charité Universitätsmedizin Berlin, Politecnico di Milano, Institute of Biochemistry and Biophysics in Warsaw, University College London and ILM in Ulm. I acknowledge the European Community for the funding: “The research leading to these results has received funding from the European Community’s Seventh Framework Programme [FP7/2007-2013] under grant agreement No. FP7-HEALTH-F5-2008-201076.”

Я искренне благодарен своим родителям и всем своим друзьям за поддержку в течении последних лет. Именно они, вновь и вновь, напоминали мне, что есть жизнь вне лаборатории и науки.

Chapter 1

Introduction

Human brain function is existential. In the past many efforts have been made to develop functional neuroimaging techniques in order to provide direct or indirect measurement of the brain activity. Undoubtedly, experimental assessment of the brain leads to better understanding of the brain function with the potential to diagnose brain dysfunction. One of the techniques capable of functional brain imaging is the functional near-infrared spectroscopy (fNIRS). The fNIRS technique measures cerebral concentration changes of oxy- and deoxyhaemoglobin. Haemoglobin is an important constituent of the blood responsible for the oxygen transport and thereby involved in the metabolism and in the neuronal activity of the brain. A typical fNIRS measurement is performed non-invasively and *in vivo* by a portable and cost-effective device which can be placed at the bedside. Since the fundamental experiments by Jöbsis [1] in 1977 fNIRS underwent a versatile but rather slow development [2]. Many methodological and modelling difficulties have been overcome in the recent years. This accelerated the commercialisation of fNIRS and its translation into the practice of psychological and clinical research. However, some fundamental challenges still remain. A reliable quantification of haemoglobin concentration changes in the brain is mainly hampered by the light scattering which also complicates the localisation and the depth resolution. In addition, superficial signal contributions resulting from systemic physiological processes can mask the true brain activation. In this thesis these issues are addressed by the time-domain fNIRS measurement technique along with data analysis based on moments of distributions of time of flight of photons.

Basic mechanisms relevant for fNIRS are well understood. Changes in the haemoglobin concentration cause absorption changes which can be measured optically. Light absorption and scattering are fundamental physical processes and have been studied and applied over centuries. In the spectral range from

1. Introduction

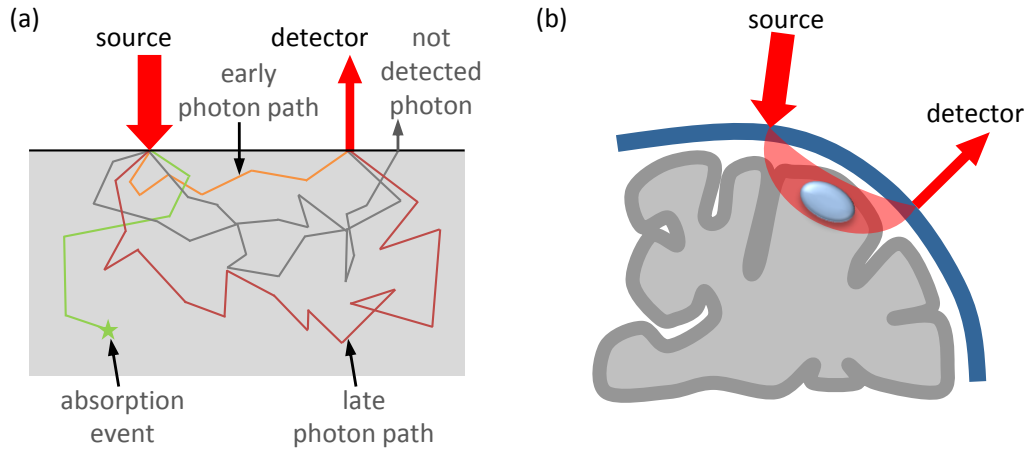


Figure 1.1: Photon propagation in strong-scattering media. (a) Photons travel along different paths in the scattering medium (grey) which influences the time of flight. Most photons get absorbed inside the medium or escape from it undetected. (b) Arrangement of source and detector fibres on the surface the head. The “banana” illustrates the sampled volume. The sensitivity to absorption changes in the brain increases with the source-detector separation.

about 650 nm to 1000 nm (NIR) living tissue exhibits rather high scattering but low absorption. As illustrated in Fig. 1.1a photons propagating through tissue undergo multiple scattering events so that the information about their initial flight direction gets lost very soon. The propagation of light can then be described as a diffusion of the photon density in the medium which is strongly different from classical optical imaging. For better differentiation often the term diffuse optical imaging (DOI) is used. The simulation of light propagation in scattering media with known optical properties (forward problem) has been successfully performed by numerical methods such as the finite element method or Monte-Carlo (MC) simulations. The MC method is computationally very expensive but due to the accuracy of the underlying models it is *de facto* the gold standard¹ for the solution of forward problems for arbitrary geometries. In order to reduce the computational effort the diffusion approximation to the equation of radiative transfer was used to obtain solutions for specific geometries. These faster solutions are useful for the characterisation of scattering media but they also exhibit inaccuracies under some conditions, e.g. for low scattering and high absorption.

In DOI the central task is the reconstruction of optical properties from data obtained by an optical measurement (inverse problem, IP). In contrast to the forward problem the IP is ill-posed and therefore much more difficult

¹The best method under given conditions.

to solve [3]. Usually, a forward simulation is needed to solve an IP. The IP is strongly simplified if only changes of absorption have to be reconstructed. This is the case in fNIRS where typically small changes of optical quantities are measured at two or more wavelengths and then used to reconstruct absorption changes and subsequently changes in haemoglobin concentrations.

The comparably low tissue absorption in the NIR range allows photons to penetrate 2 cm to 3 cm deep into the tissue and to be scattered back to the surface where they can be detected. In a typical fNIRS setup the head is illuminated by light via an optical fibre and the diffusely reflected light is then collected 2 cm to 5 cm away by a fibre bundle (Fig. 1.1b). In general, with increasing source-detector separation the total number of photons escaping from the medium strongly decreases. However, at the same time the fraction of photons which have a high probability of visiting the brain increases. This property is mainly exploited in the widely used continuous-wave (cw) fNIRS which measures changes of the light intensity at the head surface. In addition, photons can be analysed by their time of flight through tissue. Late photons have a higher probability of visiting deeper lying tissue than early photons (Fig. 1.1a). The time-of-flight (TOF) of photons can be measured using the time-domain (td-) fNIRS technique which is employed in the work presented here.

Another challenge in fNIRS is the need to separate superficial and cortical absorption changes. This requires a method which can provide depth resolution. It can be obtained from the analysis of the TOF of photons as measured by the time-domain fNIRS. The result of a time-domain measurement is the so called distribution of time of flight of photons (DTOF) with a typical width of about a nanosecond. Changes of a DTOF measured in fNIRS are in the order of a few picoseconds. This information can be used to reconstruct absorption changes at different depths. Steinbrink [4] developed a method to retrieve depth resolved absorption changes based on the analysis of the full DTOF. However, the method requires a rather inaccurate and expensive deconvolution of the measured data and the instrumental response function (IRF). Liebert et al. [5] introduced the method of moments which offers a superior handling of the IRF influence, higher robustness and other advantages. This method, its further development, verification and application to *in vivo* data is in the main focus of this thesis.

Basic theory of light propagation, optical modalities and physiology relevant for fNIRS are discussed in Chapter 2. The time-domain instrumentation used throughout the thesis as well as the configurations for the multi-modal measurements are described in Chapter 3. Chapter 4 introduces the method of moments for td-fNIRS and addresses its various aspects. First, basic definitions and properties such as accuracy and noise are discussed. A newly

1. Introduction

developed algorithm to correct for systematic deviations is also presented. Further the influence of the photon noise on the detectability of small changes of moments is investigated. In Section 4.2 the retrieval of optical properties of the head *in vivo* and associated difficulties are discussed. Sections 4.3 and 4.4 deal with the reconstruction of absorption changes using the method of moments. Two approaches based on a homogeneous semi-infinite and a layered model are presented. Both rely on sensitivity factors which are either obtained directly from the optical measurement or calculated using forward models and optical properties of tissue. These optical properties are obtained directly from individual measurements. This eliminates the need to use strongly varying optical properties from literature and accounts for the inter-subject variability. A two-layered reconstruction approach based on a measurement at a single source-detector separation and intended for the practical use in td-fNIRS is introduced. Chapter 5 presents the experimental validation of the method of moments as well as the reconstruction approaches on a two-layered liquid phantom.

The fNIRS technique can be used as a stand-alone technique or in combination with other neuroscientific modalities. The latter approach is potentially very promising because it allows to combine information about the same or related processes but obtained by independent measurements.

Magnetic resonance imaging (MRI) can provide rich anatomical and spatial information missing in fNIRS. Electroencephalography (EEG) gives direct access to the neuronal signals preceding the haemoglobin concentration changes. Systemic physiological signals (SPS), e.g. blood pressure or heart rate, are connected to signal variations in fNIRS and help to understand the underlying physiology. Multi-modal measurements can be used to verify the techniques against each other or gain new insights into neurological and physiological processes. The feasibility of *in vivo* measurements employing td-fNIRS with concurrent and/or subsequent MRI, EEG and recording of SPS is demonstrated in Chapter 6. In this context the use of the combined approaches for the investigation of neurovascular coupling and for the calibration of the BOLD signal in fMRI are discussed. The td-fNIRS data is analysed by the homogeneous and the two-layered models with the latter providing a better separation of the superficial and cortical signal contributions. This separation capability is beneficial for both the stand-alone and the multi-modal application of fNIRS.

References

- [1] F. F. Jöbsis. “Noninvasive, infrared monitoring of cerebral and myocardial oxygen sufficiency and circulatory parameters”. In: *Science* 198.4323 (Dec. 1977), pp. 1264–1267. DOI: 10.1126/science.929199 (cited on p. 1).
- [2] M. Ferrari and V. Quaresima. “A brief review on the history of human functional near-infrared spectroscopy (fNIRS) development and fields of application”. In: *NeuroImage* (Mar. 2012). DOI: 10.1016/j.neuroimage.2012.03.049 (cited on p. 1).
- [3] S. R. Arridge. “Optical tomography in medical imaging”. In: *Inverse Problems* 15.2 (Apr. 1999), R41. DOI: 10.1088/0266-5611/15/2/022 (cited on p. 3).
- [4] J. Steinbrink. “Near-infrared-spectroscopy on the adult human head with picosecond resolution”. In German. PhD Thesis. Berlin: FU Berlin, Nov. 2000 (cited on p. 3).
- [5] A. Liebert, H. Wabnitz, J. Steinbrink, H. Obrig, M. Möller, R. Macdonald, A. Villringer, and H. Rinneberg. “Time-Resolved Multidistance Near-Infrared Spectroscopy of the Adult Head: Intracerebral and Extracerebral Absorption Changes from Moments of Distribution of Times of Flight of Photons”. In: *Applied Optics* 43.15 (2004), pp. 3037–3047. DOI: 10.1364/AO.43.003037 (cited on p. 3).

Theory and Models

In this chapter the fundamentals of functional near-infrared spectroscopy (fNIRS) are introduced. Section 2.1 discusses the anatomical and physiological details important for the understanding of fNIRS. From the optical point of view biological tissue is a so called turbid medium. Theories describing light propagation in such media are discussed in Section 2.2. Over the recent years various experimental techniques have been developed to assess functional brain activity. An overview of these methods with a special focus on time-domain fNIRS is given in Section 2.3.

2.1 Functional Near-Infrared Spectroscopy

Functional near-infrared spectroscopy fNIRS is a non-invasive optical technique for indirect measurement of neuronal brain activity. Functional NIRS exploits the fact that biological tissue is comparatively transparent in the near-infrared spectral range (wavelength 600 nm to 1000 nm) where light can penetrate a few centimetres into the tissue. The fNIRS technique measures changes in light absorption induced by tissue concentration changes of oxygenated and deoxygenated haemoglobin which are caused by neuronal activity.

In 1977 Frans F. Jöbsis reported the first optical measurement performed during hyperventilation on a human adult *in vivo* [1]. This experiment was the beginning of an over 35 years long development of the fNIRS technique, its application in the clinics and neuroscience, construction of research and commercial instruments and even battery operated wearable devices. An overview of the history of fNIRS can be found in [2] (see also a special issue on fNIRS in *NeuroImage* [3]).

As illustrated in Fig. 2.1 the fNIRS method provides an indirect mea-

2.1. Functional Near-Infrared Spectroscopy

nervous system and mainly responsible for information processing, functional and behavioural control. Because of this the brain is in the main focus of neuroscientific research.

The brain is surrounded by the *dura mater*, the cerebral spinal fluid (CSF), the skull and the scalp which all can be penetrated by near-infrared light. These are the relevant compartments for the light propagation in the head. A cross section of the outer part of the brain and its surrounding tissue is shown in Fig. 2.2. In a good approximation the geometry of this part can be assumed to be layered which is an advantageous simplification for light propagation models.

The scalp forms the outer compartment outside the skull. It is made up of the epidermis, dermis and subcutaneous tissue. The subcutaneous tissue is an adipose tissue which is mainly composed of fat. The scalp contains sweat glands and blood vessels and is involved into body's temperature regulation. In fNIRS optical signals are sensitive to absorptions changes in the superficial tissue. Therefore scalp haemodynamics can potentially affect the results derived by the fNIRS technique.

The adult human skull consists of a total of 22 bones which forms a cavity for the brain and a structure for the face. The skull is made up from cancellous bone which is less dense than the compact bone and more vascular. It contains water and blood which mainly contribute to its absorption in the NIR range. The total absorption and scattering of the skull is comparable to those of the surrounding tissue [8, 9].

Underneath the skull is the *dura mater* which is a tough layer protecting the brain from movement and over-stretching of connecting blood vessels. The surface of the brain is covered by the *pia mater*. It is in direct contact to the cortex. The *arachnoid mater* and subarachnoid space are located between *pia* and *dura mater*. The subarachnoid space is filled with *trabeculae* (similar to filaments) and communicating channels which contain the cerebral spinal fluid (CSF).

The optical properties of the tissues discussed above are roughly in the same range, i.e. μ_a from 0.04 cm^{-1} to 2 cm^{-1} and μ'_s from 4 cm^{-1} to 50 cm^{-1} (see Section 4.2 for details). A controversial discussion about the scattering of the CSF layer can be found in literature. A really clear, i.e. non-scattering, CSF would strongly influence the light propagation in the head as it was shown on phantoms [10] and by Monte-Carlo simulations [11]. The absence of scattering by the CSF surrounded by other scattering tissues would produce light piping effects which cannot be modelled using light propagation models based on the diffusion approximation. However, by comparing an *in vivo* multi-distance measurement performed on a adult human with accompanying Monte-Carlo simulations head Steinbrink [12, p. 81] has shown that the CSF layer must be

2. Theory and Models

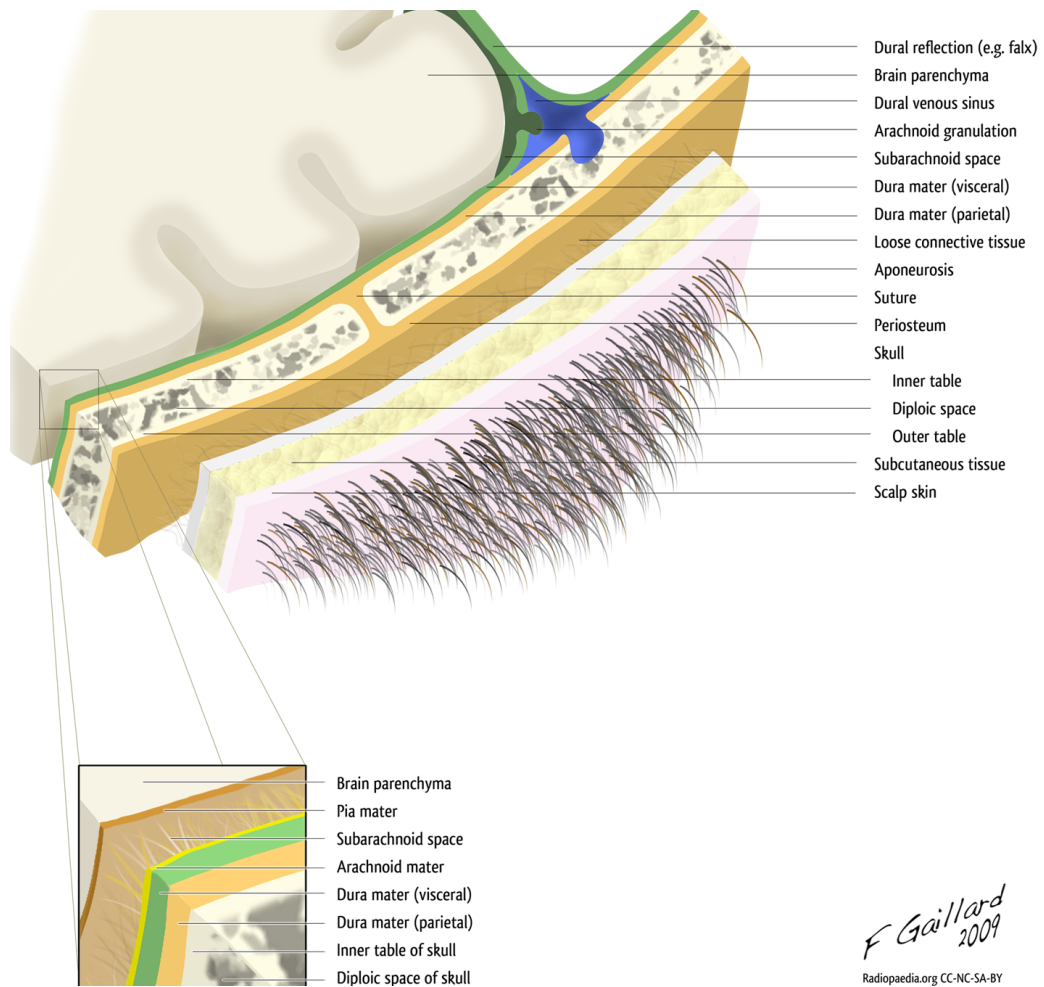


Figure 2.2: Cross section of a human scalp and skull (courtesy of Frank Gaillard published under CC-NC-CA-BY licence [7]).

at least a little scattering. In later work Okada and Delpy [13] modelled the CSF layer as a clear layer with small scattering cylinders mimicking *arachnoid trabeculae*. The Monte-Carlo method was used to investigate light propagation. They found that already a low density of cylinders produced results similar to *in vivo* data. Furthermore, the presence of even slightly scattering CSF substantially increased the partial optical path length in the brain. Therefore the scattering of the CSF is advantageous for brain imaging. In addition, Custo et al. [14] found that it is possible to use a larger scattering coefficient for the CSF layer and therefore to employ the diffusion approximation for forward models.

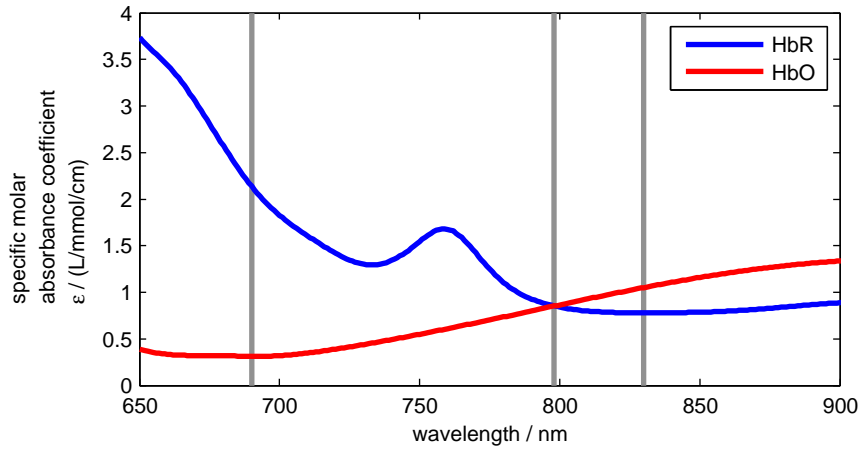


Figure 2.3: Oxy- and deoxyhaemoglobin (HbO, HbR) absorption spectra in the near-infrared region (taken from [5, 15]). Vertical lines (grey) correspond to the spectral position of the lasers used in the Brain Imager described in Section 3.1.

2.1.2 Tissue Compounds

Due to the low absorption of tissue in the range from 600 nm to 900 nm light can penetrate a few centimetres into the tissue. This spectral range is therefore frequently called the "optical biological window". Many optical applications such as pulse oxymetry, optical mammography, fNIRS and others exploit this unique property.

The main tissue compounds contributing to the absorption in the near-infrared range are water, lipids and haemoglobin. Haemoglobin (Hb) is a protein consisting of four heme groups and four polypeptide chains [16]. Hb is found in the red blood cells and is involved in the oxygen transport of all vertebrates. Compared to oxygen O_2 dissolved directly in blood Hb can carry a much larger amount of oxygen [17]. Once oxygen is bound Hb becomes oxygenated haemoglobin HbO_2 which can transport oxygen to a different place where it can be consumed, i.e. from lungs to the brain. If required for metabolism O_2 can be released and HbO_2 becomes deoxygenated. For that reason in the context of fNIRS haemoglobin without oxygen is typically called deoxygenated or reduced haemoglobin. There are numerous abbreviations for both species used throughout the literature, i.e. HbO_2 , Hb-O₂, HbO, OxyHb, O_2Hb and Hb, Hgb, DeHb, HHb, HbR, for oxygenated and deoxygenated haemoglobin, respectively. For practical reasons¹ throughout this thesis oxy-

¹ The abbreviations HbO, HbR and HbT consist from basic ASCII characters and can therefore be used without any restrictions in any written input including simple text, non-formatted documents, variable names in programming and subscripts. These properties,

2. Theory and Models

generated, deoxygenated and total haemoglobin will be abbreviated by HbO, HbR and HbT, respectively.

HbO and HbR exhibit different physical properties which are exploited in neuroimaging. Differences in the absorption spectra can be used to distinguish both species optically. In addition, HbR is a paramagnetic molecule while HbO is diamagnetic. This property is used in functional magnetic resonance imaging.

The concentration of total haemoglobin in tissue is simply the sum of the absolute concentrations of oxy- and deoxyhaemoglobin, C_{HbR} and C_{HbO} , respectively:

$$C_{\text{HbT}} = C_{\text{HbO}} + C_{\text{HbR}} \quad (2.1)$$

In fNIRS these concentrations are typically reported in $\mu\text{mol/l}$. Since mainly haemoglobin is responsible for the oxygen supply to the brain and other tissues the corresponding haemoglobin concentrations define the amount of oxygen available for metabolism. Therefore the tissue oxygen saturation S_{O_2} is defined as:

$$S_{\text{O}_2} = \frac{C_{\text{HbO}}}{C_{\text{HbT}}} \times 100\% \quad (2.2)$$

S_{O_2} is a clinically relevant parameter and typically reported in per cent. A reliable assessment of cerebral oxygen saturation still remains challenging [18].

The spectroscopic foundation of functional NIRS is the difference of the absorption spectra of HbO and HbR in the near-infrared range. Absorption spectra of HbO and HbR in terms of the specific molar absorbance coefficient ϵ are shown in Fig. 2.3. At the so called "isosbestic point" around 800 nm both haemoglobin species have equal ϵ values. In principle, at this position the concentration of the total haemoglobin can be determined from a measurement of light absorption at a single wavelength if there are no other relevant absorbers in the medium. A variety of haemoglobin absorption spectra has been published in the past [19]. Throughout this thesis spectra from [5, 15] will be used (also available online [20]).

The contribution of n tissue chromophores to the absorption coefficient μ_a can be calculated from their concentrations C_i in the tissue and their specific extinction coefficients ϵ_i :

$$\mu_a = \ln(10) \sum_{i=1}^n \epsilon_i C_i \quad (2.3)$$

An illustrative example for a tissue absorption spectrum is shown in Fig. 2.4. It was calculated using Eq. (2.3) and assuming a typical mean total haemoglobin

the resulting consistency and advantages are regarded to be superior to the chemically correct notation, i.e. Hb and HbO₂.

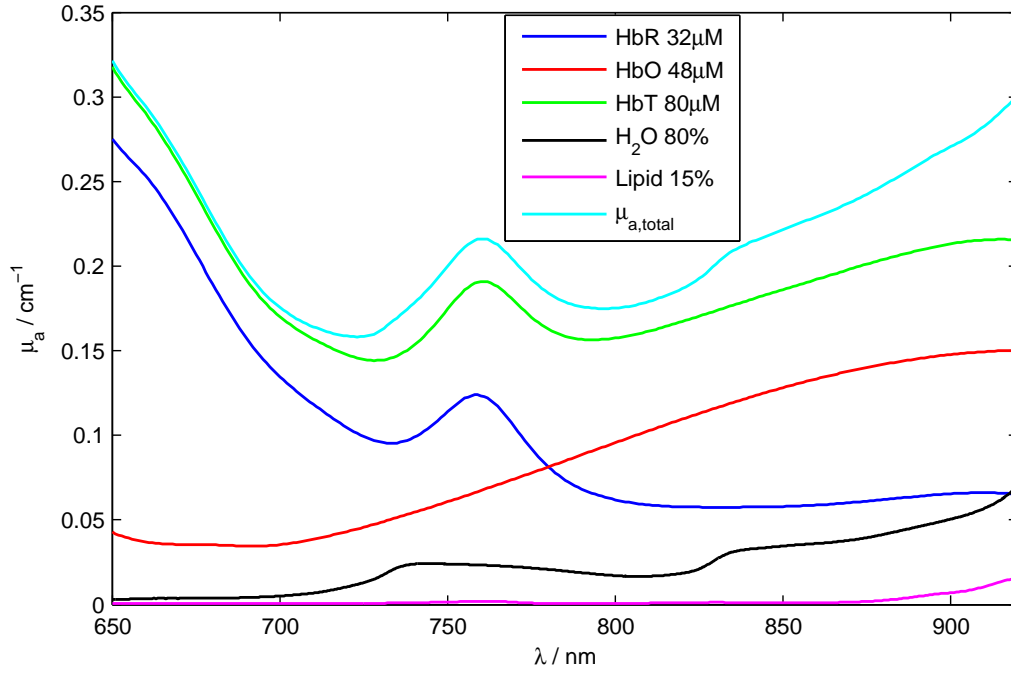


Figure 2.4: A potential absorption spectrum of tissue composed of oxy- and deoxyhaemoglobin (HbO, HbR), water and lipids. HbT denotes μ_a of the total haemoglobin which is the sum of the HbO and HbR contributions.

concentration of $80 \mu\text{mol/l}$, an oxygen saturation of 60 %, water content of 80 % and lipid content of 15 %. Absorption spectra were taken from [5, 15] for HbO and HbR, from [21] for water at 37° and from [22] for lipids. The largest contribution comes from the haemoglobin while the contribution of lipids is negligible.

2.1.3 Haemodynamics

Neuronal brain activity is accompanied by a localised vascular response which includes changes in the regional cerebral blood volume (rCBV) and flow (rCBF) and regional cerebral haemoglobin oxygen saturation. These quantities exhibit dynamic changes on a time scale of seconds and typically cover a larger volume than the actual neuronal activity. In functional MRI the vascular response $A(t)$ to a stimulus $S(t)$ is often modelled as a convolution of the stimulus $S(t)$ and the haemodynamic response function $\text{HRF}(t)$:

$$A(t) = \text{HRF}(t) \otimes S(t) \quad (2.4)$$

2. Theory and Models

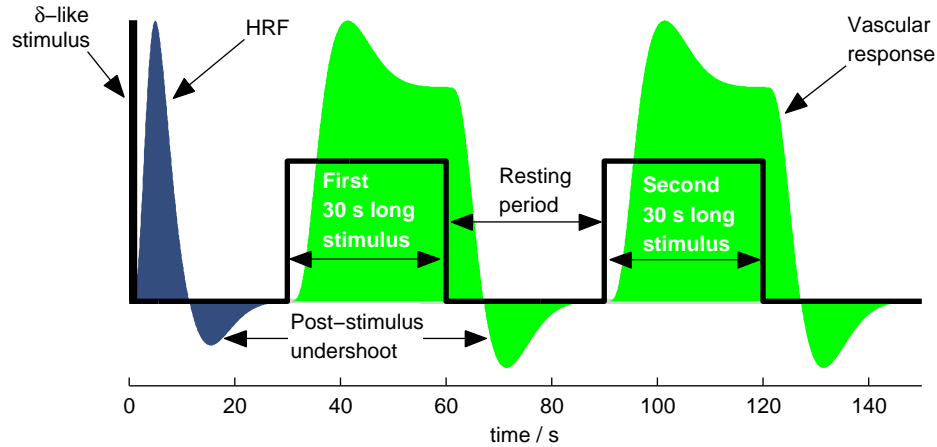


Figure 2.5: The canonical haemodynamic response function (HRF) as it used in fMRI and an example for the temporal course of a vascular response to two 30 s long stimuli (two blocks). The amplitudes of all functions have been normalised for better representation.

The HRF describes the vascular response to a δ -shaped stimulus [23]. The canonical HRF as it is used in the popular software package SPM (Statistical Parametric Mapping)² for functional MRI data analysis is shown in Fig. 2.5. The HRF exhibits a main positive part which is followed by a small negative fraction - the so called “post-stimulus” undershoot. This feature of the HRF is still under controversial discussion [24–26]. In the case of a longer stimulus, e.g. a 30 s long one as in Fig. 2.5, it is convolved with the HRF according to Eq. (2.4).

The canonical HRF from fMRI is also widely used for fNIRS data despite concerns of its appropriateness [27, 28] in particular regarding the post-stimulus undershoot [26]. Also in the fMRI community the variability of the HRF across subjects and regions of the brain is an issue [29, 30].

A typical response to a stimulus as measured by fNIRS is illustrated in Fig. 2.6. The main features of the vascular response are the increase of the concentration changes of HbO and HbT and the decrease in HbR. The signals are delayed in time compared to the stimulus and show a late return to the baseline. A clear post-stimulus undershoot as present in fMRI most often cannot be seen in fNIRS. The amplitude of the HbO signal is typically approximately twice as large as the one of HbR.

There are two typical experimental arrangements used in neuroscience:

² The SPM software package is freely available online www.fil.ion.ucl.ac.uk/spm. The code required for the computation of the HRF is located in the Matlab functions `spm_hrf.m` and `spm_gpdf.m`.

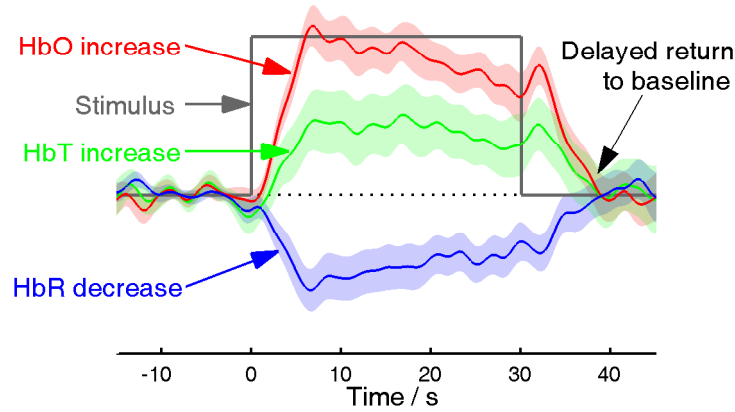


Figure 2.6: Example of a typical response to a stimulus as obtained by an fNIRS measurement.

event related and block design. In the latter case stimulation blocks like the one shown in Fig. 2.5 are repeated for several times (typically 6 to 30 times). In fMRI and fNIRS studies the resting period typically lasts for 10 s to 30 s in order to let the vascular response return to the baseline. In the event related design short stimuli - events - are presented to the subjects in a randomised order. In both cases the vascular response can be modelled using Eq. (2.4). The block design is the simpler and more robust procedure to evoke neuronal activation. This design will be used throughout this thesis for functional experiments.

In addition to brain haemodynamics, functional experiments can be accompanied by superficial haemodynamic changes in the scalp. While the fMRI technique is essentially unaffected by these changes it is a great concern for fNIRS. Due to the relatively high sensitivity of the optical signals to absorption changes in the scalp fNIRS is more prone to artefacts due to task related superficial haemodynamics. Separation and rejection of those is essential and intensively investigated.

2.1.4 Neuroscientific Measurement Modalities

During the past decades there has been a rapid growth in the field of medical imaging and neuroscience. The brain structure as well as its function have been accessed and investigated non-invasively by a number of technologies including functional magnetic resonance imaging (fMRI), electroencephalography (EEG), magnetoencephalography (MEG), single photon emission computed tomography (SPECT), positron emission tomography (PET) and (functional) NIRS. All these techniques exploit different physical principles, phys-

2. Theory and Models

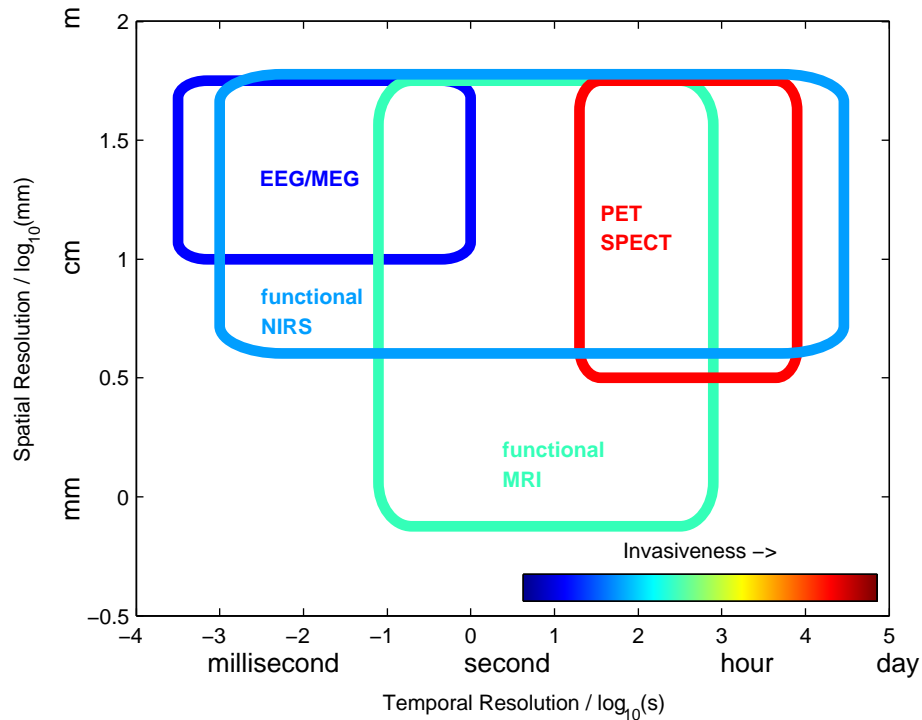


Figure 2.7: Comparison of neuroscientific modalities in terms of invasiveness, spatial and temporal resolution. Adapted from [31] and [32].

iological processes and provide different spatial and temporal resolution. In Fig. 2.7 the necessary trade-off between the properties of the modalities is visualised. In functional studies of the brain mainly fMRI, EEG, MEG and fNIRS are used. A brief description of principles of these techniques is given below.

EEG records oscillations of brain electric potentials on the scalp surface resulting from neural activity. For that typically 10 to 256 electrodes are attached to the skin of the head and differences in the voltage are measured. EEG can provide very high temporal resolution (up to 20 kHz) and measures very small voltage differences in sub μV range. EEG of the brain was first measured in 1924 by Hans Berger. Since then the technology was intensively developed. At the moment many diverse and affordable commercial devices for research and clinical use are available on the market. Recently, EEG based devices have been introduced for brain-computer interfaces.

MEG is capable of detecting neuronal activity by measuring basically the same electrical changes underlying the EEG signals. It records weak magnetic fields in the sub pT range resulting from the currents flowing across neurons. MEG requires special facilities with magnetic field shielding against

2.1. Functional Near-Infrared Spectroscopy

environmental influence and sensitive magnetometers (SQUIDs). Up to 300 sensors are used simultaneously. MEG and EEG have in common that the acquired signals are a mixture resulting from the activity from different brain regions. The inverse problem is ill-posed and requires extensive reconstruction algorithms. For EEG these procedures are hampered by the heterogeneity in conductivity between the head regions. These problems are less pronounced for MEG resulting in simpler reconstruction models [33]. MEG provides a non-contact measurement thereby reducing the preparations efforts and time of the experiment.

Functional MRI is a very popular technique in the field of neuroscientific and medical research. Functional MRI provides 3-dimensional images of the head and parts of the body. The technique is based on the detection of the relaxation of nuclear spins previously excited by a radio-frequency pulse and in a strong magnetic field (typically 1.5 T to 3 T). There is a variety of experimental parameters in MRI which can be optimised to image different organs or tissue types. For functional imaging of the brain the most widely used method is the recording of the so-called BOLD (blood oxygenated level dependent) signal. It is mainly based on the fact that the deoxygenated haemoglobin is paramagnetic while the surrounding blood plasma and oxygenated haemoglobin are diamagnetic. Therefore changes in the regional HbR concentrations produce a contribution to the MRI signals. The BOLD signal is a relative measure typically reported in percent and can be written as:

$$\text{BOLD} = \frac{\Delta S}{S_0} = T_E \kappa V_0 c_{\text{HbR},\text{B},0}^\beta \left(1 - \frac{V}{V_0} \left(\frac{c_{\text{HbR},\text{B}}}{c_{\text{HbR},\text{B},0}} \right)^\beta \right) \quad (2.5)$$

where , T_E the echo time, S_0 is the baseline signal (at $T_E = 0$) and ΔS is its change. $c_{\text{HbR},\text{B}}$ denotes the HbR concentration in the blood, V the cerebral blood volume. The parameter β depends on the diameter of blood vessels and the strength of the magnetic field. In a field of 1.5 T β is about 1.5. The parameter κ summarises multiple properties of the tissue (strength of the magnetic field, vessel geometry, susceptibility differences between blood and tissue). The subscript 0 denotes the basic state variables.

The poor knowledge of tissue dependent parameters and their variation across the head leads to the hampered quantification of the measured signals. Therefore in most studies the analysis is restricted to the detection of significant changes. For this reason the calibration of the BOLD signal is highly desired. It can be performed using additional and rather complicated experiments (hypercapnia, hypocapnia, R_2' calibration, see [34] for a review).

Finally, the functional near-infrared spectroscopy (fNIRS) measures changes in light absorption due to the variation of the concentrations of oxy- and deoxy-

2. Theory and Models

haemoglobin. The nature of the diffuse light propagation in living tissue limits fNIRS to imaging of the cortex of the brain with a spatial resolution in the centimetre range. The technique can measure changes in oxy- and deoxyhaemoglobin concentrations at a high temporal resolution up to 100 Hz which is more than sufficient to record the comparably slowly changing vascular signals.

In literature several names and abbreviations can be found referring to the optical techniques such as diffuse optical imaging or tomography (DOI or DOT), functional near-infrared spectroscopy (fNIRS or fNIR) or more generally NIRS, optical imaging or tomography (OI and OT). All these terms emphasise different aspects of the technique (i.e. diffuse light propagation, NIR spectral range) or to be associated with other techniques (i.e. computed tomography, functional MRI) and are also used in the field of optical mammography³. Throughout this thesis the term fNIRS will be used to underline the intention to use the technique for the investigation of brain function.

While fMRI is superior to fNIRS in terms of the spatial resolution and depth sensitivity there are also some disadvantages. Due to the strong magnetic field some subjects can experience mild vertigo or cannot be examined by MRI because of claustrophobia, implants and other. Sleep studies are hampered by the rather high acoustic noise level inside the MR-scanner. In general, MR-scanners are not portable and subjects are typically measured while they are resting in supine position. Furthermore, MR-facilities require special buildings and the initial and maintenance costs are high. In all these aspects fNIRS is or can potentially be superior to fMRI. Functional NIRS can be used at the bedside, to study infants and even freely moving subjects.

Apart of the many competitive aspects such as invasiveness, temporal or spatial resolution, fNIRS can be used complementary with other modalities. Concurrent measurements are possible as soon as mechanical difficulties are overcome. This implies the placement of the fNIRS optodes inside of a fMRI coil or underneath the MEG sensor or together with EEG electrodes. A combination of fNIRS with EEG or MEG can be used to study the neuro-vascular coupling in the brain and, potentially, its distortion. Combined with fMRI the vascular response in the brain can be measured by two methods simultaneously. In this case fMRI's spatial resolution can be beneficially combined with higher temporal resolution of fNIRS and its better quantification of the HbO and HbR concentration changes.

³ Optical mammography and fNIRS exploit the same principles of light propagation.

2.2 Light Propagation in Tissue

Light propagation in tissue is mainly governed by two processes: scattering and absorption. In the near-infrared spectral range tissue is strongly scattering which leads to a diffuse light propagation and the comparably strong back-scattering of light. Light absorbed by tissue compounds is released as heat or as fluorescence. Specific absorption spectra of those compounds can be exploited to determine their concentration. Below processes relevant for fNIRS are discussed.

2.2.1 Light Attenuation

In this section basic terminology and definitions of light attenuation in a non-scattering medium are introduced in agreement with international standards [35–37]. Let a homogeneous, non-scattering and non-luminescent medium be illuminated by the incident flux $\Phi_0(\lambda)$ at the wavelength λ and the transmitted flux be $\Phi(\lambda)$. The spectral transmittance $\tau(\lambda)$ is then defined as:

$$\tau(\lambda) = \frac{\Phi(\lambda)}{\Phi_0(\lambda)} \quad (2.6)$$

In addition the spectral absorbance is defined as:

$$A_s(\lambda) = -\log_{10} \tau(\lambda) \quad (2.7)$$

Similarly, using the natural logarithm the Napierian spectral absorbance is defined as:

$$A_n(\lambda) = -\ln \tau(\lambda) \quad (2.8)$$

The transmittance through a non-scattering medium of the thickness d is described by the Lambert-Bouguer’s law:

$$\tau(\lambda) = e^{-\mu_a(\lambda)d} \quad (2.9)$$

with $\mu_a(\lambda)$ being the linear absorption coefficient⁴. In this case μ_a describes the absorption of the medium empirically and does not contain any information about its origin. However, in a given spectral range the total absorption of a medium can result from the individual absorption of a number of substances in a transparent solution, e.g. chromophores like oxy- and deoxyhaemoglobin. A reformulation of Eq. (2.9) reflects this situation and is known as the Beer’s law:

$$\tau(\lambda) = e^{-k_\epsilon C} \quad (2.10)$$

⁴ In practice and throughout this thesis only the term “absorption coefficient” is used.

2. Theory and Models

where C is the amount of substance concentration and k_ϵ the absorption coefficient which is constant for the given experiment [38, p. 5]. The Lambert-Bouger's and the Beer's laws can be easily combined accounting for specific spectral absorption of multiple absorbing compounds:

$$\tau(\lambda) = e^{-\mu_a(\lambda)d} = 10^{-\sum_i \epsilon_i(\lambda)C_i d} \quad (2.11)$$

where C_i is the concentration and $\epsilon_i(\lambda)$ the specific molar absorbance coefficient of the i -th absorbing compound. In this form the equation is referred to as Beer-Lambert law. A rearrangement of the terms in Eq. (2.11) results in:

$$\mu_a(\lambda) = \ln(10) \sum_{i=1}^n \epsilon_i(\lambda)C_i \quad (2.12)$$

The spectral absorbance Eq. (2.7) is then given as:

$$A_s = \sum_{i=1}^n \epsilon_i(\lambda)C_i d \quad (2.13)$$

In the specific case when only the concentrations of the compound vary changes in the spectral absorbance ΔA_s are linearly related to the changes in concentration by:

$$\Delta A_s(\lambda) = d \sum_{i=1}^n \epsilon_i(\lambda) \Delta C_i = d \frac{\Delta \mu_a(\lambda)}{\ln(10)} \quad (2.14)$$

Using this relationship concentration changes ΔC_i can be retrieved from a measurement of $\Delta A_s(\lambda)$ at n or more wavelengths if the corresponding specific molar absorbance coefficients $\epsilon_i(\lambda)$ are known. The system of linear equations which must be solved in such a case can be written in a matrix form:

$$\begin{pmatrix} \Delta A_s(\lambda_1) \\ \vdots \\ \Delta A_s(\lambda_j) \end{pmatrix} = d \begin{pmatrix} \epsilon_1(\lambda_1) & \dots & \epsilon_i(\lambda_1) \\ \vdots & \ddots & \vdots \\ \epsilon_1(\lambda_j) & \dots & \epsilon_i(\lambda_j) \end{pmatrix} \begin{pmatrix} \Delta C_1 \\ \vdots \\ \Delta C_i \end{pmatrix} \quad (2.15)$$

Alternatively, the changes in concentrations can be calculated from the changes of the linear absorption coefficient $\Delta \mu_a$:

$$\begin{pmatrix} \Delta \mu_a(\lambda_1) \\ \vdots \\ \Delta \mu_a(\lambda_j) \end{pmatrix} = \ln(10) \begin{pmatrix} \epsilon_1(\lambda_1) & \dots & \epsilon_i(\lambda_1) \\ \vdots & \ddots & \vdots \\ \epsilon_1(\lambda_j) & \dots & \epsilon_i(\lambda_j) \end{pmatrix} \begin{pmatrix} \Delta C_1 \\ \vdots \\ \Delta C_i \end{pmatrix} \quad (2.16)$$

Strictly, the equations above are defined only for the non-scattering case but can also be used for scattering media. In the latter case the main challenge

is to reliably obtain the changes of the absorption coefficient $\Delta\mu_a(\lambda)$. The corresponding changes ΔC_i are then easily obtained by solving the set of linear equations in Eq. (2.16).

In its classical form the Beer-Lambert law does not consider scattering but only absorption. Still, the law can be modified in order to be useful for fNIRS (see Section 2.2.3).

2.2.2 Light Scattering

In biological tissue light is scattered by cells and their components with sizes ranging from nanometres to tens of microns. Cell membranes and cell organelles, e.g. nucleus (3 μm to 10 μm) and mitochondria (0.5 μm to 1.5 μm), contribute the most to the scattering relevant for fNIRS [6]. Thus the scatterers are larger or in the order of the used wavelengths about 800 nm. This is covered by the Mie and Rayleigh scattering regimes.

Scattering at a single particle is angle dependent and is described by the scattering phase function. An accurate description of this dependence at the microscopic scale is achieved by the Mie theory and requires rather computationally expensive calculations. A sufficiently good and analytical approximation of the phase function can be obtained using the Henyey-Greenstein phase function (HGP) [39]:

$$p(\theta) = \frac{1 - g^2}{4\pi(1 + g^2 - 2g \cos \theta)^{3/2}} \quad (2.17)$$

where g is the anisotropy factor, θ the scattering angle and $p(\theta)$ the phase function which is isotropic for $g = 0$. For biological tissue typical values of g are in the range from 0.6 to 0.95 which implies strong forward scattering. Figure 2.8a shows a comparison of the phase function calculated using the Mie theory and the Henyey-Greenstein formula. The HGP reproduces the general shape of the Mie prediction but does not show the fine oscillations. The amplitude at $\theta = 0$ is slightly overestimated by the HGP. Figure 2.8b illustrates the shape of the HGP for different values of g .

The diffuse propagation of near-infrared light in biological tissue is a result of multiple scattering events on multiple particles. A scattered photon travels a distance of the free path length l_s in the medium before it gets scattered again (Fig. 2.9). The scattering properties of such a medium can be sufficiently characterised by the anisotropy factor g and the scattering coefficient μ_s :

$$\mu_s = \frac{1}{\langle l_s \rangle} = \rho_s \sigma_s \quad (2.18)$$

2. Theory and Models

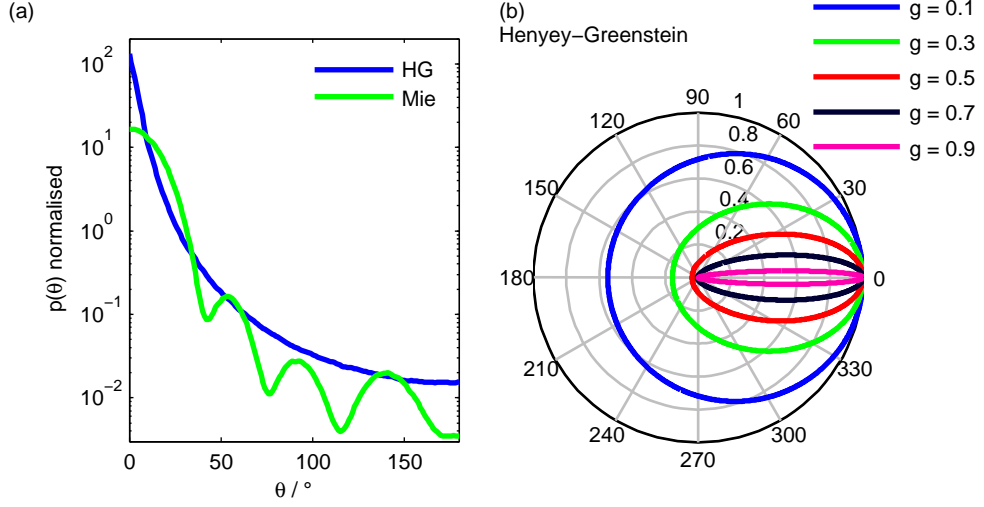


Figure 2.8: Illustration of the scattering phase function $p(\theta)$. (a) Comparison of $p(\theta)$ calculated using Mie theory and the Henyey-Greenstein (HG) phase function. Both phase functions were calculated for $g = 0.91$ and normalised for better comparison. The plot is a reproduction using data from [40, p. 46]. (b) Polar plot of the Henyey-Greenstein phase function $p(\theta)$ for several values of the anisotropy factor g . For better comparison $p(\theta)$ was normalised to the maximum value. High g value results in strong forward scattering.

where $\langle l_s \rangle$ is the mean free path length, ρ_s is the particle density and σ_s the scattering cross section of a single particle. After multiple scattering events the information about its initial direction of propagation gets lost. Therefore the scattering phase function effectively becomes isotropic. The medium is then sufficiently described by the so called reduced scattering coefficient μ'_s :

$$\mu'_s = \left(1 - \int_{4\pi} p(\theta) \cos \theta \, d\Omega \right) = (1 - g)\mu_s \quad (2.19)$$

At a depth $z_0 \approx 1/\mu'_s$ the scattering can be assumed to be effectively isotropic.

How many parameters are sufficient to characterise the medium under investigation also depends on the measurement geometry. In fNIRS typical

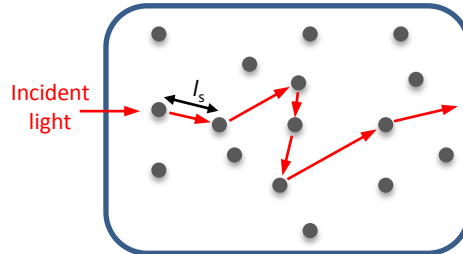


Figure 2.9: Multiple scattering of light by many particles and the free path length l_s .

source-detector separations are larger than 1 cm and μ'_s is in the order of 10 cm^{-1} . In this case the medium is sufficiently described by μ_a , μ'_s and the refractive index n . For smaller distances between the source and the detector μ_s and g instead of μ'_s should be used.

2.2.3 Modified Beer-Lambert Law

The terminology and definitions proposed in Section 2.2.1 are standardised for a non-scattering medium [35–37]. In a strongly scattering medium the total amount light measured in a given experimental geometry is influenced by both, scattering and absorption. In analogy with the Napierian spectral absorbance Eq. (2.8) here the term attenuation is introduced to empirically summarise all light losses:

$$A(\lambda) = -\ln\left(\frac{\Phi(\lambda)}{\Phi_0(\lambda)}\right) \quad (2.20)$$

here $\Phi_0(\lambda)$ is the incident flux and $\Phi(\lambda)$ the detected flux which is strongly dependent on the experimental conditions. This equation is very similar to the definition of the Napierian spectral absorbance but does not explicitly exclude losses due to light scattering. The difference of the attenuation introduced by two states Φ_1 and Φ_2 can be written as:

$$\begin{aligned} \Delta A(\lambda) &= A_2(\lambda) - A_1(\lambda) = -\ln\left(\frac{\Phi_2(\lambda)}{\Phi_0(\lambda)}\right) + \ln\left(\frac{\Phi_1(\lambda)}{\Phi_0(\lambda)}\right) \\ &= -\ln\left(\frac{\Phi_2(\lambda)}{\Phi_1(\lambda)}\right) \approx 1 - \frac{\Phi_2(\lambda)}{\Phi_1(\lambda)} \end{aligned} \quad (2.21)$$

in the last step a Taylor series expansion at $\Delta A(\lambda) = 0$ was used. This relationship is useful for fNIRS where typically small changes of the flux appear.

Cope et al. [41] and Delpy et al. [42] showed that it is possible to apply a modified Beer-Lambert law (MBL) to obtain changes in absorption of a turbid medium like the head. The MBL employs an approximation for the mean optical path $d(\lambda)$ of light through the tissue:

$$d(\lambda) = m_1(\lambda)c_m(\lambda) \approx D_{\text{PF}}(\lambda)r_{\text{sd}} \quad (2.22)$$

where $m_1(\lambda)$ is the mean time of flight of photons through the tissue, $c_m(\lambda)$ the speed of light in the medium, r_{sd} the separation between the source and the detector and $D_{\text{PF}}(\lambda)$ the differential pathlength factor. Both, $m_1(\lambda)$

2. Theory and Models

and $d(\lambda)$, depend on the optical properties of the medium, the experimental arrangement and other parameters. As discussed in detail by Sassaroli and Fantini [43] a strictly correct formulation of the attenuation in a scattering medium as modelled by the MBL is:

$$A(\mu_a) = \int_0^{\mu_a} d(\lambda\mu'_a) d\mu'_a + A(\mu_a = 0) \quad (2.23)$$

where $A(\mu_a = 0)$ represents losses of light⁵ due to the scattering only, e.g. in the absence of absorption. In literature another - strictly not correct [43] - formulation of the MBL is widely used:

$$A(\lambda) = D_{\text{PF}}(\lambda)r_{\text{sd}}\mu_a(\lambda) + A(\mu_a = 0) \quad (2.24)$$

Both formulations lead to the same expression for attenuation changes which is actually used in continuous-wave fNIRS. Assuming a small absorption change $\Delta\mu_a$ and constant scattering, one yields:

$$\Delta A(\lambda) \approx D_{\text{PF}}(\lambda)r_{\text{sd}}\Delta\mu_a(\lambda) \quad (2.25)$$

where $D_{\text{PF}}(\lambda)r_{\text{sd}}$ represents the mean average path of photons through tissue. In practice values of D_{PF} tabulated for different organs are used. For the adult human head these values range from approximately 5 to 7. For a discussion of experimental values see Section 4.3.1. However, if the tissue under investigation is approximated as a homogeneous semi-infinite medium with known optical properties $\mu_a(\lambda)$ and $\mu'_s(\lambda)$ the $D_{\text{PF}}(\lambda)$ can be calculated analytically [44]. Rearranging Eq. (2.22) with respect to $D_{\text{PF}}(\lambda)$ and using the analytical expression for the mean time of flight in Eq. (4.28) with the approximation to the diffusion coefficient in Eq. (4.30) yields:

$$D_{\text{PF}}(\lambda) = \frac{3\mu'_s(\lambda)r_{\text{sd}}}{2\left(1 + r_{\text{sd}}\sqrt{3\mu_a(\lambda)\mu'_s(\lambda)}\right)} \quad (2.26)$$

Note that this expression does not depend on c_m and therefore not on the refractive index of the medium.

The MBL in combination with the DPF approximation is widely used in cw-fNIRS. The simplicity of this concept essentially contributed to the success and popularity of fNIRS.

⁵ On many body parts, e.g. head or muscle, the measurement is performed in a reflection geometry where backscattered photons are detected. Therefore, compared to a measurement in transmission on a non-scattering medium, the scattering of a turbid medium causes a light gain rather than a light loss.

2.2.4 Time-Domain Reflectance of a Homogeneous Semi-Infinite Turbid Medium

A precise description of light propagation in the human head can be achieved using the radiation transport equation (RTE). However, exact analytical solutions for this equation exist only for a few geometries. Exact forward calculations are most often performed using the Monte-Carlo method which, however, is computationally expensive.

In the special case when the scattering is much larger than absorption ($\mu'_s/\mu_a \gg 1$) which is true for many biological tissues, the RTE can be simplified and solved using the diffusion approximation. In the past this method has been successfully applied to a number of geometries in time-, frequency- and cw-domains. Below the time-domain solution for the homogeneous semi-infinite medium (SIM) is given. In three dimensional space the SIM extends to infinity in two dimensions but only one half of the third dimension. Therefore the SIM has a boundary which is a flat plane (Fig. 1.1a). In practice this is most often an air-medium boundary. This geometry is frequently used as a homogeneous approximation of the adult human head.

During solution of the diffusion equation the boundary of the SIM is considered using special boundary conditions. Most commonly the extrapolated and zero-boundary conditions (EBC and ZBC) are used. For EBC and ZBC the diffusion equation is then solved using the method of image sources [45, 46]. The fluence rate within the medium at the depth z and the radial distance r_{sd} is then given by:

$$\Psi(r_{sd}, z, t) = \frac{c_m}{(4\pi D c_m t)^{3/2}} e^{-\mu_a c_m t} \left[e^{-\frac{(z-z_0)^2 + r_{sd}^2}{4D c_m t}} - e^{-\frac{(z-z_0+2z_b)^2 + r_{sd}^2}{4D c_m t}} \right] \quad (2.27)$$

where $D = 1/3/(\mu_a + \mu'_s)$ is the diffusion coefficient, $c_m = c_0/n$ the velocity of light in the medium, t is the time and $z_0 = 1/(\mu_a + \mu'_s)$. For the EBC z_b is:

$$z_b = 2D \frac{1 + R_{eff}}{1 - R_{eff}} \quad (2.28)$$

where R_{eff} represents the fraction of photons reflected at the boundary [47]. In the NIR spectral range the index of refraction of tissue is about 1.4 and $R_{eff} \approx 0.493$ at a tissue-air boundary⁶. The reflectance $R(r_{sd}, t)$ at the boundary can be calculated using the relationship:

$$R(r_{sd}, t) = -D \nabla \Psi(r_{sd}, z, t) (-\mathbf{z})|_{z=0} \quad (2.29)$$

⁶ For other mismatches of the refractive index at the boundary integrals over the angle dependent Fresnel reflection coefficients must to be evaluated. For details see [47].

2. Theory and Models

At the boundary, i.e. $z = 0$, r_{sd} becomes the source-detector separation. For the EBC Eqs. (2.27) and (2.29) give:

$$R(r_{\text{sd}}, t) = \frac{1}{(4\pi Dc_m)^{3/2}t^{5/2}} e^{-\mu_a c_m t} \left[z_0 e^{-\frac{r_1}{4Dc_m t}} + (z_0 + 2z_b) e^{-\frac{r_2}{4Dc_m t}} \right] \quad (2.30)$$

where $r_1 = z_0^2 + r_{\text{sd}}^2$ and $r_2 = (z_0 + 2z_b)^2 + r_{\text{sd}}^2$. For the ZBC z_b is zero and Eq. (2.30) simplifies to

$$R(\rho, t) = \frac{z_0}{(4\pi Dc_m)^{3/2}t^{5/2}} e^{-\mu_a c_m t} e^{-\frac{z_0^2 + r_{\text{sd}}^2}{4Dc_m t}} \quad (2.31)$$

Kienle and Patterson [48] published an improved solution to the diffusion approximation employing a different expression for the time-domain reflectance than the one given in Eq. (2.29). They point out that the improved version better fits the amplitude of time-domain curves simulated using the Monte-Carlo method but not necessary their shape. As emphasised by Hielscher et al. [49] various boundary conditions and definitions of the reflectance do not resolve the main intrinsic problem of the diffusion approximation which exhibits an inherent mismatch for early arrival times of photons and at short source-detector separations. Therefore results obtained using the diffusion approximation must be used with care. It is valid in turbid media with high *albedo* (high scattering and low absorption), not too short source-detector separations ($r_{\text{sd}} > 2 \text{ cm}$) and rather late photons.

2.3 Modalities of fNIRS

There are three main optical techniques used for functional NIRS: continuous wave, frequency- and time-domain NIRS (cw-, fd- and td-NIRS, respectively). As illustrated in Fig. 2.10 these modalities differ by the illumination and therefore the light detection must be adapted.

The cw-technique is the most simple, inexpensive and therefore most widely used. The tissue is illuminated with light of constant intensity, i.e. constant on a time scale of at least nanoseconds (Fig. 2.10a). As light sources typically diode lasers or LEDs are used. The light can be modulated in the kHz range in order to perform wavelength multiplexing. For detection typically photomultiplier tubes or avalanche photodiodes (APD) are used. There is a variety of commercial cw-fNIRS systems available on the market (see [2] for an overview). Approaches to cover the whole head by many source-detector combinations have first been realised using the cw-technique [50].

Another cw-NIRS modality which became popular during recent years is the spatial frequency modulation [51, 52]. It employs spatially modulated

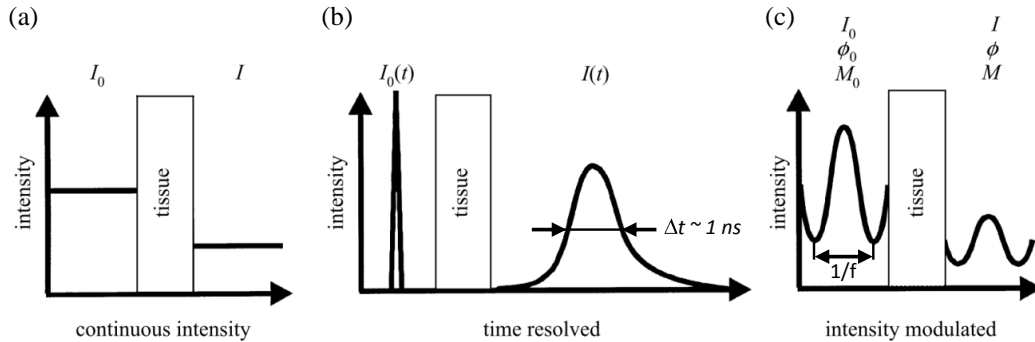


Figure 2.10: Illustration of the three most used fNIRS modalities (adapted from [55]).

illumination of the medium and space resolved light detection by a camera. This approach offers some advantages in the reconstruction procedure of optical properties or changes thereof [53, 54].

All continuous wave methods have in common that they rely on the measurement of the light intensity or its changes at a number of discrete wavelengths. Therefore the mean time of flight through the tissue must be approximated, i.e. using the DPF approach presented in Section 2.2.3. Additional difficulties arise from the need of calibration if the absolute attenuation is measured.

Instead of using discrete wavelengths a wide spectral measurement can be used for fNIRS. This approach is known as the cw-broadband technique and was first introduced by Matcher et al. [56] in combination with the second derivative analysis of the absorption spectrum. The broadband approach was recently revived by Schelkanova and Toronov in [57, 58]. This method requires a larger instrumental effort than the conventional cw-NIRS, i.e. a stabilised broadband light source and spectrally resolved light detection, but was demonstrated to be superior to cw-NIRS operating at two wavelengths only [57].

Light intensity can also be modulated on the time scale of nanoseconds or below. The frequency-domain approach uses high modulation frequencies about 100 MHz of the otherwise constant light intensity (Fig. 2.10c). This method requires fast detectors to measure phase shifts which depend on the optical properties of tissue. A commercial fd-NIRS device is available from the company ISS Inc⁷.

The time-domain technique is used throughout this thesis and will be discussed in more detail below.

In td-NIRS the medium is illuminated by short picosecond laser pulses

⁷www.iss.com

2. Theory and Models

(Fig. 2.10b) with a repetition rate in the MHz range. The scattering of the medium contributes to the temporal broadening of the laser pulse which then has a width in the nanosecond range. For light detection fast photodetectors together with time-correlated single photon counting (TCSPC)⁸ [59] are used. Although more expensive and complex td-NIRS provides more information about the light propagation in tissue. In particular, the mean time of flight of photons can be measured directly and individually for any geometry and subject. The td- and fd-NIRS approaches have in common that they exploit signals varying on a time scale of picoseconds to nanoseconds. Signals in both domains⁹ are related to each other by the Fourier transform.

In a typical time-resolved measurement a short laser pulse $L(t)$ is coupled into a fibre which delivers the light to the object under investigation. The light which escapes from the object is collected by a detection fibre or fibre bundle and delivered to a detector. Each medium or component contributes to the temporal broadening of the laser pulse $L(t)$. Computationally, the broadening is considered by the convolution of the corresponding characteristic functions. The finally measured signal $N(t)$ can be written as:

$$N(t) = D(t) \otimes F_D(t) \otimes R(t) \otimes F_S(t) \otimes L(t) \quad (2.32)$$

The characteristic functions $D(t)$, $F_S(t)$ and $F_D(t)$ denote the response of the detector, source and detector fibres to a an infinitely short laser pulse, respectively. $R(t)$ refers to the response of the medium under investigation (for example the reflectance of the semi-infinite homogeneous medium as described in Section 2.2.4). Using the commutativity property of the convolution Eq. (2.32) can be rewritten as:

$$N(t) = \underbrace{D(t) \otimes F_D(t) \otimes F_S(t) \otimes L(t)}_{:=I(t)} \otimes R(t) = I(t) \otimes R(t) \quad (2.33)$$

Here $I(t)$ is the instrument response function (IRF) which can be measured independently of the medium. The IRF summarises all instrumental influences while $R(t)$ contains the medium response. This expression is essential because it allows to describe any time-resolved measurement by only two terms. Typically, the instrument is designed and optimised in a way that the IRF is constant in time and only the medium response varies. Otherwise, a continuous recording of the IRF is required.

⁸ It is also possible to use gated cameras for time-resolved detection. However, such cameras are typically very expensive and provide a worse temporal resolution.

⁹ A fd-NIRS measurement with a broad spectrum is required to obtain the corresponding td-NIRS equivalent.

There are several terms used in the literature for the measured signal $N(t)$. From the experimental point of view $N(t)$ is built up by photon counting and therefore called distribution of times of flight of photons (DTOF). In the area of modelling of light propagation $N(t)$ is called the temporal point spread function (TPSF) which emphasises the temporal broadening of short laser pulses in a turbid medium. From the point of view of statistics $N(t)$ is a positive definite, conditional probability density function (PDF). This, on the one hand, neglects any physical causality but on the other hand suggests the application of statistical methods for data analysis such the method of moments described in Chapter 4. Throughout this thesis the term DTOF is used in order to accentuate the experimental and stochastic aspects of the $N(t)$.

For the determination of concentration changes of oxy- and deoxyhaemoglobin light absorption at least at two wavelengths must be measured. With the td-technique this is often achieved employing the time-multiplexing method. Short laser pulses of different wavelengths are delayed against each other by few nanoseconds forming a pulse train. Recently, a novel approach was introduced to increase the number of source-detector combinations in td-fNIRS and thereby to improve the spatial coverage of the head [60]. This approach employs time-multiplexing to encode different spatial positions similarly to [61], 50 μ s long bursts of light emission and a very efficient distribution of the available laser power by polarisation rotators and splitters.

2. Theory and Models

Instrumentation

This chapter describes the instrumentation and measurement procedures used to acquire experimental data for this thesis. All experiments can be subdivided into *in vivo* (mainly discussed in Chapter 6) and phantom (Chapter 5) measurements. They all have in common that pulsed lasers sources at high repetition rates, fast photomultipliers and electronics for time correlated single photon counting (TCSPC) were employed. Fibre optics were used for flexible light transport and collection. Furthermore, optical setups were coupled with other techniques to perform (concurrent) multi-modal *in vivo* measurements.

3.1 PTB Brain Imager

The PTB Brain Imager (BI) is a prototype time-domain fNIRS device and was used in most of the *in vivo* experiments. The initial version was constructed at PTB within a project¹ and for the first time described in [62]. BI has a flexible modular design which allows for comparably simple modifications of the light emission and detection modules and switching of measurement modes. In the “perfusion mode” absorption [61] and fluorescence [63, 64] of the optical tracer indocyanine green (ICG) are exploited to perform blood perfusion measurements on the human head *in vivo*. These measurements, however, are not related to fNIRS and will therefore not be discussed in the context of the current work. For the majority of the functional *in vivo* experiments presented in this thesis the “oxygenation mode” of the BI was used. In this mode concentration changes in oxy- and deoxyhemoglobin are obtained employing light absorption at three wavelengths.

A schematic view of the main modules and a photograph of the BI are

¹ BMWA VI A2-12/03 “Time-domain NIR brain imager“ (2003 to 2005)

3. Instrumentation

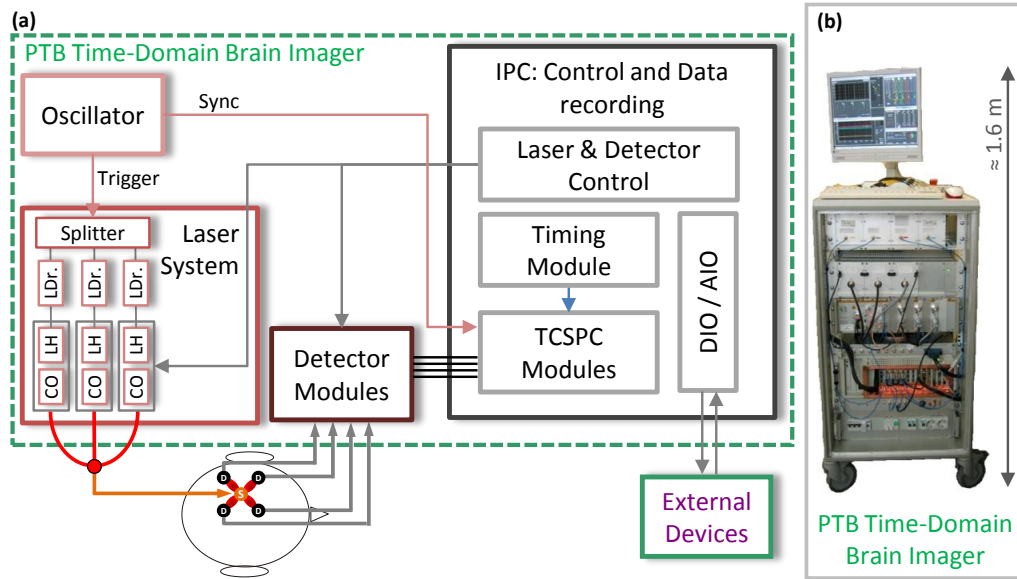


Figure 3.1: Scheme (a) and a photograph (b) of the PTB Brain Imager (LDr. - laser driver, LH - laser head, RO - relay optics, DIO/AIO - digital/analogue input and output channels). The functionality of the modules is explained in the text.

shown in Fig. 3.1. The essential parts are the light emission and detection modules as well as the 4-board system for time-correlated single photon counting. The interoperability with external instruments is provided via a number of analog and digital input and output channels (DIO/AIO) whose recordings are synchronised with the optical measurement.

Short picosecond light pulses are emitted by three diode lasers (Sepia PDL 808 driver unit with three external diode laser heads, PicoQuant, Germany) at approximately 690 nm, 800 nm and 828 nm with a spectral width of about 4 nm (FWHM). The centre wavelength can shift slightly by a few nanometres when changing the output power level. Each diode laser head is housed in a separate module containing collimator optics and a microcontroller driven shutter controlled by software from the IPC. Light emission of each laser is triggered by an external oscillator with an adjustable repetition rate which was typically chosen to be about 42 MHz. This frequency can be tuned in order to optimise the temporal position of the pulses with regard to reflections in the fibres. Unfavourable reflections can negatively affect a time-domain NIRS measurement (cf. the discussion in Section 4.1.2). As illustrated in Fig. 3.2a laser pulses of the different wavelengths are multiplexed on a nanosecond time scale by delaying the trigger signals against each other by about 8 ns. This procedure triples the effective repetition rate. Light of the different wavelengths is first combined at the end of a triple fibre (multimode, $\varnothing 50 \mu\text{m}$)

and then coupled into a single fibre (multimode, $\varnothing 200\ \mu\text{m}$ or $600\ \mu\text{m}$) which can be attached to the human head or to a phantom. The typical average output power is about 3 mW per wavelength.

The BI has four detection channels consisting of detector modules connected to one of the four cards of a multi-board TCSPC system (SPC-134, Becker&Hickl, Germany). In the standard configuration with one light source fibre this results in four source-detector pairs and therefore four spatial channels. This number can be increased to 16 if a 1 to 9 fibre switch in the light source path is used (for details see [62]). Each detector module contains a fast photomultiplier, a shutter, a filter wheel and transfer optics optimised for maximum transmission efficiency [65]. For all functional *in vivo* measurements presented in this thesis the detector modules were equipped with PMTs with a multi-alkali photocathode (R7400U-02, Hamamatsu Photonics, Japan) and with power supply and amplification electronics. The level of light transmission through the detector module is controlled by two diaphragms located in a Fourier and an image plane in the transfer optics path. The diaphragm in the Fourier plane can block light escaping from the fibre bundle at larger angles which correspond to higher order propagation modes in the multi-mode fibres. Therefore restriction of these angles reduces the width of the IRF [66]. On the other hand, the diaphragm in the image plane can block light without changing the IRF. Both diaphragms together control the amount of light which reaches the detector in a wide range. Diffusely reflected light is collected by fibre bundles ($\varnothing 4\ \text{mm}$) with a high numerical aperture of NA 0.54. In the case of the combined fNIRS and EEG measurement special fibre bundles were used (see Section 3.3). Reasonable count rates achieved with the BI are below 3 MHz. Above this level dead time effects of the TCSPC electronics produce strong distortions.

Distributions of times of flight of photons (DTOFs) are typically acquired with 1024 channels per DTOF and a channel width of 24.4 ps. A single DTOF is typically recorded every 50 ms with a photon collection time of 49 ms. The resolution of both time scales is sufficient to track processes relevant for fNIRS. The BI is capable of recording with even higher temporal resolution, i.e. recording a DTOF with a channel width of 6.1 ps every 12.5 ms. This, however, would result in a substantially larger data amount and can complicate data saving and processing. A typical 25 minutes long fNIRS session with the BI results in about 60 MB per detection channel. During this thesis the software of the BI was modified in order to enable recordings with more than 2 GB per channel which corresponds to measurements longer than 10 h. Potential application of this improvement are long term *in vivo* experiments,

3. Instrumentation

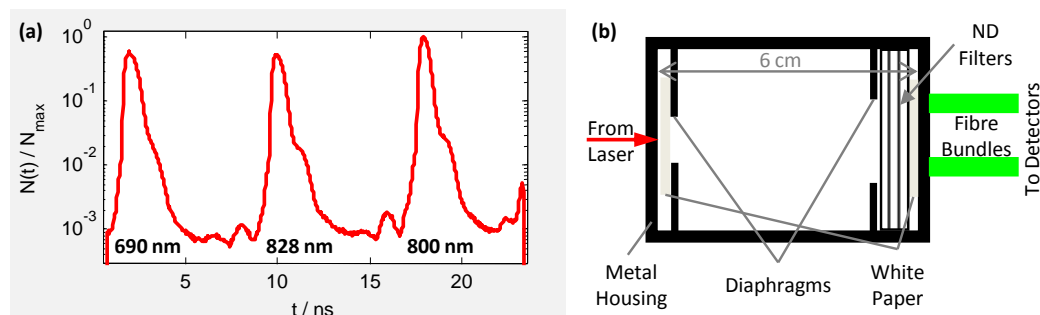


Figure 3.2: IRF measurement: (a) An example IRF obtained in conjunction with an *in vivo* fNIRS experiment. Three wavelengths are multiplexed on a nanosecond time scale. (b) Scheme of the setup used for the measurement of the IRF.

i.e. monitoring of haemoglobin concentration changes on sleeping subjects² or on epilepsy patients where the exact moment of the epileptic seizure cannot be foreseen.

The incident power on the skin is limited by the rather low power of diode lasers and safety limitations. Therefore the only way to achieve high count rates is to increase the efficacy of detection. In the BI this is achieved by large area fibre bundles with high NA, optimised transfer optics and large area PMTs. The drawback of these measures is the broadening of the instrumental response function (IRF). Its width is typically between 0.5 ns and 0.9 ns (FWHM). Compared to the response of the tissues such a broad IRF cannot be neglected. The IRF was measured as suggested in [66]. In particular two pieces of white paper were used to ensure uniform illumination of the fibre bundles and the inclusion of higher order modes propagating within multi-mode fibres. Those modes contribute to the broadening of the IRF and must be considered for a precise measurement. For the same reason the same settings of the NA diaphragm as during the actual measurement were used.

Figure 3.2b shows the setup used to measure the IRF simultaneously for four channels and a single source fibre. Four fibre bundles can be fixed in the metal housing. The count rate can be adjusted by neutral density filters in front of the detection fibre bundles. For an exact IRF measurement the same diaphragm settings were used whereby the image plane diaphragm can be tuned to simplify the choice of ND filters. Due to the distance of 6 cm between the source fibre and the detection fibre bundles the actually recorded IRF is “delayed” by 200 ps compared to the true IRF. Accordingly, to correct for that the IRF must be shifted by 200 ps to earlier times.

² Sleep measurements using the Brain Imager have been performed by the author and P. Koch (Charité) within the nEUROPt project. However, these unpublished experiments are not part of this thesis.

3.2. Concurrent Measurement of fNIRS and Systemic Physiological Signals

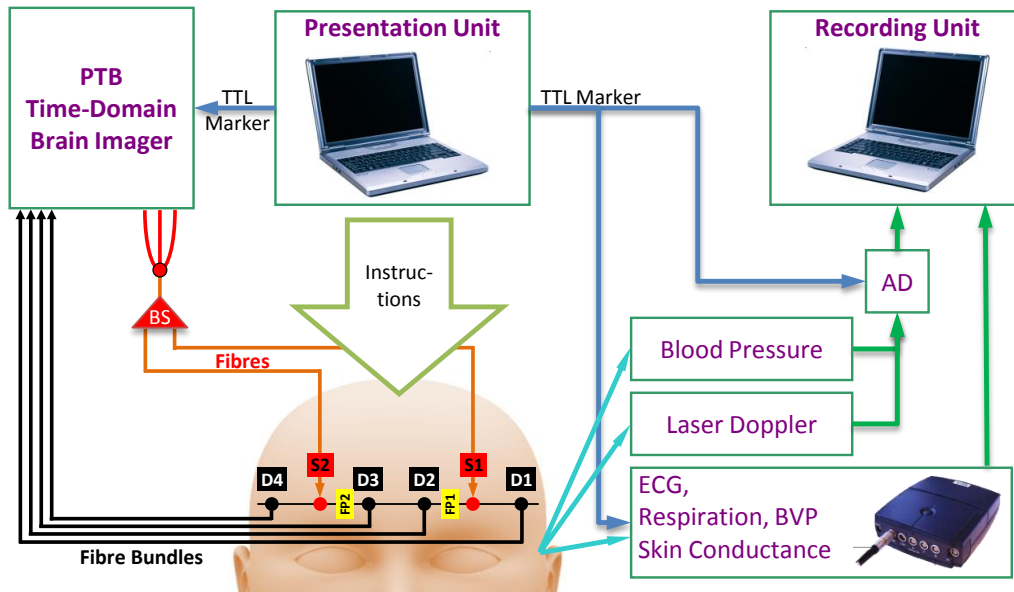


Figure 3.3: Scheme of the setup for the concurrent measurement of systemic physiological signals and fNIRS. A beamsplitter (BS) was used to achieve full coverage of the forehead with two source and four detection positions (denoted by S1-S2 and D1-D4). The recordings of the different devices were synchronised during the data analysis using the TTL marker signal. AD denotes an analog-to-digital converter.

3.2 Concurrent Measurement of fNIRS and Systemic Physiological Signals

The goal of this measurement³ was to perform a concurrent recording of systemic physiological parameters and fNIRS at the forehead during a cognitive task. In addition, all subjects underwent a subsequent functional MRI experiment employing the same task and an anatomical MRI scan to obtain individual structural information about each subject's head.

The schematic view of the combined setup is shown in Fig. 3.3. Changes in oxy- and deoxy-haemoglobin concentration were measured by the BI described in Section 3.1. The illumination part of the BI was modified in order to cover the forehead area. For that the light from the triple source fibre of the BI was split by a broadband beam splitter into two equal parts and then coupled into two separate fibres S1 and S2. Each source fibre together with two detection channels (left - S1 with D1/D2, right - S2 with D3/D4) provided two source-detector pairs probing different tissue volumes. The placement of the source

³The measurement was performed by the author of this thesis in collaboration with Dr. Ilias Tachtsidis (UCL).

3. Instrumentation

fibres and detections fibre bundles on the forehead with respect to the Fp1 and Fp2 landmarks of the 10-20 system is shown in Fig. 3.3. The repetition rate was optimised to be 41.9 MHz in order to shift unfavourable reflections. The optodes were inserted into holes of a foam rubber holding band, which was tightly fixed on the subject's head with a Velcro strap.

A comprehensive set of systemic physiological signals was obtained using three different devices. Mean blood pressure was recorded non-invasively on the index finger of the left hand using the PortaPress system (TNO TPD Biomedical Instrumentation, Netherlands). Changes in scalp blood flow (flux) and concentration of red blood cells were recorded by the floLAB Laser Doppler Perfusion Monitor (Moor Instruments, UK). The device uses a probe with a very short emitter-detector distance of about 1 mm; hence the penetration depth is less than 1 mm and it samples a volume of about 1 mm³. The probe was placed approximately 1.5 cm over S2. Furthermore, an electrocardiogram (ECG), respiration, skin conductance (SC) and blood volume pulse (BVP) signal were recorded using a Nexus-10 system (Mind Media, Netherlands). The SC probe was placed on the fingers of the left hand, whereas the BVP sensor probed the ear.

During the experiments a TTL marker signal was generated by the presentation unit and registered by the other devices. These markers were used during the analysis to synchronise the time axes of all instruments. The Nexus-10 device revealed time oscillator problems: it was stable but incorrectly calibrated. This caused a delay of about 5 s in a 20 min experiment. The recorded TTL marker signal together with the precise time axis of the BI were used to correct the time axis of the Nexus device for the delays. The recorded data was then linearly interpolated to match the common time axis of the other devices.

In the subsequent fMRI experiment⁴ subjects performed the same tasks as during the fNIRS session. These measurements were performed on a 3 T Verio scanner (Siemens, Erlangen, Germany), equipped with a 32-channel coil. A gradient echo sequence (Echo-Planar-Imaging) was used ($T_E/T_R/\text{flip angle}/\text{band width}$ were 30 ms/2000 ms/70°/1689 Hz) with a $3 \times 3 \times 3$ mm³ spatial resolution, fat saturation prior to every slice and a GRAPPA acceleration factor of 2. Thirty-two nearly axially oriented slices with an interslice gap of 0.6 mm were acquired in an interleaved order, providing whole brain coverage.

Anatomical images of each subject were acquired using a T_{1w} sequence ($T_E/T_R/T_I/\text{flip angle}/\text{band width}$ were 3.03 ms/2300 ms/900 ms /9°/130 Hz)

⁴ The MRI measurements were performed by Dr. R. Brühl (PTB) and Dr. E. Kirilina (FU Berlin) within collaborative work.

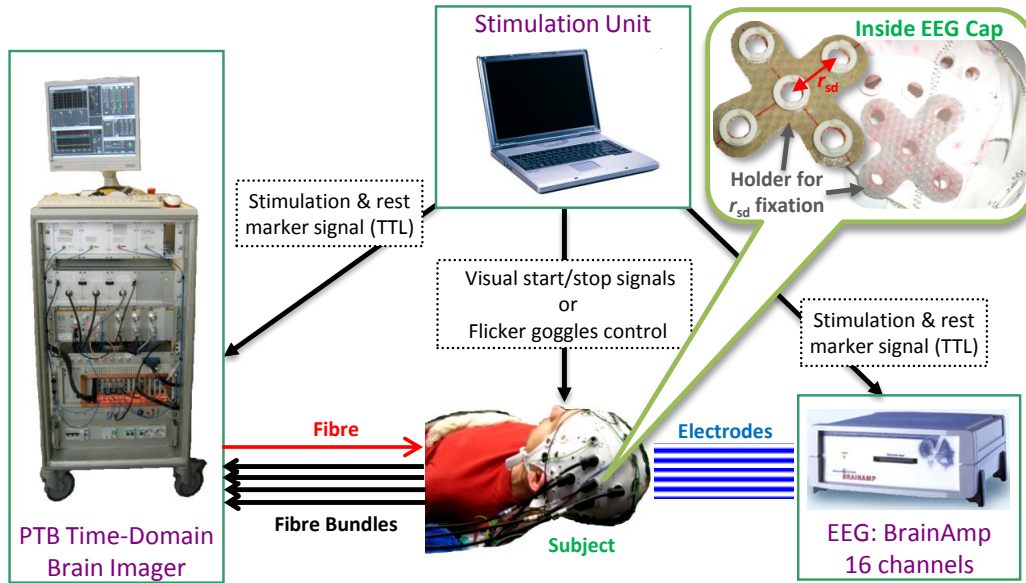


Figure 3.4: Schematic view of the combined EEG-fNIRS setup. The inset shows the inner side of the EEG cap together with the r_{sd} fixation holder.

with a spatial resolution of $1 \times 1 \times 1 \text{ mm}^3$. The spatial positions of the fNIRS optodes were marked with fiducial markers (BrainLAB AG, Germany) for later co-registration.

3.3 Concurrent fNIRS and EEG

This setup was assembled in order to study neuro-vascular coupling. It is capable of simultaneous recording of electroencephalography and time-domain fNIRS. This combination of methods potentially gives access to both the cerebral neuronal activity and the vascular response to it.

Figure 3.4 shows the scheme of the experimental assembly. A commercial EEG device (BrainAmp, g.tec medical engineering GmbH, Austria) was used to record the electroencephalogram. Twelve ring electrodes were placed on the head according to the 10-20 system using a commercially available EASY CAP (EASYCAP GmbH, Germany). The sampling rate of the EEG signals was set to 500 Hz.

Changes in oxy- and deoxy-haemoglobin were recorded by the PTB Brain Imager in the fNIRS mode. Twenty DTOFs were recorded per second. For this measurement fibre bundles with a diameter of 3 mm, a length of 2.5 m and a 90° angle on the head side were used. The specific design of the end pieces allowed the bundles to be attached directly to electrode holders of the EEG

3. Instrumentation

cap. In this way a direct co-registration of EEG and fNIRS data acquisition is achieved. Furthermore this assembly is suitable to be used on subjects during long-term measurements. For example it was applied on sleeping volunteers over night. As shown in the inset of Fig. 3.4 the fibre arrangement was cross-shaped with the source placed in the centre and a source-detector separation of 3 cm. This separation was kept constant by a thin piece of flexible plastic installed on the inner side of the EEG cap which itself is elastic. Once the cap is placed and stretched on a subject's head the plastic holder adapts to the curvature of the head but at the same time it also becomes rigid and fixes r_{sd} and the geometry of the optode arrangement.

The stimulation unit presented visual signals to the subjects in order to trigger cerebral activity. In the case of the finger tapping task “start” and “stop” commands were displayed on a computer display which was located in the field of view of the subject. For the visual activation the stimulation unit directly controlled LEDs inside of the flicker goggles placed on the subject's eyes. The EEG and fNIRS recordings were synchronised during the data analysis stage using the common marker signals generated by the stimulation unit during the experiment. On the hardware level the TTL signals and the flicker goggle control were realised via a LPT port which delivers enough current to drive a LED.

3.4 Concurrent fNIRS and fMRI

The setup described here was used for the concurrent measurement of time-domain fNIRS and fMRI. It does not employ the Brain Imager but consists of similar building blocks, i.e. picosecond pulsed lasers, fast PMTs and TCSPC electronics. Some specific experimental challenges arose from the combination of the two techniques and are discussed below.

Figure 3.5a shows a schematic view of the setup. Its main components and scheme was adopted from a combined MRI-NIRS setup intended for mammography assembled in our group before [67]. High resolution anatomical MR images, as well as echo-planar images for fMRI were recorded with a whole-body 3-T MRI scanner (Medspec 30/100, Bruker Biospin, Ettlingen, Germany) equipped with an 8-channel head coil (Rapid Biomedical, Rimpfing, Germany) and a head-gradient insert (AC 44, Siemens, Erlangen, Germany).

The fNIRS setup employed picosecond diode lasers (PDL 800, PicoQuant, Berlin, Germany) at three wavelengths (695 nm, 806 nm, 825 nm) operated at a repetition rate of 32 MHz. Laser pulse emission was delayed on a ns time scale in order to construct a pulse train similar to the one showed in Fig. 3.2a. Light from each laser was coupled into a separate 20 m long step index optical

3.4. Concurrent fNIRS and fMRI

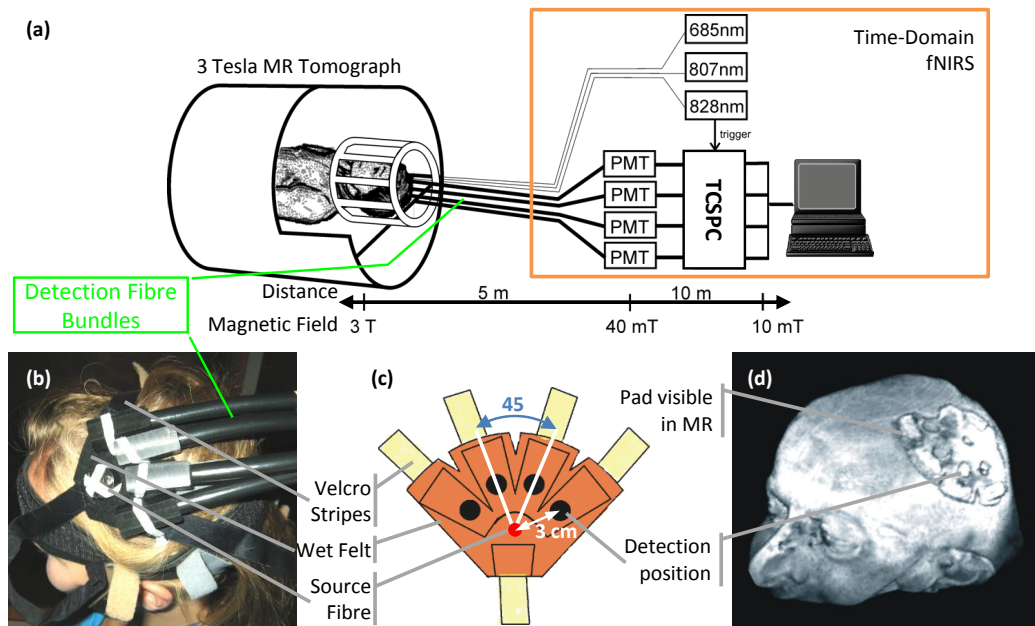


Figure 3.5: Setup for the concurrent fMRI and time-domain fNIRS *in vivo* measurement. (a) Principle scheme of the combined fMRI-fNIRS setup. (b) Photograph of a subject's head with the pad and fibre optics attached. (c) Scheme of the pad holder. (d) 3D MRI rendering of the head. The wet pad is visible in the MR image.

fibre and combined directly on the head of a subject. The output power at the tip of the source fibre was about 2 mW for each wavelength. Diffusely reflected photons were collected by four 4.8 m long fibre bundles ($\varnothing 8$ mm, NA 0.36, Loptek Glasfasertechnik, Berlin, Germany). To place the fibre bundles inside the head coil special end pieces with a 90° angle were used.

The collected light was guided to dedicated detector boxes each equipped with a fast PMT (R7400U-02, Hamamatsu Photonics, Japan), transfer optics and a built-in high-voltage supply. The detection modules were located in the same room as the MR scanner in order to minimise the distance to the subject. However, the performance of the photomultiplier tubes is potentially affected by the magnetic stray field of the unshielded MR device. Therefore the PMTs had to be placed 4.5 m away from the centre of the MR scanner. This distance is a compromise between the strength of the remaining magnetic field and the length of the fibre bundle which should be kept as short as possible. Long fibre bundles broaden the IRF of the optical setup thereby reducing the quality of the measurement. The full width at half maximum of the IRF was up to 1.1 ns which is still sufficient for an fNIRS measurement of good quality. DTOFs were recorded every 200 ms with a collection time of 170 ms. During the residual 30 ms no photons were counted because of the potential

3. Instrumentation

distortion due to the emission of strong RF pulses by the MR tomograph.

Figure 3.5c shows the radial arrangement of the optodes around the source with a source-detector separation of 3 cm. The angular distance between the source-detector pairs was 45° which results in a slight overlap of the volumes probed by the light. The optode holder was made from thick black felt which was dampened with water in order to achieve susceptibility matching between felt and tissue and to make it visible in the MRI. The pad was fixed with Velcro stripes above the left motor cortex (C3 position according to the 10-20 system).

Anatomical MR images were recorded with a spatial resolution of $1.1 \times 1.1 \times 1.2 \text{ mm}^3$ using a MPRAGE sequence (T_E , T_R , T_I were 3.1 ms, 1400 ms, 9.8 ms, respectively) and automatically segmented⁵ using the FreeSurfer software freely available online⁶. Functional MRI data was acquired using an EPI sequence (T_E , T_R were 32 ms and 2 s, respectively) with a spatial resolution of $3 \times 3 \times 4 \text{ mm}^3$.

3.5 High Density and Large Area Measurement on a Human Head

The goal of this experiment was to reconstruct optical properties of the head non-invasively and *in vivo*. For that a comprehensive experimental dataset on the head of a single subject was obtained. This includes a large area multi-distance time-domain NIRS measurement together with structural informations obtained from an anatomical MRI scan. Both types of data in combination with sophisticated light propagation models potentially allow for the reconstruction of optical properties of the head from a non-invasive *in vivo* measurement. The acquired dataset was made available to a cooperation partner⁷ for advanced data analysis.

The time-domain NIRS measurement was performed on the head of an adult healthy volunteer (27 y, male, hairless) resting in supine position. The principle scheme of the setup is shown in Fig. 3.6a. The light source was a tunable femtosecond Ti-Sa laser (Mai Tai BB, 80 MHz repetition rate, Spectra Physics) operated at 800 nm centre wavelength with a spectral FWHM of approximately 7 nm. The light was coupled into a 1:9 fibre switch (fibre diameter 200 μm , NA 0.22, Piezosystem Jena, Germany) where only six of

⁵The segmentation was done by Dr. Evgeniya Kirilina who was working at PTB at the time of the measurement. Currently, she is with the Free University Berlin.

⁶<http://surfer.nmr.mgh.harvard.edu/>

⁷Dr. J. Heiskala, Dr. M. Schweiger, Prof. S. Arridge, University College London

3.5. High Density and Large Area Measurement on a Human Head

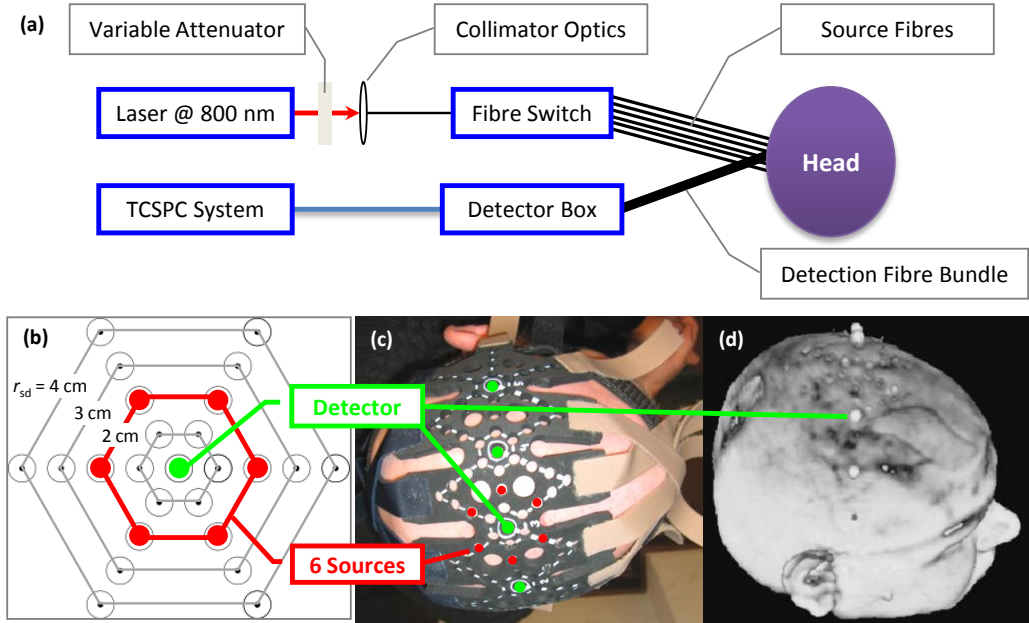


Figure 3.6: Schematic view of the setup for the large coverage and high density measurement on a human head *in vivo*. (a) Principle scheme of the optical setup. (b) Arrangement of the sources and detectors shown for a single detector position. The red hexagon shows positions of source fibres for a single source-detector separation of 2 cm. For other values of r_{sd} source fibres were attached to the corresponding positions indicated by grey hexagons. (c) Photograph of the pad holder placed on the head of the subject (top view). Green circles depict four of the five positions of the detection fibre bundles (one is outside the field of view). (d) 3D-MRI rendering of the head. The optode pad itself is invisible in MRI while the positions of sources and detectors were labelled using water soaked paper “plugs” that appear white.

the output fibres were used. The average output power of 14 mW was homogeneously distributed over an spot with 4 mm in diameter to stay within safety limits for skin exposure. The diffusely reflected light was collected by a low dispersion silica fibre bundle ($\varnothing 1$ mm, NA 0.22, Loptec, Germany) and led to a detector box containing transfer optics and a fast cooled photomultiplier (GaAs cathode, H7422P-50, Hamamatsu, Japan). 300 DTOFs with a total collection time of 15 s per single source-detector combination were recorded. The IRF was measured following the procedure described in [66]. Time-correlated single photon counting was performed by a SPC-150 (Becker & Hickl, Germany). The overall FWHM of the IRF was 320 ps.

In order to achieve a substantial overlap of the volumes sampled by the light a multi-distance hexagonal optode arrangement as shown in Fig. 3.6b was used. For that a special optode holder pad was constructed (Fig. 3.6b-c) that covered a large area of the head of about 152 cm^2 spanning over 24 cm from the right to the left ear. Using this pad the source and detector fibres

3. Instrumentation

can be placed 1 cm, 2 cm, 3 cm and 4 cm apart. The five detection positions are arranged in a line and separated by 4 cm from each other. In total optical data for 120 source-detector pairs has been acquired in this measurement.

The whole optical measurement consisted of a series of subsequent measurements of different areas of the head at the four source-detector separations. First, the detection fibre bundle was placed in the centre of a hexagon with the six sources arranged around it at the shortest r_{sd} and data were acquired. Then the source fibres were moved to the next source-detector separation and the data acquisition was repeated. Once the measurement for all of the four distances was finished the detection fibre bundle was moved to the next of the five detection positions and the whole procedure was repeated. Each time fibres have been moved the count rate was adjusted to be about 1 MHz using neutral density filters inside the detector box.

Right after the optical measurement the subject was transferred to the MRI facility located in the same building. An anatomical T_1 weighted MRI scan⁸ was performed using the MPRAGE sequence. This scan provided information about the structure of the head and the spatial positions of the optodes. To make the holes of the optode holder visible in the MRI they have been filled with pieces of paper soaked with water. As can be seen in Fig. 3.6d those pieces appear white in the MR image.

⁸The MRI scan was performed by Dr. E. Kirilina.

Analysis of Time-Domain NIRS Signals by Moments

Time-domain NIRS measures the temporal dispersion of short laser pulses propagating through living tissue. Tissue is a turbid medium and light propagation in it is governed by random processes such as scattering and absorption. Because of the scattering photons can travel along different paths which leads to differences in the time of flight of photons. Therefore the result of a td-NIRS measurement is frequently called a “distribution of time of flight of photons” (DTOF). Due to the probabilistic character of DTOFs it is promising to apply methods from the field of statistics. In particular the analysis of td-NIRS data in terms of moments of DTOFs (short: method of moments) has already been employed in the past by different authors dealing with various aspects of td-NIRS [12, 62, 68–70]. Compared to the analysis of the full DTOF this method exhibits a number of advantages such as the reduction of the voluminous original measurement data and a lower computational effort, a simple deconvolution procedure and a simpler perception by human operators. Furthermore, changes in moments are related to changes in light absorption induced by tissue chromophores. Therefore, it is possible to assess concentration changes of oxy- and deoxyhemoglobin *in vivo* provided that suitable reconstruction models are available.

In this chapter the method of moments and its application to td-NIRS measurements is discussed in detail. Fundamental properties and procedures are introduced in Section 4.1, i.e. computation of moments, noise and systematic errors due to the finite integration range. A correction algorithm to compensate for those systematic errors is presented in Section 4.1.3. In Section 4.2 approaches to derive optical properties of tissue non-invasively and *in vivo* from moments of DTOFs are discussed. Essential for the recon-

struction of concentration changes of haemoglobin *in vivo* is the computation of sensitivity factors to absorption changes for moments. Sensitivity factors for reconstructions methods based on homogeneous and layered models are discussed and applied in Sections 4.3 and 4.4.

4.1 Moments of DTOFs

The result of a time-domain NIRS measurement is the distribution of time of flight of photons (DTOF) $N(t)$ which exhibits changes on a time scale of picoseconds to nanoseconds. The total number of photons is the integral over $N(t)$ and is referred to as the 0-th moment m_0 :

$$m_0 = \int_{-\infty}^{\infty} N(t) dt \quad (4.1)$$

Note that light intensity which is measured by cw-NIRS is directly proportional to m_0 . The normalised DTOF $\hat{N}(t)$ is defined by

$$\hat{N}(t) = N(t)/m_0 \quad (4.2)$$

with the consequence that

$$\int_{-\infty}^{\infty} \hat{N}(t) dt = 1 \quad (4.3)$$

In statistics $\hat{N}(t)$ is also called the probability density function (PDF). The n -th normalised moment m_n of a DTOF $N(t)$ is defined as

$$m_n = \int_{-\infty}^{\infty} t^n \hat{N}(t) dt \quad n \in \mathbb{N} \quad (4.4)$$

The first normalised moment m_1 of a distribution corresponds to the mean time of flight of photons through tissue in fNIRS. It is further possible to define the n -th centred moment $m_{n,C}$:

$$m_{n,C} = \int_{-\infty}^{\infty} (t - m_1)^n \hat{N}(t) dt \quad n \in \mathbb{N} \quad (4.5)$$

From Eqs. (4.3) to (4.5) follows that $m_{0,C} = 1$ and $m_{1,C} = 0$ for any distribution. The $m_{2,C}$ is the variance of a distribution and is often denoted by V or σ^2 with σ being the standard deviation. In this thesis V is used to specifically refer to the variance of a DTOF while σ^2 will denote variance as related to the uncertainty or noise of a measurand.

4.1.1 Convolution Properties

Moments exhibit valuable properties if a convolution of multiple functions is involved as it is the case in time-domain NIRS (cf. Eq. (2.32)). Laury-Micoulaut [71] derived general expressions for the n -th moments and the case of multiple convolutions. Here a subset of these results is used. Explicit expression for the case of a single convolution and the moments m_1 , $m_{2,C}$, $m_{3,C}$ and $m_{4,C}$ are given. These moments are of particular interest for td-fNIRS as discussed within the scope of this thesis.

In most experiments it is sufficient to model the measured DTOF $N(t)$ as a convolution of the IRF $I(t)$ and the medium response $R(t)$:

$$N(t) = I(t) \otimes R(t) \quad (4.6)$$

Moments $m_n(N)$ of $N(t)$ can then be calculated in a simple way from moments $m_n(R)$ and $m_n(I)$ of $R(t)$ and $I(t)$, respectively:

$$m_1(N) = m_1(I) + m_1(R) \quad (4.7)$$

$$m_{2,C}(N) = m_{2,C}(I) + m_{2,C}(R) \quad (4.8)$$

$$m_{3,C}(N) = m_{3,C}(I) + m_{3,C}(R) \quad (4.9)$$

$$m_{4,C}(N) = m_{4,C}(I) + m_{4,C}(R) + 6m_{2,C}(I)m_{2,C}(R) \quad (4.10)$$

Here and below the dependence on t is neglected for the clarity of equations. Note that Eqs. (4.7) to (4.9) do not contain mixed terms and the contributions of the IRF and the medium are well separated. For $m_1(N)$, $m_{2,C}(N)$ and $m_{3,C}(N)$ this property even holds true for the convolution of multiple functions (see [71] for details). On the contrary, Eq. (4.10) contains mixed terms of lower order moments which slightly complicate the separation. Still, if the moments of $N(t)$ and $I(t)$ are known it is possible to compute the corresponding moments of $R(t)$ employing Eqs. (4.7) to (4.10) and a simple subtraction. This procedure is called “deconvolution by moments” and avoids a more complicated and computationally expensive deconvolution of $N(t)$ and $I(t)$ to obtain $R(t)$.

For m_1 , $m_{2,C}$ and $m_{3,C}$ the difference in moments Δm between two states $R_1(t)$ and $R_2(t)$ of the medium does not depend on IRF and even is equal to the change in moments of the medium. This is easily shown using Eqs. (4.7) to (4.9) under the assumption that the moments of the IRF are constant:

4. Analysis of Time-Domain NIRS Signals by Moments

$$\begin{aligned}\Delta m_1(N) &= m_1(N_2) - m_1(N_1) \\ &= m_1(R_2) - m_1(R_1) = \Delta m_1(R)\end{aligned}\quad (4.11)$$

$$\begin{aligned}\Delta m_{2,C}(N) &= m_{2,C}(N_2) - m_{2,C}(N_1) \\ &= m_{2,C}(R_2) - m_{2,C}(R_1) = \Delta m_{2,C}(R)\end{aligned}\quad (4.12)$$

$$\begin{aligned}\Delta m_{3,C}(N) &= m_{3,C}(N_2) - m_{3,C}(N_1) \\ &= m_{3,C}(R_2) - m_{3,C}(R_1) = \Delta m_{3,C}(R)\end{aligned}\quad (4.13)$$

This property is valuable for td-fNIRS where typically a continuous time series of moments is measured and, using a suitable baseline, changes in moments are calculated. An absolutely necessary requirement for the application of the above equations is the stability of the IRF of the fNIRS device. The fulfilment of this requirement is facilitated by the design of typical functional experiments where changes on a time scale of minutes are investigated. Further, it should be noted that in contrast to the absolute values of moments (cf. Section 4.1.2) changes of moments exhibit a much lower dependence on the upper integration limit. All these properties of moments are exploited in the analysis of functional *in vivo* experiments presented in Chapter 6.

4.1.2 Influence of the Finite Integration Range

In practice difficulties in the computation of moments from experimentally determined DTOFs arise due to the finite integration range in Eqs. (4.4) and (4.5). Experimentally obtained DTOFs are influenced by the finite dynamic range of the detector and therefore the integration range must be restricted. In addition the integration must be approximated by a *Riemann sum*:

$$m_n = \int_{-\infty}^{\infty} t^n \hat{N}(t) dt \approx \sum_{i=j}^k t_i^n \cdot \hat{N}_i \quad (4.14)$$

where t_i is the time and \hat{N}_i the photon count of the i -th channel. The lower and upper limits j and k are typically selected as a fraction of the maximum of the DTOF N_{max} , i.e. by relative lower and upper limits $L_L = N_j/N_{max}$ and $L_U = N_k/N_{max}$, respectively. Often used values for L_L and L_U are 1% to 3% and 1% to 5%, respectively. Furthermore the same relative limits are used for the computation of moments of the IRF and the measured DTOF.

In the specific case of time-domain NIRS mainly the truncation of the upper limit influences the result [70]. This leads to a missing contribution from the integration range $[k+1, \infty)$ the amount of which increases with the order

of the moment n due to the increasing weighting by the term t_i^n in Eq. (4.14). The absolute values of moments obtained are then underestimated.

Liebert et al. [70] studied the influence of L_L and L_U on the absolute values of m_1 and V for one specific configuration of the homogeneous SIM using a single DTOF calculated analytically using Eq. (2.31). This approach has the drawback that the influence of an IRF is completely neglected. However, in reality an IRF is always involved and its contribution to the moments of the measured DTOF has to be removed using Eqs. (4.7) to (4.10). Therefore conclusions drawn by Liebert et al. [70] about the L_U dependence do not exactly apply to a real situation.

Here a more detailed analysis of the accuracy of the calculation of moments accounting for the IRF influence and the finite integration range is presented. First, the reflectance $R(t)$ of a semi-infinite medium with same parameters as in [70] is calculated using Eq. (2.31) (parameters: $\mu_a = 0.1 \text{ cm}^{-1}$, $\mu'_s = 10 \text{ cm}^{-1}$, $n = 1.33$, $r_{\text{sd}} = 3 \text{ cm}$). Second, this theoretical curve is convolved with experimentally obtained IRFs $I(t)$ to obtain as simulated measurement result $N(t)$ following Eq. (4.6). Third, the moments m_1 and V of $N(t)$ as a function of L_U are calculated and analysed. The values of moments of all DTOFs were obtained using the same relative limits. The lower integration limit L_L was fixed to 5 % while the upper integration limit L_U was varied from 10^{-4} to 10^{-1} . Moments of the simulated measurement result were corrected for the influence of the IRF using Eqs. (4.7) and (4.8) for each value of L_U individually. Since the parameters of the theoretical curve $R(t)$ are known the true values of moments can be easily evaluated using Eqs. (4.28) and (4.29).

Left column of Fig. 4.1 shows the IRFs of three exemplary detectors used for the computations (MuA - multialkali PMT, GaAs - Gallium-Arsenide PMT, SPAD; see also Section 5.1). All IRFs have visible differences in shape which are difficult to capture by single scalars such as the full width at half maximum (FWHM) or moments of different orders (cf. Table 5.1). In particular this includes parasitic reflections or afterpeaks (afterpeaks of the MuA and GaAs are labelled by [A] and [B] in Fig. 4.1) and the high dynamic range of detection (label [C]). Afterpeaks can result from reflections within the optical path or from afterpulsing which has its origin within the dynode system of PMTs [72, p. 77]. As discussed below these specific properties of the IRFs affect the values of moments in a unfavourable way.

Retrieved and true values of moments in terms of ratios of the mean time of flight $m_1(L_U)/m_{1,true}$ and variance $V(L_U)/V_{true}$ are compared in Fig. 4.1 right. Moments of the theoretical curve (no IRF influence) demonstrate the same behaviour as the data shown in [70]. However, the corresponding curves obtained after the convolution with realistic IRFs exhibit a completely different behaviour in a number of points. In particular these are:

4. Analysis of Time-Domain NIRS Signals by Moments

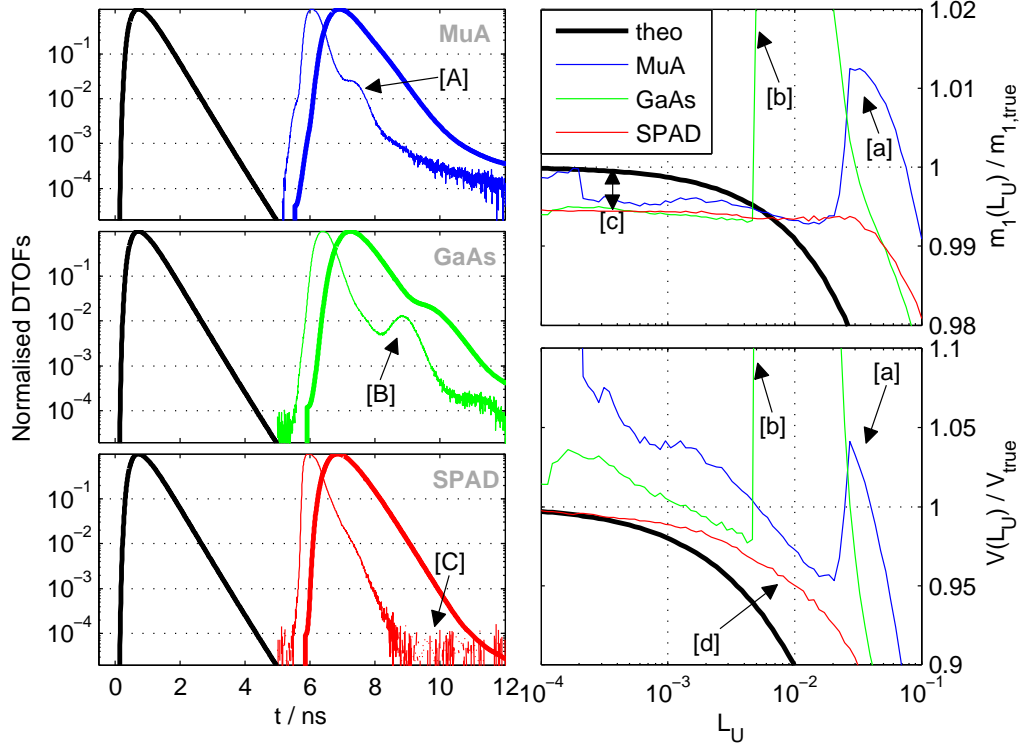


Figure 4.1: Dependence of the moments m_1 and V on the upper integrations limit L_U and the influence of experimental IRFs. Left: DTOFs that are involved into the calculation of moments shown for three different detectors (MuA, GaAs, SPAD): the theoretical curve $R(t)$ (thick black lines) is convolved with an experimental and background free IRF $I(t)$ (thin coloured lines) giving the simulated measurement result $N(t)$ (thick coloured lines). Right: Ratios of the retrieved moments to the true value as a function of the relative upper limit L_U . Curves referring to the GaAs detector (green lines) are truncated for better representation. Their maxima are 1.03 and 1.43 in the upper and lower panels, respectively. Labels [A]-[C] and [a]-[d] are discussed in the text.

- The pure theoretical curve is always below 1, i.e. values of moments are always underestimated, while in the realistic case they can be both under- and overestimated.
- Moments retrieved in the realistic case come close to the true value already for rather large values of $L_U > 3\%$. This is completely unexpected if only the behaviour of the theoretical curve is taken as a reference. However, this is not necessarily better because of the high instability in this range.
- Afterpeaks in the IRF [A] and [B] cause an overestimation and distortion of the values of moments [a] and [b]. As soon as L_U encloses the

afterpeaks in both, the IRF and the convolved curve, the retrieved values of moments return to the reasonable range close to the true value. This is especially pronounced in the case of the GaAs detector. The sudden decrease [b] in moments is caused by the inclusion of the afterpeak [B]. Before that the L_U seek procedure gets caught in the minimum right before the afterpeak [B] resulting in too low values of moments of the IRF (and therefore too high values of calculated moments) as a result of the IRF correction by Eqs. (4.7) and (4.8).

- Surprisingly, retrieved values of m_1 in the range around $L_U = 1\%$ are remarkably stable for all detectors but exhibit a constant offset [c] of about 1%.
- The high dynamic range (label [C]) of the SPAD detector in combination with the absence of any afterpeaks and a narrow IRF results in a V retrieval more similar to the theoretical curve [d]. The deviation from the true value is still less than the one of the theoretical curve.

These findings have implications for the procedure of calculation of moments and instrumental aspects if an analysis by moments is intended. First, it is unreliable to perform a "blind" calculation of moments using canonical values for L_U because the results will most probably be corrupted by IRF artefacts. Instead the values of moments should be first analysed as a function of L_U in combination with the actual IRF as shown in Fig. 4.1. This can trigger improvements of the experimental setup such as an optimisation of reflections in the optical path or detector replacement. Second, a more narrow IRF will not necessarily result in values of moments closer to the true value but will rather approach the course of the theoretical curve. A behaviour like this is exhibited by the SPAD detector in Fig. 4.1 right. Third, a detector with a higher dynamic range allows to decrease L_U and thereby to obtain more accurate values of moments as it is indicated by the pure theoretical curve.

Apart from the difficulties described above it is desirable to obtain information about the systematic offset in the retrieved moments due to the finite integrations range. An algorithm designed to estimate such an offset and to correct for it is discussed in the next section.

4.1.3 Correction Algorithm for Calculation of Moments

The finite integration range and the influence of the IRF leads to a systematic error in values of moments calculated from experimentally obtained DTOFs. This results in a systematic shift of the absolute values of moments and can

4. Analysis of Time-Domain NIRS Signals by Moments

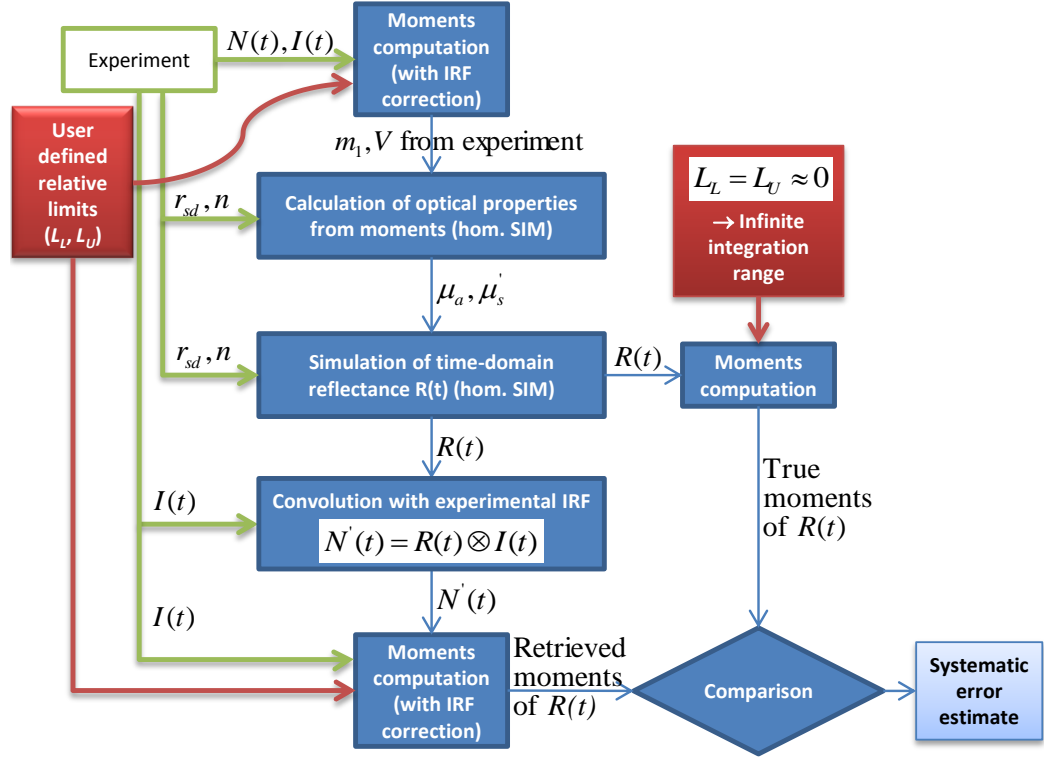


Figure 4.2: Algorithm for the computation of the systematic error estimate appearing during the calculation of moments' values from an experimental DTOF $N(t)$ under the consideration of the instrumental response function $I(t)$. The scheme shows a single iteration executed for a single set of relative limits L_L and L_U . In practice, multiple iterations need to be executed with a fixed value of L_L and L_U varying in a certain range. Here the reflectance $R(t)$ of the homogeneous semi-infinite medium (SIM) is used to approximate the unknown response of the medium under investigation. Further parameters: r_{sd} - source-detector separation, n - refractive index.

bias the output of a subsequent analysis. It should be noted that small differences of moments are virtually not affected by the unknown systematic error because it cancels out by subtraction. However, if changes in moments are converted to changes in the absorption coefficient $\Delta\mu_a$ accurate absolute values of moments are required to obtain reliable sensitivity factors (see Section 4.3). Below an algorithm is presented to estimate the mismatch between the true and retrieved moments which is introduced by those systematic errors.

The algorithm is visualised in Fig. 4.2. The main idea is to approximate the unknown medium response by a similar DTOF $R(t)$ the moments of which would be known exactly. $R(t)$ can then be convolved with the experimental IRF $I(t)$ measured separately to obtain a simulated measurement result $N'(t)$. Subsequently moments are calculated on two paths: (i) from $R(t)$ to

obtain true values of moments and (ii) from $N'(t)$ to obtained retrieved moments. In the end the values of the retrieved moments include the systematic offset caused by the convolution with the measured IRF and the finite integration range. Finally, the comparison of the true values of moments of $R(t)$ with the values retrieved from $N'(t)$ gives the systematic error estimate. It can be expressed in a relative manner for the n -th moment m_n of interest, i.e. as the ratio r :

$$r = \frac{m_{n,\text{retrieved}}}{m_{n,\text{true}}} \quad (4.15)$$

This ratio can then be used to rescale the corresponding moments' values calculated for the measured DTOF $N(t)$ and a given relative upper integration limit L_U . The corrected value $m_{n,\text{corr}}$ is then given by:

$$m_{x,\text{corr}} = m_{x,\text{uncorr}}/r \quad (4.16)$$

where $m_{n,\text{uncorr}}$ is the uncorrected value of a moment, i.e. which is calculated using Eq. (4.14) and the same L_U .

The algorithm implies that $R(t)$ is similar to the true but unknown medium response. As a consequence of this similarity the obtained systematic offset of moments is approximately equal in both cases. This is the key assumption of the algorithm. Therefore the calculation of $R(t)$ requires special care.

There are various ways how $R(t)$ can be modelled. It can be calculated as a general distribution from a finite number of moments [69] or be modelled as a similar distribution with the tail replaced by a varying exponential decay [63]. However, the most promising way is to use light propagation models which can adequately approximate the medium under investigation. Potentially, analytical solutions for any geometry (layered medium, perturbation solutions) or even Monte-Carlo simulations might be employed as long as the computational effort is acceptable. For the calculation of the moments of a single DTOF the algorithm in Fig. 4.2 is executed about one hundred times. Therefore, in practice this requires analytical models with low computational effort. Here, it is therefore suggested to use the solution of the diffusion equation for the homogeneous semi-infinite medium Eq. (2.31). It is computationally inexpensive and approximates the light propagation in a human head sufficiently for this purpose. Further, the calculation of $R(t)$ can be initialised from two moments only.

The performance of the correction algorithm was tested on a heterogeneous medium in order to avoid an intrinsic match with the homogeneous model used within the algorithm. For this various configurations of a two-layered semi-infinite medium with different optical properties were used. Light propagation was simulated using the solution published in [73]. In particular,

4. Analysis of Time-Domain NIRS Signals by Moments

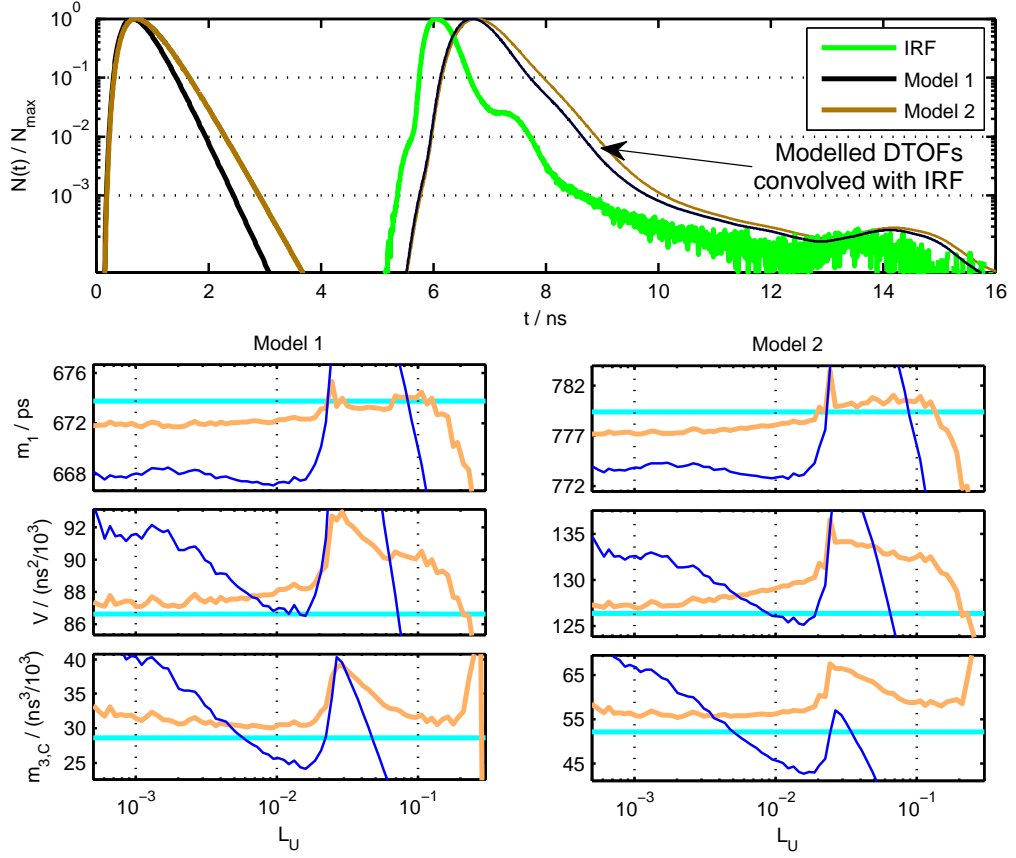


Figure 4.3: Application of the correction algorithm for moments to a DTOF simulated using a two-layered model. Top panel: IRF of the MuA detector in comparison to the two modelled DTOFs (model 1 and 2) before and after the convolution with the IRF. Lower panels: values of moments as a function of the relative upper limit L_U calculated without (blue) and with (orange) the application of the correction algorithm. The horizontal lines (cyan) represent the true values.

four different IRFs (MuA, GaAs, HPM, SPAD; also compare Fig. 5.2)¹ and four geometry configurations with mismatching μ'_s and μ_a in both layers and different thickness of the upper layer d_1 were used.

An example for moments' correction employing the IRF of the MuA detector and two modelled medium responses is shown in Fig. 4.3. Parameters of the simulated curves were $\mu'_s = 10 \text{ cm}^{-1}$, $n = 1.33$, $r_{sd} = 3 \text{ cm}$ equal for both layers while the absorption was different, i.e. $\mu_{a1} = 0.1 \text{ cm}^{-1}$ and $\mu_{a2} = 0.2 \text{ cm}^{-1}$ for the upper and lower layers, respectively. The thickness of

¹ MuA - photomultiplier (PMT) with a multi-alkali photocathode, GaAs - PMT with a Ga-As photocathode, HPM - hybrid PMT, SPAD - single photon avalanche diode.

the upper layer d_1 was 0.7 cm and 1.3 cm for models 1 and 2, respectively. The thickness of the lower layer d_2 was set to 10 cm which effectively makes the medium semi-infinite. The IRF of the MuA detector as well as the DTOFs of the both models before and after the convolution with the IRF are shown in the upper panel of Fig. 4.3. Differences between the both modelled DTOFs are clearly visible but reduced by the convolution with the IRF.

Lower panels of Fig. 4.3 show values of corrected and uncorrected moments as a function of the upper relative limit L_U in comparison to the true values. In addition to the mean time of flight and variance the correction algorithm was also used as a sensitivity factor to calculate the third centred moment $m_{3,C}$ which can be used to convert changes in variance ΔV to $\Delta\mu_a$ (see Section 4.3.1). Note that the absolute values of the moments differ substantially for models 1 and 2 (lower panels in Fig. 4.3).

The correction procedure results in more reliable values of moments for nearly any value of L_U . Indeed, an inspection of the course of the uncorrected moments as a function of L_U in Fig. 4.3 exhibits peaks and high variation. Without the prior knowledge of the true value it is even difficult to decide which L_U value is justifiable. In contrast, this is much easier if the correction algorithm is applied. The corrected values exhibit a much lower variation and smaller peaks. In the L_U range from 1‰ to 1% the signals are rather stable and close to the true value. This strongly simplifies the selection of L_U value. The effect of correction on the mean time of flight is remarkable. Already for $L_U < 10\%$ the corrected values deviate by less than 3 ps ($\approx 4\%$). The correction algorithm even compensates for most of the influence of the afterpeaks in the IRF.

In the past it was argued that moments of order higher than two would be highly unreliable and therefore not usable. However, in Fig. 4.3 an impressive correction of the values of $m_{3,C}$ can be seen. This demonstrates that the correction algorithm can even be used for the third centred moment with an acceptable deviation of better than 10%. This finding is important for the conversion of changes in variance ΔV to absorption changes $\Delta\mu_a$ as used in Section 4.3.1.

Further tests of the correction algorithm in combination with narrow IRFs (HPM, SPAD) resulted in an even better approximation of the true values of moments (examples are discussed in Appendix A.3). It should be emphasized that the correction algorithm presented here improves the accuracy of the absolute values of moments but does not affect the noise which is increasing with the order of the moment.

4.1.4 Uncertainty of Moments

The change of a signal and its noise define the detection limits of a method and/or an instrument. Also in order to judge the significance of a signal change it always has to be compared to the corresponding uncertainty. Therefore the knowledge about the sources of noise, the resulting uncertainty and its quantification is crucial for the assessment of the applicability of a method and for the optimisation of an instrument.

In fNIRS main sources of noise are the photon, electronic, “mechanical” and so called “physiological” noise. The “mechanical” noise originates from the movement of a subject and the displacement of optodes which together introduce unwanted signal variations (see also Section 5.1.3). These should be considered by the design of the experiment and be reduced as far as possible. The term “physiological” noise, although frequently used in fNIRS literature, is misleading. Systemic physiological processes, e.g. blood pressure or heart beat, can influence changes to the blood volume and oxygenation and thereby cause changes of optical signals. These changes can even mask the desired brain related signals in fNIRS. This behaviour led to the term “physiological” noise. However, signal variations caused by such systemic physiological processes are not purely stochastic and can be even task evoked (cf. Section 6.1.3). Therefore the term “physiological noise” should be avoided.

In this section only photon and instrumental noise are considered as sources of uncertainties of moments. Photon noise is well described by Poisson statistics where the uncertainty of a photon count N_i in the i -th channel is simply given by $\sqrt{N_i}$. Instrumental noise is a result of the fluctuations of the many electrical signals involved in the detection of photons in time-domain NIRS. In particular this includes the jitter of the laser pulse and the sync signal as well as fluctuations in other electronic components.

Here an analysis of noise and the resulting uncertainties with regard to the method of moments as applied in time-domain fNIRS data is performed. The contribution of the instrumental response function (IRF) to the uncertainty of moments and the detectability of small changes of moments (Δm_1 and ΔV) typically observed *in vivo* are discussed.

Instrumental Noise and Photon Noise Contributions

The total uncertainty of a moment σ_T^2 can be modelled as

$$\sigma_T^2 = \sigma_P^2 + \sigma_I^2 \quad (4.17)$$

where the variances σ_P^2 and σ_I^2 represent the uncertainty contributions of the photon and instrumental noise, respectively. Both are assumed to be

4.1. Moments of DTOFs

statistically independent. Accordingly σ denotes the corresponding standard deviation.

The influence of photon noise on the non-centred and centred moments of a DTOF of order n , m_n and $m_{n,C}$, respectively, can be calculated analytically from absolute values of moments of different order (see the derivation in Appendix A.2 and Eqs. (A.17) and (A.24)):

$$\sigma_P^2(m_n) = \frac{1}{N_T} (m_{2n} - m_n^2) \quad (4.18)$$

$$\sigma_P^2(m_{n,C}) = \frac{1}{N_T} (n^2 m_{n-1,C}^2 m_{2,C} + 2n m_{n-1,C} m_{n+1,C} - m_{n,C}^2 + m_{2n,C}) \quad (4.19)$$

Using Eqs. (4.18) and (4.19) and the identity $m_{1,C} = 0$ explicit expressions for the uncertainty of the mean time of flight m_1 and variance $V = m_{2,C}$ due to photon noise are found to be (see also [12, 70]):

$$\sigma_P^2(m_1) = \frac{m_2 - m_1^2}{N_T} = \frac{V}{N_T} \quad (4.20)$$

$$\sigma_P^2(V) = \frac{m_{4,C} - V^2}{N_T} \quad (4.21)$$

where $m_{4,C}$ is the fourth centred moment and N_T the total photon count of a DTOF. Note that m_1 , V and $m_{4,C}$ refer to the actually measured DTOF. Thus σ_P^2 can be calculated analytically for every individual DTOF from its moments.

The instrumental noise contribution to the uncertainty of moments results from the jitter of the laser pulse, the sync signal and fluctuations in other electronic components. All these influences can be modelled as a fluctuation of the time zero t_0 which is the reference time point for the measurement of the time of flight (TOF) of a single photon. As a result the individual TOF is measured with a small uncertainty. This small uncertainty becomes part of the IRF which is mainly dominated by the detector response, broad laser pulses and pulse broadening by the fibres (cf. Eq. (2.33)). The instrumental noise contribution σ_I is unknown but can be calculated using Eq. (4.17) if σ_P and σ_T are known.

The total uncertainty σ_T^2 can be obtained from repeated measurements of the IRF. For this purpose a time series of DTOFs $N_j(t)$ is recorded and moments are calculated for each $N_j(t)$. The standard deviation calculated for a sufficiently large number of values of moments $m_{1,j}$ and V_j gives the empirical variation σ_T .

4. Analysis of Time-Domain NIRS Signals by Moments

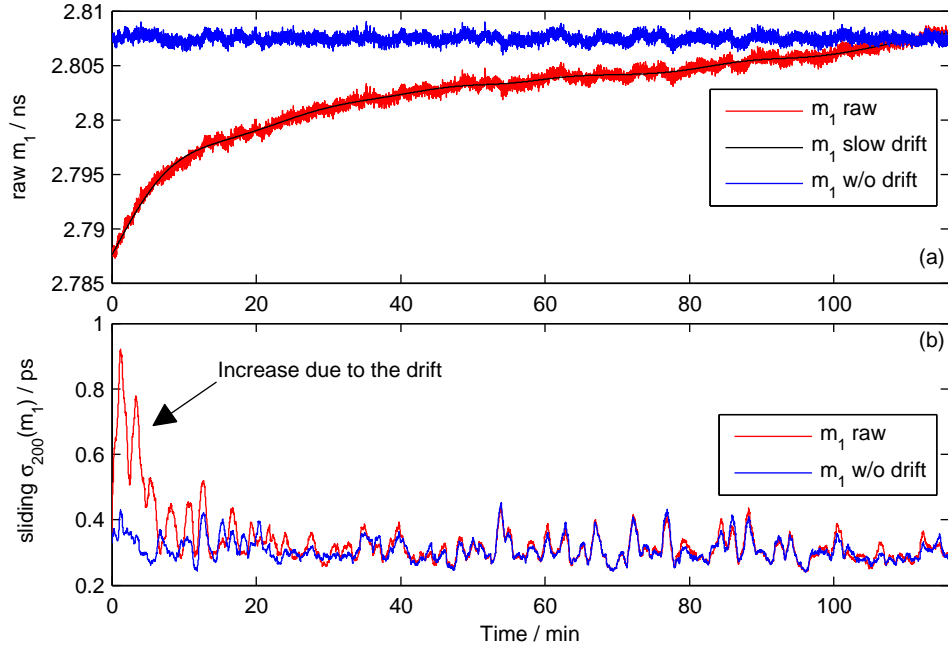


Figure 4.4: Uncertainty of the mean time of flight m_1 . (a) Time series of m_1 calculated from a series of DTOFs. The time course exhibits a substantial slow drift (black line) which can be corrected by using a high-pass filter. (b) Sliding standard deviation σ calculated from the time series of m_1 (with and without drift) shown in the top panel and using a sliding window of 200 data points. The drift increases the otherwise rather constant σ .

Figure 4.4 shows the time course of the mean time of flight obtained from an approximately 2 hours long measurement of the IRF². Not centred moments, e.g. m_1 , are subject not only to stochastic noise but also to long term drifts of the signal as shown in Fig. 4.4a. Drifts like this are not critical for fNIRS because typical stimulation related signals exhibit changes on a shorter time scale of a few minutes³. Thus the drift can be removed using a high-pass filter or a sliding average calculation (less accurate). In Fig. 4.4a the filtering of the raw m_1 signal was performed using the `filtfilt`⁴ function from Signal Processing Toolbox of Matlab and a low cut-off frequency of 0.001 Hz. In addition, a constant offset obtained as the mean value of the last piece of the raw m_1 signal was added. This last step is actually not needed

² The data used here was acquired by a SPAD detector connected to a SPC-630 module and a pulsed diode laser emitting at 690 nm.

³ Long term drift might cause problems in long term monitoring depending on the data analysis model, i.e. in how far the data analysis relies on absolute values of the time-domain measurands.

⁴ This function performs zero-phase filtering.

for the calculation of σ or Δm_1 .

Fig. 4.4b shows the course of the sliding standard deviation ($= \sigma_T$) calculated from the signals in Fig. 4.4a. If the drift is large (here during the first 10 minutes) then it influences the values of σ . Otherwise the influence is negligible. Occasional peaks in the course of σ are caused by slow fluctuations in m_1 which are faster than the drift. These fluctuations also contribute to the signal noise. In general, non-centred moments m_n are influenced by the long-term drift of t_0 but the centred moments $m_{n,C}$ are not. During the calculation of $m_{n,C}$ the drift is removed by subtracting the mean time of flight of each DTOF (cf. the term $(t - m_1)$ in Eq. (4.5)).

An important parameter which influences the empirically obtained uncertainty is the collection time T_C of a single DTOF. In TCSPC photons registered within the time period T_C contribute to the corresponding DTOF. In general, the larger T_C the more photons are collected and thus the lower the photon noise. On the other hand, with larger values of T_C also slow fluctuations of the instrumental noise are included which leads to an increase of the total uncertainty.

In practice, the dependence of noise on T_C cannot be studied by simply increasing the T_C parameter in the configuration of TCSPC electronics. At a constant count rate an increase in T_C leads to an increase of the number of photons counted per channel. In TCSPC electronics used throughout this work⁵ this number is limited to 65635 [74, p. 516]. However, this limitation can be circumvented by binning DTOFs acquired with a short collection time. For this multiple DTOFs $N_j(t)$ are summed up along the time channels to receive the binned DTOF $N_b(t)$:

$$N_b(t) = \sum_{j=1}^k N_j(t) \quad j, k \in \mathbb{N} \quad (4.22)$$

Effectively, $N_b(t)$ is a DTOF which would be acquired with the k -fold collection time of $N_j(t)$. At a constant count rate $N_b(t)$ contains approximately the k -fold number of photons of $N_j(t)$ and is therefore less influenced by the photon noise as indicated by Eqs. (4.20) and (4.21).

Here the long term IRF measurement discussed above was used to obtain a series of binned DTOFs $N_b(t)$ with k ranging from 1 to 100. This corresponds to values of the collection time T_C from 0.5 s to 50 s. Moments m_1 and V were calculated for each individual $N_b(t)$. The mean value of the sliding standard deviation calculated from the resulted series of values of moments was used as σ_T . Similarly, the photon noise σ_P was calculated from moments using

⁵ TCSPC modules produced by the Becker & Hickl GmbH.

4. Analysis of Time-Domain NIRS Signals by Moments

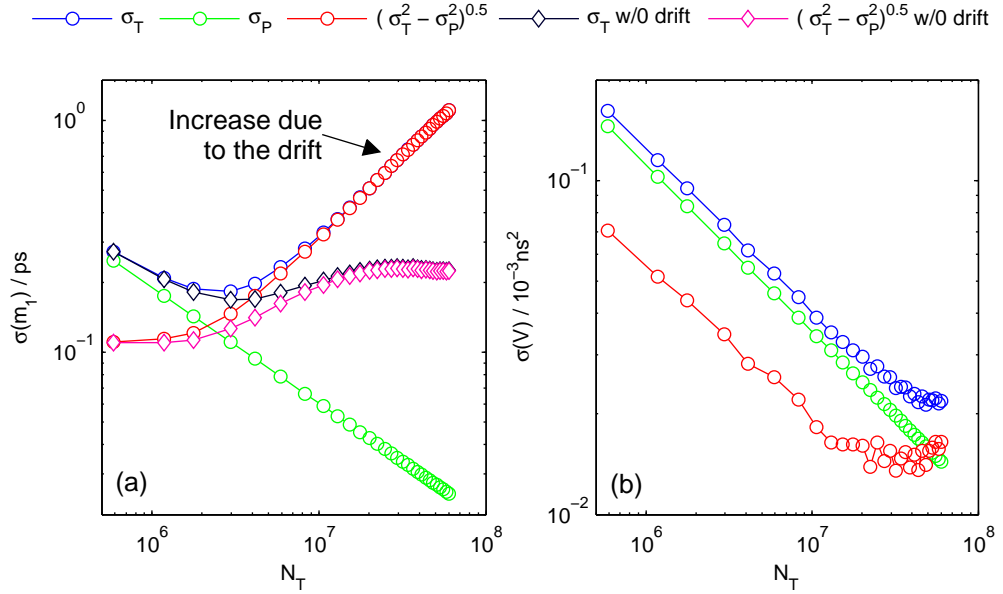


Figure 4.5: Uncertainty of the moments m_1 (a) and V (b) as a function of the total number of photons N_T . N_T was increased by binning DTOFs acquired as a time series at the same count rate (cf. Fig. 4.4). Thus here N_T is proportional to the collection time T_C . The total and photon noise are denoted by σ_T and σ_P , respectively. The instrumental noise is calculated as $\sigma_I = \sqrt{\sigma_T^2 - \sigma_P^2}$. For m_1 the noise was calculated with and without the long term drift shown in Fig. 4.4a. The variance signal is essentially drift-free because it is a centred moment.

Eqs. (4.20) and (4.21). The instrumental noise was then calculated from Eq. (4.17). In addition for the noise of m_1 the procedure was repeated with the long term drift removed. For this the time t in Eq. (4.4) was replaced by t' :

$$t' = t - t_{drift} \quad (4.23)$$

where t_{drift} is the drift of each individual DTOF $N_b(t)$ obtained from the drift of m_1 as shown in Fig. 4.4.

The results in terms of σ_T , σ_P and σ_I as a function of $N_T \sim T_C$ for the moments m_1 and V are shown in Fig. 4.5. In both cases the photon noise shows the expected N_T^{-1} dependence which appears as a straight line in the log-log plot. Due to the long term drift $\sigma_T(m_1)$ increases with longer collection times, e.g. larger N_T values. If the drift is excluded $\sigma_T(m_1)$ increases slightly and reaches a plateau.

The noise of the variance V shown in Fig. 4.5b is dominated by the photon noise and is not influenced by the long term drift. For low number of photons the fraction of the instrumental noise is small and $\sigma_I(V)$ only becomes dominant for $N_T > 6 \cdot 10^7$. However, it should be mentioned that for long

times V can exhibit real (although small) changes due to the temperature fluctuations of the diode laser head. Changes like these are likely to increase the value of σ_I . In most cases, e.g. for realistic count rates, the V signal will be dominated by the photon noise.

Simulation of Uncertainty of Moments

A measured DTOF $N(t)$ is modelled as a convolution of the response of the medium $R(t)$ with the instrument response function $I(t)$:

$$N(t) = I(t) \otimes R(t) \quad (4.24)$$

Using Eqs. (4.7) to (4.10) moments of $N(t)$ can be easily calculated from moments of $I(t)$ and $R(t)$. Further, the influence of the photon noise on moments of $N(t)$ can be calculated from its other moments using Eqs. (4.18) and (4.19). In order to see the interplay of the photon noise with different IRFs (here four different detectors combined with the same laser) a constant instrumental noise contribution σ_I^2 was added to the photon contribution as denoted by Eq. (4.17). σ_I^2 was estimated from an IRF measurement as suggested in the previous section.

The photon noise is fundamental and cannot be avoided. However, it depends on the total number of photons N_T collected. In general, the larger N_T the lower the noise. The photon noise represents a general limitation which would be present even if an ideal instrument was used for a measurement. Below such an ideal instrument is represented by the δ -IRF.

Using a fixed instrumental contribution and a simulated medium response which is similar to results obtained in real experiments on tissue (e.g. the head) the dependence on N_T can be investigated. Here a homogeneous semi-infinite medium and the diffusion approximation is used (parameters: $\mu_a = 0.1 \text{ cm}^{-1}$, $\mu'_s = 10 \text{ cm}^{-1}$, $r_{\text{sd}} = 3 \text{ cm}$ and $n = 1.4$). For this configuration the values of moments can be obtained analytically using Eqs. (4.28) and (4.29). The resulting values, e.g. $m_1 \approx 1 \text{ ns}$ and $V \approx 0.2 \text{ ns}^2$, are similar to those observed *in vivo* on an adult human head.

The total number of photons is varied in the range from 10^2 to 10^8 photons. Here two typical ranges have to be discussed which are used for functional *in vivo* and IRF or phantom measurements. Using the Brain Imager for functional experiments typically 20 DTOFs per second at ADC count rates from 0.6 MHz to 5 MHz are acquired. Each DTOF contains information about three wavelengths. This effectively results in 17000 to 83000 photons per DTOF and wavelength. In the case of an IRF or phantom measurement a much higher number of DTOFs and thus more photons can be acquired,

4. Analysis of Time-Domain NIRS Signals by Moments

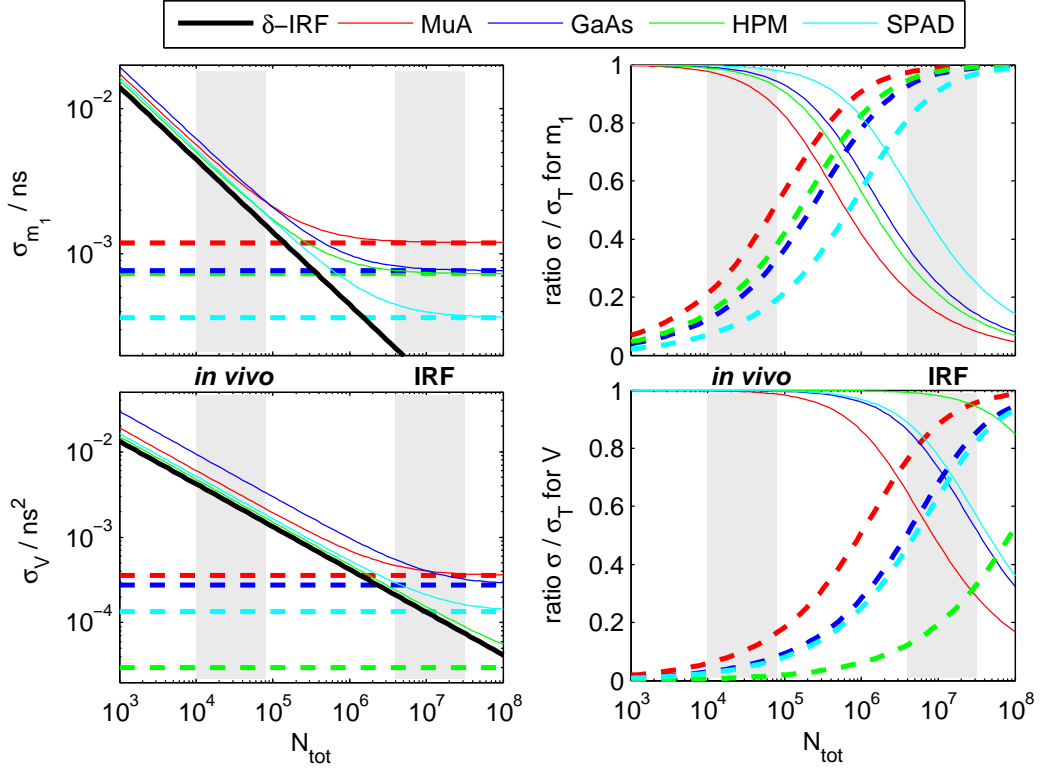


Figure 4.6: Contributions of the instrumental and photon noise to the uncertainties of the moments m_1 and V as a function of the total number of photons N_{tot} (upper and lower panels, respectively). Data is shown for a δ -IRF, e.g. photon noise only, and four exemplary detectors (MuA, GaAs, HPM, SPAD). Left: solid lines refer to the total noise σ_{m_1} and σ_V as function of the total photon count N_{tot} ; dashed lines refer to the constant level of the instrumental noise. Right: ratios σ_P/σ_T and σ_I/σ_T of the photon (solid lines) and instrumental (dashed lines) noise to the total noise, respectively. Note that the σ values are not additive but the variances σ^2 . Grey areas indicate N_{tot} ranges typical for *in vivo* and phantom or IRF measurements.

typically about 400 times more. These two experimental situations will be distinguished in the calculations performed below.

Results of the simulation of the uncertainty for m_1 and V are shown in Fig. 4.6. Computations were performed for an ideal δ -IRF and four different detectors (MuA, GaAs, HPM, SPAD, cf. Fig. 5.2 and Table 5.1). In the *in vivo* range the photon noise contribution dominates. However, in the case of the MuA detector and for the m_1 also the instrumental noise contributes substantially to the total noise. A count rate increase continuously decreases the photon noise contributions and thereby improves the measurement. Differences between detectors are small and in most cases these differences can be compensated by a slightly higher count rate. Values of noise calculated for

the δ -IRF represent the principle limit which cannot be undercut by even a perfect instrument. In the IRF range and above the instrumental noise is the more dominant contribution. A further increase of the number of collected photons does not decrease the total noise noticeably. All findings are similar for m_1 and V . For the variance even more photons ($> 10^8$) are needed to reach the instrumental noise level.

The measurement mode defines different requirements for detectors. In a phantom measurement the number of photons can be increased by prolonging the time of the measurement. In this case the system with the lowest instrumental noise should be preferred. In functional *in vivo* measurements the device should primarily collect as many photons as possible in a given but limited measurement time. A low instrumental noise level is less important here.

Significant Changes in Moments

In order to decide if a change of a signal is significant statistical tests can be used. In the situation discussed here the standard deviations of the signals can be calculated analytically. Thus the so-called Z -test (also known as the Gauß-test) can be employed. The test statistic to be calculated is:

$$Z = \frac{(\bar{Y}_2 - \bar{Y}_1) - \delta}{\sqrt{\frac{\sigma_{Y_1}^2}{k} + \frac{\sigma_{Y_2}^2}{j}}} \quad (4.25)$$

Herein \bar{Y}_1 and \bar{Y}_2 refer to the mean values describing two signals states selected for comparison. Consequently their difference $(\bar{Y}_2 - \bar{Y}_1)$ can be associated with changes in moments, i.e. Δm_1 or ΔV . Usually, one wants to know if the obtained signal change significantly differs from zero and thus $\delta = 0$. Here, with regard to *in vivo* application, a small difference in moments of two similar DTOFs is considered and therefore $\sigma_{Y_1}^2 \approx \sigma_{Y_2}^2$. These standard deviations can be calculated analytically as discussed in previous sections. Further it is assumed that both states have been measured the same number of times, i.e. $k = j$. In a fNIRS experiment with a block design k refers to the number of trials, e.g. repetitions of the task. All together the test statistics simplifies to:

$$Z = \frac{\Delta m_x}{\sqrt{2\sigma_{m_x}^2/k}} \quad (4.26)$$

where Δm_x is the change of a moment and $\sigma_{m_x}^2$ is the variance of the base value of the moment. Typical brain activation related changes in moments

4. Analysis of Time-Domain NIRS Signals by Moments

Table 4.1: Absolute values of typical changes in moments observed *in vivo* during a finger tapping task.

	690 nm	800 nm	830 nm
$ \Delta A $	0.01 to 0.05		
$ \Delta m_1 / \text{ps}$	1 to 2	2 to 5	2 to 5
$ \Delta V / (10^{-3}\text{ns}^2)$	≈ 1	1 to 2	1 to 2

observed *in vivo* for three wavelengths used in the Brain Imager are listed in Table 4.1.

For the computations below rather small changes of $\Delta m_1 = 1 \text{ ps}$ and $\Delta V = 0.001 \text{ ns}^2$ are used. As before a homogeneous semi-infinite medium was taken as an example response of tissue. Calculations were carried out for an ideal case (δ -IRF) in order to quantify a limit in general and for a realistic detector (MuA detector of the Brain Imager). The number of trials was varied from 1 to 30.

It is of particular interest to compare typical time-domain measurands, e.g. m_1 and V , to attenuation changes ΔA as a cw-fNIRS measurand. In the case of small absorption changes the count rates of two states of interest are similar and thus $\sigma^2(\Delta A) \approx 2/N_T$ (cf. Eq. (A.15)). In this case the test statistics simplify to:

$$Z = \frac{\Delta A}{\sqrt{4/N_T/k}} \quad (4.27)$$

Changes in attenuation are free of the influence of the IRF. Below significance calculations are performed for $\Delta A = 0.01$ and $\Delta A = 0.02$.

Results in terms of p -value maps are shown Fig. 4.7 for Δm_1 and ΔV and in Fig. 4.8 for attenuation changes ΔA . Levels of the canonical significance limits ($p < 0.05$ and $p < 0.01$) are indicated by contours. In all cases an increase in the number of photons N_T and in the number of trials improves the significance. A typical N_T range achieved *in vivo* for a single wavelength and 50 ms collection time is enclosed by white vertical lines. In the case of the δ -IRF, the significance levels are reached for more than 20 trials and $N_T > 5 \cdot 10^5$. In the case of the realistic detector, significance can be reached only by even higher N_T . In all cases changes in attenuation outperform changes in m_1 and V at the same count rates. This is a direct result of the considerably lower noise level of ΔA compared to Δm_1 and ΔV .

The only way to increase the significance of Δm_1 and ΔV is to increase the number of photons. This, to some extent, is possible by summing up DTOFs and therefore effectively increasing the collection time. For example $\log_{10} N_T = 6$ can be reached with a collection time of 1 s. In this case sig-

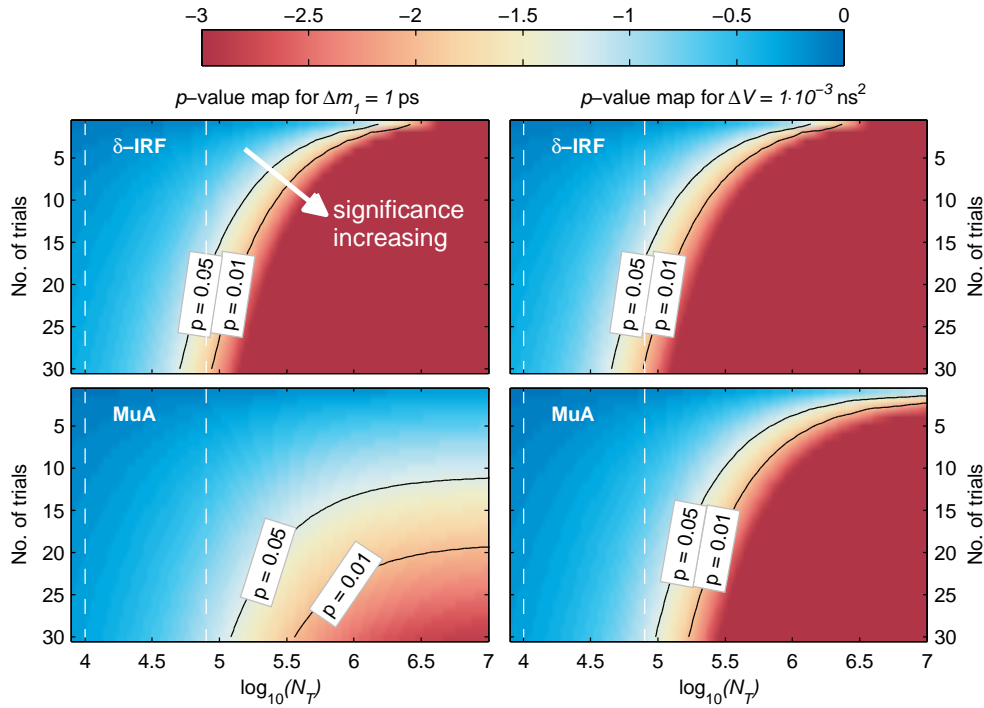


Figure 4.7: Maps of p values calculated for $\Delta m_1 = 1$ ps (left) and $\Delta V = 0.001$ ns² (right) as well as an ideal δ -IRF (upper panels) and a real detector (MuA, lower panels). The lower p (and thus $\log_{10} p$) the higher the significance of the signal change. Here $\log_{10} p$ is used instead of p for better scaling of the colours in the figure.

nificance levels can be reached already for 5 to 15 trials. However, a longer collection time also leads to an increase of the level of noise because additional signal variations caused by physiological processes, i.e. pulsation, are included. Advanced data processing may compensate for this. Pulsation exhibits a distinct spectrum with a main component around 1 Hz. Thus, it is possible to apply a low pass filter to remove large portions of its influence. Other systemic physiological processes occur on longer time scales than 1 s and might not disturb.

For count rates typically used and achieved *in vivo* the photon noise is the most dominant source of noise. To some extent the noise level can be reduced by a more narrow IRF and temporal signal filtering. In general, an improvement can only be achieved by higher count rates.

The situation is different for phantom measurements. Under laboratory conditions usually higher laser power is available and the collection time can be increased. Therefore the main limitation here is the instrumental noise which is low for the HPM and SPAD detectors. The large cathode area of the HPM detector and conventional PMTs helps to achieve high count rates.

4. Analysis of Time-Domain NIRS Signals by Moments

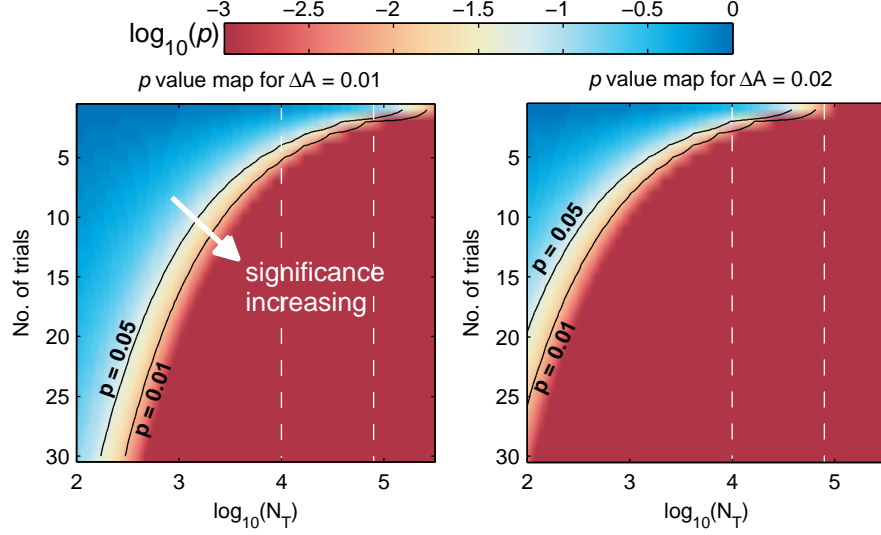


Figure 4.8: Maps of p values calculated for $\Delta A = 0.01$ (left) and $\Delta A = 0.02$ (right). The lower p and $\log_{10} p$ the higher the significance of the signal change. Note the shifted range of $\log_{10} N_T$ compared to Fig. 4.7.

Brain activation related signal changes of m_1 and V are small and therefore difficult to measure. To obtain acceptable statistical significance ($p < 0.05$) for such small changes typically at least 20 trials are needed for both m_1 and V . For single trial experiments only changes of attenuation might provide reliable information.

4.2 Optical Properties Determined from Moments of DTOFs

Light propagation models as well as methods for reconstruction of absorption changes *in vivo* are often based on the knowledge or estimation of optical properties of tissue. In literature optical properties for different tissues were reported (see [9, 75] for tabulated overviews). However, in most cases the reported data was obtained *ex vivo* and *in vitro* and therefore alterations of the tissue due to differences in temperature, structure, preparation procedures and blood content are presumable. Thus any use of *ex vivo* data as an approximation to an *in vivo* situation must be justified. In addition, there is an individual variability in optical properties which can introduce uncertainties to the analysis if values from literature are used. Determination

4.2. Optical Properties Determined from Moments of DTOFs

of individual, spatially and spectrally resolved optical properties *in vivo* is therefore highly desirable. An approach capable of this would be valuable for both, the validation of the many data sets obtained *ex vivo*, new diagnostic approaches and reconstruction models in fNIRS.

Moments of DTOFs in combination with models of light propagation in turbid media can be used to calculate optical properties of tissue or other strongly scattering media. This approach requires additional spatial information obtained from a 3D anatomical MRI image. Further, the spatial structure of the head is simplified by merging distinct voxels into few tissue types. Typically the head is subdivided into five compartments, i.e. scalp, skull, CSF, grey and white matter. The two latter can be further merged into one “brain” compartment. This heterogeneous structure can be even more simplified. Frequently, the head is approximated by the homogeneous semi-infinite medium and therefore spatially unresolved optical properties. These “background optical properties” (BOP) can easily be obtained from moments of DTOFs. The advantage is that the BOP are individual, local, spectrally resolved and do not require an additional MRI scan.

Below the model of the homogeneous SIM is discussed first. Then optical properties of the head are derived from moments of DTOFs measured *in vivo*. The results obtained using models of homogeneous and heterogeneous media are compared and discussed.

4.2.1 Moments and Optical Properties of the Homogeneous Semi-Infinite Medium

Employing the concept of optical diffusion in the homogeneous strong scattering semi-infinite medium it is possible to express moments as a function of the optical properties of the medium (μ_a , μ'_s , n) and the source-detector separation r_{sd} . Corresponding relationships for the mean time of flight m_1 and the variance V were derived in [70]. This is achieved by accomplishing the integration in Eqs. (4.4) and (4.5) with $\hat{N}(t)$ set to the normalised Eq. (2.31), i.e. the time-domain reflectance of the homogeneous SIM with the zero-boundary condition and $z_0 = 1/\mu'_s$. The result is then:

$$m_1 = \frac{r_{sd}^2}{2c_m \sqrt{D} (r_{sd} \sqrt{\mu_a} + \sqrt{D})} \quad (4.28)$$

$$V = \frac{r_{sd}^3}{4c_m^2 \sqrt{D} \mu_a (r_{sd} \sqrt{\mu_a} + \sqrt{D})^2} \quad (4.29)$$

4. Analysis of Time-Domain NIRS Signals by Moments

where $c_m = c_0/n$ is the speed of light in the medium and D is the diffusion coefficient:

$$D = [3(\mu'_s + \mu_a)]^{-1} \approx 1/(3\mu'_s) \quad (4.30)$$

The approximation on the right side holds true for strongly scattering media where typically $\mu'_s \gg \mu_a$. In addition to [70] analytical expression for centred and non-centred moments up to the fourth order as a function of μ_a , μ'_s , c_m and r_{sd} were calculated and are listed in Appendix A.1. Further, Eqs. (4.28) and (4.29) can be rearranged in order to express the optical properties μ_a and μ'_s as a function of moments (m_1 and V), c_m and r_{sd} [70]:

$$\mu_a = \frac{m_1^3}{2c_m V(m_1^2 + V)} \quad (4.31)$$

$$\mu'_s = \frac{2m_1 c_m (m_1^2 + V)}{3r_{sd}^2 V} \quad (4.32)$$

Equations (4.31) and (4.32) can be used to derive optical properties of homogeneous semi-infinite media directly [70] or to initialise a fitting routine of Eq. (2.31) to a measured DTOF. In any case the main advantage is the low computational effort and the simple handling of the IRF by moments. Note that there is a substantial difference between the method of moments and the fit. During a fit the shape of the measured DTOFs is fitted and the residual sum of squares χ^2 is minimised. This is not the case if Eqs. (4.31) and (4.32) are used. However, for verification purposes, it is possible to recalculate the time-domain reflectance using Eq. (2.31) and the obtained optical properties, convolve it with the experimentally obtained IRF and compare the result to the measured DTOF. The similarity can be quantified in terms of residuals as a function of time t or χ^2 . On the one hand this allows to decide if the application of the model is appropriate, on the other, however, the benefit from the application of moments is reduced due to the larger computational effort and the larger number of analysis steps.

In the case that the medium under investigation is heterogeneous it is still possible to calculate background optical properties of a phantom (Section 5.4) or a human head *in vivo* ([76, 77], Section 4.4). However, care must be taken because the application of a homogeneous model to an inappropriate medium might bias the results of analysis.

4.2.2 Optical Properties of the Head *in vivo*

Many models used in functional brain imaging require the prior knowledge of optical properties of the head tissues which are typically taken from the

4.2. Optical Properties Determined from Moments of DTOFs

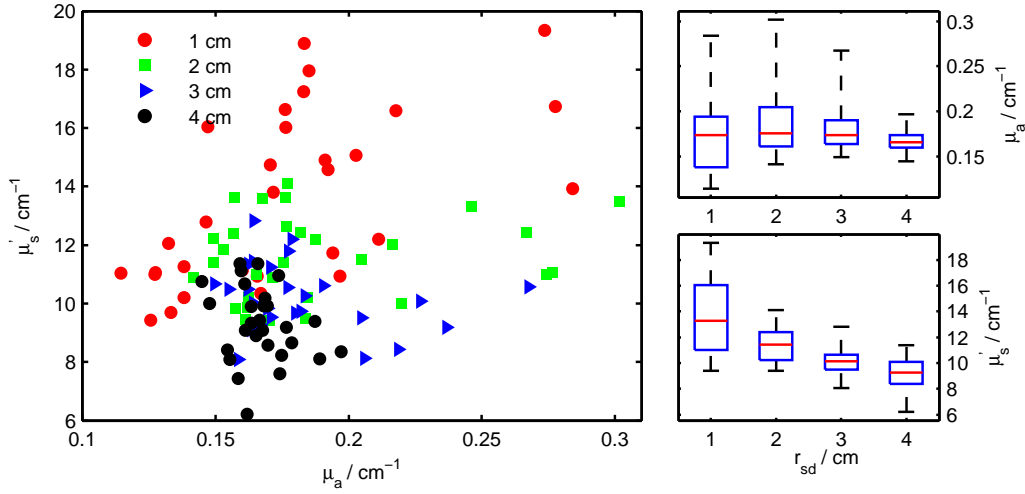


Figure 4.9: Background optical properties obtained from the moments of DTOFs measured for four source-detector separations r_{sd} from 1 to 4 cm across the head of a single subject. Left: Scatter plot of optical properties obtained for each individual source-detector pair. Right: Box plots reflect the distributions of the optical properties as a function of r_{sd} .

literature. Non-invasive *in vivo* determination of optical properties is desirable for better individual and absolute quantification.

In this section optical properties are derived from a large area and high density time-domain NIRS measurement on the head of a single adult male subject. Details of the experimental setup are described in Section 3.5. Briefly, 120 source-detector combinations with r_{sd} values of 1 cm, 2 cm, 3 cm and 4 cm distributed over an area of about 152 cm^2 were measured at the laser wavelength of 800 nm. At this wavelength oxy- and deoxyhaemoglobin exhibit the same absorption (cf. Fig. 2.3). Therefore the signal variation due to concentration changes of the individual species is the lowest. The arrangement of the source-detector pairs is illustrated in Fig. 3.6. From the acquired DTOFs moments were calculated which are the basis for the results presented below. As discussed later (cf. Fig. 4.12 on Page 76) the course of moments m_1 , V and $m_{3,C}$ as a function of r_{sd} exhibits a good agreement with the predictions made by the homogeneous semi-infinite model. This is a partial justification for the application of this model here.

Figure 4.9 (left) shows background optical properties obtained from the mean time of flight m_1 and variance V for 120 combinations of source-detector pairs across the head of the subject. The BOP were calculated using Eqs. (4.31) and (4.32). The data exhibits clustering for the individual values of r_{sd} with the most compact cluster obtained for r_{sd} of 4 cm. Distributions visualised by boxplots and arranged by μ_a and μ_s' are shown in Fig. 4.9 (right). Median

4. Analysis of Time-Domain NIRS Signals by Moments

values of the distributions are nearly constant for μ_a while for μ'_s they decrease with larger r_{sd} values. In both cases the widths of the distributions decrease with larger r_{sd} . This potentially can have two reasons. First, the measurement uncertainty for larger r_{sd} is lower because of the broader DTOFs, and second, the influence of superficial inhomogeneities, i.e. hair roots, is lower than for the smaller values of r_{sd} . The averaged values for μ_a and μ'_s (mean \pm SD) were $(0.18 \pm 0.04) \text{ cm}^{-1}$ and $(11.2 \pm 2.5) \text{ cm}^{-1}$, respectively.

The same experimental data set as above was used for a more sophisticated analysis⁶ employing a reconstruction based on a finite element method (FEM) and an approximation error model correction algorithm (AEC). The AEC method with the focus on diffuse optical imaging was introduced in [78] and applied to cylindrical geometries in [79, 80]. Although promising the AEC approach turned out to be difficult to handle. Therefore only a part of the whole analysis, i.e. the FEM results, will be discussed below. The goal of the sophisticated analysis as used here is to determine individual optical properties of three tissue types from a non-invasive *in vivo* measurement of a human head in reflection geometry.

In order to create a realistic anatomical model for the computations the measured anatomical MRI image was first segmented into scalp, skull, cerebrospinal fluid (CSF), and grey and white matter. Later the CSF, grey and white matter were combined into a single brain compartment. For the FEM calculations the voxel model was converted to a finite element mesh using the `iso2mesh` software package [81] freely available online⁷. The mesh is the geometrical basis of the FEM forward model computed using the `TOAST` (Time-resolved Optical Absorption and Scattering Tomography) software package [82] freely available online⁸. With `TOAST` it is possible to reconstruct optical properties using a diffusion model for light propagation in tissue.

Figure 4.10 shows mean optical properties of the scalp, skull and brain as retrieved by the FEM reconstruction. Mean BOP obtained using the homogeneous SIM model are included for comparison (cf. Fig. 4.9). The BOP value are similar to the mean value of the heterogeneous optical properties. The skull exhibits a rather high level of absorption and scattering while the brain shows moderate absorption with low scattering. Surprisingly, μ_a of the scalp is rather low. A higher value in the range from 0.1 cm^{-1} to 0.2 cm^{-1} would be more reasonable. This is supported by the homogeneous SIM analysis

⁶ This is collaborative work. The analysis was performed by a cooperation partner Dr. J. Heiskala from the University College London (UCL). Regarding different aspects of the analysis he was supported by the author of this thesis as well as Dr. M. Schweiger, Prof. S. Arridge, Dr. E. Kirilina, V. Kolehmainen, T. Tarvainen, J. P. Kaipio, J. Cardoso.

⁷<http://iso2mesh.sourceforge.net>

⁸<http://web4.cs.ucl.ac.uk/research/vis/toast/>

4.2. Optical Properties Determined from Moments of DTOFs

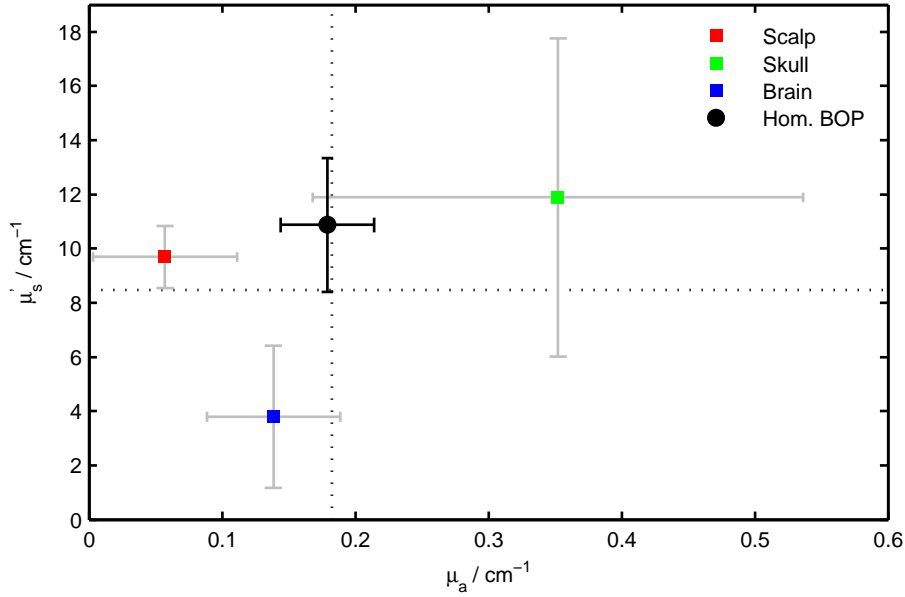


Figure 4.10: Optical properties of the head reconstructed from an *in vivo* measurement on a single subject. The TOAST reconstruction provides optical properties of the scalp, skull and the brain. The homogeneous BOP are obtained using a homogeneous semi-infinite medium model. Black dashed lines denote the mean value of the three tissue types (without BOP). Errorbars refer to the standard deviations.

of the data for $r_{\text{sd}} = 1$ cm in Fig. 4.9.

In Table 4.2 data obtained in this study is compared to values from literature. The scalp is a highly heterogeneous tissue (cf. Section 2.1.1) with largest volume fractions coming from the dermis and the subcutaneous tissue. Optical properties for these tissues, typically measured *ex vivo*, are available and some examples are listed in Table 4.2. These values exhibit differences among themselves and in comparison to the values obtained here. There are few potential reasons for these deviations. Different sample preparation, differences in the blood content as well as the temperature of the sample can lead to changes in optical properties if the measurement is performed *in vitro*. On the other hand individual variation can be expected to appear for *in vivo* measurement because differences in skin thickness, hair root density and skin colour. Choi et al. [86] reported on an *in vivo* measurement in a spectrally similar range. There the scalp and the skull were grouped into one compartment. Results for μ'_s are similar to the optical properties for scalp and skull obtained here but differ for μ_a .

The absorption and scattering of the skull are in an acceptable agreement with the *in vivo* measurement reported by Bevilacqua et al. [87]. An earlier

4. Analysis of Time-Domain NIRS Signals by Moments

Table 4.2: Optical properties of head tissues as obtained here and from literature. Data is given for 800 nm if not mentioned otherwise. Data from the current study is labelled by ✘. GM: grey matter, WM: white matter.

Tissue	μ_a / cm^{-1}	μ'_s / cm^{-1}	Ref.	Remarks
Scalp	0.06	9.7	✘	FEM method
Human dermis	1.22	22.5	[83]	<i>in vitro</i>
Human dermis	2.3	30	[84]	<i>in vitro</i> , bloodless
Subcutaneous tissue	1.07	11.6	[85]	<i>in vitro</i>
Subcutaneous tissue	1.08	20.2	[83]	<i>in vitro</i>
Scalp + Skull	0.095	12	[86]	<i>in vivo</i> , †
Skull	0.35	11.9	✘	FEM method
Skull	0.2	9.1	[87]	850 nm, <i>in vivo</i> , ‡
Cranial bone	0.11	19.5	[88], [89]	<i>in vitro</i>
Pig skull	0.25	18.5	[8]	<i>in vitro</i>
Bone	0.25	21	[90]	<i>in vitro</i>
Brain	0.14	3.8	✘	FEM method
Brain	0.14	4	[86]	<i>in vivo</i> , †
GM	0.18	7.4	[87]	811 nm, <i>in vivo</i> , ‡
GM	0.2	7.64	[91]	<i>in vitro</i>
GM	0.5	7.5	[92]	<i>in vitro</i>
WM	0.13	9.8	[87]	850 nm, <i>in vivo</i> , ‡
WM	0.87	46.1	[91]	<i>in vitro</i>
WM	0.62	45	[92]	<i>in vitro</i>

† Non-invasive multidistance measurement on the forehead. Two wavelengths were used in measurements, 758 nm and 830 nm. However, it is not clear for which wavelengths these optical properties are reported or if the values were averaged.

‡ Data was obtained invasively during brain surgery on two subjects.

multi-spectral measurement of the pig skull [8] does not match the values obtained here. A striking observation is that most reported values for μ'_s are about 20 cm^{-1} and μ_a is either about 0.1 cm^{-1} or about 0.2 cm^{-1} . Potential reasons for deviations are the same as for the scalp.

Optical properties obtained for the brain obtained here exhibit a very good agreement with the values obtained *in vivo* by Bevilacqua et al. [87]. In addition they are close to the other values reported for the grey matter but randomly differ from the optical properties reported for the white matter. A stronger influence of the GM on the optical properties of a brain compartment (GM+WM) can be expected from the fact that it stronger overlaps with the sampled volume and lies on the top of the WM. Recently, two spectrally comprehensive studies on optical properties have been published [91, 92]. They both report similar and rather high values for both μ_a and μ'_s of the

4.3. Sensitivity Factors for Retrieval of Absorption Changes

white matter and low scattering along with different values for absorption of the grey matter. Optical properties of the overall brain compartment from the current study suggest high influence of the grey matter.

Altogether the obtained results are promising. The moderate and partly good coincidence with the optical properties reported in the literature confirms the general applicability of the method. However, some doubts remain, e.g. the low absorption of the scalp. Obviously, the large data amount acquired was not sufficient to produce better results. A potential improvement may be achieved by a measurement with increased number of source-detector separations and a stronger spatial overlapping of the sampled areas. However, this can be difficult to be done if a fibre based setup is used. A scanning approach as implemented in [93] is much more promising if a subject with a bald head can be investigated. Further, a multispectral measurement might allow to retrieve the contribution of the most common chromophores, i.e. oxy- and deoxyhaemoglobin, to the total tissue absorption. Optical properties obtained by the homogeneous SIM analysis reflect some kind of mean optical properties. Although not appropriate for a heterogeneous structure it remains, due to the simplicity the calculation procedure, the most definite compromise. An approach to use homogeneous BOP to derive sensitivity factors for an inhomogeneous layered structure is discussed in Section 4.4.2. Apart from that literature data exhibit rather large differences across the studies. This variation complicates the choice of optical properties, i.e. for a simulation, making the decision less objective. An individual determination of optical properties remains the most promising but also challenging approach.

In general, the largest limitation of the presented method and of the measurement of optical properties *in vivo*, is the validation of the obtained results. If tissue samples are measured *ex vivo* alterations due to sample preparation procedures, different blood content, temperature influence, etc. will potentially bias the results. Invasive *in vivo* measurements as performed by Bevilacqua et al. [87] are ethically difficult to justify and therefore rarely reported. This strengthens further development of non-invasive methods to assess optical properties *in vivo*.

4.3 Sensitivity Factors for Retrieval of Absorption Changes

In functional time-domain NIRS as discussed within the scope of this thesis small changes in moments of DTOFs are used to monitor changes in concentrations of oxygenated and deoxygenated haemoglobin. Changes in moments

(mean time of flight, variance) offer the essential advantage of being virtually free of the influence of the IRF (cf. Section 4.1.1). Here a simple method similar to the modified Beer-Lambert law (MBL, Section 2.2.3), is reported to convert those changes in moments to corresponding absorption changes. The presented method relies on experimentally obtained *in vivo* data and the assumption of a homogeneously distributed absorption change, i.e. the same assumption which is employed by the MBL. However, since changes of higher order moments Δm_1 and ΔV are used the method automatically benefits from their increased depth selectivity (see Section 5.2.2) as compared to the integral m_0 .

The method makes use of sensitivity factors which are derived directly from the *in vivo* measurement. This gives the opportunity of fast (online) data evaluation avoiding sophisticated reconstruction models and better comparison with studies using the cw-fNIRS technique which is currently the most used fNIRS modality. The variability of sensitivity factors obtained *in vivo* and their correlations with anatomical parameters are investigated below.

4.3.1 Sensitivity Factors for Moments and Homogeneous Absorption Changes

In the simplified case of a small homogeneous absorption change $\Delta\mu_a$ the relationship to a measured change in a moment Δm_x is given by the sensitivity factor S_{m_x} defined as:

$$S_{m_x} = \frac{\partial m_x}{\partial \mu_a} \approx \frac{\Delta m_x}{\Delta \mu_a} \quad (4.33)$$

For changes in attenuation ΔA , mean time of flight Δm_1 and variance ΔV in the case of a homogeneous semi-infinite medium the corresponding sensitivity factors S_A , S_{m_1} and S_V were calculated to be [12, 68, 94]:

$$S_A = c_m m_1 \approx r_{sd} D_{PF} \quad (4.34)$$

$$S_{m_1} = -c_m V \quad (4.35)$$

$$S_V = -c_m m_{3,C} \quad (4.36)$$

where c_m is the speed of light in the medium. In principle, sensitivity factors are based on the centred moments of the next higher order, e.g. on V for S_{m_1} . An exception is S_A which is calculated from the non-centred moment m_1 . All required moments can be obtained experimentally from an *in vivo* measurement. The relationship between S_A and the differential pathlength factor D_{PF} in Eq. (4.34) is employed in the frequently used modified Beer-Lambert law (see Section 2.2.3).

4.3. Sensitivity Factors for Retrieval of Absorption Changes

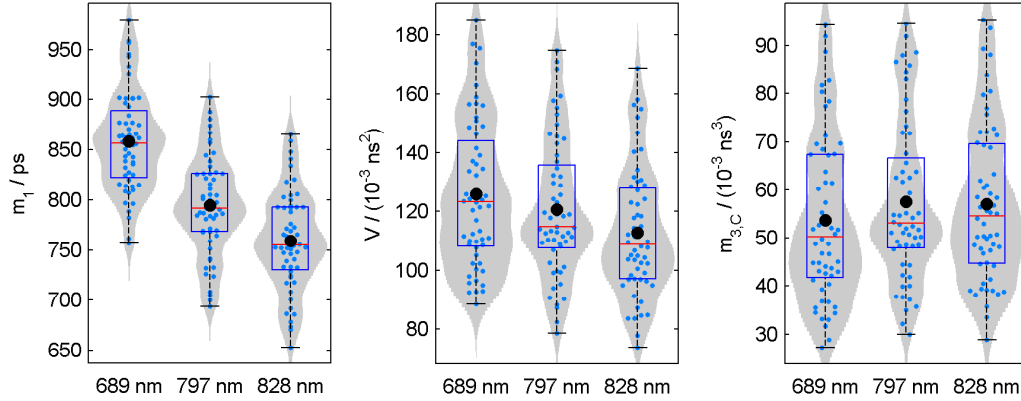


Figure 4.11: Distributions of m_1 , V and $m_{3,C}$ obtained *in vivo* on the forehead of 15 adult subjects at three wavelengths, four detection positions and a source-detector separation of 3 cm. Boxplots together with interpolated histograms (grey areas) describe the distribution of the values. Mean values (black dots) match the position of the median values (red lines) for m_1 but deviate slightly for V and $m_{3,C}$. The spread representation of the individual measurement values (blue dots) helps to reveal clusters within a distribution.

This model holds true if applied to small absorption changes in a homogeneous semi-infinite medium. If the model is applied to a human head there are basically two drawbacks. First, the absorption in the brain is localised and therefore not distributed over the whole sampled volume. The absorption change retrieved by the model is smaller than the true absorption change in the brain. As a consequence the retrieved concentration changes of haemoglobin are underestimated. In the fNIRS community this issue is known as the “partial volume effect”. Second, the approximation of the head curvature by a plane can be too rough in some cases, e.g. in the case of small heads or at the forehead.

4.3.2 Sensitivity Factors *in vivo*

Sensitivity factors obtained *in vivo*, in general, can be expected to vary spectrally, spatially and across subjects. Here, the variability and dependence of the moments relevant for sensitivity factors, i.e. m_1 , V and $m_{3,C}$, is presented using two *in vivo* datasets. The individual and spectral variability is obtained from a measurement on the forehead of 15 adult subjects at three wavelengths and four detection positions but at a single source-detector separation of 3 cm. The spatial variability was investigated on a single subject and at a single wavelength but over a large area of the head and with multiple values of r_{sd} . To the best knowledge of the author statistics for the moments V and $m_{3,C}$ are presented for the first time.

4. Analysis of Time-Domain NIRS Signals by Moments

Figure 4.11 shows distributions of m_1 , V and $m_{3,C}$ obtained at three wavelengths and four detection positions on the forehead of 15 adult subjects. These results were obtained from the same experimental data used in Section 6.1.3. Experimental details are described in Section 3.2. Mean values and coefficients of variations are summarized in Table 4.3.

Only for the m_1 values a comparison with literature is possible. From D_{PF} values published in [95, 96] corresponding values for m_1 have been calculated. Values obtained here coincide within $\pm 2\sigma$ with the published values and are always lower. Furthermore, data from this study exhibits a much lower variation compared to [95]. This difference could potentially originate from the different number of subjects measured and/or the measurement techniques employed in the studies (frequency-domain NIRS in [95] with 100 subjects, time-domain NIRS in [96], [97] and this study with 7, 8 and 15 subjects, respectively).

The review of the published D_{PF} values by Duncan et al. [98] indicates that the variation increases with the number of subjects. However, data for experimentally obtained D_{PF} values or pathlengths remain scarce, in particular from studies with a large number of subjects. Another potential source of variation is the placement of optodes on the head. As it was shown in [99, 100] m_1 measured at different positions of the head can differ by up to 40%. This kind of variation might also explain the consistently lower values of m_1 observed in this study.

Statistics for V and $m_{3,C}$ obtained *in vivo* are shown in Fig. 4.11. In general, both moment types exhibit a two to three times larger variation compared to m_1 values and no spectral dependence (as for m_1) can be observed. However, due to the large variation and the low number of wavelengths a possible spectral dependence might remain uncovered by this investigation. The spread representation of the individual measurements in Fig. 4.11 reveals small clusters within the distributions of V and $m_{3,C}$. However, the distributions do not exhibit any pronounced multi-modal shape. As indicated by the

Table 4.3: Mean values of moments for data shown in Fig. 4.11. Corresponding coefficients of variation (CV) are given in parentheses. Literature values for comparison are available for m_1 only and were reported for similar wavelengths.

λ	m_1 / ps		V / (10^{-3} ns ²)	$m_{3,C}$ / (10^{-3} ns ³)
	this study	cf. [Ref.]		
689 nm	858 (5.8%)	911 (17%) [95]	126 (20%)	54 (32%)
797 nm	794 (6.1%)	885 (7.2%) [96]	121 (19%)	58 (29%)
		910 (7.7%) [97]		
828 nm	759 (6.4%)	820 (17%) [95]	113 (20%)	57 (30%)

4.3. Sensitivity Factors for Retrieval of Absorption Changes

results of Section 4.3.3 such clusters might be correlated with the individual anatomy.

Sensitivity factors have been further investigated as a function of the source-detector separation r_{sd} in order to reveal their spatial variation. For the first time, to the best knowledge of the author, a large area multi-distance time-domain NIRS measurement was performed *in vivo* on an adult human head (see Section 3.5 for experimental details). Although time-domain measurements of multiple areas [99] of the head or even the whole head [100] have been reported they all employed only a single source-detector separation of 3 cm. The multi-distance time-domain measurements reported in [101, 102] covered only a small area of the head (forehead, close to the temple) which is not representative for the whole head [100]. Steinbrink [12] performed a multi-distance measurement (1 cm to 5.5 cm) on a single subject at 830 nm with the focus on the influence of the cerebrospinal fluid. None of these studies reported values for V and $m_{3,C}$.

A detailed description of the experimental procedure is given in Section 3.5. Briefly, a large area of the head of a single adult male subject was investigated using a wavelength of 800 nm. Totally 120 source-detector pairs with r_{sd} values of 1 cm, 2 cm, 3 cm and 4 cm covered an area of approximately 22 cm by 7 cm ranging from the left to the right ear across the cranial vertex of the head.

Results in terms of distributions of moments m_1 , V and $m_{3,C}$ as a function of r_{sd} are shown in the top row of Fig. 4.12. In all three cases a high correlation is obvious. Therefore linear and parabolic fits were performed to the mean values of the distributions, i.e. a fit of the polynomials

$$m_x(r_{sd}) = \sum_{i=0}^{i=k} b_i r_{sd}^i \quad (4.37)$$

with $k = 1$ and $k = 2$. The results of the regression in terms of the coefficients are summarised in Table 4.4.

For the mean time of flight the linear relationship is obvious and there is no essential improvement by the quadratic fit. The value $m_1(r_{sd} = 4 \text{ cm}) = 1.08 \text{ ns}$ coincides within $\pm 2\sigma$ with $m_1 = 1.18 \text{ ns}$ reported by Essenpreis et al. [96]. The difference of 0.1 ns probably originates from the spatial variation of m_1 . The main idea of the DPF concept, i.e. $D_{PF} \approx \text{const.}$, is in a satisfactory agreement with this observation. Combining Eq. (4.34) and Eq. (4.37) for $k = 1$ gives

$$D_{PF}(r_{sd}) = \frac{c_m m_1}{r_{sd}} = c_m \left(\frac{b_0}{r_{sd}} + b_1 \right) \quad (4.38)$$

In early publications related to the DPF concept ([42, 68, 97, 101]) it is mainly emphasised that D_{PF} is almost constant for $r_{sd} \geq 2.5 \text{ cm}$, i.e. independent

4. Analysis of Time-Domain NIRS Signals by Moments

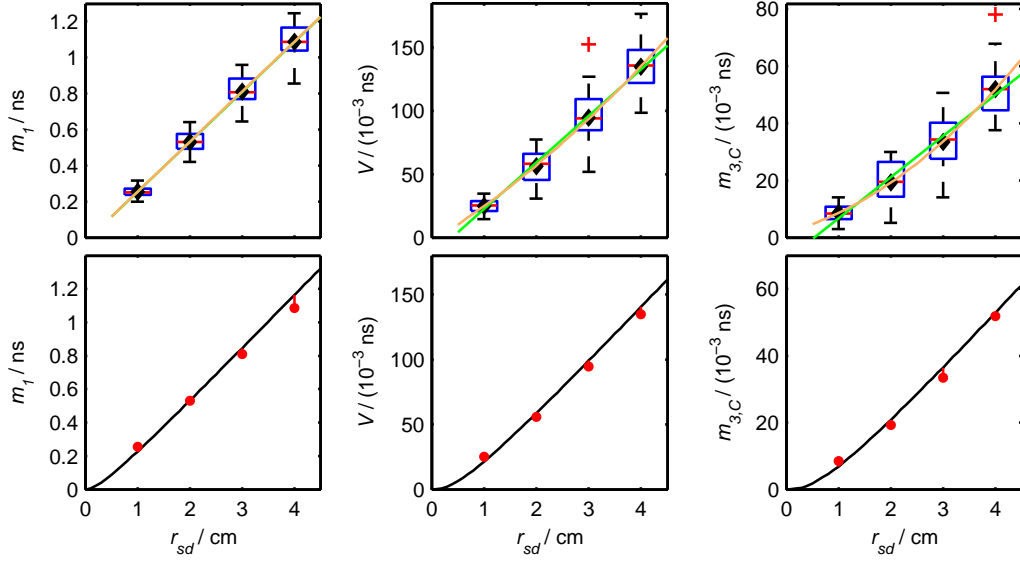


Figure 4.12: Relationship of moments relevant for the calculation of sensitivity factors on the source-detector separation r_{sd} . Top row: Box plots reflect the distribution of the values. Linear (green lines) and parabolic (orange lines) fits were performed to the mean values of the distributions (black dots). Red crosses label outliers (points outside the $\pm 2.7\sigma$ range). Bottom row: Moments calculated from averaged background optical properties (black lines) fit well to the mean values (red dots) measured *in vivo*.

of r_{sd} . Indeed, larger source-detector separations were and are still of main interest in fNIRS as they provide a higher sensitivity to absorption changes in the deeper lying cortex. However, measurements at shorter r_{sd} are frequently used in order to assess scalp haemodynamics. From Eq. (4.38) with the corresponding values from Table 4.4 one can see that the ratio of the D_{PF} values for 1 cm and infinity, i.e.

$$D_{PF}(r_{sd} = 1 \text{ cm}) / \lim_{r_{sd} \rightarrow \infty} D_{PF}(r_{sd}) = \frac{1}{(1 \text{ cm})} \frac{b_0}{b_1} + 1 \approx 0.92$$

is close to 1. Therefore the assumption that the D_{PF} is independent of r_{sd} is satisfactory but still an approximation. Additional deviations will arise from the large inter-subject variability of the D_{PF} values.

The value of m_1 exhibits a linear relationship on r_{sd} but the values of V and $m_{3,C}$ do not. Here the usage of a polynomial of second order improves the fit and therefore provides a better approximation. It should be noted that the quadratic fit used here offers a good empirical approximation in the r_{sd} range from 1 cm to 4 cm but might fail beyond it. Remarkably, the variation of the moments is almost equal for all values of r_{sd} . Mean coefficients of variation observed in this measurement were 10 %, 21 % and 30 % for m_1 , V and $m_{3,C}$,

4.3. Sensitivity Factors for Retrieval of Absorption Changes

Table 4.4: Results of the linear and quadratic fits to data shown in Fig. 4.12 in terms of coefficients $b_i \pm \Delta b_i$.

		b_0	b_1	b_2	R^2
m_1	lin.	(-22.7 ± 0.4) ps	(276.85 ± 0.15) ps/cm	–	0.99999938
	quadr.	(-23.3 ± 1.2) ps	(277.4 ± 1.1) ps/cm	(0.11 ± 0.41) ps/cm ²	0.99999951
V	lin.	(-14 ± 4) 10^{-3} ns ²	(36.8 ± 1.5) 10^{-3} ns ² /cm	–	0.9967
	quadr.	(-3 ± 4) 10^{-3} ns ²	(25 ± 4) 10^{-3} ns ² /cm	(2.3 ± 0.7) 10^{-3} ns ² /cm ²	0.99974
$m_{3,C}$	lin.	(-8 ± 4) 10^{-3} ns ³	(14.4 ± 1.2) 10^{-3} ns ² /cm ²	–	0.986
	quadr.	(1.8 ± 0.6) 10^{-3} ns ³	(4.8 ± 0.6) 10^{-3} ns ² /cm ²	(1.91 ± 0.11) 10^{-3} ns ³ /cm ²	0.99995

respectively.

The bottom row of Fig. 4.12 compares mean values of moments obtained *in vivo* with the prediction by the homogeneous semi-infinite medium model. To perform this comparison first background optical properties (BOP) were calculated from the mean values of m_1 and V for the four source-detector separations using Eqs. (4.31) and (4.32) and a refractive index of 1.37. Averaged values of BOP were $\mu_a = (0.166 \pm 0.007)$ cm⁻¹ and $\mu'_s = (11.6 \pm 1.7)$ cm⁻¹ (all values mean \pm SD). These optical properties were then used to compute $m_1(r_{sd})$, $V(r_{sd})$ and $m_{3,C}(r_{sd})$ using Eqs. (4.28), (4.29) and (A.6) and are shown in the lower panels of Fig. 4.12. The good prediction made by the homogeneous SIM model suggests that absolute values of moments can be calculated using BOP obtained from a measurement at a single r_{sd} . This also supports the assumption that the adult human head can be approximated by the simple homogeneous SIM model, at least with regard to the dependence of moments on the source-detector separation.

4.3.3 Correlations of *in vivo* Sensitivity Factors with Anatomical Parameters

Variation of the sensitivity factors as discussed above can potentially originate from different optical properties of the tissue, varying concentration of chromophores or differences in the individual geometry. Results presented in Section 5.2 suggest that moments can be sensitive to changes of the thickness of layers in a turbid medium. Therefore here correlations of the moments m_1 ,

4. Analysis of Time-Domain NIRS Signals by Moments

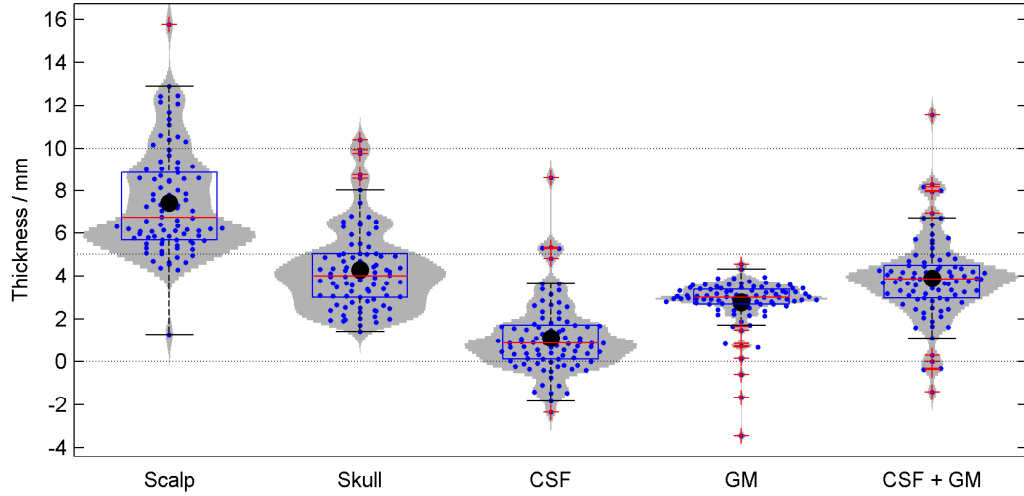


Figure 4.13: Distributions of tissue thickness d obtained from *in vivo* segmented anatomical MRI data of 15 subjects on 6 positions of the forehead. Boxplots together with interpolated histograms (grey areas) describe the distributions of the values. Mean values (black dots) in some cases deviate slightly from median positions (red lines). Blue dots refer to individual measurement values, red crosses to outliers (values outside the range $\langle d \rangle \pm 2.7\sigma$).

V , $m_{3,C}$ with the thickness of different tissue types of the head are investigated.

For the analysis optical and MRI data⁹ obtained on the forehead of 15 subjects was used. The detailed experimental procedure is described in Section 3.2. The anatomical MRI scans of all subjects were segmented¹⁰ into several tissue types. Briefly, an automated segmentation was performed using the **Freesurfer** software freely available online¹¹. The T_1 weighted anatomical MRI images recorded with a spatial resolution of $(1 \times 1 \times 1)$ mm³ were used. Five tissue types were distinguished by the segmentation: scalp, skull, cerebrospinal fluid (CSF), grey (GM) and white (WM) matter. Distances from the surface to tissues were obtained by a simple algorithm, i.e. as shortest distances from the head surface under the source and the detector positions (six in total) to the nearest voxel of tissue of interest. The thickness of the corresponding tissues was then calculated as the difference of corresponding distances.

Figure 4.13 shows the distribution of the thickness values. Table 4.5 lists

⁹ The MRI recording were performed by Dr. R. Brühl (PTB) and Dr. E. Kirilina (FU Berlin) within a collaboration. Experimental details are described in Section 3.2 and [103].

¹⁰ The segmentation was performed by Dr. Michael Niessing (FU Berlin) within a collaboration and kindly made available to the author of this thesis for further analysis.

¹¹ <http://surfer.nmr.mgh.harvard.edu/>

4.3. Sensitivity Factors for Retrieval of Absorption Changes

Table 4.5: Mean thickness $\langle d \rangle$ of the different tissue types obtained *in vivo* on the forehead; σ denotes the standard deviation, CV - the coefficient of variation, $N = 15$.

	Scalp	Skull	CSF	GM	CSF + GM
$\langle d \rangle / \text{mm}$	7.4	4.3	1.1	2.8	3.9
σ / mm	2.4	1.9	1.7	1.2	1.9
CV / %	33	44	153	52	50

mean values, corresponding standard deviations and coefficients of variation. The automatic segmentation procedure obviously produces artefacts in particular in the case of the thin CSF space as indicated by a few negative values for the thickness.

Obviously, most artefacts appear for the thickness of the CSF. Its mean value of 1.1 mm is in the order of the spatial resolution of the MRI scan making a precise measurement of thin layers difficult. For the thickness of GM also some negative values are found. But in comparison to the other tissues the thickness of GM exhibits the lowest inter-subject variation in terms of the absolute σ value. Potentially, it might be less artificial if GM and CSF are treated as single tissue type (CSF+GM). The mean thickness of the CSF can then be retrieved from the group averaged data, i.e. as $\langle d_{CSF} \rangle = \langle d_{CSF + GM} \rangle - \langle d_{GM} \rangle$. Interestingly, the result does not change in this case ($3.9 \text{ mm} - 2.8 \text{ mm} = 1.1 \text{ mm}$).

The scalp thickness exhibits the largest inter-subject variability ($\sigma = 2.4 \text{ mm}$) and ranges from 4 mm to 13 mm. Furthermore, the mean distance from the surface to GM was found to be 12.8 mm ($\sigma = 2.3 \text{ mm}$). These values are of particular interest for the estimation of the extra-cranial signal contribution (see Section 6.1) or the construction head-mimicking phantoms (see Chapter 5).

A correlation analysis was performed between the optical and the anatomical parameters. Correlation coefficients of moments m_1 , V , $m_{3,C}$ vs. thicknesses and distances to the different tissue types were calculated. Three types of correlation coefficients were used (Pearson's r , Kendall's τ and Spearman's ρ) which all were similar. Therefore only Pearson's r are reported below. The significance level was set to $p = 0.05$. All calculations were performed with outliers removed because otherwise the results were strongly biased by the few outliers. Values were classified as outliers if they were outside the range $\langle d \rangle \pm 2.7\sigma$. For normally distributed data this range covers approximately 99.3% of the data.

Results in terms of Pearson's r values are shown in Fig. 4.14. In general, rather low correlations coefficients were obtained and they are similar for 797 nm and 828 nm, which lie spectrally close to each other. Only few signif-

4. Analysis of Time-Domain NIRS Signals by Moments

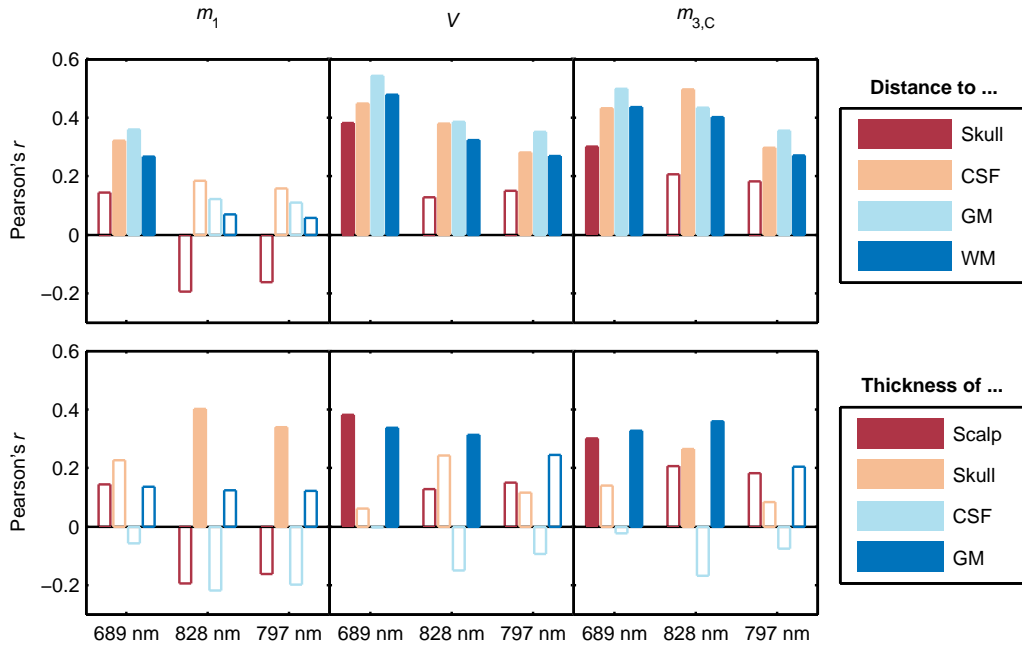


Figure 4.14: Correlation of moments m_1 , V , $m_{3,C}$ and anatomical parameters, i.e. thickness of tissues and distances to those. Pearson's correlation coefficients r were calculated for three wavelengths. Significant correlations ($p < 0.05$) are indicated by filled bars.

Significant correlations for m_1 were found. At 797 nm and 828 nm m_1 correlates with the thickness of the skull; at 689 nm there is a low correlation with the distances to the sub-cranial tissues which are associated with the thickness of scalp and skull. This indicates that m_1 is mainly influenced by the (rather high) scattering of the skull. V and $m_{3,C}$ mainly exhibit significant correlations with the distances to all tissues and in some cases to the thickness of the scalp and grey matter. In addition, at 689 nm correlations with scalp thickness appear. This sensitivity to the many tissues types might explain (to some extent) the higher variability of V and $m_{3,C}$ observed in Section 4.3.2.

These results suggest that V and $m_{3,C}$ are rather sensitive to geometrical variations, i.e. positions of boundaries between tissues with mismatching optical properties. On the other hand low correlations found for m_1 explain its relatively low inter-subject variability and justify the DPF concept.

4.4 Sensitivity Factors and Retrieval of Absorption Changes in a Layered Medium

The human head is not homogeneous and thus, all models employing a homogeneous assumption must be classified as simplified. With regard to the layered structure of the head a model consisting of planar layers can be considered to be more realistic. In such a model the optical properties of the layers can be chosen to be either different or the same. In the first case the optical properties of tissue taken from literature can be used. These, however, can vary a lot (see Section 4.2.2) making the choice subjective. In the case that optical properties are set to the same values one receives a homogeneous medium but with a layered geometry. Below such a medium will be referred to as *quasi-layered*¹². The advantage of this simplification is that only a single set of optical properties must be selected which strongly reduces the number of parameters.

Liebert et al. [94] used a quasi-layered model in conjunction with changes in moments to calculate depth-resolved absorption changes. They used a computationally expensive Monte-Carlo simulation with a single and fixed set of optical properties to calculate sensitivity factors for changes in moments. In his thesis Steinbrink [12] also used Monte-Carlo simulations in a quasi-layered medium and a method based on the analysis of changes of the full DTOF to recover absorption changes in layers. Employing a few illustrative calculations he found that the results of a layered reconstruction depend on background optical properties (BOP) of the quasi-layered medium [12, p. 66]. This, however, can in principle be different for the analysis based on the changes of the full DTOF and the changes of moments. Here, the idea of pre-calculated sensitivity factors for moments in a quasi-layered medium is extended towards multiple values of the BOP μ_a and μ'_s .

For this purpose time-resolved light propagation in a quasi-layered structure was simulated. In order to obtain layered sensitivity factors for small absorption changes the absorption coefficient of a single layer was slightly increased while the optical properties of the other layers were kept constant. The procedure was repeated for each layer independently. This concept is similar to perturbation methods such as the absorbing point-like perturbation approach [104]. However, the volume affected by the absorption change of a layer is much larger. In both cases the unperturbed state is represented by the homogeneous semi-infinite medium (Section 2.2.4).

¹² An neutral observer would not be able to recognise the layered structure of the medium because of the equality of the optical properties. The subdivision into layers seems to be virtual which is reflected by the term *quasi-layered*.

4. Analysis of Time-Domain NIRS Signals by Moments

The actual calculations were performed using the analytical solution for a n -layered cylinder [73] and a numerical implementation provided by the authors¹³ of the paper. A set of DTOFs was calculated using a grid of BOP (μ_a between 0.04 cm^{-1} and 0.35 cm^{-1} in steps of 0.01 cm^{-1} , μ'_s between 4 cm^{-1} and 19.5 cm^{-1} in steps of 0.5 cm^{-1}). This range of BOP was observed in *in vivo* measurements if the homogeneous model was applied for data analysis. Other parameters of the simulation were: $r_{sd} = 3 \text{ cm}$, $n_{out} = 1$, $n_{in} = 1.4$, cylinder radius and thickness 6 cm , time zero $t_0 = 0$. The single source detector separation is the one which was used for functional *in vivo* experiments presented in Chapter 6. The number of time channels was fixed within the software while the time channel width Δt was varied depending on the BOP. This was necessary in order to sample the simulated DTOF properly. These specific selected parameters and the variation of the time channel width were proven to yield numerically stable results. Otherwise, instabilities within the simulation appeared due to the parameters of Bessel functions and the FFT¹³ employed within the simulation.

Every individual sensitivity factor $S(j)$ of the j -th layer was calculated as following. Two DTOFs were simulated with $\mu_{a,j}$ of the j -th layer being changed by $\pm 2\%$ around the basic value of μ_a . This “perturbed” layer had a thickness of 2 mm and was shifted through the medium in steps of 2 mm . The rest of the medium was configured to have unperturbed BOP. In particular the scattering coefficient μ'_s was held constant. In total 25 perturbed layers were used. Thus, the deepest perturbed layer was located at a depth of 48 mm to 50 mm . Next, changes in moments for each perturbed layer Δm_j were calculated and divided by the corresponding change in the absorption coefficient $\Delta \mu_{a,j}$ to obtain the sensitivity factor $S(j)$ of the j -th layer. Only changes in attenuation, mean time of flight and variance were used. For the moments calculations the upper and lower relative integration limits were set to 1% and 0.01% , respectively. The obtained data set, i.e. sensitivity factors for moments as a function of BOP μ_a and μ'_s , was organised as a compact lookup table (LUT, about 1 MB in size) to be used with interpolation procedures.

4.4.1 Dependence on Background Optical Properties

Results of the simulation are illustrated in Fig. 4.15. The figure shows maps of sensitivity factors for changes in attenuation ΔA , mean time of flight Δm_1 and variance ΔV as a function of the layer number j (which is proportional to the depth Z) and μ'_s for three selected values of μ_a (0.05 cm^{-1} , 0.1 cm^{-1} and 0.2 cm^{-1}). For a better visualisation of the μ_a dependence depth sensitivity

¹³ Private communication with A. Liemert and E. Simon (ILM, Ulm, Germany)

4.4. Sensitivity Factors and Retrieval of Absorption Changes in a Layered Medium

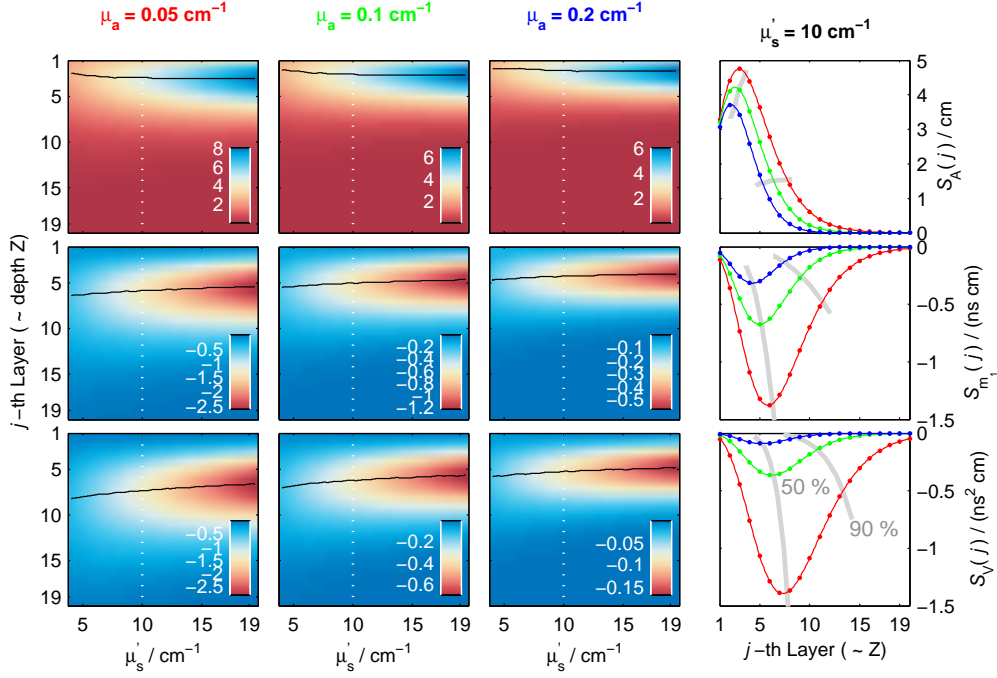


Figure 4.15: Sensitivity factors (SF) for absorption changes in a quasi-layered medium obtained from a simulation. The three rows refer to SF of the attenuation S_A , the mean time of flight S_{m_1} and the variance S_V , respectively. Units of the colour scale are the same for each row and are shown on the right. Three columns on the left: Colour maps show SF of the j -th layer as a function of μ'_s for three selected values of μ_a (columns). Black lines show the position of the extrema of the $S(j)$ profiles. Note that with increasing μ_a the relative changes of the colour scales for $S_{m_1}(j)$ and $S_V(j)$ are larger than for $S_A(j)$. Column on the right: Slices through the colour maps at $\mu'_s = 10 \text{ cm}^{-1}$ (white dashed lines on the colour maps) for the three values of μ_a (0.05 cm^{-1} , 0.1 cm^{-1} and 0.2 cm^{-1} coloured in red, green and blue, respectively). The shift of the 50 % (median) and 90 % percentiles is indicated by the thick grey lines. This illustrates the reduction in depth sensitivity with increasing μ_a . Data in the right column was interpolated with splines to guide the eye. All sensitivity factors are given for 2 mm thick layers, i.e. not normalised to the thickness or volume of the layers.

profiles $S(j)$ are shown for a single value of $\mu'_s = 10 \text{ cm}^{-1}$ in the right column of the figure. Note that the sum over all layers gives the sensitivity factor of the homogeneous semi-infinite medium as defined in Eqs. (4.34) to (4.36).

The results of the simulation demonstrate that the sensitivity factors depend strongly on the BOP. This includes variation of the absolute values as well as the spatial position of the extrema, i.e. depth of the maximum sensitivity, and the shape of the depth sensitivity profiles. A striking observation is that depth profiles for m_1 and V exhibit much larger relative changes with μ_a and μ'_s than those for A . Therefore, if changes in m_1 and V are used to reconstruct changes in μ_a it is crucial to use sensitivity factors adapted

4. Analysis of Time-Domain NIRS Signals by Moments

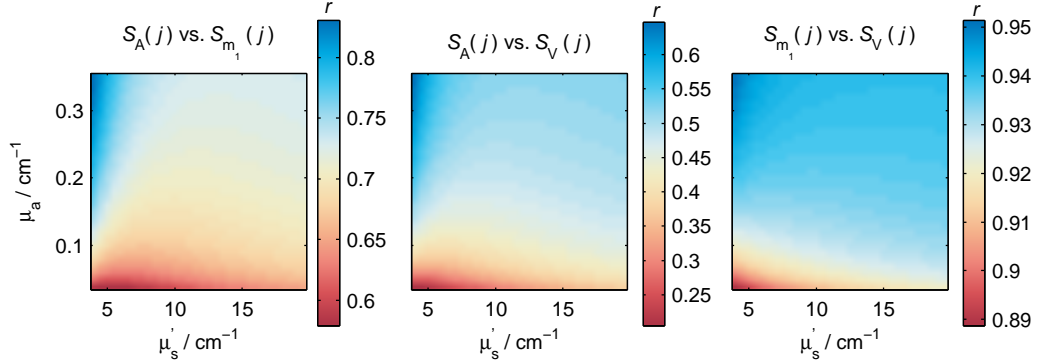


Figure 4.16: Maps of the absolute values of correlation coefficients r of depth sensitivity profiles of moments as a function of μ_a and μ'_s . Here, lower values of r are better for the reconstruction of absorption changes from changes in moments. For better comparison of the scales absolute values of r were taken. Note the different ranges of the r colour scales.

to the individual BOP. Otherwise, the reconstruction will produce biased results. A reconstruction of absorption changes based on ΔA only can benefit from the rather small variation of the shape of the $S_A(j)$ profiles. This weak dependence on the BOP is beneficial if it is difficult to estimate individual BOP (which is most often the case in cw-fNIRS). Still, a systematic bias of the results of the reconstruction can be expected.

In all cases the total sensitivity as well as the absolute and relative sensitivity factors at certain depths are reduced with increasing μ_a . This reduction in the total sensitivity can be understood using the homogeneous SIM model. In the linear approximation the sum of sensitivity factors over all layers gives the homogeneous sensitivity factor S_m :

$$S_m = \sum_j S_m(j) \quad (4.39)$$

Homogeneous sensitivity factors, on the other hand, are proportional to moments of the next order (i.e. V for S_{m_1} , Eqs. (4.34) to (4.36)) and can be calculated using Eqs. (4.28), (4.29) and (A.6). As illustrated in Fig. A.1 in the appendix the relevant moments m_1 , V and $m_{3,C}$ are non-linearly and monotonically decreasing with μ_a and thus the absolute total sensitivity to absorption changes decreases, too.

The position of the extrema of the depth sensitivity profiles is illustrated by black solid lines overlaid the colour maps in Fig. 4.15. This peak sensitivity as a function of μ'_s is different for the three moments. For the attenuation A the maximum sensitivity lies deeper in the medium with higher μ'_s while for m_1 and V the extrema shift toward the surface. This is a result of an interplay of the increasing scattering with the specific source-detector separation used

4.4. Sensitivity Factors and Retrieval of Absorption Changes in a Layered Medium

here. Such a convergence of the depth sensitivity profiles of the moments implies that they become less distinct and thus less suitable for a layered reconstruction.

The similarity of the profiles depends on the BOP. In order to quantitatively compare these effects correlations between the depth profiles $S_A(j)$, $S_{m_1}(j)$ and $S_V(j)$ were calculated, i.e. using the Pearson's correlation coefficients $r[S_A(j), S_{m_1}(j)]$ etc. Figure 4.16 shows maps of correlation coefficients as a function of BOP. For better comparison of the scales absolute values of r were taken¹⁴. In the case when changes in moments (ΔA , Δm_1 , ΔV) are used in a linear reconstruction lower values of $|r|$ are better because the resulting equations become less linearly dependent. Here lowest $|r|$ values are exhibited by the combination of S_A vs. S_V while S_{m_1} vs. S_V turns out to be highly correlated for all values of μ_a and μ'_s . Effectively, the combinations of ΔA with ΔV or of ΔA with Δm_1 appear to be advantageous for layered reconstructions.

Recently, Liebert et al. [105] investigated the accuracy of the reconstruction of absorption changes in a two layered medium based on changes in moments. They used a single combination of BOP ($\mu_a = 0.1 \text{ cm}^{-1}$ and $\mu'_s = 10 \text{ cm}^{-1}$) but in conjunction with a multi-distance time-resolved simulated data set. The authors found that if ΔA and Δm_1 are used for the reconstruction adding changes in variance to the analysis results in a little improvement only. This finding is in agreement with the results obtained here and is a direct consequence of the high correlation of $S_{m_1}(j)$ and $S_V(j)$ depth profiles. According to Fig. 4.16 (right) this conclusion is valid for a wide range of BOP. On the other hand, Fig. 4.16 (left and centre) indicates that with increasing absorption coefficient a reconstruction based on ΔA with Δm_1 or with ΔV will become worse concerning accuracy and uncertainty of the reconstruction. The results suggest that changes in all three moments should be used if available while a reconstruction based only on Δm_1 and ΔV , i.e. the time-domain NIRS specific measurands, will give poor results.

In the computations presented above rather the "ideal" sensitivity factors have been discussed. Under experimental conditions, however, a realistic IRF and a finite integration range have to be considered. To investigate the influence of these parameters sensitivity factors were additionally calculated employing a convolution of the simulated DTOFs with an experimentally obtained IRF (MuA detector, see Section 5.1) and using three values of the relative upper integration limit L_U , i.e. 1 %, 0.1 % and 0.01 %. The background optical properties were 0.1 cm^{-1} and 10 cm^{-1} for μ_a and μ'_s , respectively.

Figure 4.17 shows the results of the computations in comparison to ideal

¹⁴ The values of r are negative if $S_A(j)$ is involved and positive else.

4. Analysis of Time-Domain NIRS Signals by Moments

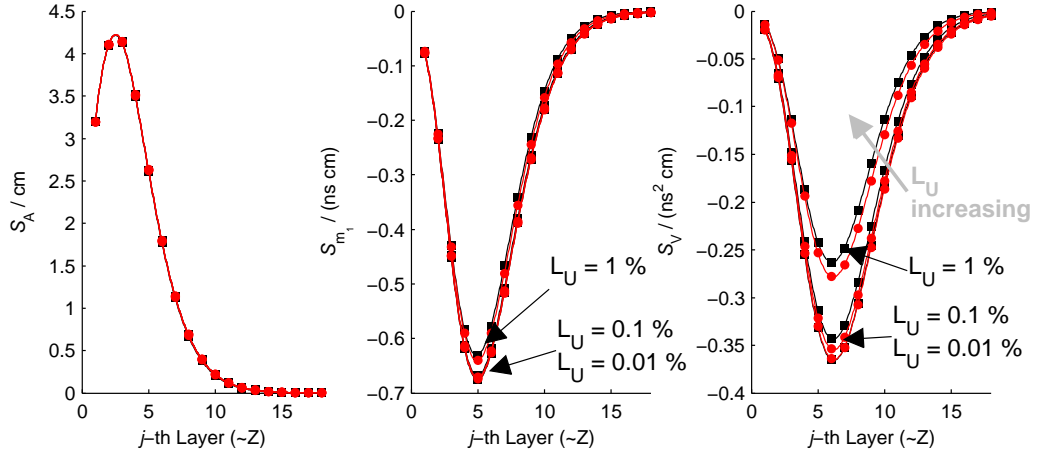


Figure 4.17: Dependence of layered sensitivity factors $S_A(j)$, $S_{m_1}(j)$ and $S_V(j)$ for $\mu_a = 0.1 \text{ cm}^{-1}$ and $\mu'_s = 10 \text{ cm}^{-1}$ on the IRF and upper integration limit L_U . Red and black lines refer to sensitivity factors calculated from data with and without a convolution with an experimental IRF, respectively. Sensitivity profiles are shown for three values of the upper integration limit L_U (0.01 %, 0.1 % and 1 %). All data (dots) was interpolated with splines (solid lines) to guide the eye. The layer thickness is 2 mm.

depth sensitivity profiles. For S_A virtually no influence of the IRF nor L_U can be observed. This behaviour is expected because Δm_0 and therefore ΔA do not strongly depend on L_U (cf. Section 4.1.2). Further, the convolution with the IRF simply distributes photons over a longer time period. This is partially compensated by the wider integration range in Eq. (4.14) resulting from the relative limit seeking procedure¹⁵. The situation is different in the case of m_1 and V where mainly the finite integration range has an effect. The absolute values of the sensitivity factors of all layers are smaller than in the “ideal” case if the L_U increases and correspondingly the integration range is reduced. The IRF has only minor effects which are only visible in the case of $S_V(j)$ (cf. black vs. red line for $L_U = 1\%$ in right panel of Fig. 4.17). The shape of the profiles is not visibly influenced by L_U and the IRF maintaining the depth sensitivity and selectivity features of the moments.

The results discussed above are promising. Before, the general expectation was that the depth sensitivity would be lost if “late” photons of the DTOF would be cut off. However, according to Fig. 4.17 the effect of this truncation

¹⁵ Among other things a convolution with the IRF flattens the peak of the DTOF, i.e. reduces the maximum photon count, which is used to find the temporal position of a given relative limit L_U . As a consequence the corresponding temporal position is found at later times t leading to a wider integration range and thus more photons included by the integration.

4.4. Sensitivity Factors and Retrieval of Absorption Changes in a Layered Medium

on the sensitivity factors is still acceptable. In principle, the calculation procedure for sensitivity factors used in this section could be modified in order to account for the influence of both the experimental IRF and the actually used relative upper integration limit L_U and thus to increase the accuracy. For that, first, the simulated DTOFs must be convolved with the experimental IRF and, second, all moments and their changes must be calculated using the individual value for L_U . This would lead to values of SF which are adjusted for the influence of these parameters. This also means an increased computational effort which could be compensated by the specific solution to the time-domain reflectance of a layered medium with an equal refractive index and μ'_s in all layers [73]. The authors reported that a single DTOF can be calculated in about 10 ms on a standard machine. This is potentially fast enough for an on-the-fly calculation of individual layered SF including the influence of an IRF and L_U . In addition, this modified approach would replace the lookup table procedure.

From the experimental point of view any reduction of the absolute value of the SF leads to a smaller measured signal change which, of course, is a disadvantage. Therefore, apart from the computational aspects, it is desirable to achieve a high dynamic range to be able to set L_U as low as possible. In practice, the dynamic range of a time-domain NIRS measurement is influenced by the ambient light level and the afterpulsing of the detector. The influence of the ambient light can be reduced by darkening the experimental environment or, in the case of an *in vivo* measurement, by covering the head of the subject with light absorbing materials. In opposite, the afterpulsing level is a property of the detector and therefore a unalterable attribute of the fNIRS instrument.

4.4.2 Reconstruction Procedure for Two Layers

In the case of a time-domain fNIRS experiment performed at a single source-detector separation the available data amount is limited, i.e. changes in attenuation, mean time of flight and variance if the moments method is used. In practice only absorption changes in two layers can be reconstructed because of the high correlation of the two latter measurands. In the case of fNIRS measurements the number of unknowns can be reduced using physiological assumptions. Functional haemodynamic changes induced on the typical time scale of a functional experiment can be restricted to take place in the scalp and brain compartments. Thereby only two absorption changes must be reconstructed.

The adult human head can be modelled as a layered structure. In such a

4. Analysis of Time-Domain NIRS Signals by Moments

model of n contiguous layers a change in a moment Δm is given by:

$$\Delta m = \sum_{j=1}^n S_m(j) \Delta \mu_a(j) \quad (4.40)$$

where $S_m(j)$ is the sensitivity factor of the moment m in the j -th layer and $\Delta \mu_a(j)$ is the change of the absorption coefficient in the corresponding layer. The sensitivity factors $S_m(j)$ can be obtained from the LUT of the precalculated SF discussed above. For that μ_a and μ'_s are calculated from the moments m_1 and V using Eqs. (4.31) and (4.32). These BOP are then used to interpolate SF for each layer and moment type from the LUT.

Changes in the three moments ΔA , Δm_0 and ΔV and then be used as Δm resulting in a system of three linear equations with n unknowns. This number of unknowns can be reduced by (i) grouping layers together and (ii) neglecting layers with no absorption changes. First, scalp and brain layers can be stacked into two compartments of interest. Second, the skull and CSF compartments can be assumed to have constant absorption on the time scale of the experiment and thus the corresponding absorption change to be zero. In the spectral range of interest optical properties of the scalp and brain compartments are dominated by the oxy- and deoxyhaemoglobin. The scalp and the brain also exhibit strong blood flow and therefore time-varying optical properties caused by haemodynamics which supports the second assumption. This concept of grouping layers is similar to the procedure used by Kacprzak et al. [76].

Further, sensitivity factors $S_m(j)$ given as a function of the layer number j can be interpolated to obtain the quasi-continuous depth sensitivity profile $S_m(Z)$ as function of depth Z . This simplifies the procedure of the calculation of the reduced sensitivity factors. A change of a moment can then be expressed as

$$\Delta m = \Delta \mu_{a,up} \int_0^{z_1} S_m(Z) dZ + \Delta \mu_{a,low} \int_{z_2}^{z_3} S_m(Z) dZ \quad (4.41)$$

Here the upper layer ranges from the surface ($Z = 0$) to the depth z_1 and the lower layer from z_2 to z_3 . Layers which are not included by these intervals are automatically neglected. The upper layer can be associated with the scalp and therefore z_1 corresponds to the scalp thickness. Associating the lower layer with the brain defines z_2 as the distance to the cortex, i.e. grey matter, whereas z_3 can be set to infinity because all sensitivity profiles converge to zero for larger values of Z .

The reduction of the number of the sensitivity factors for two layers as described above makes use of prior knowledge about the anatomical structure of the head. In particular, the scalp thickness and the depth of the cortex are

4.4. Sensitivity Factors and Retrieval of Absorption Changes in a Layered Medium

needed for the calculations. Typically, these quantities would be obtained from an anatomical MRI record which, however, might not be available for every individual measurement. In such cases mean values obtained from a group of subjects can be used as an approximation. Another promising approach is to use head atlas models in combination with a simple measurement of the head circumference to estimate the anatomical parameters.

4.4.3 Comparison of the Reconstruction in Layered and Homogeneous Media

Both analysis approaches - homogeneous and layered - exhibit advantages and drawbacks. The layered method allows for the separation of the signal into a scalp and brain related parts. While this is a highly desired feature it requires some additional assumptions about the geometry parameters to be made. The application of the homogeneous method, on the other hand, is straight forward and does not make any assumptions about model parameters. However, it does not perform a clear depth separation but, instead, dedicates the consideration of the depth selectivity properties of the measurands to the user. This is a drawback because it requires the user to be experienced in fNIRS, be familiar with the measurement technique and its potential pitfalls.

The different steps of the both analysis methods and their order permutations are visualised in Fig. 4.18. The workflows of both methods are very similar. Several steps of the analysis can be permuted resulting in basically the same final results. The initial steps of the analysis are model independent. This part deals with moments, contains mainly the actual measurement data and basic data processing. Indeed, already block averaged changes in moments can be used to identify brain activation in single channels [62]. Typical changes of moments for brain activation obtained *in vivo* are 1.01 to 1.05 for m_0 ratio ($\approx -\Delta A + 1$, cf. Eq. (2.21)), 1 ps to 5 ps for Δm_1 and 0.001 ns² to 0.003 ns² for ΔV . It is, however, more useful to distinguish between oxy- and deoxyhaemoglobin concentration changes in absolute units. For that, first changes in the absorption coefficients $\Delta\mu_a$ at all wavelengths have to be calculated. This requires sensitivity factors which are different for the homogeneous and layered analysis. The subsequent conversion of $\Delta\mu_a$ to oxy- and deoxyhaemoglobin concentration changes is performed using Eq. (2.16) and is computationally and mathematically the same in both cases.

The block averaging and rebaselining¹⁶ procedures with respect to the stimulus onset can be performed at different stages of the analysis. Since the

¹⁶ To rebaseline a signal its value from a appropriate window is subtracted from the signal itself. In fNIRS typically a window right before the stimulus onset is selected.

4. Analysis of Time-Domain NIRS Signals by Moments

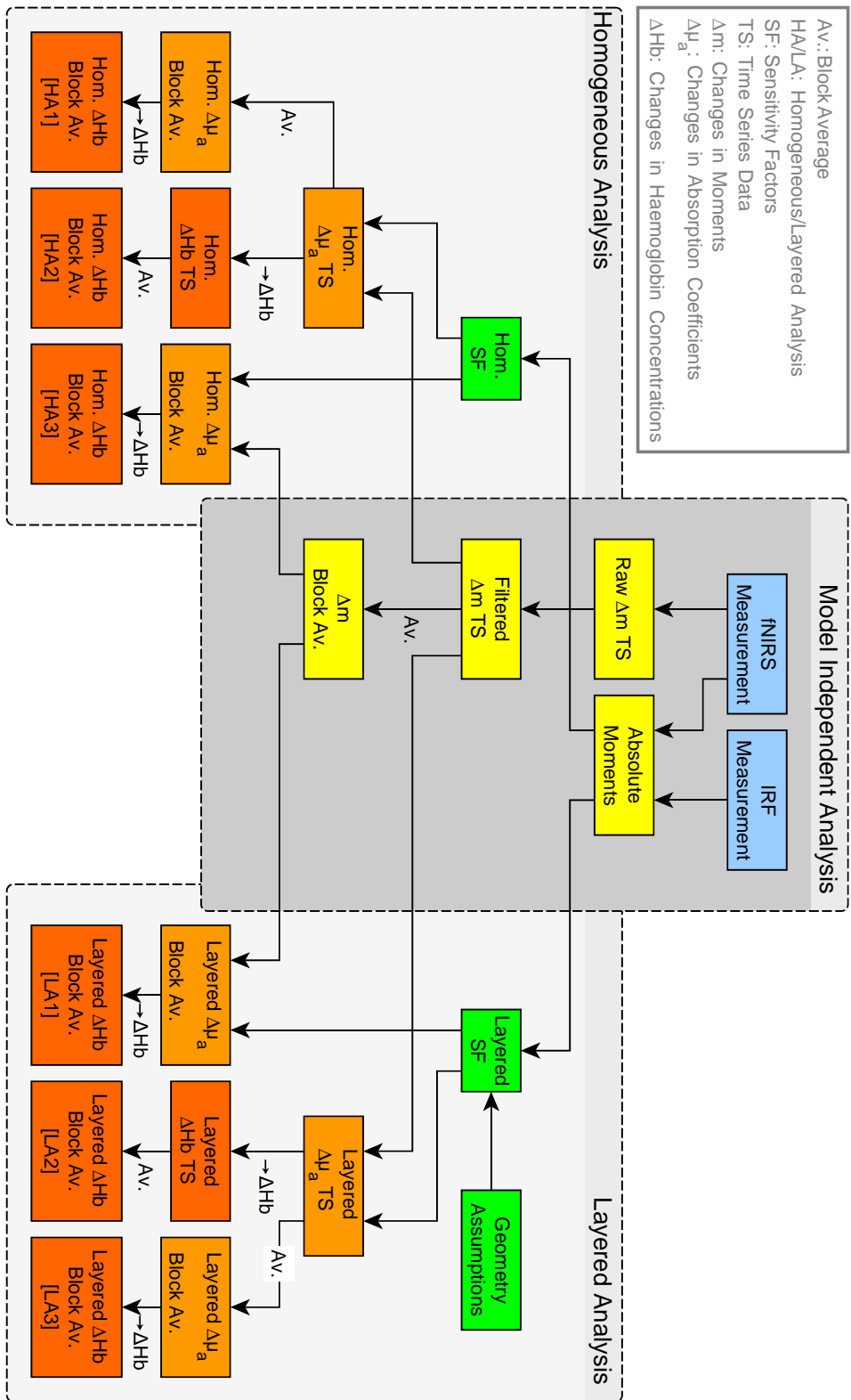


Figure 4.18: Workflow of the fNIRS data analysis showing model dependent and independent steps.

4.4. Sensitivity Factors and Retrieval of Absorption Changes in a Layered Medium

employed models are linear the results are the same. However, it is advantageous to do it as the last step (cf. HA1 and LA2 in Fig. 4.18). In this case it is easier to obtain the variation over the single blocks which is typically the dominating source of signal variation of the block averaged results. On the other hand calculating the block averaged data on an earlier stage, i.e. during the model independent analysis, has the advantage that most of the noise and stimulus uncorrelated effects is averaged out. The resulting system of equations can then be solved faster and the solution is more stable because of the reduced level of noise.

Another issue which negatively affects both methods is the partial volume effect (PVE). Both methods assume that the retrieved absorption change is distributed over a certain volume. In reality, however, the actual haemoglobin concentration changes might be more localised and take place in a smaller volume. Therefore the PVE causes the calculated haemoglobin concentration changes to be underestimated. This effect is more pronounced for the homogeneous analysis method than for the layered one. Below the influence of the PVE is discussed on an *in vivo* fNIRS measurement.

The *in vivo* measurement discussed here was carried out on an adult subject performing a squeeze ball exercise, i.e. a motor task. One of the four channels with strongest activation was selected for the analysis. The time series data was filtered using a low pass zero-phase filter with a cutoff frequency of 0.5 Hz in order to remove high frequency noise and pulsation contributions. All of the 10 task repetitions each 30 s long were averaged (see HA2 and LA2 as discussed before).

For the layered analysis the medium was subdivided into two layers as described in Section 4.4.2. For that mean values for distances and thicknesses from Table 4.5 were used because an individual anatomical MRI recording was not available in this case. Left column of Fig. 4.19 shows exemplary sensitivity factors for the scalp and brain compartments at 690 nm. In this case the background optical properties calculated from averaged absolute moments at 690 nm were 7.9 cm^{-1} and 0.18 cm^{-1} for μ'_s and μ_a , respectively. With respect to the depth sensitivity this is a rather unfavourable combination: absolute values of the sensitivity factors as well as depth selectivity are reduced because of rather high absorption and low scattering (cf. Fig. 4.15). For comparison: the corresponding sensitivity factors for the homogeneous analysis were 14.9 cm, -1.68 ns cm and $-0.52 \text{ ns}^2 \text{ cm}$ for S_A , S_{m_1} and S_V at 690 nm, respectively.

The results of the layered and homogeneous analysis are shown in the middle and left columns of Fig. 4.19, respectively. The concentration changes of oxy- and deoxyhaemoglobin in the lower layer exhibit a spreading and shape typical for a brain activation. In the upper layer no such spreading

4. Analysis of Time-Domain NIRS Signals by Moments

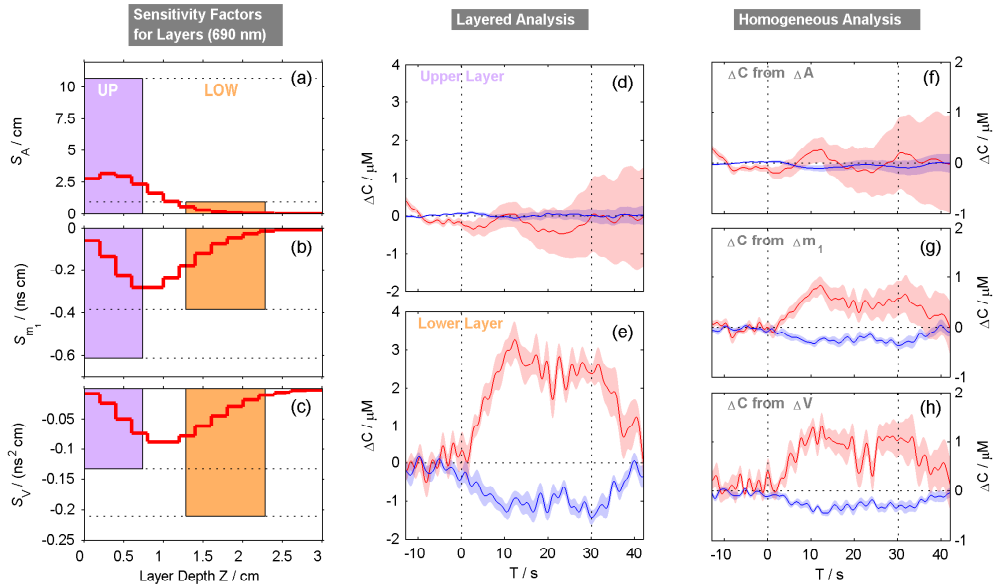


Figure 4.19: Example of the application of the layered and homogeneous analysis methods to an *in vivo* measurement. (a-c) Example of sensitivity factors for the three moments used by the layered analysis (here data obtained at 690 nm). Red lines represent the full depth sensitivity profiles. Coloured bars represent the sensitivity factors for the upper and lower layers obtained by integration of the depth profiles (bars' width is the integration range). Concentration changes in oxy- (red lines) and deoxy-haemoglobin (blue lines) obtained by the layered (d-e) and homogeneous (f-h) analysis are shown in the middle and right columns, respectively. Coloured areas surrounding the lines represent the standard error ($N=10$) from multiple repetitions of the motor task. Time zero is the onset of the 30 s long stimulation. The layered analysis methods can distinguish two layers while the homogeneous analysis results in separate traces for the three measurands ΔA , Δm_1 and ΔV .

is present. Instead the HbO signal resembles a triangular shape which is similar to the superficial signals found on the forehead but with a period of approximately 20 s (cf. the discussion in Section 6.1). The amplitude of the superficial contribution is low compared to the brain related signals but is similar to the superficial contributions on the forehead (approx. $0.5 \mu\text{mol/l}$, cf. Fig. 6.4). The results of the homogeneous analysis qualitatively confirm these findings. Concentration changes obtained from ΔA (Fig. 4.19f) resemble the signal from the superficial layer due to the low depth sensitivity of S_A . Note that no activation-like shape is visible in the $\Delta C(A)$ signals which is also a consequence of the low depth sensitivity of the attenuation signal in this case. On the other hand ΔC obtained from Δm_1 and ΔV exhibit time courses similar to the signals from the lower layer and thereby reveals brain activation. This *in vivo* measurement is an example where time-domain fNIRS can demonstrate its superior depth selectivity. In addition, this example also

demonstrates the benefits of the layered reconstruction. The observer does not need to consider the individual depth sensitivity of the moments to identify brain activation identifiable in the signals of the lower layer.

Both data analysis methods are subject to the partial volume effect. The amplitudes of concentration changes obtained from the variance signal by the homogeneous method are approximately three times smaller than those of the lower layer derived by the layered method. This demonstrates that the layered approach can compensate for the PVE. However, in general, also in the layered case the actual activation might occupy a smaller volume than the one considered by the analysis method. It is challenging to quantify the PVE in this case. It could be done theoretically using 3D Monte-Carlo simulations or experimentally by concurrent fNIRS-fMRI measurements .

4.5 Summary

This chapter deals with many different aspects of the method of moments for time-domain functional NIRS. Section 4.1 explains the basic definitions and the advantages of the method. In practice the accuracy of the calculated values of moments depends on the finite integration and the instrumental response function. This issue is discussed in detail in Section 4.1.2. A correction algorithm was developed to compensate for those systematic offsets and is presented in Section 4.1.3. Using this approach the mean time of flight can be calculated with a precision of a few picoseconds and even centred moments of the third order $m_{3,C}$ with a deviation of less than 10 %. Section 4.1.4 deals with the fundamental detectability limits of small absorption due to the photon and instrumental noise present in time-domain fNIRS. A general finding is that in the *in vivo* case mainly a high count rate improves the detectability. The optimisation of the instrumental response function has positive effects with regard to phantom measurements but only minor influence on the *in vivo* data.

Optical properties of the head obtained *in vivo* using homogeneous and heterogeneous models are discussed in Section 4.2. Reliable *in vivo* determination of the OP of the head tissue remains challenging with the largest difficulty being the validation of the obtained results. The approximation of the heterogeneous structure of the head by homogeneous OP is much easier to use and works without additional measurement. Given the difficulties with the heterogeneous OP the use of homogeneous models remains the most reasonable choice from the practical point of view.

The reconstruction of small absorption changes appearing in fNIRS is based on sensitivity factors (SF). The individual and spatial variation of the

4. Analysis of Time-Domain NIRS Signals by Moments

SF measured *in vivo* for the homogeneous reconstruction method is presented in Section 4.3. The main drawback of this approach is the missing spatial distinction of the absorption changes in the brain and in the scalp. This is compensated by the layered reconstruction discussed in Section 4.4 which is a powerful approach for time-domain fNIRS. It is capable of separating signal contributions from the superficial and brain compartments. The required layered SF are precalculated using homogeneous optical properties estimated from the individual *in vivo* measurement. This allows to individually adapt sensitivity factors for the reconstruction of absorption changes. The dependence of SF on background OP is discussed in Section 4.4.1. A comparison of the both methods is given in Section 4.4.3 using *in vivo* data.

Validation of Data Analysis by Moments Using a Two-Layered Phantom

In biomedical optics phantoms are used to mimic biological tissue under laboratory conditions with the main focus lying on the emulation of optical properties of the organ of interest. Depending on the research objective phantoms may differ in shape, geometry, materials and the way of operation. Phantoms are used for many purposes including validation of light propagation models, calibration and testing of instruments, intra-laboratory studies and others [106–111]. A key requirement of phantoms in the context of fNIRS is the ability to change the absorption and thereby to mimic concentration changes of tissues chromophores. In particular, this can be achieved by using a set of solid phantoms with fixed optical properties, solid phantoms with thermally induced absorption changes [112], solid phantoms with embedded liquid crystals [113] or liquid phantoms [114]. Solid phantoms obviously offer certain advantages considering long term stability, usability, reproducibility, etc. However, their optical characteristics are basically fixed which limits the experimental options. Liquid phantoms, on the other hand, overcome these difficulties allowing for a flexible choice of optical properties as well as their changes. The main drawback in this case is that liquid phantoms must be prepared carefully for each experiment thus limiting the reproducibility and long term stability. An additional advantage of liquid phantoms is that an (absorbing) inclusion can be easily moved within the fluid. A review of tissue simulating phantoms and common phantom materials is given in [110].

In the context of fNIRS the organ of interest is the human head which is often approximated by a semi-infinite geometry with (multiple) compart-

ments or inhomogeneities [115, 116]. A homogeneous SIM phantom is a rough approximation of the human head because it does not reflect the heterogeneity of the head. Still, it is suitable to emulate the strong scattering and the overall light attenuation to be similar to the human tissue. A layered phantom offers a more realistic design (cf. Figs. 2.2 and 5.9) which mimics the head in a more appropriate way.

In this chapter time-resolved measurements on a liquid phantom consisting of two planar layers are presented. This design simplifies the structure of the head considering the curvature, the number of distinguishable compartments as well as their structure, i.e. gyri. The employment of liquids allows for independent absorption changes in two compartments mimicking the scalp and the brain. The experimental data is analysed in terms of moments of DTOFs and compared to simulated values obtained by a recently published solution to the light propagation in a multi-layered semi-infinite turbid medium [117]. Furthermore, changes in absorption are reconstructed from changes in moments using the homogeneous and layered approaches as introduced in Chapter 4. In addition, the influence of four hardware configurations on the results of the analysis is discussed throughout the chapter.

5.1 Two-layered Phantom Setup

5.1.1 Phantom Design and Preparation

A schematic view and a photograph of the liquid two-layered phantom is shown in Fig. 5.1. The cuvette used here was provided within the nEUROPT¹ consortium by Prof. Dr. G. Zaccanti². The two-layered design is an approximation of the head anatomy. The employment of liquids allows to simulate optical properties of living tissue and to gradually change the absorption coefficient of the phantom during the experiment.

Both layers of the phantom were filled with a mixture of intralipid, water and black ink. These three components were proven to be suitable for the construction of relatively stable liquid tissue simulating phantoms in the near-infrared range [118, 119]. Optical properties of the basic mixture were chosen to be similar to background optical properties of an adult human head ($\mu_a = 0.1 \text{ cm}^{-1}$, $\mu'_s = 10 \text{ cm}^{-1}$). The upper (1 cm thick) and lower ($\approx 6 \text{ cm}$ and therefore approximately infinite) layers of the phantom were separated by a

¹ Within the nEUROPT project a multi-laboratory study was carried out on identical phantoms. More information about the project can be found on www.neuropt.eu.

² Prof. Dr. G. Zaccanti is affiliated with the Dipartimento di Fisica dell'Universit  degli Studi di Firenze, Via G Sansone 1, 50019 Sesto Fiorentino, Firenze, Italy

5.1. Two-layered Phantom Setup

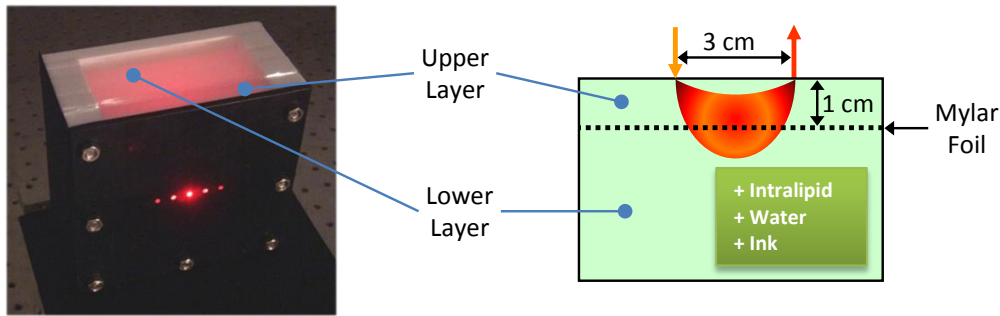


Figure 5.1: Photograph (left) and a schematic view (right) of the two-layered phantom.

thin and slightly scattering Mylar foil. The source-detector separation was fixed to 3 cm.

All mixtures were prepared from accurately characterised solutions. A batch of Intralipid was characterised within the nEUROPt consortium by Dr. G. Zaccanti² and provided to all partners of the project. A solution of black Indian ink was further diluted in water and characterised³ using a photometer method. The result of the characterisation is a set of parameters which can be used to calculate the change in the absorption coefficient resulting from adding a specific amount of the ink solution to the phantom. Both procedures are described in detail in [120].

The level of absorption was changed independently in both layers of the phantom in the μ_a range from 0.1 cm^{-1} to 0.2 cm^{-1} while μ'_s was kept constant at 10 cm^{-1} . First, the absorption was increased in the upper layer, then the content of the upper layer was removed and replaced with the basic solution. Second, the absorption was increased in the lower layer. Special care has been taken to make this procedure as precise as possible. A single absorption increase was performed by adding a small volume of higher absorbing mixture (higher ink concentration) to the phantom. This mixture was prepared from intralipid, water and black ink in a way that its addition to the phantom would not change the scattering coefficient (μ'_s matching⁴). A certain pre-calculated amount of this mixture (typically a few ml) was filled into a small syringe with a capacity of 2 ml or 5 ml. However, it was not possible to fill the syringes with the exact amount of the solution required for a desired change in the absorption coefficient. Therefore not the whole content of a syringe was injected into the phantom but rather a certain number of drops. Every single

³ This auxiliary measurement was carried out by Dr. M. Mazurenka, PTB Berlin.

⁴ This μ'_s matching procedure was necessary because otherwise the adding of the pure, non-scattering ink solution would lead to a decrease of μ'_s , e.g. about 5% and 1.5% for the upper and lower layers, respectively. This would lead to a severe distortion of the measurement objective, e.g. keeping μ'_s constant.

5. Validation of Data Analysis by Moments Using a Two-Layered Phantom

syringe was weighed before and after the experiment to obtain the actual amount of the mixture added to the phantom. From the difference in mass the achieved change in absorption was calculated.

The weighing of syringes and other fluid containers turned out to be more accurate than calculations based on volume measurements. An analytical balance (Mettler Toledo Excellence XS205DU) was used in order to achieve high weighting accuracy ($\sigma \approx 0.02$ mg for a total mass below 81 g). For heavier containers (> 0.5 kg) a standard laboratory balance (Kern EW2200-2NM) with an uncertainty of $\sigma < 1$ g was used.

5.1.2 Light Emission and Detection

The measurement on the two layered phantom was performed using a single diode laser from the Brain Imager (Section 3.1) emitting light at 806 nm. Four different detectors were employed in the measurement: (i) the standard PMT employed in the Brain Imager with a multi-alkali cathode (MuA), (ii) a newer type cooled PMT with a Ga-As photocathode (GaAs, H7422P-50, Hamamatsu, Japan) intended to replace (i) in the Brain Imager, (iii) a hybrid-type PMT with a GaAs cathode (HPM, HPM-100-50, Becker&Hickl, Berlin, Germany) and (iv) a pigtailed single photon avalanche photodiode (SPAD, PFCCTB, MPD, Bolzano, Italy). The first two detectors are common type PMTs which employ a well known assembly containing a photocathode, a dynode system and an anode for the detection of single photon. Both PMTs have been available on the market for many years. The HPM and the SPAD are novel type detectors in the field of the time-domain fNIRS. A hybrid PMT still has a photocathode but no dynode system and no anode any more. Instead, photoelectrons emitted from the cathode are accelerated by a strong electrical field generated by a high voltage of about 8 kV and finally injected directly into a silicon avalanche diode [121]. As a consequence the HPM features a narrow and clean IRF and a low afterpulsing level combined with a large area photocathode [122]. A SPAD is basically a photodiode operated in the Geiger mode. Photons are absorbed directly in the diode material and launch an electron avalanche. Thus a single photon can produce a comparably large current which can be detected by electronics without further amplification. SPADs are very similar to standard APDs but are optimised for single photon detection and, as needed here, for time-resolved measurements [123]. The decay of the IRF is exponential, similarly to the one of the HPM.

The small area (typically $\varnothing < 100$ μm) of a fast SPAD is its largest drawback with regard to the application *in vivo* in diffuse optics. The number of photons collected is considerably smaller than with other detectors. While

5.1. Two-layered Phantom Setup

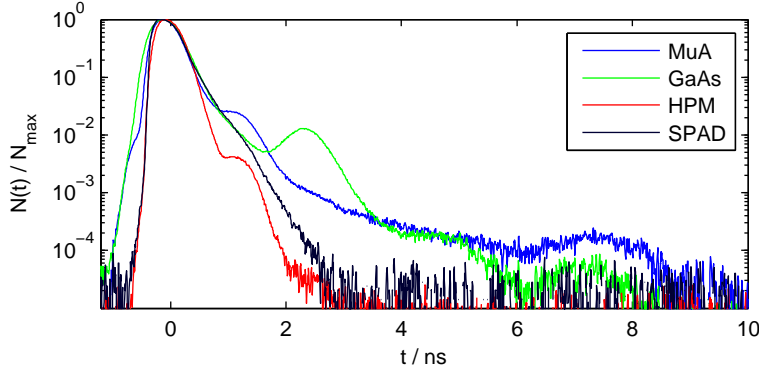


Figure 5.2: IRFs of the four detectors used for experiments on the two-layered phantom. The laser source was a diode laser emitting at 806 nm. All curves were centred to the mean time of flight and normalised to their maximum photon count.

this can be compensated by higher laser power typically available for measurements on phantoms, it is not an option in the *in vivo* due to safety regulations.

The MuA and GaAs PMTs are used in the Brain Imager for regular *in vivo* measurements. Consequently, a complete *in vivo* configuration was used including fibre bundles ($\varnothing 4$ mm, length 1.4 m, NA 0.54) for light collection. For the HPM detector a rather short multimode fibre ($\varnothing 1$ mm, length 1 m, NA 0.39) was used to minimise temporal dispersion. The SPAD had a pigtailed graded index fibre ($\varnothing 62.4$ μm , length 2.1 m, NA 0.275) persistently connected to the detector. Graded index fibres are virtually free from temporal dispersion which helps to optimise the IRF.

An IRF measurement was performed for each detector separately after every single change of the phantom absorption. This allowed to correct for possible drifts and fluctuation that appeared during the 8 h overall duration of the measurement. The setup for the IRF measurement was adapted from Fig. 3.2b. Representative IRFs of the four detectors are shown in Fig. 5.2. These IRFs mainly differ due to different detectors. However, the IRFs also include the shape of the laser pulse as it is emitted by the laser diode and the broadening caused by the source and detection fibres (cf. Eq. (2.33)). Main parameters characterising the IRFs are summarised in Table 5.1. In many publications and detector specifications only the FWHM (full width at half maximum) is reported. However, this parameter alone is insufficient to reflect all differences in the IRFs reported here. Higher order centred moments which are suitable to describe an IRF's shape in a more informative and comparable way are listed in Table 5.1. For example, while the FWHM is very similar for all IRFs (about 500 ps) presented here, the variance V accounts for differences

5. Validation of Data Analysis by Moments Using a Two-Layered Phantom

which appear below the 50% of the maximum level. Higher order moments such as $m_{3,C}$ and $m_{4,C}$ reflect the influence of afterpulses located at the tail of the DTOF even more. Furthermore, V and $m_{4,C}$ are used in the calculation of the photon noise (cf. Section 4.1.4).

During the experiment all detectors were connected to the TSCPC system of the Brain Imager. For each level of absorption realised in the phantom 100 DTOFs with a collection time of 1 s per DTOF were recorded. Only one detector was used at a time. Fibres or fibre bundles were removed and then reattached to the phantom to switch between the detectors. In the beginning of the experiment (lowest absorption) all detection channels (except the SPAD) were adjusted to an ADC count rate of about 1 MHz. The settings were kept with increasing absorption to measure absolute changes in attenuation without recalibration. At the highest absorption level the count rate was about 0.2 MHz. Due to the small area of the SPAD the maximum count rate achieved by this detector was only about 30 kHz even for the lowest absorption. Nevertheless, a limited analysis of the data was still possible even though the noise level was considerably higher. The fibre reattachment procedure is supposed to introduce additional signal variation. This is discussed below in Section 5.1.3.

5.1.3 Reproducibility of Fibre Reattachment

In experimental practice fibres and fibre bundles are attached and removed to a phantom or a human head many times. This procedure potentially results in varying coupling between the fibres and the object in a way that the previous situation is not exactly reproduced. Procedures like this introduce additional signal variation and have an impact comparable to noise. This type of uncertainty introduced by operators affects many phantom experiments, interlaboratory studies and the application of handheld probes. For the latter case, however, the results presented might be rather the lower bound because

Table 5.1: Parameters characterising IRFs used in the phantom experiment and shown in Fig. 5.2. The values describe the IRFs as a whole including contributions of the laser and fibres. The main differences are introduced by the detectors. For the calculation of moments $L_U = 1\%$ was used.

	MuA	GaAs	HPM	SPAD
FWHM / ps	504	580	490	510
$V / (10^{-3}\text{ns}^2)$	104	180	46	74
$m_{3,C} / (10^{-3}\text{ns}^3)$	73	250	12	33
$m_{4,C} / (10^{-3}\text{ns}^4)$	114	600	15	40

5.1. Two-layered Phantom Setup

even slight subject or probe holder movement will produce considerably higher signal variation.

During the measurement performed on the two-layered phantom described above fibres have been frequently removed and reattached to the phantom in order to switch between different detectors. In a subsequent experiment the corresponding signal variation has been estimated. For that fibres have been removed and then reattached to the phantom which was filled with the same basic solution which was used for the actual phantom experiment (see Section 5.1). Each time 20 DTOFs with a collection time of 1 s each were recorded. This measurement allows to separate the total standard deviation of moments σ_{tot} into its parts σ_{in} and σ_{out} using:

$$\sigma_{tot}^2 = \sigma_{in}^2 + \sigma_{out}^2 \quad (5.1)$$

Herein σ_{in} is the inner standard deviation which reflects the signal variation while the fibres stay attached and σ_{out} quantifies the noise alike contribution due to the fibre reattachment. The contributions σ_{in} and σ_{out} can be easily calculated directly from the measured moments of DTOFs.

Results in terms of standard deviations of the moments or of the integral ratio are shown in Fig. 5.3. In the case of the integral ratio $m_0/m_{0,mean}$ the largest part of variation results from fibre reattachment and is similar for all detectors. Also the absolute level of σ_{in} is the same because of the equal count rate set in the experiment. In the case of the mean time of flight and variance the situation changes: the contribution of fibre reattachment is similar or less than σ_{in} . This is in line with the observation made in [61] where the variance signal was found to be more robust against subject movement than the integral signal. Furthermore, there is an indication that reattachment of fibre bundles (MuA and GaAs) is introducing a higher variation to the variance signal than of a single fibre (HPM). This potentially originates from small differences in properties of individual fibres used in the bundles. Differences between detectors are reflected by σ_{in} but are better quantified by the values of V and $m_{4,C}$ (cf. Table 5.1 and Eq. (4.21)).

For all types of moments the standard deviations are similar to typical changes of moments observed during *in vivo* fNIRS measurements (cf. Table 4.1). Therefore fibre reattachment can introduce a substantial uncertainty. Consequently, this increases the total noise and hampers both, the analysis and the comparison of measurements performed on different objects and phantoms.

5. Validation of Data Analysis by Moments Using a Two-Layered Phantom

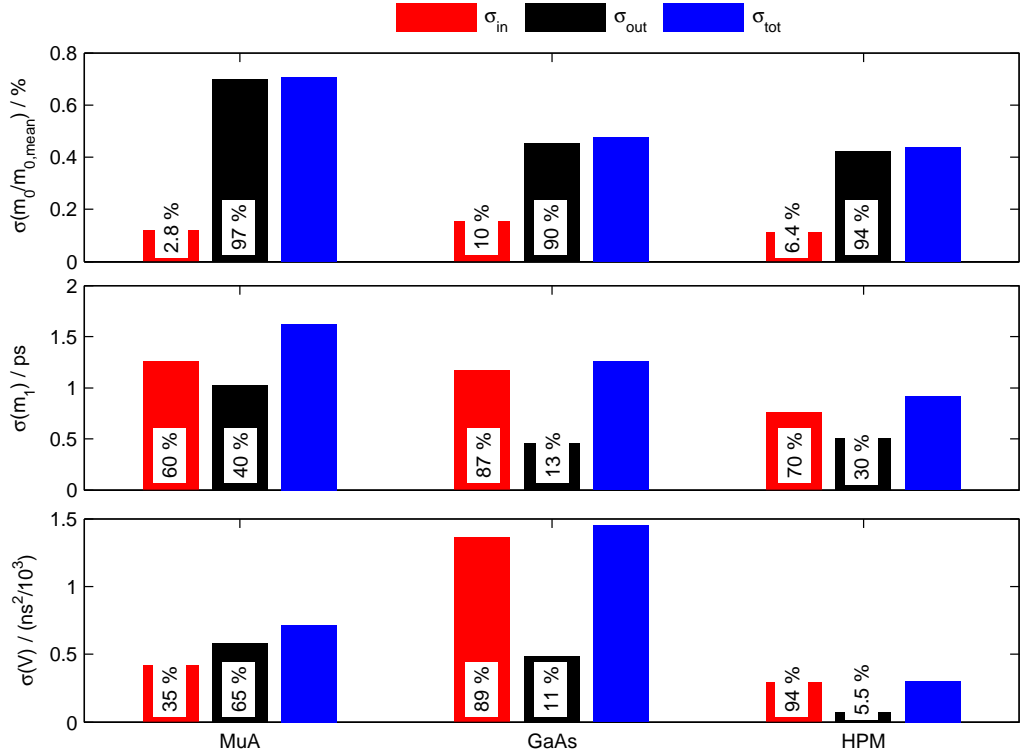


Figure 5.3: Noise induced by fibre (bundle) reattachment shown for three detectors (MuA, GaAs, HPM) in terms of the standard deviation σ for the ratio of the integral $m_0/m_{0,mean}$, mean time of flight m_1 and variance V . Standard deviations calculated from inner, outer and total variances are denoted by σ_{in} , σ_{out} and σ_{tot} , respectively. Effects of fibre reattachment are reflected by σ_{out} . Numbers in white rectangles reflect the fractions $\sigma_{in}^2/\sigma_{tot}^2$ and $\sigma_{out}^2/\sigma_{tot}^2$. The SPAD detector was excluded due to the considerably lower count rate.

5.2 Basic Experimental Results

In this section experimental results obtained by a time-domain measurement on the two-layered phantom are discussed. The data was analysed by the method of moments and is presented in terms of absolute values, relative contrasts and depth selectivity of moments.

5.2.1 Absolute Moments and Relative Contrasts

Results in terms of moments of DTOFs obtained for four different detectors (MuA, GaAs, HPM, SPAD, see Section 5.1 for technical details) are shown in Fig. 5.4 in comparison with the theoretically predicted values. The theoretical values were calculated using a simulation published in [117] and optical properties calculated from the characterised liquids used in the experiment. The

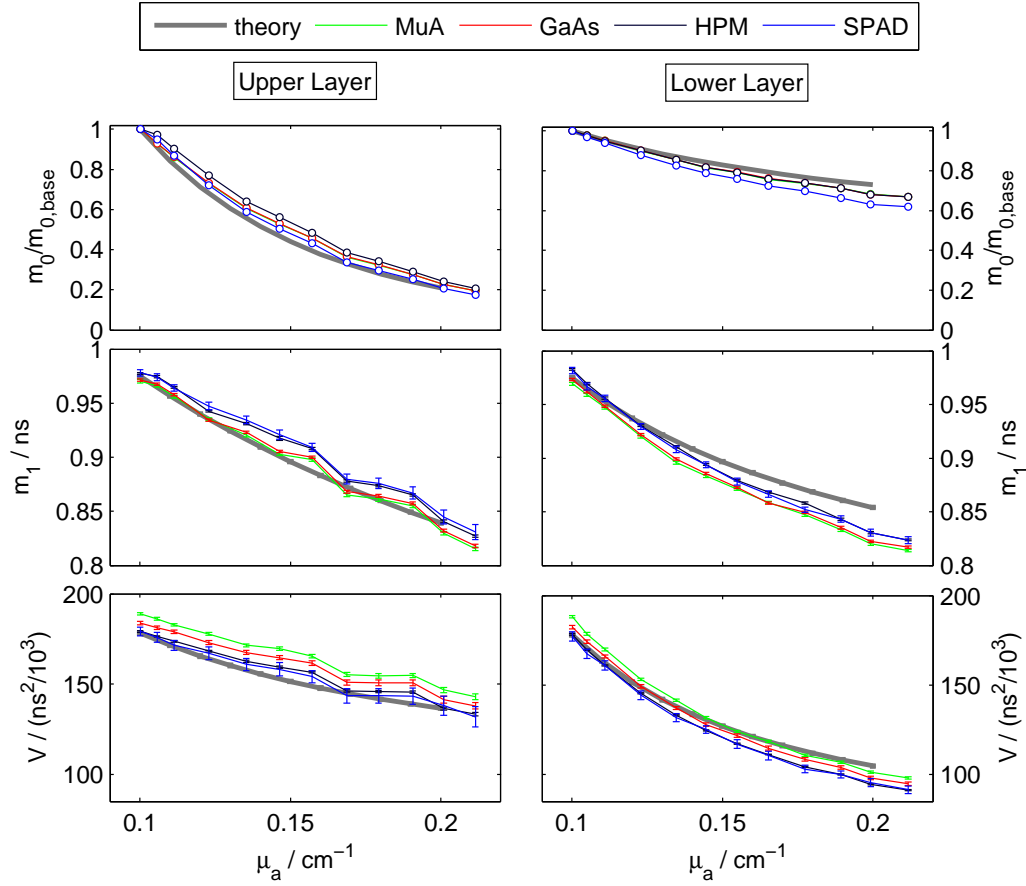


Figure 5.4: Ratio of the integral m_0 to the base value $m_{0,base}$, mean time of flight m_1 and variance V of DTOFs vs. the absorption coefficient in the upper and lower layers changed independently in a two-layered phantom. Experimental data obtained by four detectors (MuA, GaAs, HPM, SPAD) was corrected for the influence of the IRF and can be directly compared to values calculated theoretically from the optical properties of the characterised components of the phantom. The error bars reflect the standard deviation ($N = 100$). For $m_0/m_{0,base}$ the error bars are smaller than the symbols and for some detectors the overlap is high, so that they cannot be distinguished visually.

experimentally obtained values of moments were corrected for the influence of the IRF and can therefore be directly compared to the simulated ones. As expected all measurands exhibit a decrease with increasing absorption. A striking observation is the linearity of $m_1(\mu_a)$ and $V(\mu_a)$ over nearly the whole range of the absorption change in the upper layer. On the opposite, the linearity is much less pronounced if the absorption is increased in the lower layer. Data from the four detectors differ by slight offsets which are most pronounced for the variance signal. These offsets can be attributed to

5. Validation of Data Analysis by Moments Using a Two-Layered Phantom

the influence of the different IRFs. Data from the most narrow IRF (HPM, SPAD) exhibit basically the same course while MuA and GaAs are slightly different.

Theoretically expected and experimentally obtained results are in a good agreement. A slight mismatch between the theoretical and the experimental curves can be observed for the highest absorption ($\mu_a \approx 0.2 \text{ cm}^{-1}$) in the lower layer in all measurands. This behaviour might be explained by either a higher μ_a increase than expected or a reduction of the thickness of the upper layer. With regard to the experimental procedure the second explanation appears to be more likely. During the experiment a mixture of ink, water and intralipid was added to the lower layer in order to increase μ_a . This leads to a higher fluid level in the lower compared to the upper layer because in reality both layers were arranged vertically (cf. Fig. 5.1). According to additional simulations (not shown here) an approximately 0.86 cm thick upper layer would match the observed differences $\Delta m_1 \approx 24 \text{ ps}$ and $\Delta V \approx 0.01 \text{ ns}^2$ between experimental and theoretical results at $\mu_a = 0.2 \text{ cm}^{-1}$ of the lower layer. A reduction of the thickness by only 0.14 cm appears realistic because the foil separating the layers cannot be stretched perfectly. A way how to avoid foil related influence on the measurement is discussed in Section 5.5. Additional experimental uncertainties which might contribute to the deviations are the fibre reattachment discussed in Section 5.1.3 and signal fluctuation due to the inhomogeneous distribution of the injected ink solution in the layers. The latter one was reduced as far as possible by repeating the same stirring procedure (∞ -shaped movement) after adding the ink solution for twenty times.

In addition to the analysis of absolute values it is possible to define the relative contrast $C(M)$ of a measurand M for each measured sample M_i :

$$C_i(M) = \frac{M_i - M_b}{M_b} = \frac{\Delta M_i}{M_b} = \frac{M_i}{M_b} - 1 \quad (5.2)$$

The basic value M_b must be defined reasonably with regard to the actual experiment. For example, M_b can be a baseline value of an fNIRS measurement or refer to a homogeneous medium as it is done here. Relative contrasts have been used for the analysis of *in vivo* data based on time windows [124] and suggested for comparison of different instruments within the performance assessment of time-domain optical brain imagers [125]. An advantage of the definition in Eq. (5.2) is that $C(M)$ is free of units and therefore potentially contrasts calculated from signals of different types can be compared. Another important feature of relative contrasts of the mean time of flight and variance is that they mainly rely on the changes ΔM of moments which are virtually free of the influence of the IRF (cf. Section 4.1). However, the basic value

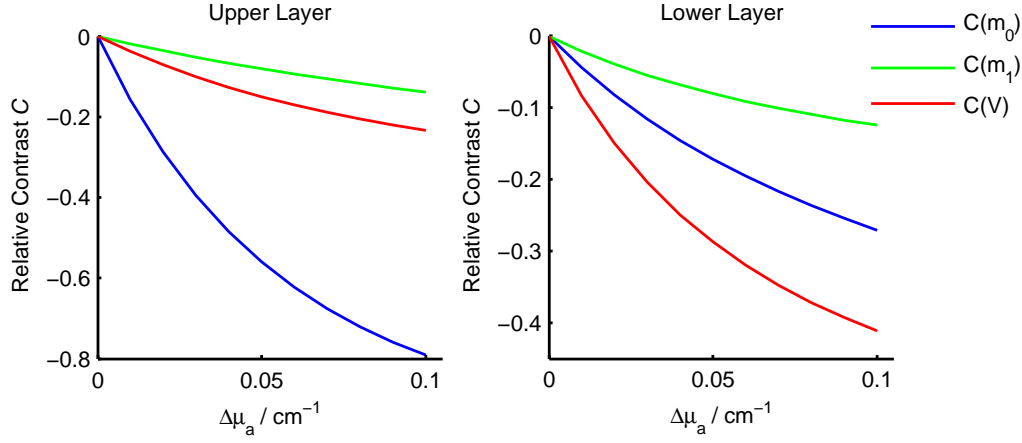


Figure 5.5: Relative contrasts C of the integral m_0 , mean time of flight m_1 and variance V during changes of the absorption coefficient $\Delta\mu_a$ in the upper and lower layers of a two-layered phantom. Here the data from the simulated case shown in Fig. 5.4 was used. Note that the contrasts do not reflect the depth selectivity of the moments.

M_b can potentially be IRF dependent and must therefore be treated carefully. Below the values of m_1 and V used as M_b were corrected for the influence of the IRF. It should be noted that the relative contrast of the integral m_0 is related to the attenuation change ΔA and for small absorption changes it is approximately equal to the negative attenuation change ΔA (cf. Eq. (2.21)):

$$C_i(m_0) = \frac{m_{0,i}}{m_{0,b}} - 1 = \exp(-\Delta A) \approx -\Delta A \quad (5.3)$$

In the last step a Taylor series expansion for small ΔA was used.

Figure 5.5 shows relative contrasts calculated from the simulated case in Fig. 5.4 as a function of the change of the absorption coefficient in the upper and lower layer. The basic value M_b was the homogeneous state with no absorption change. In comparison, $C(A)$ exhibits the largest absolute contrast for the absorption changes in the upper layer and a three times smaller contrast in the lower layer. $C(V)$ is dominant for μ_a changes in the lower layer and moderate for changes in the upper layer. Surprisingly, in both cases $C(m_1)$ exhibits the lowest absolute contrast. A reasonable expectation would be that contrasts reflect the depth sensitivity of moments which increases with the order of the moments (cf. Section 4.4.1). But they do not. The reason for this is the normalisation to the base value M_b in Eq. (5.2). For example, for the absorption change $\Delta\mu_{a,up}$ in the upper layer the corresponding contrast of the mean time of flight can be written as:

$$C(m_1) = \frac{\Delta m_1}{m_1} = \frac{S_{m_1,up} \Delta\mu_{a,up}}{S_{A,hom}/c_m} = \frac{S_{m_1,up}}{S_{A,hom}} c_m \Delta\mu_{a,up} \quad (5.4)$$

5. Validation of Data Analysis by Moments Using a Two-Layered Phantom

Here m_1 was replaced using Eq. (4.35); $S_{m_1,up}$ is the sensitivity factor of m_1 for absorption changes in the upper layer and $S_{A,hom}$ is the sensitivity factor for attenuation changes in the homogeneous SIM. Due to the normalisation to the absolute value of m_1 the contrast contains a mixture of sensitivity factors of different measurands, e.g. $S_{m_1,up}/S_{A,hom}$. This, however, does not make any sense. Thus, although normalised and free of units, relative contrasts of different moments do not provide any advantages compared to the analysis of changes of moments.

5.2.2 Depth Sensitivity and Selectivity of Moments

High sensitivity to absorption changes in deeper lying compartments is desired in non-invasive fNIRS. This potentially allows for better assessment and quantification of brain hemodynamics. The sensitivity itself is quantified by the sensitivity factors as discussed in Section 4.3 and defined in Eq. (4.33).

Here sensitivity factors of moments are calculated from the experimental data obtained on the two-layered phantom. The values listed in Table 5.2 are equal to the slope obtained by a linear fit to the data shown in Fig. 5.4 in the μ_a range from 0.1 cm^{-1} to 0.11 cm^{-1} . This range corresponds to a 10% change of μ_a . In the table S_U and S_L denote sensitivity factors for absorption changes in the upper and lower layers, respectively. The values for S_U and S_L have been averaged over the four detectors.

For comparison the same procedure was applied to the simulated data to obtain theoretical sensitivity factors. In addition Eqs. (4.34) to (4.36) were used to calculate sensitivity factors S_{hom} for homogeneous absorption changes in a homogeneous semi-infinite medium. In the case of the ratio $m_0/m_{0,base}$ the relationship $S_A \approx -S_{m_0/m_{0,base}}$ was used which results directly from the application of Eq. (4.33) to Eq. (2.21).

Table 5.2: Sensitivity factors of moments S_U and S_L for absorption changes in the upper and lower layers, respectively. S_{hom} denotes sensitivity factors for homogeneous absorption changes in a homogeneous semi-infinite medium. Values expected from the theoretical simulation are given in parenthesis.

Measurand	S_U	S_L	S_L/S_U	S_{hom}
$S_{m_0/m_{0,base}} / (1/\text{cm}^{-1})$	-11.6 (-15.7)	-4.6 (-4.4)	0.4 (0.28)	-17.1 (-20.9)
$S_{m_1} / (\text{ns}/\text{cm}^{-1})$	-1.57 (-1.81)	-2.2 (-2.0)	1.44 (1.13)	-3.9 (-3.8)
$S_V / (\text{ns}^2/\text{cm}^{-1})$	-0.51 (-0.67)	-1.46 (-1.47)	2.9 (2.2)	-2.3 (-2.1)

The experimentally obtained and theoretically expected sensitivity factors are in an acceptable agreement. Largest differences of about 25% are observed for the upper layer whereas for the lower layer differences are below 10%. As

expected the sum of S_U and S_L is approximately equal to S_{hom} . Sensitivity factors for different moments cannot be compared in an absolute manner because of the different units and therefore a ratio S_L/S_U was calculated. This ratio provides a metric of the so called “depth selectivity” which is of particular interest for *in vivo* brain imaging. There it is essential to have a low influence of absorption changes in the scalp while high sensitivity to absorption changes in the depth is desired, i.e. low S_U and high S_L . A high depth selectivity is therefore reflected by a high ratio S_L/S_U . Comparison of ratios given in Table 5.2 reveals that the depth selectivity of the mean time of flight and the variance in this experiment is clearly higher than the one of the integral ratio $m_0/m_{0,base}$, i.e. by a factor of four and eight, respectively.

These results, although promising, first of all reflect the specific situation in this particular phantom. The sensitivity factors and therefore the depth selectivity depend on the optical properties of the medium and the actual geometry. In a layered structure, in general, the mean time of flight and the variance will still exhibit a higher depth selectivity than the light intensity based measurands even in other configurations of the turbid medium. But neither the value of the ratio S_L/S_U nor the relationship between the ratios for different measurands will probably stay the same. Further investigations are needed to clarify this issue.

5.3 Reconstruction of Absorption Changes

An accurate reconstruction of absorption changes is of fundamental interest for fNIRS. Here homogeneous and layered methods (cf. Sections 4.3.1 and 4.4.2) are applied to experimental data obtained using the two-layered phantom and accompanying simulated data. The retrieved absorption changes are compared to the input values. The sensitivity factors required for this purpose are also calculated from a heterogeneous medium.

Results of a homogeneous reconstruction applied to simulated data (see Fig. 5.4) are shown in Fig. 5.6. Here the sensitivity factors for the changes of moments were calculated from the homogeneous state where $\mu_{a,1} = \mu_{a,2}$. These sensitivity factors then were used to calculate $\Delta\mu_a$ from changes of moments which appear if $\mu_{a,1}$ or $\mu_{a,2}$ are varied. As expected, in none of the cases a completely correct retrieval of the actual μ_a changes was achieved. The best retrieval for an absorption change of $\Delta\mu_a = 0.01 \text{ cm}^{-1}$ is observed from ΔA in the upper layer (78%) and from ΔV in the lower layer (69%) while data from Δm_1 lies in-between. This behaviour is expected and basically reflects the different depth sensitivity of the measurands. These calculations also demonstrate the strong limitation of the linearity with respect to absorption

5. Validation of Data Analysis by Moments Using a Two-Layered Phantom

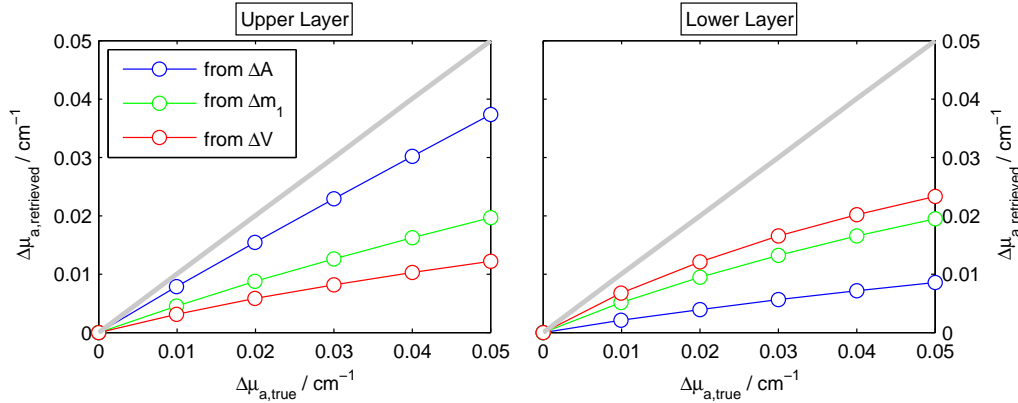


Figure 5.6: Retrieval of the absorption changes in the upper and lower layers in a simulated two-layered phantom using sensitivity factors for a homogeneous semi-infinite medium. The retrieval was performed from changes of attenuation ΔA , mean time of flight Δm_1 and variance V . The grey line depicts a perfect retrieval, i.e. true values.

changes. From this the linear range for $\Delta\mu_a$ can be estimated to be below 10% of the basic μ_a value. It should be noted that typical absorption changes induced by vascular responses in the brain can be estimated⁵ to be lower than 10%.

The procedure used above could now be applied to different homogeneous basic states with other levels of absorption and/or scattering. The results confirmed that the homogeneous method cannot exactly recover the true absorption change and that the linear range is limited. Also, with regard to fNIRS where typical absorption changes are not homogeneous, the results would be of limited value. Therefore a different approach was used where homogeneous and layered methods are applied to inhomogeneous states of the phantom and rather small $\Delta\mu_a$ are recovered.

Results of a more general application of the homogeneous and layered reconstruction methods are shown in Fig. 5.7. The sensitivity factors used for the retrieval of $\Delta\mu_a$ were calculated from the corresponding basic state which implies that the medium is not homogeneous any more. For this the data in Fig. 5.4 was first fitted using a polynomial of third degree and then evaluated at 21 equidistantly spaced data points. The last step means a slight upsampling of the original data so that smaller $\Delta\mu_a$ steps can be used. The whole procedure smooths the data and simplifies the reconstruction⁶. The $\Delta\mu_a$

⁵ For example, using a HbT concentration of 80 μm and Eq. (2.3) an increase in HbO of about 5 μm would introduce a 6% μ_a change around 800 nm ($(80 + 5)/80 \approx 1.06$).

⁶ The reconstruction is based on changes of moments. If those are calculated from noisy or otherwise disturbed data the changes exhibit an even noisier behaviour than the original data. This complication can be avoided by reasonably smoothing the original data.

5.3. Reconstruction of Absorption Changes

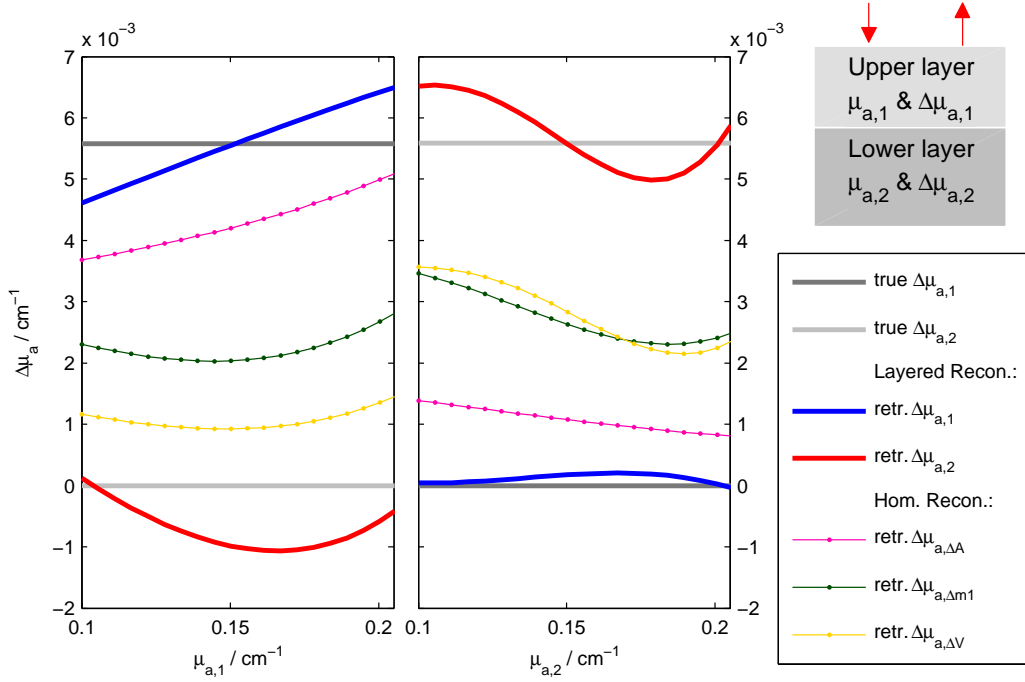


Figure 5.7: Reconstruction of absorption changes in the two-layered phantom using homogeneous and layered approaches. Experimental data obtained on the two-layered phantom was fitted by a polynomial to simplify the reconstruction procedure. Absorption coefficients of the upper and lower layers are denoted by $\mu_{a,1}$ and $\mu_{a,2}$, the absorption changes by $\Delta\mu_{a,1}$ and $\Delta\mu_{a,2}$, respectively. On the left the absorption coefficient of the upper layer $\mu_{a,1}$ is changing while the remaining optical properties are kept constant. The same but with $\mu_{a,2}$ changing is shown on the right.

step resulting from the upsampling is 0.0056 cm^{-1} which is equivalent to about 2.5 % to 5.6 % change with respect to the absolute absorption coefficients $\mu_{a,1}$ and $\mu_{a,2}$. All changes of moments and μ_a were calculated as the difference of adjacent points. For clarity the results discussed here are based only on the data obtained with the MuA detector⁷. The other detectors exhibit a similar behaviour.

Figure 5.7 compares absorption changes $\Delta\mu_a$ retrieved by both methods. The homogeneous method gives three estimates for each of the moments, i.e. $\Delta\mu_{a,A}$, $\Delta\mu_{a,m1}$ and $\Delta\mu_{a,V}$, while the layered reconstruction combines all three moments and results in separate estimates $\Delta\mu_{a,1}$ and $\Delta\mu_{a,2}$ for each of the layers. In the first scenario (Fig. 5.7 left) only $\mu_{a,1}$ of the upper layer is changing while in the second only $\mu_{a,2}$ of the lower layer varies (Fig. 5.7 right). The homogeneous analysis recovers different fractions of the true absorption

⁷ This detector was used for the *in vivo* measurements presented in Chapter 6.

5. Validation of Data Analysis by Moments Using a Two-Layered Phantom

change with the best retrieval achieved by ΔA for $\Delta\mu_{a,1}$. This mainly reflects the high sensitivity of the intensity based signal to the superficial region of the phantom. As a consequence of the comparably higher depth sensitivity the Δm_1 and ΔV signals result in $\Delta\mu_a$ values lying closer to $\Delta\mu_{a,2}$. However, in any case the retrieved values do not reflect the actual absorption changes. This is basically an another occurrence of the partial volume effect.

In contrary to the homogeneous method, the layered reconstruction can decompose the changes in both layers, i.e. the retrieved $\Delta\mu_{a,1}$ and $\Delta\mu_{a,2}$ are in the same region as the true values. The dependence of the retrieved values on the absolute absorption coefficients is moderate. Some linear and non-linear modulations can be seen (blue and red lines in Fig. 5.7). The origin of these deviations is not completely clarified. Potentially, they result from an interplay of the fitting of the moment's data, the calculation of sensitivity factors and the crosstalk during the reconstruction. Taking these deviations into account the accuracy of the layered reconstruction can be estimated to be $\pm 0.0065 \text{ cm}^{-1}$. Another limitation which is not investigated here is the influence of layers with constant but different scattering μ'_s . In general, this must introduce changes to sensitivity factors but might be compensated by the reconstruction procedure. Further test are needed here.

All together the layered reconstruction method is superior to the pure homogeneous approach. The latter returns absorption changes which are underestimated and not clearly assigned to the depth. On the other hand, the layered reconstruction method promises a highly desired separation of depth dependent absorption changes. With regard to the application to fNIRS data this allows to separate superficial and brain haemodynamics without making any assumptions about the relationship between the time courses of both signals.

5.4 Optical Properties Derived by a Homogeneous Model

Homogeneous models are usually not intended to be applied to heterogeneous media because of the obvious model mismatch. In some cases however, the employment of homogeneous models can be justified if the results are not seriously altered or no other models are available. In any case, the simplicity and the low computational effort of homogeneous methods is a clear benefit. There is a number of publications where fitting of the homogeneous SIM model (Section 2.2.4) to *in vivo* data has been applied in order to obtain background optical properties (BOP) on piglets [77] and the human head [76, 100, 102,

5.4. Optical Properties Derived by a Homogeneous Model

126]. In order to justify similar procedures the limitations must be known. In this section data from the two-layered phantom is analysed using the model for the semi-infinite homogeneous medium. Optical properties were obtained using the moment's method (Section 4.2.1, [70]) and a fit⁸ of Eq. (2.31) to the complete DTOF. Experimental data used here was recorded by four different detectors and therefore the influence of IRF on the results can be studied. The fit was performed to the DTOF in a certain range where the left limit was set to be 20% of the maximum on the rising edge and the right limit was 1% of the maximum on the tail. For the moments calculation the left and right limits were 1% and 0.1%, respectively.

Figure 5.8 shows optical properties retrieved by both methods in comparison to the true values. A general observation is that both procedures tend to retrieve the absorption coefficient $\mu_{a,low}$ of the lower layer and are rather insensitive to absorption of the upper layer $\mu_{a,up}$ (see panels a, b, e, f). The fit method exhibits a higher insensitivity to the superficial $\mu_{a,up}$ than the moments method. The situation is different for the scattering coefficient μ'_s which was kept constant in both layers throughout the whole experiment. Both procedures exhibit an obvious cross talk between the retrieved μ_a and μ'_s values which cover a wide range around the true values. In particular μ'_s ranges from 5 cm^{-1} to 18 cm^{-1} for the fit and from 8 cm^{-1} to 13 cm^{-1} for the moment's method. Therefore both methods provide only rough estimates for μ'_s . Interestingly, the fit results in relatively low μ'_s values if $\mu_{a,up}$ is high. Similarly, low μ'_s values have been obtained by the same SIM fit applied to *in vivo* data. This might be an indication that the scalp has a higher absorption than the lower tissue compartments.

The influence of the IRF of the different detectors produces offsets in the curves of retrieved optical properties. There is a certain order of the curves which slightly differs for both methods. The reason for that order remains unclear. This finding suggests that the shape of the IRF can potentially introduce additional deviations.

Optical properties derived by homogeneous methods are commonly known as “background optical properties” (BOP). However, the understanding and usage of BOP varies. In the context of perturbation models and optical mammography BOP refer to the medium without perturbations (absorbing inclusions) or tissue with no tumours. This understanding is obviously in conflict with layered geometries which rather match the head anatomy. As discussed above BOP derived from a layered medium do not necessarily

⁸ During the fit procedure the modelled reflectance of the SIM is convolved with the IRF. This curve and the experimentally obtained DTOF were compared in terms of the reduced residual sum χ^2 which was minimised by a Simplex-Downhill algorithm. Fit parameters were μ_a , μ'_s and time-zero t_0 .

5. Validation of Data Analysis by Moments Using a Two-Layered Phantom

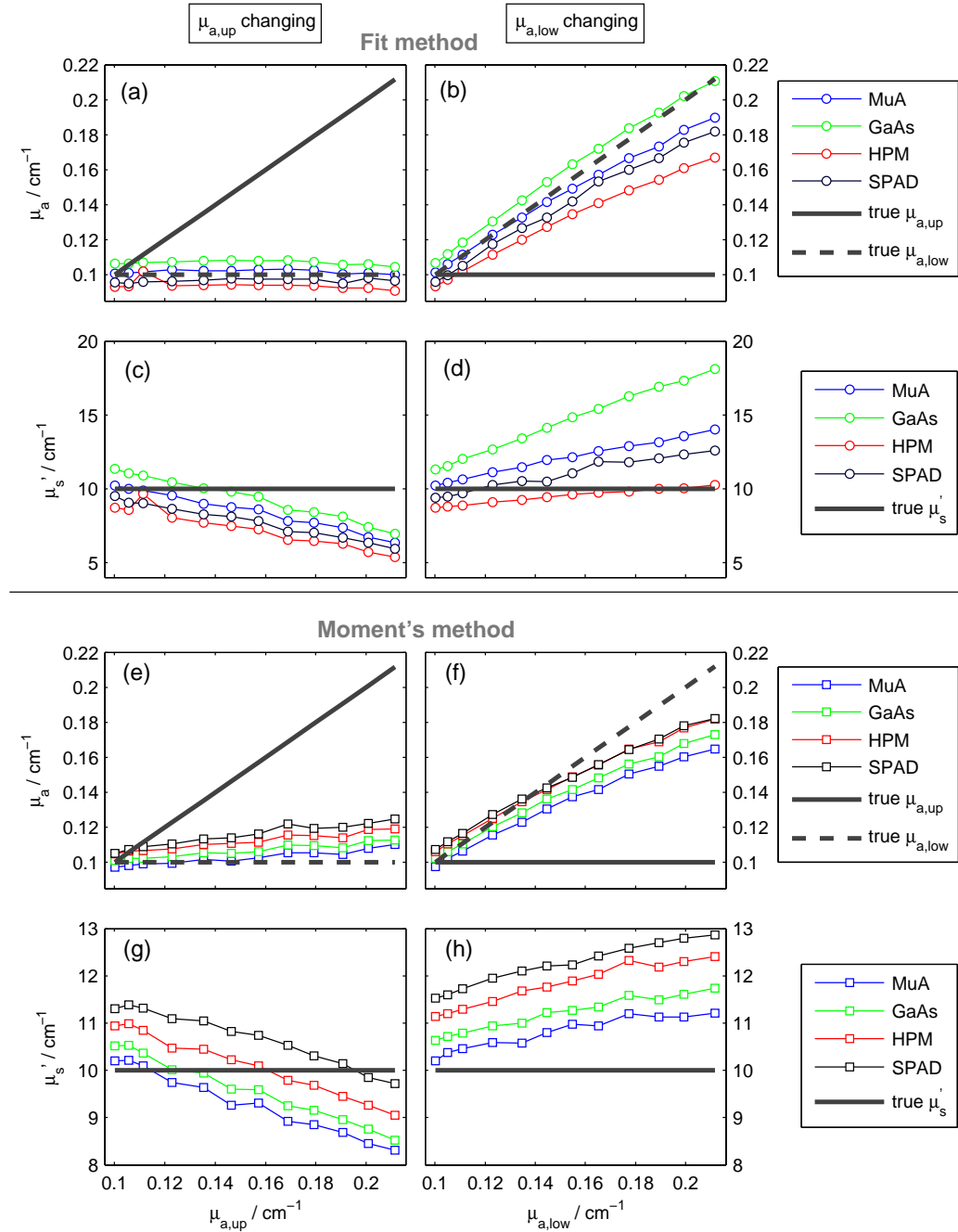


Figure 5.8: Optical properties as retrieved by the application of the homogeneous semi-infinite model to the experimental data from the two-layered phantom. Values have been obtained by fitting (a-d) and by the method of moments (e-h).

describe a kind of “mean optical properties” and exhibit a crosstalk between μ_a and μ'_s . The last point also implies that scattering and absorption are not clearly separated. To some part these difficulties affect the calculation of the sensitivity factors (SF) as discussed in Section 4.4.1. In the end, for the reconstruction of absorption changes in fNIRS, the dependence of the SF on the BOP is the more crucial issue than the absolute value of BOP.

5.5 Future Layered Phantom Design

The two-layered phantom treated in this chapter consisted of two liquid layers which were separated by a thin foil. This type of design allows for independent absorption changes in two compartments mimicking scalp and brain and is relatively easy to realise. However, as discussed in 5.2.1, probably the increasing fluid level in the phantom led to variations of the upper layer thickness therefore inducing a severe systematic modification of experimental conditions. It was proved by simulations that thickness changes of some tenths of a millimetre can already result in significant changes of moments. There are two potential solutions to this problem. (a) The foil might be replaced with a solid scattering material which will not be stretched by low forces resulting from liquid level mismatch. (b) The foil is strongly stretched and in addition carefully glued to an additionally inserted solid frame with a window. The smaller the size of the window the higher are the required forces needed to change the position of the foil. However, a too small window will perturb the light propagation in the phantom and therefore bias the experiment depending on the source-detector separation and optical properties of the medium.

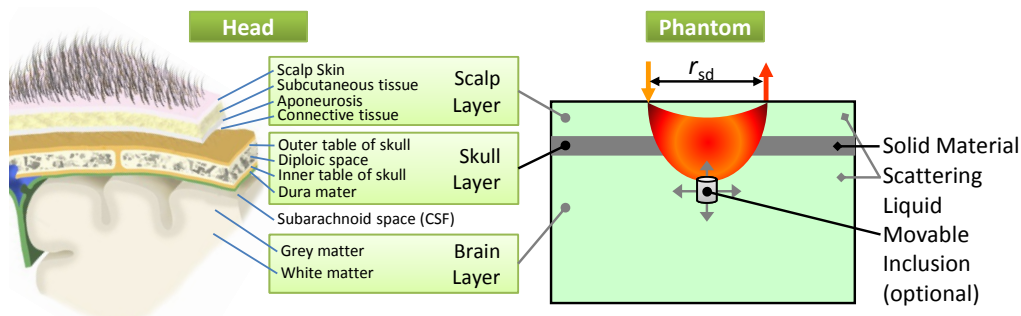


Figure 5.9: Potential future phantom design employing solid and liquid materials.

For future studies the combined solid-liquid phantom design as suggested in (a) and depicted in Fig. 5.9 is the most promising one. A similar mixed material phantom with only one liquid compartment has been suggested for (functional) NIRS tomography [127]. There, a moveable inclusion was used to

5. Validation of Data Analysis by Moments Using a Two-Layered Phantom

test the spatial resolution of a fNIRS instrument which is also possible with the design suggested here. In addition, optical properties of the upper layer can be adjusted to mimic superficial haemodynamics.

The second and solid layer can be produced from preferably resin [109, 128] or polyoxymethylene. Its thickness and optical properties can be selected in order to mimic the skull [8], therefore resulting in an even more realistic geometry. Optical properties of the solid material can be measured in advance and be used as an input to simulations or fitting procedures. The thickness of the upper layer can be selected in order to study effects of different scalp thickness. The cerebrospinal fluid (CSF) is neglected in the suggested phantom. Potentially, an additional CSF simulating layer can be introduced in a similar way to [127].

A phantom design with two liquid layers allows to mimic absorption changes in the superficial as well as in cerebral compartment. In addition, such a phantom can be easily employed for absorption and fluorescence experiments using fluorescing chromophores (i.e. using indocyanine green). A further development towards a dynamic phantom similar to [129] is greatly simplified by the liquid design.

5.6 Summary

In this chapter time-domain NIRS measurements performed on a two-layered liquid phantom with varying absorption are discussed. The measurements are analysed in terms of moments of DTOFs and compared to a recently published analytical solution to light propagation in a turbid layered medium. The comparison resulted in a good agreement. It was proven that very small absorption changes in order of $\Delta\mu_a \approx 0.005 \text{ cm}^{-1}$ can be experimentally realised in a liquid phantom and even smaller steps appear feasible. Furthermore, a comparison with the analytical solution helped to reveal conceptual experimental problems arising from reduced thickness of the upper layer due to the increasing fluid level. This finding has implications for future phantom designs and as a consequence a three-layered mixed material phantom design is suggested as a most promising and flexible solution.

The depth sensitivity and selectivity of moments was investigated and compared to the values expected from the simulation. The mean time of flight and the variance of DTOFs were proven to be superior to the light intensity based signals. Changes of moments were used to reconstruct absorption changes in both layers using a homogeneous and layered model. The homogeneous approach achieved only partial retrieval while the layered method was able to separate absorption changes in both compartments.

The retrieval of “background optical properties” for the layered medium using homogeneous models gave inconsistent results. The procedures returned μ_a values which were closer to those of the lower layer. However, a cross talk to the μ_a of the upper layer was obviously present. The retrieved μ'_s value lay in a wide range and can therefore only be used as a very rough estimate.

Throughout the chapter a phantom geometry with two layers and equal scattering was used. This simplification can limit the transfer of the results to more general cases where also μ'_s is heterogeneous. This is also the case in a real head and therefore the influence of a μ'_s mismatch must be studied in the future. This can be performed using forward models such as the one employed in this chapter.

5. Validation of Data Analysis by Moments Using a Two-Layered Phantom

Applications of Time-Domain fNIRS *in vivo*

Application of time-domain fNIRS *in vivo* in clinical or neuroscientific research is the main purpose of the whole instrumental and methodological development of the technique. In the past many studies using fNIRS have been published investigating different tasks. A clear majority of these employed used continuous wave fNIRS and no combinations with other neuroscientific modalities.

Here the focus lies on multi-modal *in vivo* measurements where td-fNIRS is combined with concurrent or subsequent fMRI, EEG and systemic physiological data acquisition. This approach allows to study brain responses to the same stimuli but measured by different techniques and therefore to use one's technique specific advantages to validate or improve the other. In particular, this applies to the identification of brain activation and superficial artefacts as measured by fNIRS. Further, multi-modal measurements help to improve the understanding of how physiological processes are interconnected which might pave the way to new diagnostic approaches.

6.1 Concurrent Measurement of fNIRS and Systemic Physiological Signals

Vascular responses to stimuli recorded by fNIRS were frequently found to differ in shape from those recorded by fMRI (cf. the example in Fig. 2.5 and [130]). In such cases it was often hypothesised that signals might be distorted by systemic physiological artefacts. Indeed, systemic physiological processes (SPP), either independent or correlated with the stimulation task,

6. Applications of Time-Domain fNIRS *in vivo*

were shown to likely influence optical fNIRS signals making its interpretation challenging [130–132]. In this section results of a multi-modal experiment employing concurrent recording of td-fNIRS and SPP with subsequent functional and anatomical MRI measurements are presented¹. Experiments and results discussed in this section together with additional MR-angiography measurements on individual subjects revealed that superficial artefacts in fNIRS originate from the vasoconstriction of superficial veins. This finding was published in [103].

In the study presented here subjects performed a cognitive task which leads to activation in the frontal lobe. This area of the brain is known to be responsible for many other higher level cognitive functions [133] and is therefore of particular interest for the neuroscientific research. The optical measurement was carried out on the forehead which is well accessible by fNIRS but also known to be influenced by superficial haemodynamics [130]. In this case the employment of the time-domain fNIRS method is promising because it provides depth selective access to vascular responses. This helps to attribute certain signals contribution to either the superficial or the cerebral compartment. The multi-modal data acquisition was performed on 15 healthy adult volunteers and included (i) time-domain fNIRS measurements at four spatial positions on the forehead with simultaneous acquisition of a number of systemic physiological signals during the execution of a semantic continuous performance task (CPT), (ii) subsequent fMRI measurements during the same task and (iii) anatomical MRI recordings. The experimental setup and all employed instruments are described in Section 3.2.

6.1.1 Subjects and Tasks

Fifteen healthy subjects (5 female/10 male, age 34.9 ± 7.2 years (mean \pm SD)) performed a semantic continuous performance task described below. Thirteen subjects first took part in the fNIRS experiment, and subsequently, 1 h later, in the fMRI experiment. For one subject the fNIRS and fMRI sessions were separated by 1 week, and one subject took part first in the fMRI and 1 week later in the fNIRS experiments. Total duration of a single subject measurement was about 2 h.

In order to trigger activation in the Broadman Area 10 located in the forehead region a semantic categorization task was used which is a variation of the continuous performance task (CPT) used in [134]. A list of German words was presented on a computer monitor to the subjects using rapid serial visual

¹ This is collaborative work. The fNIRS and SPP measurements were performed by Dr. I. Tachtsidis (UCL) and the author of this thesis. All MRI experiments were done by Dr. E. Kirilina (FU Berlin), Dr. R. Brühl (PTB) and Dr. M. Niessing (FU Berlin).

6.1. Concurrent Measurement of fNIRS and Systemic Physiological Signals

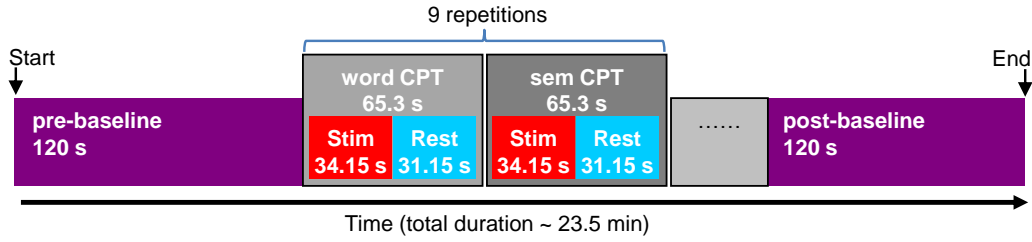


Figure 6.1: Paradigm of the concurrent fNIRS and SPP experiment. “Stim” and “Rest” denote the stimulation and resting periods, respectively.

presentation with a word presentation time of 1 s and a 1 s long interstimulus period. Each of the words represented either a concrete or an abstract concept. In the semantic-CPT condition (sem-CPT) the subjects had to press the left arrow button of a keyboard if they recognised a concrete word following an abstract one. Otherwise they were instructed to press the right arrow button. In a control task (word-CPT) the target condition was replaced by a fixed word sequence, i.e. the word “VORZUG” (preference) followed by “KOFFER” (suitcase). A task like this is more challenging for the subjects than a simple motor task and is similar to other tasks frequently used in the neuroscientific research.

The temporal structure of the paradigm is illustrated in Fig. 6.1. The fNIRS part of the experiment consisted of 18 stimulation blocks (9 word-CPT and 9 sem-CPT blocks) with a duration of 34.15 s each. All blocks were separated by 31.15 s long resting periods with a fixation cross drawn on a black screen and presented to the subjects. A 0.5 s long instruction screen (“KOFFER>VORZUG” for word-CPT and “ABSTRACT>CONCRETE” for sem-CPT) was displayed before each block. A pre- and post-baseline of approximately 120 s duration was recorded in the beginning and the end of each individual session. For the fMRI part the paradigm was modified in a way that it was subdivided into three subsequent runs consisting of 6 blocks each and the baselines shortened to about 30 s.

6.1.2 Brain Activation

The time-domain fNIRS data was analysed in terms of changes of moments. Ratios of the integral $m_0/m_{0,base}$, as well as changes of the mean time of flight Δm_1 and variance ΔV measured at three wavelengths were converted to concentration changes in oxy- and deoxyhaemoglobin ΔC_{HbO} and ΔC_{HbR} using the homogeneous model as described in Section 4.3.1. Two subjects were excluded from the analysis due to motion artefacts resulting in strong signal distortion. Due to the poor SNR of this measurement a group average

6. Applications of Time-Domain fNIRS in vivo

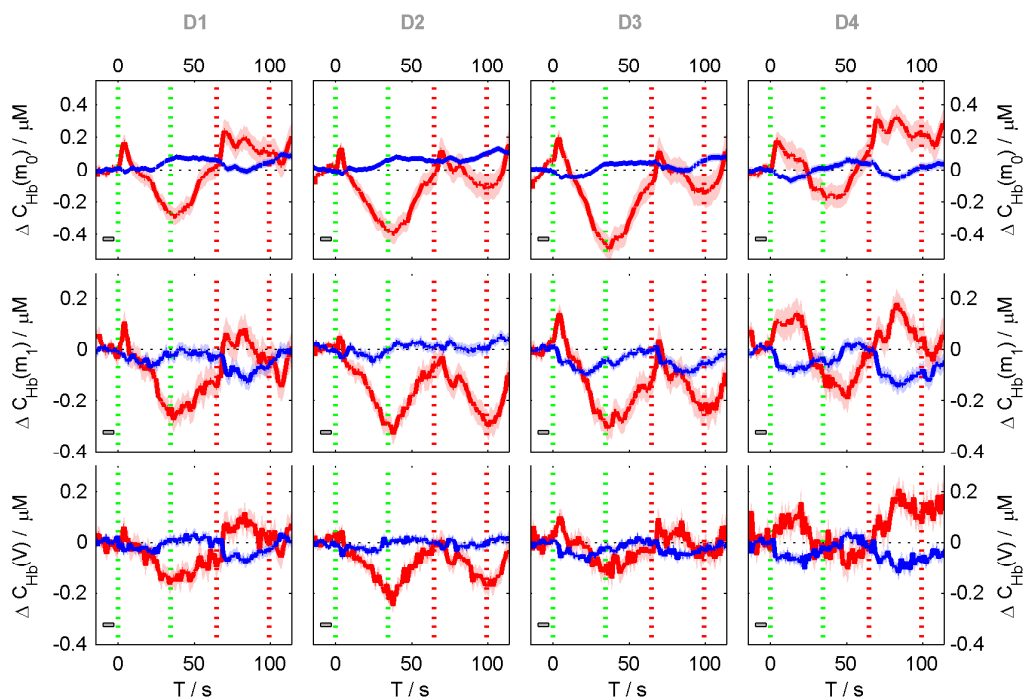


Figure 6.2: Group averaged fNIRS signals obtained on 13 subjects during the performance of a cognitive task (see task). Changes in oxy- (red) and deoxyhemoglobin (blue) are shown for the four detection channels (columns, denoted by D1 to D4) and obtained from ratios of the integral $m_0/m_{0,base}$ as well as changes in the mean time of flight Δm_1 and variance ΔV . Coloured bands represent the standard error of mean (N=117). Periods of the word-CPT and sem-CPT are enclosed by green and red vertical dashed lines, respectively. Small grey rectangles mark the baseline interval.

analysis was performed. For that ΔC_{HbO} and ΔC_{HbR} signals from all subjects were block averaged keeping the discrimination in location and moments. Procedures like this are frequently used to analyse neuroscientific data and also help to discover common effects across a collective of subjects. It should be noted that the poor SNR is also a consequence of the rather low brain activation in this experiment as confirmed by the fMRI findings discussed below.

Group-averaged concentration changes in HbO and HbR obtained from the td-fNIRS measurements are presented in Fig. 6.2. Task-evoked changes are observed in all four channels and for both haemoglobin species. However, the time courses of the signals differ strongly for the four channels, HbO and HbR. Signal changes similar to a typical cerebral activation can be seen in channel four, less clear in channel one and preferably in the HbR signal calculated from changes in V and m_1 . These findings are in a good agreement with the

6.1. Concurrent Measurement of fNIRS and Systemic Physiological Signals

localization of the activation obtained from fMRI recordings (see Fig. 6.3a). Mean concentration changes were found to be in the order of $0.2 \mu\text{mol/l}$ (HbO, homogeneous analysis). This value is smaller than the changes typically found for motor task activation which can reach several $\mu\text{mol/l}$ for HbO [135].

Signals in other channels do not show the typical shape of a cerebral haemodynamic response. The most prominent features of the HbO signals are (i) a short increase right after the stimulus onset, (ii) a subsequent steady decrease during the stimulus period and (iii) a steady increase during the rest period. This behaviour is visually very similar to the shape of a triangle. No clear baseline during the rest period and no activation plateau can be identified. Therefore it is hypothesised that these optical signals are distorted by systemic artefacts which correlate with the stimulus.

Furthermore there are visible differences in the signals obtained from attenuation changes (i.e. the m_0 based signal) and changes in the variance ΔV . The changes in HbO obtained from the attenuation clearly show the triangular shape in the first three channels and less clear in channel four. At the same time the variance signal is mainly affected by such triangular components in channels D2 and D3 only. The prominent triangular shape is present in the oxygenated haemoglobin but is not visible in HbR. It is more pronounced in the light attenuation signal compared to the signals derived from the variance. Having in mind that the depth sensitivity profile for variance peaks at a larger depth compared to the integral, this finding is an indication of a superficial origin of the triangular-shaped signal component. The HbO signals in D2 are very similar in shape for all three moments. This indicates that they are dominated by superficial absorption changes only.

None of the physiological signals shown in Fig. 6.5 matches the triangular shape exactly. The heart rate signal partially resembles the increase of ΔC_{HbO} during the resting period. Other SPP signals exhibit prominent shapes which cannot be recognised in optical signals. Therefore the triangular artefact cannot be tracked back to a single physiological source in this experiment. It is, however, possible that a combination of several systemic physiological signals might to some part explain the distorted shape of the optical signals.

The activation map obtained from the group analysis of the fMRI data is shown in Fig. 6.3a. Task-induced bilateral activation in the Brodmann area 10 (BA 10) was observed in the area covered by the optical channels D1 and D4 with stronger activation on the right side (D4). The time course of the fMRI signal averaged over the subject population and over all repetitions of the task blocks is shown in Fig. 6.3b. The amplitude of the fMRI signal changes is in the order of 0.2% to 0.4% which is much lower than what is usually obtained for motor cortex activation (about 4%). The time course of the fMRI signal in the activated area is in a good agreement with the typical haemodynamic

6. Applications of Time-Domain fNIRS in vivo

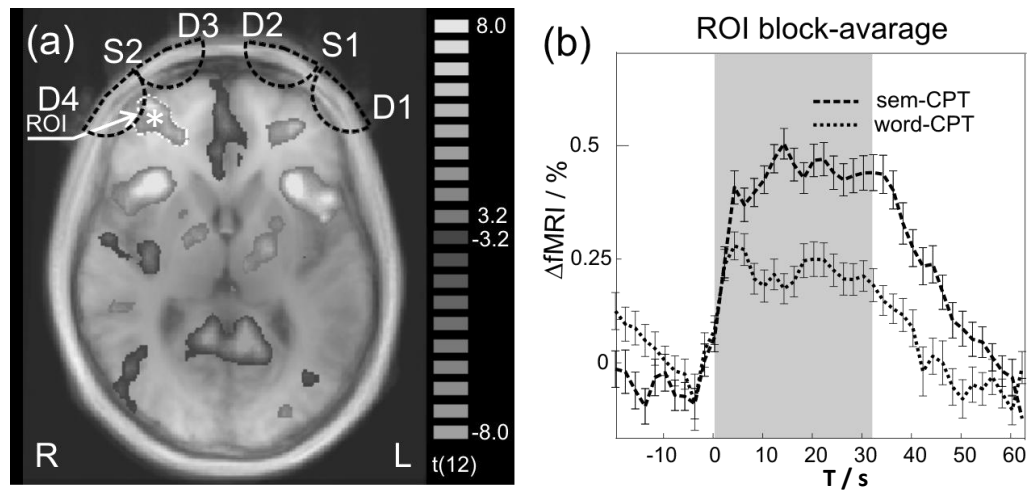


Figure 6.3: Results of the group analysis of the fMRI experiment. (a) The group averaged activation map overlaid on a group anatomical template. Positions of light sources and detectors used in fNIRS are denoted by S1, S2 and D1 to D4, respectively. The relevant activated regions in the bilateral BA 10 are indicated with a white asterisk and potentially have the largest overlap with D3 and D4. (b) The time course of the fMRI signal (BOLD) from the Region-Of-Interest (ROI) in the right BA 10 averaged over the whole subject population and all repetitions of the word-CPT and sem-CPT tasks. (Courtesy of Dr. E. Kirilina)

response to cerebral activation. Furthermore a difference between both tasks is clearly visible. In the case of fNIRS data a similar ratio of the amplitudes can be seen for the deoxyhaemoglobin changes obtained from the mean time of flight only. This confirms that fNIRS was able to localise the main activation correctly.

In our paper [103] - which is based on the results discussed above - the measurement is complemented by an additional fMRI measurement of the scalp at the forehead (also called skin fMRI) and an MRI angiography². It should be noted that during fMRI data analysis typically a so called brain mask is introduced as one of the first steps. This mask spatially restricts the analysis to the brain volume only and excludes the skull and the scalp. In general, this is advantageous because the data amount and the computational effort is reduced and due to the brain autoregulation all voxels can be analysed by the same algorithms. In the case of the skin fMRI approach the scalp area is included into the analysis but the interpretation of the BOLD signal is not the same as for the brain area (see Appendix 2 in [103] for details).

Skin fMRI signals reported in [103] showed a triangular shape very similar to the HbO traces discussed above. The subsequent MR-angiography measurement revealed that these signals were found in voxels which coincide

²These MR measurements were done by Dr. E. Kirilina (FU Berlin)

6.1. Concurrent Measurement of fNIRS and Systemic Physiological Signals

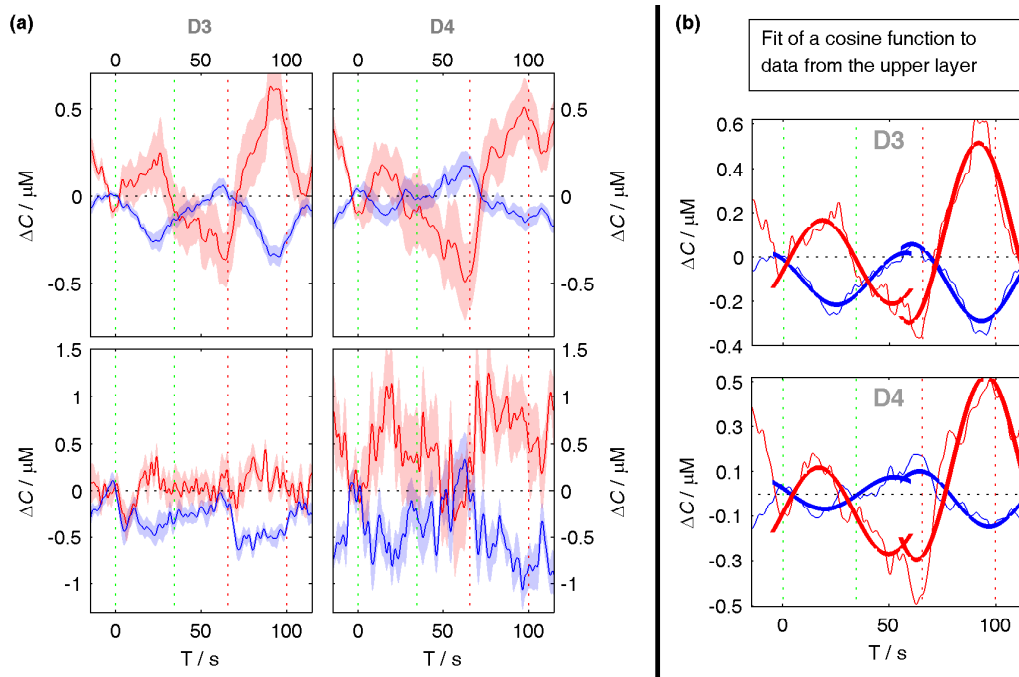


Figure 6.4: (a) Results from the two-layered separation of block averaged data of a single subject shown for two detection channels D3 and D4. Upper row: upper layer (superficial). Lower row: lower layer (cerebral). (b) Fit of the cosine function (thick lines) to data obtained for the superficial compartment (thin lines). The fit was performed piecewise individually for each task and Hb species. The period of the cosine function was fixed to 65.3s which includes the duration of a single task and the subsequent resting period. Red and blue solid lines correspond to oxy- and deoxyhaemoglobin related concentration changes, respectively. Coloured areas mark the standard error of mean ($N = 9$). Green and red dashed lines enclose the period of the word-CPT and sem-CPT tasks, respectively.

with the location of the scalp veins. All together these findings confirm the assertion that the triangular shaped artefacts are of superficial origin.

Conclusions drawn in [103] were mainly based on data from a group average analysis of fNIRS and fMRI recordings. It is, however, highly desirable to confirm or to transfer this insight to an individual level. Here, the two-layered reconstruction method introduced in Section 4.4.2 was applied to data collected on a single subject. The SNR of this selected measurement although not high was sufficient to perform an analysis on the individual block averaged data from two detection channels D3 and D4.

The results of the separation into the superficial and cerebral signals are shown in Fig. 6.4a. The deoxyhaemoglobin signal obtained for D3 shows a clear albeit low activation signal. It even exhibits a similar amplitude ratio of the word-CPT and sem-CPT task of approximately 1:2 as the BOLD

6. Applications of Time-Domain fNIRS in vivo

signals shown in Fig. 6.3b. The cerebral ΔC_{HbO} signal from the same channel shows some initial peaks followed by a rather constant plateau during the resting period. The increase during the sem-CPT period is low and does not match any typical pattern. Cerebral signals for D4 are noisy, exhibit many oscillations and do not show clear patterns.

Time courses obtained for the superficial layer show pronounced triangular shapes in both channels and both haemoglobin species. In our paper [103] a cosine function was used to construct a superficial predictor³ fitting the fMRI signal from the vein. In Fig. 6.4b a cosine function with a fixed period of 65.3 s (cf. Fig. 6.1) is fitted to the time courses of oxy- and deoxyhaemoglobin concentrations changes obtained for the superficial layer. The fit is performed individually to the data from the word-CPT and sem-CPT tasks (piecewise fit). The best fits are achieved for ΔC_{HbR} while for the ΔC_{HbO} data the fits are slightly worse. The HbO signals show a much more pronounced structure which obviously cannot be explained by a simple cosine function. Fitting each of the task individually is necessary because the signals exhibit different amplitudes. Thus a single cosine function with a single amplitude factor cannot model both task simultaneously. This demonstrates that a (single) superficial predictor constructed blindly using a cosine function and the duration of the task might not be able to fit in all cases. Thus a separation of the superficial and cerebral signals on an individual level and separately for each detection channel as performed here is advantageous.

6.1.3 Systemic Physiological Signals

For analysis of the systemic physiological data the same averaging procedure as for the fNIRS was used. The group-averaged SPP signals are shown in Fig. 6.5. Changes in the mean blood pressure (BP), heart rate (HR), respiration frequency f_{resp} and skin conductance (SC) show clear stimulation related changes. All these signals exhibit an increase after the stimulus onset, but the behaviour at later times differs. The BP has a shape very similar to a haemodynamic response to a stimulus (cf. Fig. 2.5) with a return to the baseline during the rest. The heart rate exhibits a short spike at the beginning of the stimulation followed by a slow increase. During the resting period HR is decreasing slowly. Changes of the respiration frequency f_{resp} also show clear task evoked changes which nearly resemble a boxcar function. The mean absolute respiration frequency was about 0.3 Hz resulting in rather large relative changes of up to 20 %.

³ This predictor was then used for the analysis of the optical data by a generalised linear model (GLM).

6.1. Concurrent Measurement of fNIRS and Systemic Physiological Signals

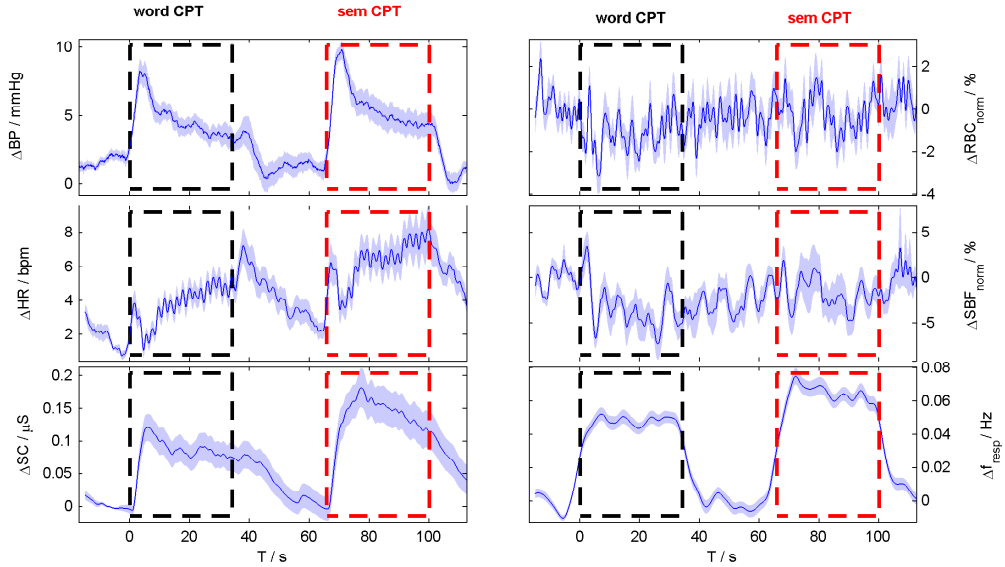


Figure 6.5: Group averaged systemic physiological signals obtained on 13 subjects during the performance of a cognitive task. Coloured bands represent the standard error. BP - mean blood pressure, HR - heart rate, SC - skin conductance, RBC - red blood cells concentration, SBF - scalp blood flow, f_{resp} - respiration frequency.

The SC signal shows clear task-evoked changes with a slow decay to baseline during rest. An increase in skin conductance can be interpreted as an increase of the activity of the autonomic nervous system which among others affects vasoconstriction⁴ in the scalp. The SC changes are larger for the sem-CPT than for the word-CPT task.

Red blood cells concentration changes (RBC) do not show a visible correlation with the task. The scalp blood flow (SBF) exhibits fast oscillation with a fast decrease at the beginning of the word-CPT task and a slow decrease which reaches a maximum change of about 5%. The task evoked changes of SBF are much less pronounced than changes in other systemic physiological signals. Recently, Takahashi et al. [132] reported task evoked changes in SBF measured on the forehead during a verbal fluency task. In contrast to the findings here, they recorded an increase in SBF. Other researches reported a decrease of facial blood flow in the case of mental stress [136]. Considering these conflicting observations and differences in the experimental design, i.e. task, placement of the probe, subject population etc., different patterns of the SBF changes seem to be possible.

⁴ Constriction and dilation of the vascular compartment also affects the amount of blood and thus the amount of haemoglobin in the scalp.

6. Applications of Time-Domain fNIRS in vivo

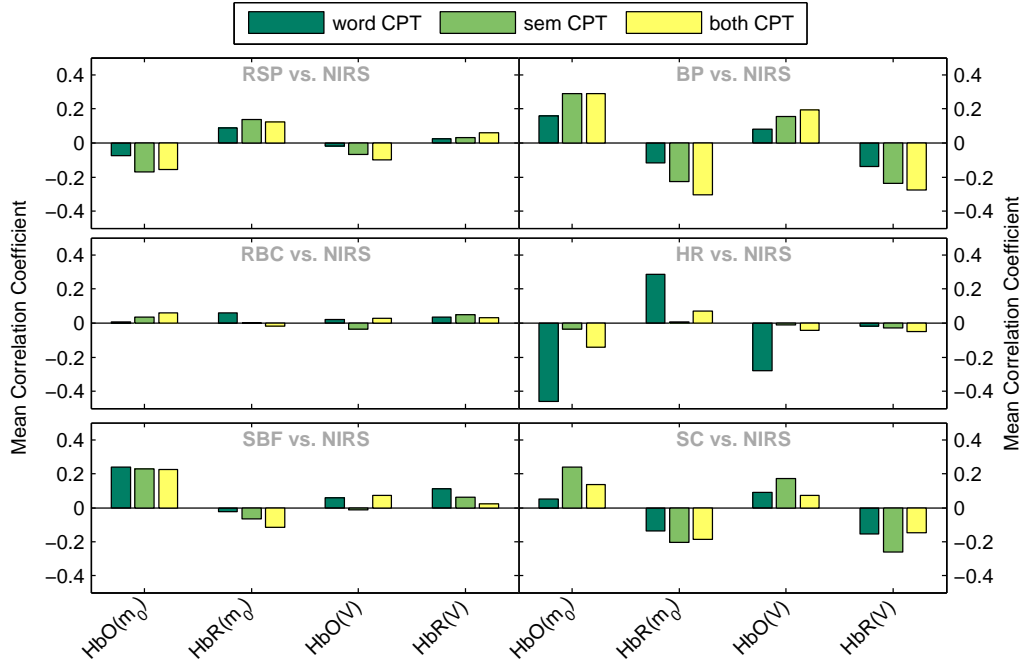


Figure 6.6: Correlation between systemic physiological signals (RSP: respiration frequency, SBF: skin blood flow, SC: skin conductance, BP: mean blood pressure, RBC: red blood cells concentration changes, HR: heart rate) and oxy- and deoxyhaemoglobin (HbO, HbR) calculated from the integral m_0 and variance V . Mean correlation coefficients over all subjects are shown for wordCPT, semCPT and both task together.

6.1.4 Correlation Between fNIRS and Systemic Physiological Signals

In order to identify the most pronounced influence of systemic physiological signals on changes in oxy- and deoxyhemoglobin, linear correlations between the acquired signals were calculated. For the quantification Pearson's r , Kendall's τ and Spearman's ρ coefficients were used. Results for the three correlations coefficients were similar. Therefore the discussion below is restricted to the Pearson's r without any constraints. The r values were obtained on the individual subject level for all haemoglobin signals (HbO and HbR from m_0 and V and using the homogeneous model analysis) and all detectors. Signals from m_0 and V were chosen to reflect potentially superficial and more cerebral processes.

The averaged values of correlation coefficients are shown in Fig. 6.6 for three different periods, i.e. during (i) word-CPT only, (ii) sem-CPT only and (iii) both CPTs together. The highest average correlation coefficients were found for the mean blood pressure and the skin conductance. In both cases the

situation is similar for all HbO and HbR signals and all tasks. The reversing sign of the r values for HbO and HbR changes is a consequence of the typical behaviour of these signals: usually, there is a decrease in HbR if HbO is increasing. The SBF signal shows remarkable correlation with the superficial light attenuation signal only and only for HbO. This can be expected because of the high superficial sensitivity of the measurement principle underlying the SBF and RBC measurement. An interesting behaviour can be observed for the heart rate. Here the absolute value of r is high only for the word-CPT task, the superficial light attenuation signal and HbO while the HbR signal from the variance is always uncorrelated. The reason for this selective behaviour remains unclear. The respiration rate shows low correlation for the superficial light attenuation signal and none for the variance signal. Indeed, only very low and slow influence of the respiration on the cerebral haemodynamic can be expected from fMRI experiments [137]. Therefore in this case correlations potentially can not be found either because of the rather high noise level or because of the rather fast task design compared to the respiration effects. The RBC signal shows no correlation at all. This, however, might also be a result of the rather high noise present in the RBC signals.

Altogether the results indicate a complex interplay of systemic physiological signals and the haemoglobin concentration changes. The highest and most stable effects come from the mean blood pressure and the skin conductance indicating sympathetic and parasympathetic influences. The heart rate exhibits a selective and task-dependent behaviour. In the future a new insight into this interplay might be gained by a GLM analysis of the optical data with predictors constructed from the systemic physiological signal.

6.2 Concurrent fNIRS and EEG

Neurovascular coupling summarises processes linking the neuronal activity and the vascular response to it. This includes a number of interconnected cellular, metabolic and vascular processes whose detailed investigation is an active field of research. Better understanding of these processes should also provide a better understanding of the neurovascular coupling in general. A more practical approach with a potential clinical application is to measure the neuronal and vascular responses independently. In particular, concurrent experimental assessment of the neuronal and vascular responses promises better understanding of the coupling processes and is required to investigate neurological disorders such as epilepsy, stroke or Alzheimer disease [138–145]. Experimentally, neuronal responses can be measured using EEG (electroencephalography) or MEG (magnetoencephalography) while haemodynamic

6. Applications of Time-Domain fNIRS in vivo

responses can be assessed by fNIRS or fMRI.

The temporal relationship between the vascular and neuronal response is still under investigation. It was measured invasively and non-invasively in animals using electrophysiological recordings and fMRI [146–148]. Non-invasive studies using dc-MEG and time-resolved fNIRS were performed on healthy adults [149–151] and on stroke patients [140]. Another study utilizing concurrent EEG and continuous wave fNIRS [152] mainly addressed the relationship between the amplitudes of the neuronal and vascular responses.

Here results of a small feasibility study employing concurrent and spatially co-registered EEG and time-domain fNIRS performed on four healthy adult volunteers is presented⁵. Two different tasks were used to achieve activation in the motor and visual cortices. The analysis focuses on the comparison of the time traces of the neuronal activation and vascular responses. A detailed description of the experimental setup is given in Section 3.3.

6.2.1 Subjects and Task

Two types of stimulation paradigms were performed by each of four adult volunteers (3 male, 1 female, aged 29, 32, 40 and 53 years). First, each subject performed a motor task (finger tapping) with the right hand. Second, a visual stimulation of the occipital cortex was achieved by 8 Hz flicker light presented to the subjects. For the motor and visual tasks the fNIRS pad holder was placed with its centre right over the C3 and O2 positions, respectively. EEG signals were acquired on the whole head but only the data from the electrode with the strongest response to the task was used for the main analysis.

For both tasks a block design was used. Each subject performed 20 blocks each consisting of 20 s of stimulation followed by 20 s of rest. A pre- and post-baseline of two minutes duration was recorded in the beginning and the end of each individual measurement. All experiments were performed in a darkened room with subjects resting in a supine position.

6.2.2 Data Analysis and Results

The optical data was analysed in terms of relative concentration changes ΔC in oxy- and deoxyhaemoglobin calculated from m_0 , m_1 and V which are measured by time-domain fNIRS. A homogeneous model was used for the calculation of the concentration changes. Time series data for each subject, spatial channel and haemoglobin species were block averaged. These averaged

⁵ This is collaborative work. All measurements were performed by Dr. Stefan P. Koch (Charité, Berlin) and the author of this thesis. Parts of the EEG analysis were done with the support by Dr. S. P. Koch

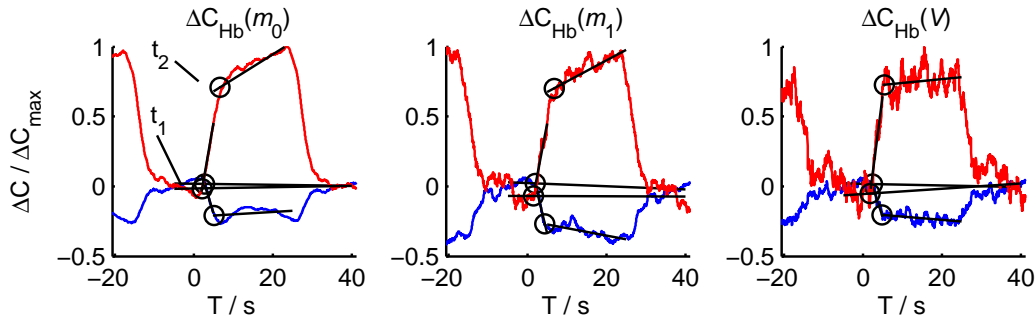


Figure 6.7: Fit of the skewed tophat function to the averaged responses to a motor task (black lines). Red and blue lines refer to changes in oxy- and deoxyhaemoglobin concentrations, respectively. The time courses are normalised to the maximum of ΔC_{HbO} . The intersection points t_1 and t_2 are labelled with black circles. The onset of the 20s long stimulation period is at $T = 0$.

signals were analysed by a piecewise linear approximation, i.e. a fit of a skewed top hat function similar to the method described in [149]. As illustrated in Fig. 6.7 the procedure returns the intersection points t_1 and t_2 which can be interpreted as the onset of the stimulation and the onset of the plateau period, respectively.

Values for t_1 and t_2 were obtained for all block averages suitable for the analysis. Some of the fNIRS block averages were excluded if no typical activation pattern was observed (essentially no changes) or the signals were obviously corrupted by superficial artefacts (similar to those shown in Fig. 6.2). The variance signal was more often suitable for the skewed top hat analysis than the m_0 signal (in approximately 15 % more cases) and had a more often a top hat like shape. This observation can be explained by the higher depth sensitivity of the variance signal which more reliably reflects the cerebral activation.

Neuronal signals were derived from EEG electrodes exhibiting the strongest activation, i.e. the C3 and O2 locations for the motor and visual tasks, respectively. As shown in Fig. 6.8a differences in the spectra during the rest and activation periods reveal active spectral bands. Those were different for the motor (α band: 8 Hz to 14 Hz, β bands: 14 Hz to 30 Hz) and visual (main activity around 8 Hz accompanied by higher harmonics [153]) tasks.

A time-frequency (TF) analysis was applied to the time series EEG data employing the Morlet wavelet method⁶ [154]. The time-frequency data was

⁶ For the time-frequency analysis the function `traces2TFA` from the `4DToolbox` implemented in Matlab by Ole Jensen (Helsinki University of Technology, Finland) and optimised by Dr. S. P. Koch (Charité, Berlin) was used.

6. Applications of Time-Domain fNIRS in vivo

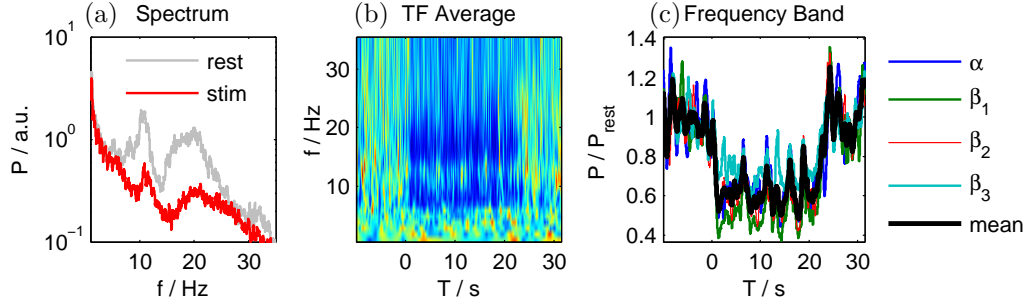


Figure 6.8: Data obtained from EEG signals recorded during the performance of a motor task by a single subject. (a) Averaged spectra of the EEG signals obtained during the rest and stimulation periods. (b) Block averaged time-frequency (TF) representation of the EEG signal. (c) Averaged time traces from the α and β bands as well as its mean trace. The onset of the 20 s long stimulation period is at $T = 0$.

Table 6.1: Results of the skewed top hat fit to the neuronal (EEG) and vascular (ΔC_{HbO} and ΔC_{HbR}) responses to a motor task. All values are reported as (mean \pm SD) and the number of samples used for averaging in brackets. Data for comparison from Ref. [149] is only available for the t_1 values.

	t_1 / s		t_2 / s
	this study	Ref. [149]	this study
dc-MEG		-1.6 ± 0.7 (7)	
EEG	0.06 ± 0.09 (3)		1.26 ± 0.16 (3)
ΔC_{HbO}	0.9 ± 1.1 (34)	-0.7 ± 2.4 (6)	6.1 ± 1.0 (34)
ΔC_{HbR}	1.7 ± 0.9 (34)	-0.8 ± 0.3 (5)	5.9 ± 0.9 (34)

block averaged to obtain the TF-block averaged representation shown in Fig. 6.8b. Finally, the active frequency bands were isolated and averaged over time resulting in time traces of the neuronal response shown in Fig. 6.8c. In general, an increase of the power in the corresponding bands was found for the visual stimulation and a decrease for the motor task. Both observations are in agreement with literature [153, 155]. The shape of these signals can be directly compared with block averaged fNIRS data, i.e. Fig. 6.7 with Fig. 6.8c. The EEG time traces were analysed by the skewed top hat fit procedure in the same way as the fNIRS block averages.

Results obtained for the motor task are summarised in Table 6.1 in terms of the mean values for the estimated stimulus onset t_1 and the approximate onset of the plateau period t_2 . Data obtained for the visual task was excluded because of the low number of evaluable block averages of the optical data, only few successful fits and for better comparability with data from [149] where a similar motor task was used.

The neuronal signal exhibits a nearly instant onset and includes the moment of the stimulus presentation to the subject. A delay of the vascular response compared to the neuronal one can be observed. The onset is slightly different for ΔC_{HbO} and ΔC_{HbR} but all values overlap within one standard deviation. The plateau level is reached approximately five seconds after the neuronal response and is nearly the same for ΔC_{HbO} and ΔC_{HbR} . These observations appear to be more reasonable than the finding by Sander et al. [149] where negative values for the onset of the stimulation were reported (cf. Table 6.1). The authors explain this behaviour by a reduced time resolution⁷ of 2.5 s and artefacts of the skewed top hat model. In contrast, the combined EEG-fNIRS approach used here demonstrates that more accurate measurements are possible.

In conclusion, the feasibility of the concurrent time-domain fNIRS and EEG assembly for studies of the neurovascular coupling was demonstrated. Unlike fMRI, MEG and combinations with these techniques the EEG-fNIRS approach is applicable at the bedside. It is well suitable for continuous long time monitoring which can be a key feature for clinical research and applications. Future research should focus on subjects' responses to different tasks and on the relationship of amplitudes. This and the analysis of the temporal relationship between neuronal and vascular signals could potentially reveal distortions in the pathological case.

6.3 Concurrent td-fNIRS and fMRI

Functional MRI and functional NIRS are two techniques which are widely used in neuroscientific and clinical research to measure vascular responses to neuronal activity. Both techniques measure signals which depend on the haemoglobin content in the tissue but they are based on completely different physical principles. This leads to differences in depth sensitivity, spatial resolution and assessed quantities as already discussed in Section 2.1.4. Briefly, fMRI exploits paramagnetic properties of deoxyhaemoglobin and measures the so called blood oxygen depended signal (BOLD). It mainly reflects changes in the deoxyhaemoglobin concentration but also depends on the environmental baseline parameters and other processes [34]. Functional MRI features superior depth sensitivity and spatial resolution. However, the quantification in terms of absolute concentration changes is difficult and MR-devices are stationary and expensive. In opposite to that fNIRS devices can be stationary

⁷ The actual sampling rate of the MEG unit was 250 Hz. However, the time resolution is determined by the modulation frequency of the bed movement which was 0.4 Hz.

or mobile and feature better quantification of haemoglobin concentrations but with lower spatial resolution and depth sensitivity.

A combination of both methods is promising. On the one hand, fNIRS can benefit from the comprehensive spatial and anatomical information provided by MRI. On the other, fMRI's BOLD signal can potentially be calibrated using the quantification from fNIRS. The calibration would allow to transform the relative BOLD signal to absolute changes of deoxyhaemoglobin concentration. This is in particular important for reliable comparison across different subjects. Here results of concurrent fMRI and time-domain fNIRS measurements obtained from individual subjects during a motor task are presented⁸. A Monte-Carlo (MC) forward model for light propagation and a two-layered reconstruction method combined with MR anatomical data are used to derive changes in haemoglobin concentration. These are compared to relative changes of the measured BOLD signal.

6.3.1 Subjects and Task

A group of adult subjects (4 male, 2 female, mean age 38.5 y) executed a finger tapping task with their right hand. Each individual experiment consisted of 20 repetitions of a 30 s long task followed by a 30 s long rest period. After this functional part an anatomical scan of the head was performed. During the whole experiment subjects were resting in supine position inside the MR tomograph. The start signal was presented on a screen outside the scanner. Mirrors attached to the head coil gave subjects a limited view on the screen. A detailed description of the experimental setup is given in Section 3.4.

6.3.2 Data Analysis and Results

For the complete data analysis only two of six subjects were selected (1 male, 1 female). These subjects exhibited clearly visible brain activation as obtained by the analysis employing the homogeneous fNIRS model (Section 4.3.1) and negligible movement artefacts. Among the whole collective a rather large number of detection channels were corrupted due to the difficult experimental conditions and thus not available for the evaluation. The results presented below should therefore be considered as a proof of concept of concurrent fMRI and td-fNIRS.

The workflow used to combine information obtained by functional and structural (anatomical) MRI as well as fNIRS is shown in Fig. 6.9a. The

⁸ This is collaborative work. All measurements were performed by Dr. E. Kirilina (FU Berlin) and the author of this thesis. Further, Dr. E. Kirilina segmented the anatomical MR data, modified the Monte-Carlo code and ran the simulation.

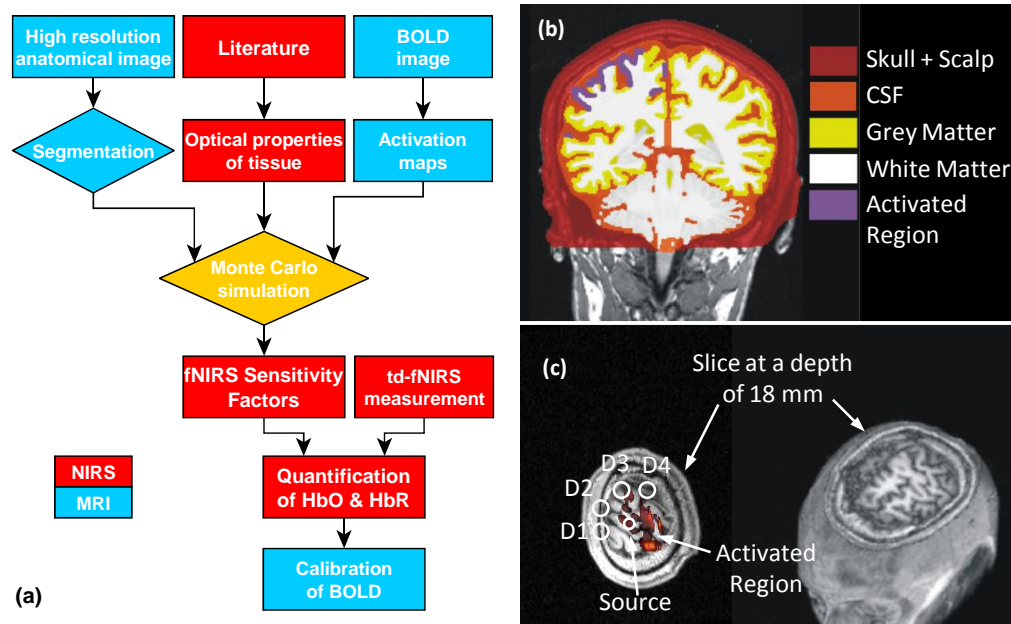


Figure 6.9: (a) Workflow for the combined fMRI-fNIRS analysis employing a Monte-Carlo simulation. (b) Cross section of the segmented anatomical MR image of a subject. (c) Cross section of a 3D rendering of the subject's head. The activated brain region as revealed by fMRI is labelled in red. The projected positions of detection fibre bundles (D1-D4) and the light source are denoted by white circles. Figures (b-c) are courtesy of Dr. E. Kirilina.

anatomical MR image was automatically segmented using the *Freesurfer* software freely available online⁹. The resulting head model was then used for a forward calculation of light propagation by means of a Monte-Carlo simulation [156]. The source code of the original software is freely available online¹⁰. The MC code is capable of simulating time-resolved light propagation in 3D turbid media constructed from voxels which can have individual - and therefore spatially varying - optical properties. This MC code was modified in order to register the time of flight of photons through the different tissue types and in particular through the activated brain region.

The head model contained five tissue types, i.e. skull with scalp, cerebrospinal fluid (CSF), grey and white matter and the activated brain regions obtained from the fMRI data. A cross section of the segmented head model is shown in Fig. 6.9b. Tissue optical properties were taken from [157]. Optical properties of the activated region were the same as for the grey matter. By the means of MC simulation it was possible to calculate sensitivity factors

⁹<http://surfer.nmr.mgh.harvard.edu>

¹⁰<https://orbit.nmr.mgh.harvard.edu/wiki/index.cgi?Home>

6. Applications of Time-Domain fNIRS in vivo

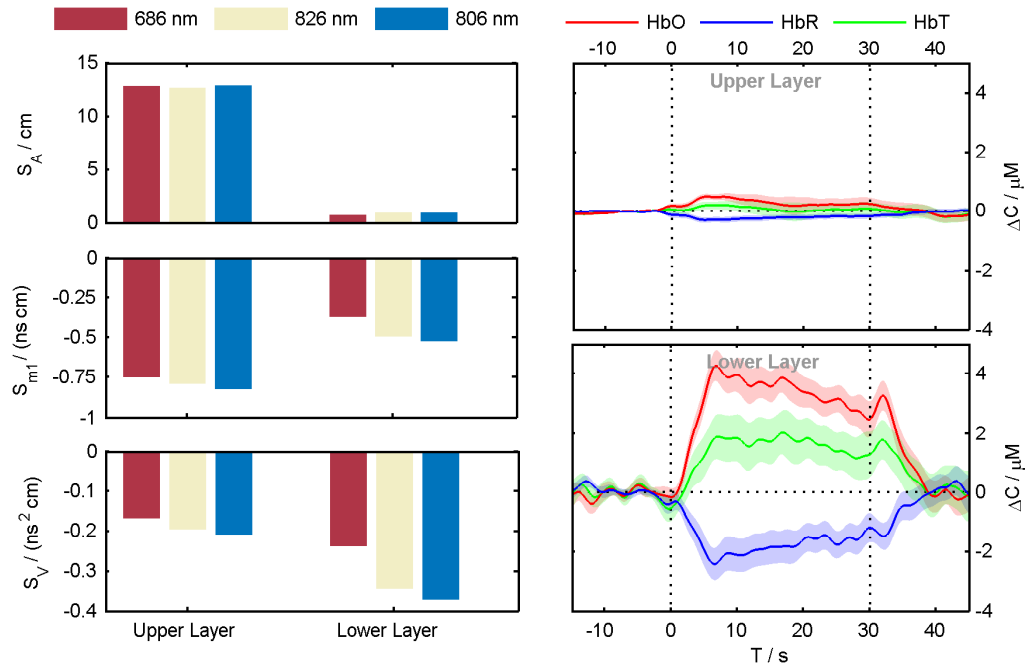


Figure 6.10: Changes in oxy- and deoxyhemoglobin derived using the layered model from data of a single subject and detection position. Left: individual sensitivity factors for the three moments and three wavelengths used in the analysis. Right: courses of haemoglobin concentration changes in the upper and lower layers. HbO, HbR and HbT denote oxy-, deoxy- and total haemoglobin, respectively. Coloured bands represent (± 1 SE) calculated from 20 repetitions of the task. Vertical dashed lines mark the period of the task execution.

(cf. [94]) for changes of moments measured by td-fNIRS using a real geometry. Note that sensitivity factors obtained in this way, in principle, correctly account for the partial volume effect which is a central challenge in spatial localisation and reliable quantification of fNIRS signals. Compared to an analysis by a homogeneous or a layered model the employment of a MC simulation is much more complicated, computationally expensive and requires more assumptions to be made (optical properties of tissue, accuracy of the segmentation procedure, etc.).

In addition to the analysis based on the MC simulation, a layered model reconstruction introduced in Section 4.4.2 was applied to the fNIRS data. Individual scalp thickness and depth of the cortex were extracted from anatomical MRI scans. Corresponding sensitivity factors were calculated for a layered geometry. Activated regions as revealed by fMRI were not considered.

An example of the layered analysis of fNIRS data as obtained from a single subject and a single detection channel is shown in Fig. 6.10. Sensitivity factors

Table 6.2: Mean amplitudes of signals reflecting brain activation obtained from optical data using the Monte-Carlo simulation based method and the layered analysis in comparison to the relative changes of the fMRI BOLD signal for two subjects.

	Monte-Carlo		Layered Analysis		MRI
	$\Delta C / (\mu\text{mol/l})$		$\Delta C / (\mu\text{mol/l})$		BOLD / %
	HbR	HbO	HbR	HbO	
Subj. 1	(-4 ± 3)	(8 ± 4)	(-1.7 ± 0.3)	(3.4 ± 0.5)	3.2
Subj. 2	(-2 ± 1)	(3 ± 2)	(-2.3 ± 0.8)	(6.7 ± 1.2)	4

(SF) for layered changes in attenuation, mean time of flight and variance derived for this specific detection channel, subject and the three wavelengths involved in the experiment exhibit an expected behaviour. All sensitivity factors show a rather weak wavelength dependence and an increasing depth selectivity with increasing order of the moments. Note that mean time of flight m_1 and variance V signals also have a non-negligible sensitivity to absorption changes in the upper layer. However, in total, both moments exhibit a considerably higher depth selectivity than the attenuation signal. Block averages of the derived changes in the haemoglobin concentration in the upper and lower layers revealed by the layered analysis are shown on the right side of Fig. 6.10. Changes in the lower layer exhibit an increase in ΔC_{HbO} and a decrease in ΔC_{HbR} with a smaller amplitude which is a typical brain activation pattern. Haemoglobin concentration changes derived for the upper layer are very low. In this example there are no superficial artefacts comparable to those found on the forehead (Section 6.1).

A comparison of signal amplitudes obtained using the Monte-Carlo simulation method, layered analysis and fMRI is given in Table 6.2. The values were obtained as the average value around the maximum of the activation, i.e. within a period of about 20 s. For the first subject haemoglobin concentration changes obtained from the layered analysis are roughly a factor of two smaller than those from the MC analysis. This might result from the residual partial volume effect which is still present in the layered model. The volume of the layer can potentially be larger than the actual activation region. Since the MC method is based on voxels it can take this into account in contrast to the layered reconstruction method.

For the second subject the results are less consistent. The amplitudes of the ΔC_{HbR} exhibit a very good agreement but differ for ΔC_{HbO} by a factor of two. The reason for that remains unclear. Potential inaccuracies might arise from a mismatch between the real optical properties of tissue and values taken from literature for the MC method. Further, it should be noted that

6. Applications of Time-Domain fNIRS in vivo

while the spatial resolution of the anatomical MRI scan is sufficient, the analysis based on the MC simulation method can suffer from the reduced spatial resolution of the functional MRI scan. Its voxel size of $3 \times 3 \times 4 \text{ mm}^3$ can potentially cause systematic distortions for voxels located on the border of NIRS sensitivity regions and exhibiting different levels of activation. This would cause the simulation of light propagation to produce optical signal changes in regions which are not activated in reality.

The comparison of the relative changes of the BOLD signal with ΔC_{HbR} derived by the layered reconstruction gives rather consistent results¹¹. The ratio ρ of HbR concentration changes and BOLD signal (expressed in %) is

$$\rho = \frac{\Delta C_{\text{HbR}}}{\text{BOLD}} \quad \left[\frac{\mu\text{mol}}{1} \frac{1}{\%} \right] \quad (6.1)$$

is approximately $0.53 \mu\text{mol}/(1\%)$ and $0.58 \mu\text{mol}/(1\%)$ for subject 1 and 2, respectively. The two values are rather similar. In general, however, scattering of ρ must be expected from the theory of the BOLD signal.

In a recently published study Yücel et al. [158] employed concurrent fMRI and cw-fNIRS together with arterial spin labelling (ASL) and a sophisticated data fusion model. For the four subjects measured the authors reported ratios¹² of 0.72, 4.6, 0.31 and 1.4 (all values in $\mu\text{mol}/(1\%)$). Here the first value seems to be the most realistic¹³ one while the others vary strongly. This comparison demonstrates that the BOLD calibration is a potentially difficult task which is even more hampered by the individual variability.

In conclusion, successful concurrent fMRI and time-domain fNIRS measurements together with a sophisticated data analysis were presented. The performed analysis employed complementary information from both modalities. Both techniques can benefit from this combination. The spatial information provided by functional and anatomical MRI is valuable for fNIRS and can be considered for each individual subject. This can be used for the validation of models of light propagation in tissue and for improved quantification of haemoglobin concentration changes. In fMRI the calibration of the BOLD signal can benefit from the quantification of haemoglobin concentration changes by fNIRS. In principle, a fNIRS device equipped with few channels only can be sufficient for this task if the measurement parameters

¹¹The ratios scatter much more if ΔC_{HbR} derived by the MC method are used.

¹² Using an oxygen saturation of $S_{\text{O}_2} = 70\%$ and values for M and C_{HbT} from Table 1 in [158] the ratios are calculated as: $\Delta C_{\text{HbR}}/(\text{BOLD in } \%) = C_{\text{HbT}}(1 - S_{\text{O}_2})/M/100$.

¹³ For this one subject Yücel et al. [158] reported a realistic concentration of the total haemoglobin of $70 \mu\text{mol}/\text{l}$. For the remaining subjects the values were outside the physiologically reasonable range (which is $60 \mu\text{mol}/\text{l}$ to $100 \mu\text{mol}/\text{l}$) and therefore a considerable bias can be expected.

are optimised and software routines are adapted and automated. Compared to the total costs of a commercial MRI scanner such an optical device can be treated as a rather low-cost accessory.

6.4 Summary

In this chapter *in vivo* applications of time-domain fNIRS were demonstrated. The focus lied on combined measurements with other modalities including concurrent recording of systemic physiological signals, EEG and fMRI. These multi-modal approaches pursue two objectives: *in vivo* validation of fNIRS principles and models and expansion of fNIRS applications. The validation is important for the stand-alone as well as the combined operation of fNIRS.

Section 6.1 addressed superficial influences on fNIRS signals by systemic physiological processes (SPP). It was found that several SPP are correlated with distortions present in time traces of haemoglobin concentration changes. To some amount these distortions originate from the vasoconstriction of the scalp veins. For one subject the separation of the cerebral and superficial components using the two-layered reconstruction method was demonstrated. This is promising but at the moment still needs auxiliary data from MRI. In general, the rather low signal change related to the brain activation in the frontal lobe turned out to be difficult to measure but still detectable by time-domain fNIRS.

Assessment of neurovascular coupling by the concurrent td-fNIRS and EEG was demonstrated in Section 6.2 using a motor and a visual task. This neuroscientific approach is promising for the investigation of neurological disorders such as stroke, Alzheimer disease and epilepsy. Due to the mobility and compatibility both techniques are potentially applicable in clinics for diagnostic purposes.

The combination of fNIRS and fMRI for concurrent measurements discussed in Section 6.3 is beneficial for both modalities. Rich spatial information available from the MRI helps to account for the partial volume effect and thereby to validate and improve the quantification in fNIRS. The separation of oxy- and deoxyhaemoglobin concentration changes provided by fNIRS can help to calibrate the BOLD signal which, on the other hand, improves the quantification in fMRI.

Combined applications of fNIRS with different techniques benefit from the complementary information provided by every individual modality. This expands the existing fields of application for fNIRS in the neuro-scientific and potentially in the clinical research. The unique property of fNIRS in this context is its mobility and its compatibility not only with EEG and MRI

6. Applications of Time-Domain fNIRS in vivo

but also with MEG and PET. Potentially, this could establish fNIRS as a connector of these modalities.

Summary

This work focused on the improvement of the quantification of haemoglobin concentration changes derived by time-domain functional NIRS. In particular, two methods based on a homogeneous and layered structure of the semi-infinite scattering media (SIM) have been developed which both exhibit different advantages. These methods were validated on a phantom and applied to *in vivo* data.

The key task in fNIRS is to convert the experimentally obtained changes in optical measurands to changes in the absorption coefficient. This was addressed by two methods based on the analysis of moments of DTOFs measured in time-domain NIRS. The approach based on the homogeneous SIM exploits solely the values of moments and their changes. The advantage is that no supplementary information provided by additional measurements or other modalities is needed. The major drawback of the approach is the poor depth separation and the notorious underestimation of haemoglobin concentration changes (partial volume effect). The method benefits from the intrinsic depth selectivity of moments with the highest one provided by the variance of DTOFs. In contrast, the method based on the two-layered geometry of the SIM combines the changes in the attenuation, the mean time of flight and the variance in one procedure and thereby provides changes of the absorption coefficient in two layers. This highly desired feature allows to separate cerebral and superficial haemodynamics. The approach based on layers employs precalculated sensitivity factors obtained from a forward simulation of light propagation in a layered turbid medium. Individual background optical properties calculated from the moments m_1 and V of DTOFs are used to adapt the sensitivity factors to the actual measurement, wavelength and spatial position. The method requires the thickness of the scalp and the distance to the brain to be known. These values can be obtained from individual anatomical

7. Summary

MR images or, as an approximation, from mean values of an adequate group of subjects. Values of moments needed for both analysis methods and measured *in vivo* exhibit a moderate to large inter-subject and spatial variability. Therefore an individual adjustment during the reconstruction is beneficial.

The calculation of the sensitivity factors required for the reconstruction of absorption changes relies on the absolute values of moments. However, due to the finite integration range and the influence of the IRF these values exhibit an inherent systematic inaccuracy. An investigation of this issue revealed a dramatic impact of the IRF producing large systematic deviations. An algorithm was developed to compensate for this and thereby to improve the accuracy of the moments obtained for the semi-infinite and similar geometries. For validation a two-layered geometry with heterogeneous optical properties was used. Using this approach the mean time of flight can be calculated with a precision of few picoseconds and even centred moments of the third order $m_{3,C}$ with a deviation of less than 10 %.

Optical properties (OP) of the head were obtained *in vivo* using models of homogeneous and heterogeneous SIM and employing moments of DTOFs. In the heterogeneous case a reconstruction based on the finite-element method was applied. Reliable *in vivo* determination of the OP of the head tissue was found to remain challenging with the largest difficulty being the validation of the obtained results. The approximation of the heterogeneous structure of the head by a homogeneous SIM is much easier to use and works without additional measurement. Given the difficulties with the heterogeneous OP the use of the model of the homogeneous SIM remains the most reasonable choice from the practical point of view.

The reconstruction methods based on the models of homogeneous and layered SIM were validated experimentally on a two-layered phantom. Absorption changes $\Delta\mu_a$ retrieved by using the model of the homogeneous SIM are in general underestimated. The depth selectivity of higher order moments has a beneficial effect on the retrieved values which, however, still reflect only a fraction of the true $\Delta\mu_a$. In contrast, using the approach based on the layered geometry absorption changes in both layers were separated successfully with a good accuracy of $\pm 10\%$.

The data obtained on the two-layered phantom was also used to experimentally validate the solution to the light propagation in a scattering layered medium [117] in terms of moments. The positive results of the validation suggest that many questions related to the layered geometry can be answered using this relatively fast solution and thereby avoiding time consuming phantom experiments. In the same measurement it was demonstrated that very small absorption changes of about $\Delta\mu_a \approx 0.005 \text{ cm}^{-1}$ can be realised experimentally in a liquid phantom with a good accuracy and even smaller steps

appear feasible.

In this thesis the focus of the *in vivo* application of time-domain fNIRS was on combined measurements with MRI, EEG and recoding of systemic physiological processes (SPP). These multi-modal approaches pursue the validation of fNIRS principles *in vivo* and the expansion of fNIRS applications. The concurrent measurement of fNIRS and SPP signals during a cognitive task showed correlations of the derived haemoglobin concentration changes with blood pressure, heart rate and skin conductance. Additional measurements employing the skin-MRI technique revealed the source of distortions present in the fNIRS signals to be the vasoconstriction in the scalp veins. These non-cerebral signals strongly correlate with the mental task and can mask the actual brain activity. It was shown that the superficial and the cerebral contributions can be separated successfully using the reconstruction method based on the layered SIM geometry developed in this thesis.

The combination of EEG with fNIRS allows to study the mechanisms of the neuro-vascular coupling. Here the experimental realisation of recording of neuronal and vascular responses by concurrent time-domain fNIRS and EEG measurements has been demonstrated. Time courses of the brain related signals obtained by both modalities have been compared in terms of the retrieved activation onset and saturation (plateau onset). The data obtained here contained less artefacts compared to a former study employing MEG instead of EEG [149]. This combined approach is a tool which potentially can provide more insight into neurological disorders such as stroke, Alzheimer disease and epilepsy.

Concurrent fNIRS-fMRI measurements are beneficial for both modalities. Rich spatial information available from the MRI was used to account for the partial volume which leads to underestimated haemoglobin concentration changes in fNIRS. The reconstruction method for absorption changes based on the two-layered geometry benefits from the anatomical information obtained by MRI. The separation of oxy- and deoxyhaemoglobin concentration changes provided by fNIRS can be used to calibrate the BOLD signal which improves the quantification in fMRI which is in particular important for inter-subject comparison.

The combination of fNIRS with other modalities allows to collect complementary information about the physiological processes under investigation. This expands the existing fields of application for fNIRS in the neuro-scientific and potentially in the clinical research. Unique features of fNIRS in this context are its mobility and compatibility not only with EEG and MRI but also with MEG and PET. This could establish fNIRS as a connector of the modalities.

7. Summary

Supplementary Materials

A.1 Moments of Homogeneous SIM

Below analytical expressions for centred and non-centred moments up to the 4-th order are given. All expression were obtained by accomplishing analytical integration of Eqs. (4.4) and (4.5) with $\hat{N}(t)$ set proportional to the time-resolved reflectance of the homogeneous semi-infinite medium given in Eq. (2.31). All moments can be calculated from the optical properties describing the homogeneous SIM ($\mu'_s, \mu_a, c_m = c_0/n$) and the source-detector separation r_{sd} . The calculations were performed using the symbolic toolbox of Matlab. To perform the integration in Matlab the variables $\mu'_s, \mu_a, c_m, r_{sd}$ and the time t were assumed to be real and positive.

Analytical expressions for moments of order 1 to 4 are given below; m_1 is the mean time of flight.

$$m_1 = \frac{\sqrt{\mu_a} r_{sd}^2}{2\sqrt{D} c_m \alpha} \quad (\text{A.1})$$

$$m_2 = \frac{r_{sd}^3}{4D c_m^2 \alpha} \quad (\text{A.2})$$

$$m_3 = \frac{(D + r_{sd}\sqrt{D\mu_a}) r_{sd}^3}{8\mu_a D^2 c_m^3 \alpha} \quad (\text{A.3})$$

$$m_4 = \frac{(3D + 3r_{sd}\sqrt{D\mu_a} + r_{sd}^2\mu_a) r_{sd}^3}{16\mu_a^2 D^2 c_m^4 \alpha} \quad (\text{A.4})$$

Analytical expressions for centred moments of order 2 to 4 are given below.

A. Supplementary Materials

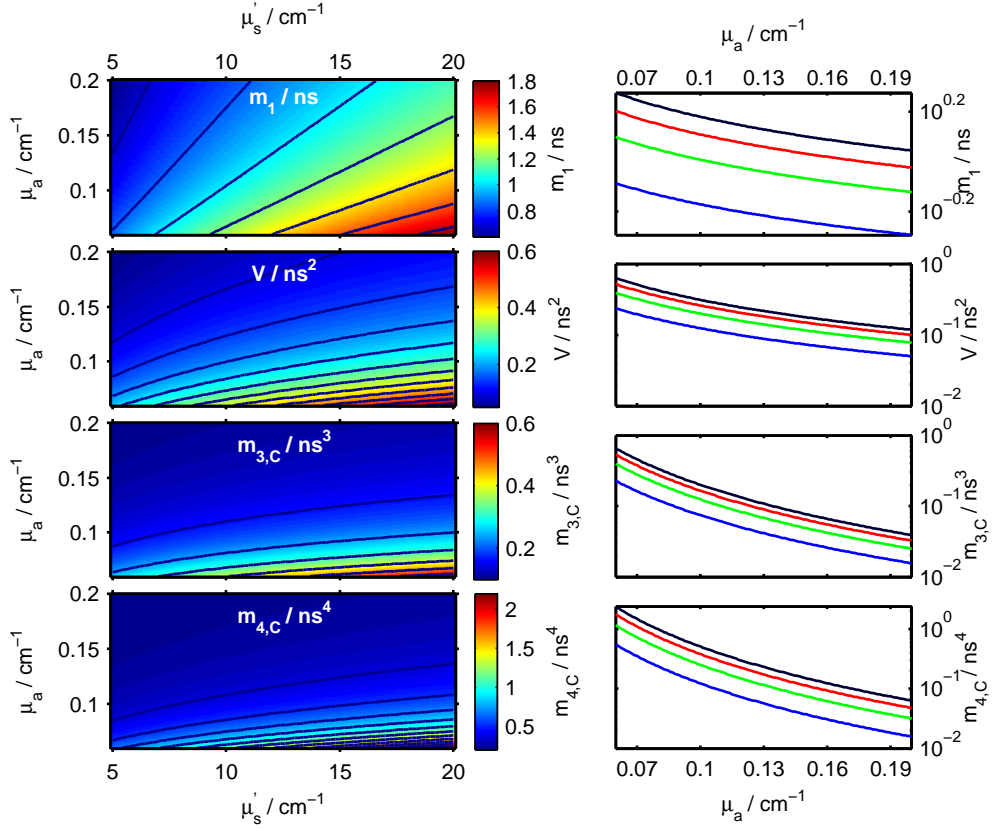


Figure A.1: Examples for values of moments m_1 , V , $m_{3,C}$ and $m_{4,C}$ as a function of μ_a and μ'_s . Left column: colour maps for various μ'_s combinations of μ_a and μ'_s . Right column: moments as a function of μ_a for selected values of μ'_s (blue, red, green and black lines for 5 cm^{-1} , 10 cm^{-1} , 15 cm^{-1} and 20 cm^{-1} , respectively).

$m_{1,C}$ is zero by definition; $m_{2,C} = V$ is the variance.

$$m_{2,C} = V = \frac{r_{\text{sd}}^3 \sqrt{\mu_a}}{4c_m^2 \sqrt{D} \alpha^2} \quad (\text{A.5})$$

$$m_{3,C} = \frac{r_{\text{sd}}^3 (3r_{\text{sd}} \sqrt{\mu_a} + \sqrt{D})}{8c_m^3 \sqrt{D} \alpha^3} \quad (\text{A.6})$$

$$m_{4,C} = \frac{3r_{\text{sd}}^3 (D^{3/2} \mu_a^2 r_{\text{sd}}^3 + 5D^2 \mu_a^{3/2} r_{\text{sd}}^2 + 4D^{5/2} \mu_a r_{\text{sd}} + D^3 \sqrt{\mu_a})}{16c_m^4 D^{5/2} \mu_a \alpha^4} \quad (\text{A.7})$$

In all equations above α is

$$\alpha = \mu_a r_{\text{sd}} + \sqrt{\mu_a D}$$

A.2. Uncertainty of Moments Due to Photon Noise

and D is the diffusion coefficient:

$$D = [3(\mu'_s + \mu_a)]^{-1} \approx 1/(3\mu'_s)$$

The approximation on the right side holds true for strongly scattering media where $\mu'_s \gg \mu_a$.

Examples for values of moments m_1 , V , $m_{3,C}$ and $m_{4,C}$ in the μ_a range 0.06 cm^{-1} to 0.2 cm^{-1} and μ'_s range 5 cm^{-1} to 20 cm^{-1} ($n = 1.4$, $r_{\text{sd}} = 3 \text{ cm}$) are shown in Fig. A.1. In general, all moments decrease with larger absorption and increase with larger scattering. The functions are monotonous and non-linear.

A.2 Uncertainty of Moments Due to Photon Noise

One of the advantages of moments is that their photon noise can be calculated analytically. Below general expressions for the photon noise of non-centred and centred moments of order n are given. To derive these expression it is more comfortable to start with an alternative formulation of the definition of moments (cf. Eq. (4.14)):

$$m_n = \frac{\sum_i t_i^n N_i}{\sum_i N_i} = \frac{1}{N_T} \sum_i t_i^n N_i \quad (\text{A.8})$$

where t_i denotes the time of the i -th channel of the DTOF and N_i is the photon count in the corresponding time channel. In practice i runs over a number of contiguous time channels selected for the calculation. In Eq. (A.8) the normalisation of the DTOF to the total photon count N_T

$$N_T = m_0 = \sum_i N_i \quad (\text{A.9})$$

is explicitly included in the equation. The uncertainty of the photon count N_i in terms of the standard deviation σ results from the Poisson statistics:

$$\sigma(N_i) = \sqrt{N_i} \Rightarrow \sigma^2(N_i) = N_i \quad (\text{A.10})$$

In order to calculate the photon noise of N_T the Gaussian error propagation with respect to the photon noise of the photon counts N_i must be calculated. It

A. Supplementary Materials

can be assumed that the N_i in different channel are statistically independent. The corresponding uncertainty is then calculated as:

$$\sigma^2(N_T) = \sum_j \left(\frac{\partial N_T}{\partial N_j} \right)^2 \sigma^2(N_j) = \sum_j (\sqrt{N_j})^2 = \sum_j N_j = N_T \quad (\text{A.11})$$

$$\Rightarrow \sigma(N_T) = \sqrt{N_T} \quad (\text{A.12})$$

Here j runs over the photon counts N_j in all channels involved in the calculation of N_T in Eq. (A.9).

The photon noise of the attenuation change ΔA (cf. Eq. (2.21)) is of particular interest in fNIRS:

$$\Delta A(\lambda) = A_2 - A_1 = -\ln \left(\frac{N_{T,2}}{N_{T,1}} \right) \quad (\text{A.13})$$

calculated from two states of the medium represented by $N_{T,2}$ and $N_{T,1}$. The corresponding uncertainty $\sigma^2(\Delta A)$ is:

$$\sigma^2(\Delta A) = \sum_{l=1}^2 \left(\frac{\partial \Delta A}{\partial N_{T,l}} \right)^2 \sigma^2(N_{T,l}) = \sum_{l=1}^2 \frac{1}{N_{T,l}^2} \sigma^2(N_{T,l}) = \frac{1}{N_{T,1}} + \frac{1}{N_{T,2}} \quad (\text{A.14})$$

In the last step Eq. (A.11) was used. If the absorption changes are small, as it is frequently the case in fNIRS, the corresponding total photon counts are similar, e.g. $N_{T,1} \approx N_{T,2} =: N_T$. Thus Eq. (A.14) can be approximated as:

$$\sigma^2(\Delta A) \approx \frac{2}{N_T} \quad (\text{A.15})$$

The photon noise of non-centred moments is calculated taking into account fluctuation of the photon counts N_i only. For this the derivative of Eq. (A.8) with respect to N_j is needed:

$$\frac{\partial m_n}{\partial N_j} = \frac{t_j^n \sum_i N_i - \sum_i t_i^n N_i}{\left(\sum_i N_i \right)^2} = \frac{t_j^n N_T - m_n N_T}{N_T^2} = \frac{1}{N_T} (t_j^n - m_n) \quad (\text{A.16})$$

Using this relationship and Eq. (A.8) the variance of m_n is calculated to be:

$$\begin{aligned} \sigma^2(m_n) &= \sum_j \left(\frac{\partial m_n}{\partial N_j} \right)^2 \sigma^2(N_j) = \sum_j \frac{(t_j^n - m_n)^2}{N_T^2} N_j \\ &= \frac{1}{N_T^2} \left(\underbrace{\sum_j t_j^{2n} N_j}_{m_{2n} N_T} - 2m_n \underbrace{\sum_j t_j^n N_j}_{2m_n^2 N_T} + m_n^2 \underbrace{\sum_j N_j}_{m_n^2 N_T} \right) \\ &= \frac{1}{N_T} (m_{2n} - m_n^2) \end{aligned} \quad (\text{A.17})$$

A.2. Uncertainty of Moments Due to Photon Noise

In analogy to Eq. (A.8) the n -th centred moment can be defined as:

$$m_{n,C} = \frac{1}{N_T} \sum_i (t_i - m_1)^n N_i \quad \text{where} \quad m_1 = \frac{1}{N_T} \sum_i t_i N_i \quad (\text{A.18})$$

The derivative of $m_{n,C}$ with respect to N_j can be obtained using quotient and chain rules and Eq. (A.16) for $n = 1$:

$$\frac{\partial m_{n,C}}{\partial N_j} = \frac{1}{N_T^2} \left[N_T \underbrace{\frac{\partial}{\partial N_j} \left(\sum_i (t_i - m_1)^n N_i \right)}_{=:[I]} - \underbrace{\left(\sum_i (t_i - m_1)^n N_i \right)}_{=m_{n,C} N_T} \underbrace{\frac{\partial N_T}{\partial N_j}}_{=1} \right] \quad (\text{A.19})$$

$$[I] = \underbrace{\sum_i N_i \frac{\partial}{\partial N_j} [(t_i - m_1)^n]}_{=:[Ia]} + \underbrace{(t_i - m_1)^n \frac{\partial N_i}{\partial N_j}}_{(t_j - m_1)^n} \quad (\text{A.20})$$

$$\begin{aligned} [Ia] &= \sum_i N_i n (t_i - m_1)^{n-1} \frac{\partial m_1}{\partial N_j} \\ &= n \sum_i N_i (t_i - m_1)^{n-1} \frac{t_j N_T - m_1 N_T}{N_T^2} \\ &= n \frac{t_j N_T - m_1 N_T}{N_T^2} \underbrace{\sum_i N_i (t_i - m_1)^{n-1}}_{=m_{n-1,C} N_T} \\ &= n m_{n-1,C} (t_j - m_1) \end{aligned} \quad (\text{A.21})$$

Combining Eqs. (A.19) to (A.21) results in:

$$\frac{\partial m_{n,C}}{\partial N_j} = \frac{1}{N_T} (n m_{n-1,C} (t_j - m_1) + (t_j - m_1)^n - m_{n,C}) \quad (\text{A.22})$$

The photon noise in terms of the variance of $m_{n,C}$ is calculated as:

$$\begin{aligned} \sigma^2(m_{n,C}) &= \sum_j \left(\frac{\partial m_{n,C}}{\partial N_j} \right)^2 \sigma^2(N_j) \\ &= \sum_j \left(\frac{1}{N_T} (n m_{n-1,C} (t_j - m_1) + (t_j - m_1)^n - m_{n,C}) \right)^2 N_j \\ &= \frac{1}{N_T^2} \sum_j N_j \left(\underbrace{n m_{n-1,C} (t_j - m_1)}_{=:[A]} + \underbrace{(t_j - m_1)^n}_{=:[B]} - \underbrace{m_{n,C}}_{=:[C]} \right)^2 \end{aligned} \quad (\text{A.23})$$

A. Supplementary Materials

Now sums over products of [A], [B] and [C] must to be calculated:

$$\begin{aligned}
[S1] &:= \frac{1}{N_T^2} \sum_j N_j [A]^2 = \frac{n^2 m_{n-1,C}^2}{N_T^2} \underbrace{\sum_j N_j (t_j - m_1)^2}_{m_{2,C} N_T} = \frac{n^2}{N_T} m_{n-1,C}^2 m_{2,C} \\
[S2] &:= \frac{1}{N_T^2} \sum_j N_j [B]^2 = \frac{1}{N_T^2} \sum_j N_j (t_j - m_1)^{2n} = \frac{m_{2n,C}}{N_T} \\
[S3] &:= \frac{1}{N_T^2} \sum_j N_j [C]^2 = \frac{1}{N_T^2} \sum_j N_j (-m_{n,C})^2 = \frac{m_{n,C}^2}{N_T} \\
[S4] &:= \frac{1}{N_T^2} \sum_j N_j [A][B] = \frac{1}{N_T^2} \sum_j N_j n m_{n-1,C} (t_j - m_1) (t_j - m_1)^n \\
&= \frac{n m_{n-1,C}}{N_T^2} \underbrace{\sum_j (t_j - m_1)^{n+1} N_j}_{m_{n+1,C} N_T} = \frac{n}{N_T} m_{n-1,C} m_{n+1,C} \\
[S5] &:= \frac{1}{N_T^2} \sum_j N_j [A][C] = \frac{1}{N_T^2} \sum_j N_j n m_{n-1,C} (t_j - m_1) (-m_{n,C}) \\
&= -\frac{n}{N_T^2} m_{n-1,C} m_{n,C} \underbrace{\sum_j N_j (t_j - m_1)}_{=m_{1,C} N_T = 0} = 0 \\
[S6] &:= \frac{1}{N_T^2} \sum_j N_j [B][C] = \frac{1}{N_T^2} \sum_j N_j (t_j - m_1)^n (-m_{n,C}) \\
&= -\frac{m_{n,C}}{N_T^2} \underbrace{\sum_j N_j (t_j - m_1)^n}_{=m_{n,C} N_T} = -\frac{m_{n,C}^2}{N_T}
\end{aligned}$$

Finally, using [S1] to [S6] Eq. (A.23) becomes:

$$\begin{aligned}
\sigma^2(m_{n,C}) &= [S1] + [S2] + [S3] + 2 \cdot [S4] + 2 \cdot [S5] + 2 \cdot [S6] \\
&= \frac{n^2}{N_T} m_{n-1,C}^2 m_{2,C} + \frac{m_{2n,C}}{N_T} + \frac{m_{n,C}^2}{N_T} \\
&\quad + 2 \frac{n}{N_T} m_{n-1,C} m_{n+1,C} - 2 \frac{m_{n,C}^2}{N_T} \\
&= \frac{1}{N_T} \left(n^2 m_{n-1,C}^2 m_{2,C} + 2n m_{n-1,C} m_{n+1,C} - m_{n,C}^2 + m_{2n,C} \right)
\end{aligned} \tag{A.24}$$

A.3 Correction Algorithm for Moments Calculation: SPAD and HPM Detectors

In Section 4.1.3 the correction algorithm for the calculation of moments was applied to two configurations of a two-layered medium and a single IRF of the MuA detector. Here two additional examples are shown employing different detectors, i.e. SPAD and HPM (see also Fig. 5.2 for comparison of the IRFs), and a configuration of the two-layered medium with different optical properties in both layers.

The simulated DTOF was obtained in the same way as described in Section 4.1.3. The parameters were $d_1 = 10$ mm, $\mu'_{s,1} = 13$ cm⁻¹, $\mu_{a,1} = 0.1$ cm⁻¹ for the upper layer and $d_2 = 100$ mm, $\mu'_{s,2} = 10$ cm⁻¹, $\mu_{a,2} = 0.2$ cm⁻¹ for the lower layer. Common parameters were $n = 1.33$ and $r_{sd} = 3$ cm. The simulated DTOF was then convolved with the experimental IRFs to create a simulated measurement result. All involved DTOFs are shown in upper panels of Fig. A.2.

Results of the application of the correction algorithm in terms of corrected and uncorrected moments as a function of the relative upper integration limit L_U are shown in Fig. A.2. Main conclusions about the performance of the correction are the same as in Section 4.1.3. In addition, very good results are obtained for the correction of $m_{3,C}$. In the L_U range from 1‰ to 10% the corrected values come very close to the true values and exhibit low variation.

A. Supplementary Materials

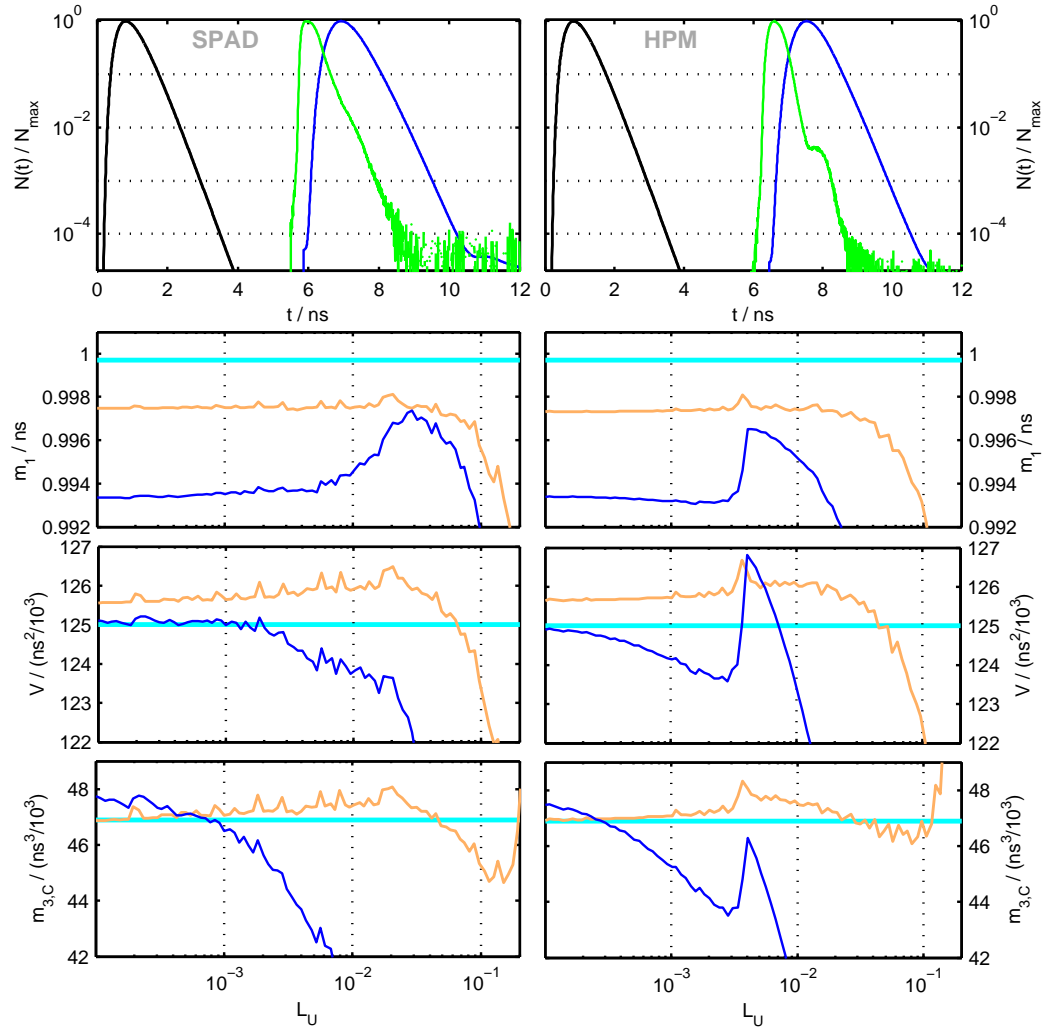


Figure A.2: Application of the correction algorithm for moments to a two-layered model and two detectors. Panels on the left and right side correspond to the SPAD and HPM, respectively. Top panels: IRFs (green) of the detectors in comparison to the modelled DTOF (black) and the result of the convolution of the both (blue). Lower panels: values of moments as a function of the relative upper limit L_U calculated without (blue) and with (orange) the application of the correction algorithm. The horizontal cyan line represents the true value.

Appendix **B**

Publications and Output

B.1 Publications

For more information on the impact of the publications see:

<http://scholar.google.com/citations?user=DCTHEZwAAAAJ>

Printed Sources

- A. Jelzow, H. Wabnitz, H. Obrig, R. Macdonald, and J. Steinbrink. “Separation of indocyanine green boluses in the human brain and scalp based on time-resolved in-vivo fluorescence measurements”. In: *Journal of Biomedical Optics* 17.5 (May 2012), DOI: doi:10.1117/1.JBO.17.5.057003.
- O. Steinkellner, H. Wabnitz, A. Jelzow, R. Macdonald, C. Gruber, J. Steinbrink, and H. Obrig. “Cerebral Perfusion in Acute Stroke Monitored by Time-Domain Near-Infrared Reflectometry”. In: *Journal Biocybernetics and Biomedical Engineering* 32.1 (2012).
- E. Kirilina, A. Jelzow, A. Heine, M. Niessing, H. Wabnitz, R. Brühl, B. Ittermann, A. M. Jacobs, and I. Tachtsidis. “The physiological origin of task-evoked systemic artefacts in functional near infrared spectroscopy”. In: *NeuroImage* 61.1 (May 2012), pp. 70–81. DOI: 10.1016/j.neuroimage.2012.02.074.
- M. Mazurenka, A. Jelzow, H. Wabnitz, D. Contini, L. Spinelli, A. Pifferi, R. Cubeddu, A. D. Mora, A. Tosi, F. Zappa, and R. Macdonald. “Non-contact time-resolved diffuse reflectance imaging at null source-detector separation”. In: *Optics Express* 20.1 (Jan. 2012), pp. 283–290. DOI: 10.1364/OE.20.000283.

B. Publications and Output

- O. Steinkellner, C. Gruber, H. Wabnitz, A. Jelzow, J. Steinbrink, J. B. Fiebach, R. Macdonald, and H. Obrig. “Optical bedside monitoring of cerebral perfusion: technological and methodological advances applied in a study on acute ischemic stroke”. In: *Journal of Biomedical Optics* 15.6 (2010), p. 061708. DOI: 10.1117/1.3505009.
- H. Wabnitz, A. Jelzow, M. Mazurenka, O. Steinkellner, R. Macdonald, A. Pifferi, A. Torricelli, D. Contini, L. M. G. Zucchelli, L. Spinelli, R. Cubeddu, D. Milej, N. Zolek, M. Kacprzak, P. Sawosz, A. Liebert, S. Magazov, J. C. Hebden, F. Martelli, P. Di Ninni, and G. Zaccanti. “Performance assessment of time-domain optical brain imagers: a multi-laboratory study”. In: *Proc. SPIE 8583*. Feb. 2013, pp. 85830L–85830L. DOI: 10.1117/12.2002438.
- A. Farina, A. Pifferi, A. Torricelli, I. Bargigia, L. Spinelli, R. Cubeddu, F. Foschum, M. Jäger, E. Simon, O. Fugger, A. Kienle, F. Martelli, P. Di Ninni, G. Zaccanti, A. Jelzow, E. Kirilina, H. Wabnitz, J. Heiskala, M. Schweiger, and S. Arridge. “Multi-laboratory investigation of the optical properties of the human head”. In: *Proc. SPIE 8804, Neurophotonics* (June 2013), pp. 880408–880408. DOI: 10.1117/12.2032577.
- H. Wabnitz, A. Jelzow, M. Mazurenka, O. Steinkellner, R. Macdonald, A. Pifferi, A. Torricelli, D. Contini, L. Zucchelli, L. Spinelli, R. Cubeddu, D. Milej, N. Zolek, M. Kacprzak, A. Liebert, S. Magazov, J. Hebden, F. Martelli, P. Di Ninni, and G. Zaccanti. “Performance Assessment of Time-Domain Optical Brain Imagers: The nEUROPt Protocol”. In: *Biomedical Optics and 3-D Imaging*. OSA Technical Digest. Optical Society of America, Apr. 2012, BSu2A.4. DOI: 10.1364/BIOMED.2012.BSu2A.4.
- M. Mazurenka, A. Jelzow, B. Ebert, H. Wabnitz, D. Contini, L. Spinelli, A. Pifferi, A. Dalla Mora, A. Tosi, and R. Macdonald. “Non-contact time-domain scanning brain imager: results of proof of principle tests”. In: *Proceedings of SPIE 8088.1* (June 2011), DOI: doi:10.1117/12.889708.
- H. Wabnitz, A. Pifferi, A. Torricelli, D. R. Taubert, M. Mazurenka, O. Steinkellner, A. Jelzow, A. Farina, I. Bargigia, D. Contini, M. Caffini, L. Zucchelli, L. Spinelli, P. Sawosz, A. Liebert, R. Macdonald, and R. Cubeddu. “Assessment of basic instrumental performance of time-domain optical brain imagers”. In: *Proceedings of SPIE 7896.1* (Feb. 2011), DOI: doi:10.1117/12.874654.
- F. Martelli, S. Del Bianco, G. Zaccanti, A. Liemert, A. Kienle, M. Schweiger, S. R. Arridge, S. Prerapa, A. Jelzow, H. Wabnitz, N. Zolek, and A. Liebert. “Comparison of independent forward solvers for photon migration through layered media”. In: *Proceedings of SPIE 7896.1* (Feb. 2011), DOI: doi:10.1117/12.874823.
- A. Jelzow, I. Tachtsidis, E. Kirilina, M. Niessing, R. Brühl, H. Wabnitz, A. Heine, B. Ittermann, and R. Macdonald. “Simultaneous measurement of time-domain fNIRS and physiological signals during a cognitive task”. In: *Proceedings of SPIE 8088.1* (June 2011), DOI: doi:10.1117/12.889484.

- H. Wabnitz, T. H. Sander, A. Jelzow, F. Peters, F. Geisler, M. Wachs, S. Leistner, B.-M. Mackert, L. Trahms, and R. Macdonald. “Cortical and Superficial Responses to Motor Activation Retrieved by Time-Domain Optical Brain Imaging”. In: *Biomedical Optics and 3-D Imaging*. OSA Technical Digest (CD). Optical Society of America, Apr. 2010, BTuB3. DOI: 10.1364/BIOMED.2010.BTuB3.
- A. Jelzow, S. P. Koch, H. Wabnitz, J. Steinbrink, H. Obrig, and R. Macdonald. “Combined EEG and Time-Resolved NIRS to Study Neuro-Vascular Coupling in the Adult Brain”. In: *Biomedical Optics and 3-D Imaging*. OSA Technical Digest (CD). Optical Society of America, Apr. 2010, JMA63. DOI: 10.1364/BIOMED.2010.JMA63.

B.2 Awards

Best Poster Prize

446. WE-Heraeus-Seminar on Optical Imaging of the Brain Function, 7-10 Dec. 2009 at the Physikzentrum Bad Honnef (Germany)

Poster: “*Towards improved quantification of functional activation in human brain by concurrent fMRI and time-resolved NIRS*,” A. Jelzow, E. Kirilina, H. Wabnitz, A. Kummrow, R. Bruehl, B. Ittermann, R. Macdonald.

2010 Biomedical Optics Best Student Poster Award

OSA Biomedical Optics (BIOMED) 2010, 11-14 Apr. 2010 Miami, Florida (USA)

Poster: “*Combined EEG and time-resolved NIRS to study neuro-vascular coupling in the adult brain*,” A. Jelzow, H. Wabnitz, R. Macdonald, S. P. Koch, J. Steinbrink, H. Obrig.

2nd Poster Prize

Innovative Verarbeitung Bioelektrischer und Biomagnetischer Signale 2012 — BBS2012, 19-20 Apr. 2012 at Physikalisch-Technische Bundesanstalt, Berlin (Germany)

Poster: “*Combined EEG and time-resolved NIRS to study neuro-vascular coupling in the adult brain*,” A. Jelzow, H. Wabnitz, R. Macdonald, S. P. Koch, J. Steinbrink, H. Obrig.

B.3 Conferences

ORAL PRESENTATION at *European Conferences on Biomedical Optics (ECBO)*, part of the 19th International Congress on Photonics in Europe, 14-18 June 2009 at International Congress Centre Munich, Munich, Germany. “*Time-Resolved in vivo Fluorescence from an ICG Bolus in the Adult Human Head,*” A. Jelzow, H. Wabnitz, R. Macdonald, H. Obrig, J. Steinbrink.

POSTER PRESENTATION at *446. WE-Heraeus-Seminar on Optical Imaging of the Brain Function*, 7-10 Dec. 2009 at the Physikzentrum Bad Honnef (Germany).

“*Towards improved quantification of functional activation in human brain by concurrent fMRI and time-resolved NIRS,*” A. Jelzow, E. Kirilina, H. Wabnitz, A. Kummrow, R. Bruehl, B. Ittermann, R. Macdonald.

POSTER PRESENTATION at *OSA Biomedical Optics Conference (BIOMED) 2010*, 11-14 Apr. 2010 Miami, Florida, USA.

“*Combined EEG and time-resolved NIRS to study neuro-vascular coupling in the adult brain,*” A. Jelzow, H. Wabnitz, R. Macdonald, S.P. Koch, J. Steinbrink, H. Obrig.

ORAL PRESENTATION at *BiOS 2011*, part of SPIE Photonics West, 22–27 January 2011, San Francisco, California, USA.

“*Correlations between time-domain NIRS and systemic physiological signals studied for a cognitive task,*” A. Jelzow, I. Tachtsidis, E. Kirilina, M. Niessing, R. Brühl, H. Wabnitz, A. Heine, B. Ittermann, R. Macdonald.

ORAL PRESENTATION at *European Conferences on Biomedical Optics (ECBO)*, part of the 20th International Congress on Photonics in Europe, 22-26 May 2011 at International Congress Centre Munich, in Munich, Germany.

“*Simultaneous measurement of time-domain fNIRS and physiological signals during a cognitive task,*” A. Jelzow, I. Tachtsidis, E. Kirilina, M. Niessing, R. Brühl, H. Wabnitz, A. Heine, B. Ittermann, R. Macdonald.

POSTER PRESENTATION at *Innovative Verarbeitung Bioelektrischer und Biomagnetischer Signale 2012 — BBS2012*, 19-20 Apr. 2012 at Physikalisch-Technische Bundesanstalt, Berlin, Germany.

“*Combined EEG and time-resolved NIRS to study neuro-vascular coupling in the adult brain,*” A. Jelzow, H. Wabnitz, R. Macdonald, S.P. Koch, J. Steinbrink, H. Obrig.

Appendix **C**

List of Acronyms

Abbreviation	Description
BOP	Background optical properties
c_0, c_m	speed of light in vacuum or medium
CV	Coefficient of variation
cw	Continuous wave
DTOF	Distribution of times of flight of photons
DPF	Differential pathlength factor
fMRI	Functional magnetic resonance imaging
fNIRS	Functional near-infrared spectroscopy
FWHM	Full width at half maximum
GaAs	PMT with a Ga-As photocathode
HbO, HbR, HbT	Oxy-, deoxy- and total haemoglobin
HPM	Hybrid PMT
IRF	Instrument Response Function
m_n	n-th moment (non-centred)
$m_{n,C}$	n-th centred moment
μ_a	absorption coefficient
μ_s	Scattering coefficient
μ'_s	Reduced scattering coefficient
MC	Monte Carlo
MBL	Modified Beer-Lambert law
MuA	PMT with a multi-alkali photocathode
NIR	Near-infrared
NIRS	Near-infrared spectroscopy

C. List of Acronyms

PMT	Photomultiplier
PTB	Physikalisch-Technische Bundesanstalt
SD, σ	Standard deviation
SEM	Standard error of mean
SIM	Semi-infinite medium
SNR	Signal to noise ratio
S_{O_2}	Blood oxygen saturation
SPAD	Single photon avalanche photodiode
SPP	Systemic physiological processes
TCSPC	Time correlated single photon counting
td, tr	Time-domain or time-resolved
$V = m_{2,C}$	Variance of a DTOF, i.e. second centred moment

List of Figures

1.1	Illustration of photon propagation in a strong scattering medium	2
2.1	Simplified schematic view of the formation of the optical signals.	8
2.2	Cross section of a human head	10
2.3	Oxy- and deoxyhaemoglobin absorption spectra in the near-infrared region	11
2.4	A potential absorption spectrum of tissue composed from chromophores.	13
2.5	The canonical haemodynamic response function (HRF) and an example for vascular response.	14
2.6	Example of a typical response measured by fNIRS	15
2.7	Comparison of neuroscientific modalities in terms of invasiveness, spatial and temporal resolution.	16
2.8	Illustration of the scattering phase function	22
2.9	Illustration of multiple scattering	22
2.10	Illustration of the three most used fNIRS modalities.	27
3.1	Scheme and a photograph of the PTB Brain Imager.	32
3.2	IRF setup and an exemplary IRF measurement	34
3.3	Setup for the concurrent measurement of systemic physiological signals and fNIRS.	35
3.4	Schematic view of the combined EEG-fNIRS setup.	37
3.5	Concurrent fMRI-fNIRS setup	39
3.6	Setup for the large coverage and high density optical measurement on a human head <i>in vivo</i>	41
4.1	Dependence of the moments m_1 and V on the upper integrations limit and IRF.	48

List of Figures

4.2	Algorithm for the computation of the systematic error estimate appearing during moments calculations	50
4.3	Application of the correction algorithm for moments to a two-layered model	52
4.4	Long time recording of the drift and noise of m_1	56
4.5	Noise of the moments m_1 and V as a function of the total number of photons N_T	58
4.6	Contributions of the instrumental and photon noise for the moments m_1 and V	60
4.7	Maps of significant changes of moments.	63
4.8	Maps of significant changes of attenuation.	64
4.9	Background optical properties obtained from the moments of DTOFs measured at four source-detector separations	67
4.10	Reconstructed optical properties of the head	69
4.11	Distributions of m_1 , V and $m_{3,C}$ obtained <i>in vivo</i> on the forehead 73	
4.12	Moments relevant for the sensitivity factors as a function of r_{sd} . 76	
4.13	Tissue thickness distributions obtained <i>in vivo</i> on the forehead 78	
4.14	Correlation of moments m_1 , V , $m_{3,C}$ and anatomical parameters 80	
4.15	Sensitivity factors of a layered quasi-homogeneous medium	83
4.16	Correlation of depth sensitivity profiles of moments as a function of μ_a and μ'_s	84
4.17	Dependence of layered sensitivity factors on the IRF and upper integration limit	86
4.18	Workflow of the fNIRS data analysis showing model dependent and independent steps.	90
4.19	Comparison of the layered and homogeneous analysis methods applied to an <i>in vivo</i> measurement	92
5.1	Photograph and a schematic view of the two-layered phantom. 97	
5.2	IRFs of four detectors used for the two-layered phantom measurement.	99
5.3	Noise induced by fibre reattachment	102
5.4	Moments of DTOFs as a function of the absorption coefficient in the upper and lower layer of a two-layered phantom	103
5.5	Relative contrasts of moments during absorption changes in a two-layered phantom (simulated case)	105
5.6	Retrieval of absorption changes in a simulated two-layered geometry using sensitivity factors for the homogeneous SIM.	108
5.7	Reconstruction of absorption changes in the two-layered phantom using homogeneous and layered approaches.	109

5.8	Optical properties of the two-layered phantom retrieved using homogeneous semi-infinite models.	112
5.9	Potential future phantom design employing solid and liquid materials.	113
6.1	Paradigm of the concurrent fNIRS and SPP experiment	119
6.2	Group averaged fNIRS signals during a cognitive task	120
6.3	Group averaged fMRI signals during a cognitive task	122
6.4	Two-layered separation of the data from a single subject during frontal lobe activation	123
6.5	Group averaged systemic physiological signals during cognitive task	125
6.6	Correlation of systemic physiological signals and fNIRS in terms of mean correlation coefficients.	126
6.7	Fit of the skewed tophat function to the averaged responses to a motor task	129
6.8	Data obtained by the EEG during a motor task.	130
6.9	Data analysis of the concurrent fMRI and fNIRS measurement: workflow and segmentation	133
6.10	Concurrent fMRI and fNIRS: changes in oxy- and deoxyhemoglobin derived by the layered analysis	134
A.1	Examples for values of moments as a function of μ_a and μ'_s	144
A.2	Application of the correction algorithm for moments to a two-layered model: SPAD and HPM detectors.	150

List of Tables

4.1	Absolute values of typical changes in moments observed <i>in vivo</i> during a finger tapping task.	62
4.2	Optical properties of head tissues	70
4.3	Mean values of moments obtained <i>in vivo</i> on the forehead of 15 adult subjects	74
4.4	Results of the linear and quadratic fits to sensitivity factors $S(r_{sd})$	77
4.5	Mean thickness of the different tissue types obtained <i>in vivo</i> on the forehead of 15 subjects.	79
5.1	Parameters characterising IRFs used in the phantom experiment	100
5.2	Sensitivity factors of moments obtained on a two-layered phantom	106
6.1	Results of the skewed top hat fit to the neuronal and vascular responses	130
6.2	Comparison of haemoglobin concentration changes from fNIRS to the fMRI's BOLD signal	135

References

- [1] F. F. Jöbsis. “Noninvasive, infrared monitoring of cerebral and myocardial oxygen sufficiency and circulatory parameters”. In: *Science* 198.4323 (Dec. 1977), pp. 1264–1267. DOI: 10.1126/science.929199 (cited on p. 7).
- [2] M. Ferrari and V. Quaresima. “A brief review on the history of human functional near-infrared spectroscopy (fNIRS) development and fields of application”. In: *NeuroImage* (Mar. 2012). DOI: 10.1016/j.neuroimage.2012.03.049 (cited on pp. 7, 26).
- [3] Elsevier. *NeuroImage Special Issue on Functional Near Infrared Spectroscopy (fNIRS)*. URL: <http://www.sciencedirect.com/science/journal/aip/10538119> (cited on p. 7).
- [4] D. Kleinfeld, P. Blinder, P. J. Drew, J. D. Driscoll, A. Muller, P. S. Tsai, and A. Y. Shih. “A Guide to Delineate the Logic of Neurovascular Signaling in the Brain”. In: *Frontiers in Neuroenergetics* 3 (2011). DOI: 10.3389/fnene.2011.00001 (cited on p. 8).
- [5] M. Cope. “The application of near infrared spectroscopy to non invasive monitoring of cerebral oxygenation in the newborn infant”. English. PhD Thesis. London: Univercity College London, 1991 (cited on pp. 8, 11–13).
- [6] A. K. Dunn, C. L. Smithpeter, A. J. Welch, and R. R. Richards-Kortum. “Finite-difference time-domain simulation of light scattering from single cells”. In: *Journal of Biomedical Optics* 2.3 (July 1997), pp. 262–266. DOI: 10.1117/12.275219 (cited on pp. 8, 21).
- [7] F. Gaillard. *Illustration depicting the layers of the scalp and meninges*. http://commons.wikimedia.org/wiki/File:Layers_of_the_scalp_and_meninges.png. 2009 (cited on p. 10).
- [8] M. Firbank, M. Hiraoka, M. Essenpreis, and D. T. Delpy. “Measurement of the optical properties of the skull in the wavelength range 650-950 nm”. In: *Physics in Medicine and Biology* 38.4 (Apr. 1993). PMID: 8488176, pp. 503–510. DOI: 10.1088/0031-9155/38/4/002 (cited on pp. 9, 70, 114).
- [9] V. V. Tuchin. *Tissue optics: light scattering methods and instruments for medical diagnosis*. 2nd ed. Bellingham, Wash: SPIE/International Society for Optical Engineering, 2007 (cited on pp. 9, 64).

References

- [10] M. Firbank, M. Schweiger, and D. T. Delpy. “Investigation of light piping through clear regions of scattering objects”. In: *Proc. SPIE, Optical Tomography, Photon Migration, and Spectroscopy of Tissue and Model Media: Theory, Human Studies, and Instrumentation* 2389 (1995), pp. 167–173. DOI: 10.1117/12.209964 (cited on p. 9).
- [11] E. Okada, M. Firbank, M. Schweiger, S. R. Arridge, M. Cope, and D. T. Delpy. “Theoretical and experimental investigation of near-infrared light propagation in a model of the adult head”. In: *Applied Optics* 36.1 (Jan. 1997), pp. 21–31. DOI: 10.1364/AO.36.000021 (cited on p. 9).
- [12] J. Steinbrink. “Near-infrared-spectroscopy on the adult human head with picosecond resolution”. In German. PhD Thesis. Berlin: FU Berlin, Nov. 2000 (cited on pp. 9, 43, 55, 72, 75, 81).
- [13] E. Okada and D. T. Delpy. “Near-Infrared Light Propagation in an Adult Head Model. I. Modeling of Low-Level Scattering in the Cerebrospinal Fluid Layer”. In: *Applied Optics* 42.16 (June 2003), pp. 2906–2914. DOI: 10.1364/AO.42.002906 (cited on p. 10).
- [14] A. Custo, W. M. Wells III, A. H. Barnett, E. M. C. Hillman, and D. A. Boas. “Effective scattering coefficient of the cerebral spinal fluid in adult head models for diffuse optical imaging”. In: *Applied Optics* 45.19 (July 2006), pp. 4747–4755. DOI: 10.1364/AO.45.004747 (cited on p. 10).
- [15] S. J. Matcher and C. E. Cooper. “Absolute quantification of deoxyhaemoglobin concentration in tissue near infrared spectroscopy”. In: *Physics in Medicine and Biology* 39.8 (Aug. 1994), pp. 1295–1312. DOI: 10.1088/0031-9155/39/8/008 (cited on pp. 11–13).
- [16] R. F. Schmidt and G. Thews. *Physiologie des Menschen: mit 100 Tabellen*. German. 27. Berlin; Heidelberg; New York; Barcelona; Budapest; Hongkong; London; Mailand; Paris; Santa Clara; Singapur; Tokio: Springer, 1997 (cited on p. 11).
- [17] AnaesthesiaUK. *Oxygen content of blood*. URL: <http://www.frca.co.uk/article.aspx?articleid=100175> (cited on p. 11).
- [18] S. N. Davie and H. P. Grocott. “Impact of Extracranial Contamination on Regional Cerebral Oxygen Saturation: A Comparison of Three Cerebral Oximetry Technologies”. In: *Anesthesiology* (Feb. 2012). PMID: 22343469. DOI: 10.1097/ALN.0b013e31824c00d7 (cited on p. 12).
- [19] Scott Prahl, Oregon Medical Laser Center. *Optical Absorption of Hemoglobin*. URL: <http://omlc.ogi.edu/spectra/hemoglobin/index.html> (cited on p. 12).
- [20] Biomedical Optics Research Laboratory, UCL. *Tissue Spectra*. URL: <http://www.ucl.ac.uk/medphys/research/borl/intro/spectra> (cited on p. 12).
- [21] V. S. Hollis, T. Binzoni, and D. T. Delpy. “Noninvasive monitoring of brain tissue temperature by near-infrared spectroscopy”. In: *Proc. SPIE 4250*. June 2001, pp. 470–481. DOI: 10.1117/12.434506 (cited on p. 13).
- [22] R. L. van Veen, H. Sterenborg, A. Pifferi, A. Torricelli, and R. Cubeddu. “Determination of VIS- NIR absorption coefficients of mammalian fat, with time- and spatially resolved diffuse reflectance and transmission spectroscopy”. In: *Biomedical Topical Meeting*. OSA Technical Digest. Optical Society of America, Apr. 2004, SF4 (cited on p. 13).

- [23] G. H. Glover. “Deconvolution of Impulse Response in Event-Related BOLD fMRI”. In: *NeuroImage* 9.4 (Apr. 1999), pp. 416–429. DOI: 10.1006/nimg.1998.0419 (cited on p. 14).
- [24] J. J. Chen and G. B. Pike. “Origins of the BOLD post-stimulus undershoot”. In: *NeuroImage* 46.3 (July 2009), pp. 559–568. DOI: 10.1016/j.neuroimage.2009.03.015 (cited on p. 14).
- [25] J. Hua, R. D. Stevens, A. J. Huang, J. J. Pekar, and P. C. v. Zijl. “Physiological origin for the BOLD poststimulus undershoot in human brain: vascular compliance versus oxygen metabolism”. en. In: *Journal of Cerebral Blood Flow & Metabolism* 31.7 (2011), pp. 1599–1611. DOI: 10.1038/jcbfm.2011.35 (cited on p. 14).
- [26] P. C. van Zijl, J. Hua, and H. Lu. “The BOLD post-stimulus undershoot, one of the most debated issues in fMRI”. In: *NeuroImage* 62.2 (Aug. 2012), pp. 1092–1102. DOI: 10.1016/j.neuroimage.2012.01.029 (cited on p. 14).
- [27] J. Cohen-Adad, S. Chapuisat, J. Doyon, S. Rossignol, J.-M. Lina, H. Benali, and F. Lesage. “Activation detection in diffuse optical imaging by means of the general linear model”. In: *Medical Image Analysis* 11.6 (Dec. 2007), pp. 616–629. DOI: 10.1016/j.media.2007.06.002 (cited on p. 14).
- [28] C. Martin, J. Martindale, J. Berwick, and J. Mayhew. “Investigating neural–hemodynamic coupling and the hemodynamic response function in the awake rat”. In: *NeuroImage* 32.1 (Aug. 2006), pp. 33–48. DOI: 10.1016/j.neuroimage.2006.02.021 (cited on p. 14).
- [29] D. A. Handwerker, J. M. Ollinger, and M. D’Esposito. “Variation of BOLD hemodynamic responses across subjects and brain regions and their effects on statistical analyses”. In: *NeuroImage* 21.4 (Apr. 2004), pp. 1639–1651. DOI: 10.1016/j.neuroimage.2003.11.029 (cited on p. 14).
- [30] G. Aguirre, E. Zarahn, and M. D’Esposito. “The Variability of Human, BOLD Hemodynamic Responses”. In: *NeuroImage* 8.4 (Nov. 1998), pp. 360–369. DOI: 10.1006/nimg.1998.0369 (cited on p. 14).
- [31] G. Strangman, D. A. Boas, and J. P. Sutton. “Non-invasive neuroimaging using near-infrared light”. In: *Biological Psychiatry* 52.7 (Oct. 2002), pp. 679–693 (cited on p. 16).
- [32] P. H. Koh. “Methodology of Optical Topography Measurements for Functional Brain Imaging and the Development and Implementation of Functional Optical Signal Analysis Software”. English. Supervisors: Prof. David T. Delpy, Dr. Clare E. Elwell. PhD Thesis. London: Univercity College London, 2007 (cited on p. 16).
- [33] G. Barnes, A. Hillebrand, and M. Hirata. “Magnetoencephalogram”. In: *Scholarpedia* 5.7 (2010), p. 3172. DOI: 10.4249/scholarpedia.3172 (cited on p. 17).
- [34] N. P. Blockley, V. E. M. Griffeth, A. B. Simon, and R. B. Buxton. “A review of calibrated blood oxygenation level-dependent (BOLD) methods for the measurement of task-induced changes in brain oxygen metabolism”. en. In: *NMR in Biomedicine* (2012). DOI: 10.1002/nbm.2847 (cited on pp. 17, 131).
- [35] CIE. *International electrotechnical vocabulary chapter 845: Lighting*. CIE Publication 17.4. Geneve, Suisse: Bureau Central de la Commission Electrotechnique Internationale, 1987 (cited on pp. 19, 23).

References

- [36] International Organization for Standardization. *ISO Standard 6286-1982: Molecular absorption spectrometry - Vocabulary - General - Apparatus*. 1982 (cited on pp. 19, 23).
- [37] International Electrotechnical Commission. *Electropedia: The World's Online Electrotechnical Vocabulary*. URL: <http://www.electropedia.org> (cited on pp. 19, 23).
- [38] International Organization for Standardization. *ISO Standard 6286-1982: Molecular absorption spectrometry - Vocabulary - General - Apparatus*. 1982 (cited on p. 20).
- [39] L. C. Henyey and J. L. Greenstein. "Diffuse radiation in the Galaxy". In: *The Astrophysical Journal* 93 (Jan. 1941), p. 70. DOI: 10.1086/144246 (cited on p. 21).
- [40] A. K. Dunn. "Light Scattering Properties of Cells". PhD Thesis. The University of Texas at Austin, 1997 (cited on p. 22).
- [41] M. Cope, D. T. Delpy, E. O. Reynolds, S. Wray, J. Wyatt, and P. van der Zee. "Methods of quantitating cerebral near infrared spectroscopy data". In: *Advances in Experimental Medicine and Biology* 222 (1988). PMID: 3129910, pp. 183–189 (cited on p. 23).
- [42] D. T. Delpy, M. Cope, P. v. d. Zee, S. Arridge, S. Wray, and J. Wyatt. "Estimation of optical pathlength through tissue from direct time of flight measurement". In: *Physics in Medicine and Biology* 33.12 (Dec. 1988). PMID: 3237772, pp. 1433–1442. DOI: 10.1088/0031-9155/33/12/008 (cited on pp. 23, 75).
- [43] A. Sassaroli and S. Fantini. "Comment on the modified Beer–Lambert law for scattering media". en. In: *Physics in Medicine and Biology* 49.14 (July 2004), N255. DOI: 10.1088/0031-9155/49/14/N07 (cited on p. 24).
- [44] S. Fantini, D. Hueber, M. A. Franceschini, E. Gratton, W. Rosenfeld, P. G. Stubblefield, D. Maulik, and M. R. Stankovic. "Non-invasive optical monitoring of the newborn piglet brain using continuous-wave and frequency-domain spectroscopy". en. In: *Physics in Medicine and Biology* 44.6 (June 1999), p. 1543. DOI: 10.1088/0031-9155/44/6/308 (cited on p. 24).
- [45] M. S. Patterson, B. Chance, and B. C. Wilson. "Time resolved reflectance and transmittance for the non-invasive measurement of tissue optical properties". In: *Applied Optics* 28.12 (June 1989), pp. 2331–2336. DOI: 10.1364/AO.28.002331 (cited on p. 25).
- [46] J. D. Moulton. "Diffusion modelling of picosecond laser pulse propagation of turbid media". Master's thesis. McMaster University, Hamilton, Ontario, Canada, 1990 (cited on p. 25).
- [47] R. C. Haskell, L. O. Svaasand, T.-T. Tsay, C. Feng, M. S. McAdams, and B. J. Tromberg. "Boundary conditions for the diffusion equation in radiative transfer". In: *Journal of the Optical Society of America A* 11.10 (Oct. 1994), p. 2727. DOI: 10.1364/JOSAA.11.002727 (cited on p. 25).
- [48] A. Kienle and M. S. Patterson. "Improved solutions of the steady-state and the time-resolved diffusion equations for reflectance from a semi-infinite turbid medium". In: *Journal of the Optical Society of America A* 14.1 (Jan. 1997), pp. 246–254. DOI: 10.1364/JOSAA.14.000246 (cited on p. 26).

- [49] A. H. Hielscher, S. L. Jacques, L. Wang, and F. K. Tittel. “The influence of boundary conditions on the accuracy of diffusion theory in time-resolved reflectance spectroscopy of biological tissues”. In: *Physics in Medicine and Biology* 40.11 (Nov. 1995), pp. 1957–1975. DOI: 10.1088/0031-9155/40/11/013 (cited on p. 26).
- [50] M. A. Franceschini, D. K. Joseph, T. J. Huppert, S. G. Diamond, and D. A. Boas. “Diffuse optical imaging of the whole head”. In: *Journal of Biomedical Optics* 11.5 (Oct. 2006), DOI: doi:10.1117/1.2363365 (cited on p. 26).
- [51] D. J. Cuccia, F. Bevilacqua, A. J. Durkin, and B. J. Tromberg. “Modulated imaging: quantitative analysis and tomography of turbid media in the spatial-frequency domain”. In: *Optics Letters* 30.11 (June 2005), pp. 1354–1356. DOI: 10.1364/OL.30.001354 (cited on p. 26).
- [52] T. D. O’Sullivan, A. E. Cerussi, D. J. Cuccia, and B. J. Tromberg. “Diffuse optical imaging using spatially and temporally modulated light”. In: *Journal of Biomedical Optics* 17.7 (July 2012), DOI: 10.1117/1.JBO.17.7.071311 (cited on p. 26).
- [53] J. C. Schotland and V. A. Markel. “Inverse scattering with diffusing waves”. In: *Journal of the Optical Society of America A* 18.11 (Nov. 2001), pp. 2767–2777. DOI: 10.1364/JOSAA.18.002767 (cited on p. 27).
- [54] V. Lukic, V. A. Markel, and J. C. Schotland. “Optical tomography with structured illumination”. In: *Optics Letters* 34.7 (Apr. 2009), pp. 983–985. DOI: 10.1364/OL.34.000983 (cited on p. 27).
- [55] D. T. Delpy and M. Cope. “Quantification in Tissue Near-infrared Spectroscopy”. In: *Philosophical Transactions of the Royal Society of London. Series B: Biological Sciences* 352.1354 (June 1997), pp. 649–659. DOI: 10.1098/rstb.1997.0046 (cited on p. 27).
- [56] S. J. Matcher, M. Cope, and D. T. Delpy. “Use of the water absorption spectrum to quantify tissue chromophore concentration changes in near-infrared spectroscopy”. In: *Physics in Medicine and Biology* 39.1 (Jan. 1994), pp. 177–196. DOI: 10.1088/0031-9155/39/1/011 (cited on p. 27).
- [57] I. Schelkanova and V. Toronov. “Optimal quantitation of the cerebral hemodynamic response in functional near-infrared spectroscopy”. In: *Optics Express* 18.18 (Aug. 2010), p. 19386. DOI: 10.1364/OE.18.019386 (cited on p. 27).
- [58] I. Schelkanova and V. Toronov. “Independent component analysis of broadband near-infrared spectroscopy data acquired on adult human head”. In: *Biomedical Optics Express* 3.1 (Jan. 2012), pp. 64–74. DOI: 10.1364/B0E.3.000064 (cited on p. 27).
- [59] W. Becker. *Advanced time-correlated single photon counting techniques*. English. Berlin; New York: Springer, 2005 (cited on p. 28).
- [60] O. Steinkellner, H. Wabnitz, A. Walter, and R. Macdonald. “Multiple Source Positions in Time-Domain Brain Imaging: A Novel Approach; In Press”. In: *Proc. SPIE 8799 Diffuse Optical Imaging IV* (2013) (cited on p. 29).
- [61] O. Steinkellner, C. Gruber, H. Wabnitz, A. Jelzow, J. Steinbrink, J. B. Fiebach, R. Macdonald, and H. Obrig. “Optical bedside monitoring of cerebral perfusion: technological and methodological advances applied in a study on acute ischemic stroke”. In: *Journal of Biomedical Optics* 15.6 (2010), p. 061708. DOI: 10.1117/1.3505009 (cited on pp. 29, 31, 101).

References

- [62] H. Wabnitz, M. Moeller, A. Liebert, A. Walter, R. Macdonald, H. Obrig, J. Steinbrink, R. Erdmann, and O. Raitza. “A Time-Domain NIR Brain Imager Applied in Functional Stimulation Experiments”. In: *Photon Migration and Diffuse-Light Imaging II*. Ed. by K. Licha and Cubeddu. Vol. 5859. Proc. SPIE. Optical Society of America, June 2005, WA5 (cited on pp. 31, 33, 43, 89).
- [63] A. Jelzow. “Untersuchungen zur zeitaufgelösten Fluoreszenzdetektion von optischen Kontrastmittelboli in Gewebe (Studies on Time-Resolved Fluorescence Detection of Boluses of Optical Contrast Agents in Tissue)”. German. Diploma Thesis. Berlin Institute of Technology, Mar. 2008 (cited on pp. 31, 51).
- [64] A. Jelzow, H. Wabnitz, H. Obrig, R. Macdonald, and J. Steinbrink. “Separation of indocyanine green boluses in the human brain and scalp based on time-resolved in-vivo fluorescence measurements”. In: *Journal of Biomedical Optics* 17.5 (May 2012), DOI: doi:10.1117/1.JBO.17.5.057003 (cited on p. 31).
- [65] M. Möller, H. Wabnitz, A. Kummrow, D. Grosenick, A. Liebert, B. Wassermann, R. Macdonald, and H. Rinneberg. “A four-wavelength multi-channel scanning time-resolved optical mammograph”. In: *Photon Migration and Diffuse-Light Imaging*. Ed. by D. Boas. Vol. 5138. Proc. SPIE. Optical Society of America, June 2003, 5138_290 (cited on p. 33).
- [66] A. Liebert, H. Wabnitz, D. Grosenick, and R. Macdonald. “Fiber dispersion in time domain measurements compromising the accuracy of determination of optical properties of strongly scattering media”. In: *Journal of Biomedical Optics* 8.3 (2003), p. 512. DOI: 10.1117/1.1578088 (cited on pp. 33, 34, 41).
- [67] A. Kummrow, B. Ittermann, M. Moller, F. Seifert, F. Wojcik, W. Hoffmann, and H. Rinneberg. “Concurrent multiple-projection optical and MR mammography”. In: *Proceedings of SPIE* 5693.1 (Apr. 2005), pp. 137–146. DOI: doi:10.1117/12.589659 (cited on p. 38).
- [68] S. R. Arridge, M. Cope, and D. T. Delpy. “The theoretical basis for the determination of optical pathlengths in tissue: temporal and frequency analysis”. In: *Physics in Medicine and Biology* 37.7 (July 1992), pp. 1531–1560. DOI: 10.1088/0031-9155/37/7/005 (cited on pp. 43, 72, 75).
- [69] S. R. Arridge and M. Schweiger. “Direct calculation of the moments of the distribution of photon time of flight in tissue with a finite-element method”. In: *Applied Optics* 34.15 (1995), pp. 2683–2687. DOI: 10.1364/AO.34.002683 (cited on pp. 43, 51).
- [70] A. Liebert, H. Wabnitz, D. Grosenick, M. Möller, R. Macdonald, and H. Rinneberg. “Evaluation of Optical Properties of Highly Scattering Media by Moments of Distributions of Times of Flight of Photons”. In: *Applied Optics* 42.28 (2003), pp. 5785–5792. DOI: 10.1364/AO.42.005785 (cited on pp. 43, 46, 47, 55, 65, 66, 111).
- [71] C. A. Laury-Micoulaut. “The n-th centered moment of a multiple convolution and its applications to an intercloud gas model”. In: *Astronomy and Astrophysics* 51.3 (Sept. 1976), pp. 343–346 (cited on p. 45).
- [72] Hamamatsu Photonics K.K. *Photomultiplier Tubes. Basics and Applications*. 3rd Edition (3a). Hamamatsu Photonics K.K., Electron Tube Division, 2007 (cited on p. 47).

- [73] A. Liemert and A. Kienle. “Light diffusion in a turbid cylinder. II. Layered case”. In: *Optics Express* 18.9 (Apr. 2010), pp. 9266–9279. DOI: 10.1364/OE.18.009266 (cited on pp. 51, 82, 87).
- [74] W. Becker. *The bh TCSPC Handbook*. 5th Edition. Berlin: Becker & Hickl GmbH, 2012 (cited on p. 57).
- [75] D. A. Boas, C. Pitris, and N. Ramanujam. *Handbook of biomedical optics*. English. Boca Raton, FL: CRC Press, 2011 (cited on p. 64).
- [76] M. Kacprzak, A. Liebert, W. Staszkiwicz, A. Gabrusiewicz, P. Sawosz, G. Madycki, and R. Maniewski. “Application of a time-resolved optical brain imager for monitoring cerebral oxygenation during carotid surgery”. In: *Journal of Biomedical Optics* 17.1 (2012), p. 016002. DOI: 10.1117/1.JBO.17.1.016002 (cited on pp. 66, 88, 110).
- [77] M. Diop, K. M. Tichauer, J. T. Elliott, M. Migueis, T.-Y. Lee, and K. S. Lawrence. “Comparison of time-resolved and continuous-wave near-infrared techniques for measuring cerebral blood flow in piglets”. In: *Journal of Biomedical Optics* 15.5 (2010), p. 057004. DOI: 10.1117/1.3488626 (cited on pp. 66, 110).
- [78] S. R. Arridge, J. P. Kaipio, V. Kolehmainen, M. Schweiger, E. Somersalo, T. Tarvainen, and M. Vauhkonen. “Approximation errors and model reduction with an application in optical diffusion tomography”. In: *Inverse Problems* 22.1 (Feb. 2006), pp. 175–195. DOI: 10.1088/0266-5611/22/1/010 (cited on p. 68).
- [79] V. Kolehmainen, M. Schweiger, I. Nissilä, T. Tarvainen, S. R. Arridge, and J. P. Kaipio. “Approximation errors and model reduction in three-dimensional diffuse optical tomography”. In: *Journal of the Optical Society of America A* 26.10 (Oct. 2009), pp. 2257–2268. DOI: 10.1364/JOSAA.26.002257 (cited on p. 68).
- [80] T. Tarvainen, V. Kolehmainen, J. P. Kaipio, and S. R. Arridge. “Corrections to linear methods for diffuse optical tomography using approximation error modelling”. In: *Biomedical Optics Express* 1.1 (Aug. 2010), pp. 209–222. DOI: 10.1364/BOE.1.000209 (cited on p. 68).
- [81] Q. Fang and D. A. Boas. “Tetrahedral mesh generation from volumetric binary and gray-scale images”. In: *Proceedings of the Sixth IEEE international conference on Symposium on Biomedical Imaging: From Nano to Macro*. ISBI’09. Piscataway, NJ, USA: IEEE Press, 2009, 1142–1145 (cited on p. 68).
- [82] S. R. Arridge. “Use of multiple data types in time-resolved optical absorption and scattering tomography”. In: vol. 2035. SPIE, 1993, pp. 218–229. DOI: 10.1117/12.146604 (cited on p. 68).
- [83] E. Salomatina, B. Jiang, J. Novak, and A. N. Yaroslavsky. “Optical properties of normal and cancerous human skin in the visible and near-infrared spectral range”. In: *Journal of Biomedical Optics* 11.6 (2006), p. 064026. DOI: 10.1117/1.2398928 (cited on p. 70).
- [84] M. J. van Gemert, S. L. Jacques, H. J. Sterenborg, and W. M. Star. “Skin optics”. In: *IEEE Transactions on Bio-Medical Engineering* 36.12 (1989), pp. 1146–1154 (cited on p. 70).

References

- [85] A. N. Bashkatov, E. A. Genina, V. I. Kochubey, and V. V. Tuchin. “Optical properties of human skin, subcutaneous and mucous tissues in the wavelength range from 400 to 2000 nm”. In: *Journal of Physics D: Applied Physics* 38.15 (Aug. 2005), pp. 2543–2555. DOI: 10.1088/0022-3727/38/15/004 (cited on p. 70).
- [86] J. Choi, M. Wolf, V. Toronov, U. Wolf, C. Polzonetti, D. Hueber, L. P. Safonova, R. Gupta, A. Michalos, W. Mantulin, and E. Gratton. “Noninvasive determination of the optical properties of adult brain: near-infrared spectroscopy approach”. In: *Journal of Biomedical Optics* 9 (2004), p. 221. DOI: 10.1117/1.1628242 (cited on pp. 69, 70).
- [87] F. P. Bevilacqua, D. Piguet, P. Marquet, J. D. Gross, B. J. Tromberg, and C. Depeursinge. “In Vivo Local Determination of Tissue Optical Properties: Applications to Human Brain”. In: *Applied Optics* 38.22 (1999), pp. 4939–4950. DOI: 10.1364/AO.38.004939 (cited on pp. 69–71).
- [88] A. N. Bashkatov, E. A. Genina, V. I. Kochubey, and V. V. Tuchin. “Optical properties of human cranial bone in the spectral range from 800 to 2000 nm”. In: *Proceedings of SPIE* 6163.1 (Aug. 2006), DOI: doi:10.1117/12.697305 (cited on p. 70).
- [89] E. A. Genina, A. N. Bashkatov, and V. V. Tuchin. “Optical Clearing of Cranial Bone”. In: *Advances in Optical Technologies 2008* (2008), pp. 1–8. DOI: 10.1155/2008/267867 (cited on p. 70).
- [90] N. Ugryumova, S. J. Matcher, and D. P. Attenburrow. “Measurement of bone mineral density via light scattering”. In: *Physics in Medicine and Biology* 49.3 (Feb. 2004), pp. 469–483. DOI: 10.1088/0031-9155/49/3/009 (cited on p. 70).
- [91] A. N. Yaroslavsky, P. C. Schulze, I. V. Yaroslavsky, R. Schober, F. Ulrich, and H.-J. Schwarzmaier. “Optical properties of selected native and coagulated human brain tissues in vitro in the visible and near infrared spectral range”. In: *Physics in Medicine and Biology* 47.12 (June 2002), pp. 2059–2073. DOI: 10.1088/0031-9155/47/12/305 (cited on p. 70).
- [92] S. C. Gebhart, W. C. Lin, and A. Mahadevan-Jansen. “In vitro determination of normal and neoplastic human brain tissue optical properties using inverse adding-doubling”. In: *Physics in Medicine and Biology* 51.8 (Apr. 2006), pp. 2011–2027. DOI: 10.1088/0031-9155/51/8/004 (cited on p. 70).
- [93] M. Mazurenka, A. Jelzow, H. Wabnitz, D. Contini, L. Spinelli, A. Pifferi, R. Cubeddu, A. D. Mora, A. Tosi, F. Zappa, and R. Macdonald. “Non-contact time-resolved diffuse reflectance imaging at null source-detector separation”. In: *Optics Express* 20.1 (Jan. 2012), pp. 283–290. DOI: 10.1364/OE.20.000283 (cited on p. 71).
- [94] A. Liebert, H. Wabnitz, J. Steinbrink, H. Obrig, M. Möller, R. Macdonald, A. Villringer, and H. Rinneberg. “Time-Resolved Multidistance Near-Infrared Spectroscopy of the Adult Head: Intracerebral and Extracerebral Absorption Changes from Moments of Distribution of Times of Flight of Photons”. In: *Applied Optics* 43.15 (2004), pp. 3037–3047. DOI: 10.1364/AO.43.003037 (cited on pp. 72, 81, 134).

- [95] A. Duncan, J. H. Meek, M. Clemence, C. E. Elwell, L. Tyszczuk, M. Cope, and D. Delpy. “Optical pathlength measurements on adult head, calf and forearm and the head of the newborn infant using phase resolved optical spectroscopy”. In: *Physics in Medicine and Biology* 40.2 (Feb. 1995), pp. 295–304. DOI: 10.1088/0031-9155/40/2/007 (cited on p. 74).
- [96] M. Essenpreis, C. E. Elwell, M. Cope, P. van der Zee, S. R. Arridge, and D. T. Delpy. “Spectral dependence of temporal point spread functions in human tissues”. In: *Applied Optics* 32.4 (Feb. 1993), pp. 418–425. DOI: 10.1364/AO.32.000418 (cited on pp. 74, 75).
- [97] M. Ferrari, Q. Wei, R. A. De Blasi, V. Quaresima, and G. Zaccanti. “Variability of human brain and muscle optical pathlength in different experimental conditions”. In: *Proceedings of SPIE* 1888.1 (Sept. 1993), pp. 466–472. DOI: doi:10.1117/12.154666 (cited on pp. 74, 75).
- [98] A. Duncan, J. H. Meek, M. Clemence, C. E. Elwell, P. Fallon, L. Tyszczuk, M. Cope, and D. T. Delpy. “Measurement of Cranial Optical Path Length as a Function of Age Using Phase Resolved Near Infrared Spectroscopy”. In: *Pediatric Research* 39.5 (May 1996). PMID: 8726247, pp. 889–894. DOI: 10.1203/00006450-199605000-00025 (cited on p. 74).
- [99] H. Zhao, Y. Tanikawa, F. Gao, Y. Onodera, A. Sassaroli, K. Tanaka, and Y. Yamada. “Maps of optical differential pathlength factor of human adult forehead, somatosensory motor and occipital regions at multi-wavelengths in NIR”. In: *Physics in Medicine and Biology* 47.12 (June 2002), pp. 2075–2093. DOI: 10.1088/0031-9155/47/12/306 (cited on pp. 74, 75).
- [100] A. Katagiri, I. Dan, D. Tuzuki, M. Okamoto, N. Yokose, K. Igarashi, T. Hoshino, T. Fujiwara, Y. Katayama, Y. Yamaguchi, and K. Sakatani. “Mapping of Optical Pathlength of Human Adult Head at Multi-Wavelengths in Near Infrared Spectroscopy”. In: *Oxygen Transport to Tissue XXXI*. Ed. by E. Takahashi and D. F. Bruley. Vol. 662. Advances in Experimental Medicine and Biology. Springer US, 2010, pp. 205–212 (cited on pp. 74, 75, 110).
- [101] P. van der Zee, M. Cope, S. R. Arridge, M. Essenpreis, L. A. Potter, A. D. Edwards, J. S. Wyatt, D. C. McCormick, S. C. Roth, and E. O. Reynolds. “Experimentally measured optical pathlengths for the adult head, calf and forearm and the head of the newborn infant as a function of inter optode spacing”. In: *Advances in Experimental Medicine and Biology* 316 (1992). PMID: 1288074, pp. 143–153 (cited on p. 75).
- [102] C. Bonn ery, P.-O. Leclerc, M. Desjardins, R. Hoge, L. Bherer, P. Pouliot, and F. Lesage. “Changes in diffusion path length with old age in diffuse optical tomography”. In: *Journal of Biomedical Optics* 17.5 (May 2012), DOI: doi:10.1117/1.JBO.17.5.056002 (cited on pp. 75, 110).
- [103] E. Kirilina, A. Jelzow, A. Heine, M. Niessing, H. Wabnitz, R. Br uhl, B. Ittermann, A. M. Jacobs, and I. Tachtsidis. “The physiological origin of task-evoked systemic artefacts in functional near infrared spectroscopy”. In: *NeuroImage* 61.1 (May 2012), pp. 70–81. DOI: 10.1016/j.neuroimage.2012.02.074 (cited on pp. 78, 118, 122–124).

References

- [104] S. Carraresi, T. S. M. Shatir, F. Martelli, and G. Zaccanti. “Accuracy of a Perturbation Model to Predict the Effect of Scattering and Absorbing Inhomogeneities on Photon Migration”. In: *Appl. Opt.* 40.25 (Sept. 2001), pp. 4622–4632. DOI: 10.1364/AO.40.004622 (cited on p. 81).
- [105] A. Liebert, H. Wabnitz, and C. Elster. “Determination of absorption changes from moments of distributions of times of flight of photons: optimization of measurement conditions for a two-layered tissue model”. In: *Journal of Biomedical Optics* 17.5 (May 2012), DOI: doi:10.1117/1.JBO.17.5.057005 (cited on p. 85).
- [106] H. Wabnitz, P. Taroni, D. Grosenick, A. Pifferi, A. Torricelli, A. Liebert, M. Moeller, R. Cubeddu, and H. Rinneberg. “Performance assessment of two time-domain-scanning optical mammographs”. In: *Proc. SPIE 5138, Photon Migration and Diffuse-Light Imaging* (2003), pp. 281–289. DOI: 10.1117/12.500533 (cited on p. 95).
- [107] L. Spinelli, A. Torricelli, A. Pifferi, P. Taroni, and R. Cubeddu. “Experimental Test of a Perturbation Model for Time-Resolved Imaging in Diffusive Media”. In: *Applied Optics* 42.16 (June 2003), pp. 3145–3153. DOI: 10.1364/AO.42.003145 (cited on p. 95).
- [108] F. Martelli, S. Del Bianco, G. Zaccanti, A. Pifferi, A. Torricelli, A. Bassi, P. Taroni, and R. Cubeddu. “Phantom validation and in vivo application of an inversion procedure for retrieving the optical properties of diffusely layered media from time-resolved reflectance measurements”. In: *Optics Letters* 29.17 (Sept. 2004), pp. 2037–2039. DOI: 10.1364/OL.29.002037 (cited on p. 95).
- [109] A. Pifferi, A. Torricelli, A. Bassi, P. Taroni, R. Cubeddu, H. Wabnitz, D. Grosenick, M. Möller, R. Macdonald, J. Swartling, T. Svensson, S. Andersson-Engels, R. L. P. van Veen, H. J. C. M. Sterenborg, J.-M. Tualle, H. L. Nghiem, S. Avrillier, M. Whelan, and H. Stamm. “Performance assessment of photon migration instruments: the MEDPHOT protocol”. In: *Applied Optics* 44.11 (Apr. 2005), pp. 2104–2114. DOI: 10.1364/AO.44.002104 (cited on pp. 95, 114).
- [110] B. W. Pogue and M. S. Patterson. “Review of tissue simulating phantoms for optical spectroscopy, imaging and dosimetry”. In: *Journal of Biomedical Optics* 11.4 (Sept. 2006), DOI: doi:10.1117/1.2335429 (cited on p. 95).
- [111] H. Wabnitz, A. Pifferi, A. Torricelli, D. R. Taubert, M. Mazurenka, O. Steinkellner, A. Jelzow, A. Farina, I. Bargigia, D. Contini, M. Caffini, L. Zucchelli, L. Spinelli, P. Sawosz, A. Liebert, R. Macdonald, and R. Cubeddu. “Assessment of basic instrumental performance of time-domain optical brain imagers”. In: *Proceedings of SPIE* 7896.1 (Feb. 2011), DOI: doi:10.1117/12.874654 (cited on p. 95).
- [112] J. C. Hebden, J. Brunker, T. Correia, B. D. Price, A. P. Gibson, and N. L. Everdell. “An electrically-activated dynamic tissue-equivalent phantom for assessment of diffuse optical imaging systems”. In: *Physics in Medicine and Biology* 53.2 (Jan. 2008), pp. 329–337. DOI: 10.1088/0031-9155/53/2/002 (cited on p. 95).
- [113] R. L. Barbour, R. Ansari, R. Al abdi, H. L. Graber, M. B. Levin, Y. Pei, C. H. Schmitz, and Y. Xu. “Validation of near infrared spectroscopic (NIRS) imaging using programmable phantoms”. In: *Proc. SPIE* 6870 (Feb. 2008), pp. 687002–687002. DOI: 10.1117/12.769160 (cited on p. 95).

- [114] L. Spinelli, A. Pifferi, A. Torricelli, R. Cubeddu, P. Di Ninni, F. Martelli, G. Zaccanti, F. Foschum, A. Kienle, M. Mazurenka, H. Wabnitz, M. Kacprzak, N. Zolek, D. Milej, and A. Liebert. “Towards the Definition of Accurately Calibrated Liquid Phantoms for Photon Migration at NIR Wavelengths: A Multi-Laboratory Study”. In: *Biomedical Optics*. OSA Technical Digest (CD). Optical Society of America, Apr. 2010, BTuD47 (cited on p. 95).
- [115] A. Kienle, T. Glanzmann, G. Wagnières, and H. v. d. Bergh. “Investigation of Two-Layered Turbid Media with Time-Resolved Reflectance”. In: *Applied Optics* 37.28 (Oct. 1998), pp. 6852–6862. DOI: 10.1364/AO.37.006852 (cited on p. 96).
- [116] M. A. Franceschini, S. Fantini, L. A. Paunescu, J. S. Maier, and E. Gratton. “Influence of a Superficial Layer in the Quantitative Spectroscopic Study of Strongly Scattering Media”. In: *Applied Optics* 37.31 (Nov. 1998), pp. 7447–7458. DOI: 10.1364/AO.37.007447 (cited on p. 96).
- [117] A. Liemert and A. Kienle. “Light diffusion in N-layered turbid media: frequency and time domains”. In: *Journal of Biomedical Optics* 15.2 (2010), p. 025002. DOI: 10.1117/1.3368682 (cited on pp. 96, 102, 140).
- [118] P. Di Ninni, F. Martelli, and G. Zaccanti. “The use of India ink in tissue-simulating phantoms”. In: *Optics Express* 18.26 (2010), pp. 26854–26865. DOI: 10.1364/OE.18.026854 (cited on p. 96).
- [119] P. Di Ninni, F. Martelli, and G. Zaccanti. “Intralipid: towards a diffusive reference standard for optical tissue phantoms”. In: *Physics in Medicine and Biology* 56.2 (Jan. 2011), N21–N28. DOI: 10.1088/0031-9155/56/2/N01 (cited on p. 96).
- [120] F. Martelli and G. Zaccanti. “Calibration of scattering and absorption properties of a liquid diffusive medium at NIR wavelengths. CW method”. In: *Optics Express* 15.2 (Jan. 2007), pp. 486–500. DOI: 10.1364/OE.15.000486 (cited on p. 97).
- [121] Hamamatsu Corporation. *Datasheet of the Hamamatsu R10467U-40 Detector*. 2012 (cited on p. 98).
- [122] Becker & Hickl GmbH. *The HPM-100-40 Hybrid Detector (Application Note)*. 2009. URL: <http://www.becker-hickl.de/pdf/hpm-appnote03.pdf> (cited on p. 98).
- [123] S. Cova, M. Ghioni, A. Lacaita, C. Samori, and F. Zappa. “Avalanche photodiodes and quenching circuits for single-photon detection”. In: *Applied Optics* 35.12 (Apr. 1996), p. 1956. DOI: 10.1364/AO.35.001956 (cited on p. 98).
- [124] A. Torricelli, D. Contini, A. Pifferi, M. Caffini, R. Re, L. Zucchelli, and L. Spinelli. “Time domain functional NIRS imaging for human brain mapping”. In: *NeuroImage* (June 2013). DOI: 10.1016/j.neuroimage.2013.05.106 (cited on p. 104).
- [125] H. Wabnitz, A. Jelzow, M. Mazurenka, O. Steinkellner, R. Macdonald, A. Pifferi, A. Torricelli, D. Contini, L. M. G. Zucchelli, L. Spinelli, R. Cubeddu, D. Milej, N. Zolek, M. Kacprzak, P. Sawosz, A. Liebert, S. Magazov, J. C. Hebden, F. Martelli, P. Di Ninni, and G. Zaccanti. “Performance assessment of time-domain optical brain imagers: a multi-laboratory study”. In: *Proc. SPIE* 8583. Feb. 2013, pp. 85830L–85830L. DOI: 10.1117/12.2002438 (cited on p. 104).
- [126] C. Sato, T. Yamaguchi, M. Seida, Y. Ota, I. Yu, Y. Iguchi, M. Nemoto, and Y. Hoshi. “Intraoperative monitoring of depth-dependent hemoglobin concentration changes during carotid endarterectomy by time-resolved spectroscopy”. In: *Applied Optics* 46.14 (2007), pp. 2785–2792. DOI: 10.1364/AO.46.002785 (cited on p. 110).

References

- [127] H. Kakuta, H. Kawaguchi, and E. Okada. “A Head Phantom for Use in Near Infrared Topography for Brain Function Measurements”. In: *Digital Holography and Three-Dimensional Imaging*. OSA Technical Digest (CD). Optical Society of America, Apr. 2010, JMA58 (cited on pp. 113, 114).
- [128] M. Firbank and D. T. Delpy. “A design for a stable and reproducible phantom for use in near infra-red imaging and spectroscopy”. In: *Physics in Medicine and Biology* 38.6 (June 1993), pp. 847–853. DOI: 10.1088/0031-9155/38/6/015 (cited on p. 114).
- [129] D. Milej, M. Kacprzak, N. Żołek, P. Sawosz, A. Gerega, R. Maniewski, and A. Liebert. “Advantages of fluorescence over diffuse reflectance measurements tested in phantom experiments with dynamic inflow of ICG”. In: *Opto-Electronics Review* 18.2 (Apr. 2010), pp. 208–213. DOI: 10.2478/s11772-010-0013-z (cited on p. 114).
- [130] I. Tachtsidis, T. S. Leung, A. Chopra, P. H. Koh, C. B. Reid, and C. E. Elwell. “False positives in functional near-infrared topography”. In: *Advances in Experimental Medicine and Biology* 645 (2009). PMID: 19227487, pp. 307–314. DOI: 10.1007/978-0-387-85998-9_46 (cited on pp. 117, 118).
- [131] N. M. Gregg, B. R. White, B. W. Zeff, A. J. Berger, and J. P. Culver. “Brain specificity of diffuse optical imaging: improvements from superficial signal regression and tomography”. In: *Frontiers in Neuroenergetics* (2010). DOI: 10.3389/fnene.2010.00014 (cited on p. 118).
- [132] T. Takahashi, Y. Takikawa, R. Kawagoe, S. Shibuya, T. Iwano, and S. Kitazawa. “Influence of skin blood flow on near-infrared spectroscopy signals measured on the forehead during a verbal fluency task”. In: *NeuroImage* 57.3 (Aug. 2011), pp. 991–1002. DOI: 10.1016/j.neuroimage.2011.05.012 (cited on pp. 118, 125).
- [133] D. Y. Kimberg and M. J. Farah. “A unified account of cognitive impairments following frontal lobe damage: The role of working memory in complex, organized behavior.” In: *Journal of Experimental Psychology: General* 122.4 (1993), pp. 411–428. DOI: 10.1037/0096-3445.122.4.411 (cited on p. 118).
- [134] T. S. Braver and S. R. Bongiolatti. “The Role of Frontopolar Cortex in Subgoal Processing during Working Memory”. In: *NeuroImage* 15.3 (Mar. 2002), pp. 523–536. DOI: 10.1006/ning.2001.1019 (cited on p. 118).
- [135] W. N. J. M. Colier, V. Quaresima, B. Oeseburg, and M. Ferrari. “Human motor-cortex oxygenation changes induced by cyclic coupled movements of hand and foot”. In: *Experimental Brain Research* 129.3 (1999), pp. 457–461. DOI: 10.1007/s002210050913 (cited on p. 121).
- [136] P. Drummond. “Adrenergic receptors in the forehead microcirculation”. In: *Clinical Autonomic Research* 6.1 (1996), pp. 23–27. DOI: 10.1007/BF02291402 (cited on p. 125).
- [137] R. M. Birn, M. A. Smith, T. B. Jones, and P. A. Bandettini. “The respiration response function: The temporal dynamics of fMRI signal fluctuations related to changes in respiration”. In: *NeuroImage* 40.2 (Apr. 2008), pp. 644–654. DOI: 10.1016/j.neuroimage.2007.11.059 (cited on p. 127).
- [138] H. Obrig. “NIRS in clinical neurology — a ‘promising’ tool?” In: *NeuroImage* (2013). DOI: 10.1016/j.neuroimage.2013.03.045 (cited on p. 127).

- [139] S. Leistner, T. Sander, M. Wachs, M. Burghoff, G. Curio, L. Trahms, and B.-M. Mackert. “Differential Infraslow (<0.1 Hz) Cortical Activations in the Affected and Unaffected Hemispheres From Patients With Subacute Stroke Demonstrated by Noninvasive DC-Magnetoencephalography”. In: *Stroke* 40.5 (Mar. 2009), pp. 1683–1686. DOI: 10.1161/STROKEAHA.108.536110 (cited on p. 127).
- [140] S. Leistner, T. Sander-Thoemmes, H. Wabnitz, M. Moeller, M. Wachs, G. Curio, R. Macdonald, L. Trahms, and B.-M. Mackert. “Non-invasive simultaneous recording of neuronal and vascular signals in subacute ischemic stroke”. In: *Biomedizinische Technik/Biomedical Engineering* 56.2 (Apr. 2011), pp. 85–90 (cited on pp. 127, 128).
- [141] M. D’Esposito, L. Y. Deouell, and A. Gazzaley. “Alterations in the BOLD fMRI signal with ageing and disease: a challenge for neuroimaging”. In: *Nature Reviews Neuroscience* 4.11 (Nov. 2003), pp. 863–872. DOI: 10.1038/nrn1246 (cited on p. 127).
- [142] H. Girouard and C. Iadecola. “Neurovascular coupling in the normal brain and in hypertension, stroke, and Alzheimer disease”. In: *Journal of Applied Physiology* 100.1 (Jan. 2006), pp. 328–335. DOI: 10.1152/jappphysiol.00966.2005 (cited on p. 127).
- [143] C. Hock, K. Villringer, F. Müller-Spahn, M. Hofmann, S. Schuh-Hofer, H. Heekeren, R. Wenzel, U. Dirnagl, and A. Villringer. “Near Infrared Spectroscopy in the Diagnosis of Alzheimer’s Disease”. In: *Annals of the New York Academy of Sciences* 777.1 (1996), 22–29. DOI: 10.1111/j.1749-6632.1996.tb34397.x (cited on p. 127).
- [144] C. Hock, K. Villringer, F. Müller-Spahn, R. Wenzel, H. Heekeren, S. Schuh-Hofer, M. Hofmann, S. Minoshima, M. Schwaiger, U. Dirnagl, and A. Villringer. “Decrease in parietal cerebral hemoglobin oxygenation during performance of a verbal fluency task in patients with Alzheimer’s disease monitored by means of near-infrared spectroscopy (NIRS) — correlation with simultaneous rCBF-PET measurements”. In: *Brain Research* 755.2 (1997), pp. 293–303. DOI: 10.1016/S0006-8993(97)00122-4 (cited on p. 127).
- [145] C. Iadecola. “Neurovascular regulation in the normal brain and in Alzheimer’s disease”. In: *Nature Reviews Neuroscience* 5.5 (2004), pp. 347–360. DOI: 10.1038/nrn1387 (cited on p. 127).
- [146] N. K. Logothetis, J. Pauls, M. Augath, T. Trinath, and A. Oeltermann. “Neurophysiological investigation of the basis of the fMRI signal”. In: *Nature* 412.6843 (July 2001), pp. 150–157. DOI: 10.1038/35084005 (cited on p. 128).
- [147] A. Shmuel, M. Augath, A. Oeltermann, and N. K. Logothetis. “Negative functional MRI response correlates with decreases in neuronal activity in monkey visual area V1”. In: *Nature Neuroscience* 9.4 (2006), pp. 569–577. DOI: 10.1038/nn1675 (cited on p. 128).
- [148] B. Li and R. D. Freeman. “High-Resolution Neurometabolic Coupling in the Lateral Geniculate Nucleus”. In: *The Journal of Neuroscience* 27.38 (Sept. 2007), pp. 10223–10229. DOI: 10.1523/JNEUROSCI.1505-07.2007 (cited on p. 128).

References

- [149] T. H. Sander, A. Liebert, B. M. Mackert, H. Wabnitz, S. Leistner, G. Curio, M. Burghoff, R. Macdonald, and L. Trahms. “DC-magnetoencephalography and time-resolved near-infrared spectroscopy combined to study neuronal and vascular brain responses”. In: *Physiological Measurement* 28.6 (June 2007), pp. 651–664. DOI: 10.1088/0967-3334/28/6/004 (cited on pp. 128–131, 141).
- [150] W. Ou, I. Nissilä, H. Radhakrishnan, D. A. Boas, M. S. Hämäläinen, and M. A. Franceschini. “Study of neurovascular coupling in humans via simultaneous magnetoencephalography and diffuse optical imaging acquisition”. In: *NeuroImage* 46.3 (July 2009), pp. 624–632. DOI: 10.1016/j.neuroimage.2009.03.008 (cited on p. 128).
- [151] B.-M. Mackert, S. Leistner, T. Sander, A. Liebert, H. Wabnitz, M. Burghoff, L. Trahms, R. Macdonald, and G. Curio. “Dynamics of cortical neurovascular coupling analyzed by simultaneous DC-magnetoencephalography and time-resolved near-infrared spectroscopy”. In: *NeuroImage* 39.3 (Feb. 2008), pp. 979–986. DOI: 16/j.neuroimage.2007.09.037 (cited on p. 128).
- [152] S. P. Koch, S. Koendgen, R. Bourayou, J. Steinbrink, and H. Obrig. “Individual alpha-frequency correlates with amplitude of visual evoked potential and hemodynamic response”. In: *NeuroImage* 41.2 (June 2008), pp. 233–242. DOI: 10.1016/j.neuroimage.2008.02.018 (cited on p. 128).
- [153] C. S. Herrmann. “Human EEG responses to 1–100 Hz flicker: resonance phenomena in visual cortex and their potential correlation to cognitive phenomena”. In: *Experimental Brain Research* 137.3 (2001), pp. 346–353. DOI: 10.1007/s002210100682 (cited on pp. 129, 130).
- [154] R. Kronland-Martinet, J. Morlet, and A. Grossmann. “Analysis of Sound Patterns through Wavelet Transforms”. In: *International Journal of Pattern Recognition and Artificial Intelligence* 01.02 (Aug. 1987), pp. 273–302. DOI: 10.1142/S0218001487000205 (cited on p. 129).
- [155] G. Pfurtscheller, C. Brunner, A. Schlögl, and F. Lopes da Silva. “Mu rhythm (de)synchronization and EEG single-trial classification of different motor imagery tasks”. In: *NeuroImage* 31.1 (2006), pp. 153–159. DOI: 10.1016/j.neuroimage.2005.12.003 (cited on p. 130).
- [156] D. Boas, J. Culver, J. Stott, and A. Dunn. “Three dimensional Monte Carlo code for photon migration through complex heterogeneous media including the adult human head”. In: *Optics Express* 10.3 (Feb. 2002), pp. 159–170 (cited on p. 133).
- [157] G. Strangman, M. A. Franceschini, and D. A. Boas. “Factors affecting the accuracy of near-infrared spectroscopy concentration calculations for focal changes in oxygenation parameters”. In: *NeuroImage* 18.4 (Apr. 2003), pp. 865–879. DOI: 10.1016/S1053-8119(03)00021-1 (cited on p. 133).
- [158] M. A. Yücel, T. J. Huppert, D. A. Boas, and L. Gagnon. “Calibrating the BOLD signal during a motor task using an extended fusion model incorporating DOT, BOLD and ASL data”. In: *NeuroImage* 61.4 (July 2012), pp. 1268–1276. DOI: 10.1016/j.neuroimage.2012.04.036 (cited on p. 136).